THE UNIVERSITY *of* EDINBURGH

Phenolic Oxime Copper Complexes:

A Gas Phase Investigation

Benjamin David Roach

Doctor of Philosophy

University of Edinburgh

November 2010

Dedicated to the Memory of

John Bennett Fenn 1917–2010

“It’s character building”

Peter Tasker

“Humanity needs practical men, who get the most out of their work, and, without forgetting the general good, safeguard their own interests. But humanity also needs dreamers, for whom the disinterested development of an enterprise is so captivating that it becomes impossible for them to devote their care to their own material profit. Without doubt, these dreamers do not deserve wealth, because they do not desire it. Even so, a well-organized society should assure to such workers the efficient means of accomplishing their task, in a life freed from material care and freely consecrated to research.”

Marie Curie

Preface and Declaration

Since graduating from the University of Manchester in 2006 with a MChem (Hons) degree in Chemistry with German, the author has been engaged in a programme of full time research under the supervision of Professor P. A. Tasker at the University of Edinburgh.

No part of the work referred to in this thesis has been submitted previously in whole or in part for another degree or qualification from this or any other university or institute of learning. In accordance with the regulations this thesis does not exceed 70,000 words in length.

Benjamin David Roach
November 2010

Abstract

This thesis explores the use of mass spectrometry to define the strengths, and understand solution phase speciation of phenolic oxime-based solvent extractants of the types used in the hydrometallurgical recovery of copper.

Chapter 1 reviews briefly the current extraction technology for copper and focuses on hydrometallurgy and the use of phenolic oximes such as 5-nonylsalicylaldoxime. The modification of the latter to improve extraction efficiency is discussed, focussing on the introduction of X-substituents in the 3 position of the benzene ring. Modern mass spectrometry techniques are also discussed with a focus on their application to inorganic systems and their use in achieving the aims of this thesis, as defined above. The work described in chapter 2 involves the development of collision induced dissociation (CID) techniques to determine the relative gas phase stabilities of copper complex anions of the type $[Cu(\mathbf{L})(\mathbf{L}\text{-H})]^-$, where **LH** is a 5-alkyl-3-X-2-hydroxybenzaldehyde oximes and X a range of substituents. The importance of inter-ligand interactions in the *outer*-coordination sphere and their influence on gas phase anion stability, as defined by CID, is reported.

The work described in Chapter 2 on CID is extended in chapter 3 and looks at the effect of charge, of ligand type, **LH**, and of the nature of the metal on the stability of ionic forms of $[M(\mathbf{L})_2]$ complexes, where L**H** is extended to include 5-alkyl-2-hydroxyphenylethanone oximes . The effects of substitution at the azomethine carbon atom and at the 3-position of the benzene ring and of variation of the nature of the metal on the ion dissociation mechanisms are shown to have a major influence on ion stability under CID conditions.

In chapter 4 density functional theory calculations have been used to investigate the influences of substitution at the azomethine carbon atom and at the 3-position of the benzene ring and of variation of the nature of the metal on the gas phase structures of the neutral complexes, $[M(\mathbf{L})_2]$. Gas phase deprotonation and dimerisation enthalpies of the ligands, **LH**, and enthalpies of formation of $[M(\mathbf{L})_2]$ complexes have been

calculated and correlates with experimentally determined ligand extraction strength. The ligand type has been extended to include 3-X-2-hydroxybenzaldehyde hydrazones, which have previously been shown to have lower distribution coefficients for copper than the analogous 3-X-substituted oximes. The calculated gas phase formation enthalpies for $[M(\mathbf{L})_2]$ show a strong correlation with the strengths as extractants **LH**, measured as their $pH_{0.5}$ values for metal uptake.

Chapter 5 considers whether mass spectrometry can be used to define the solution equilibria when two different oxime-based ligands, **LXH** and **LYH,** compete for Cu(II) in a single phase solution. It has been established that shifts in the relative peak intensities of deprotonated ions derived from the Cu(II) complexes, $[Cu(\mathbf{LX})_2]$, $[Cu(\mathbf{LY})_2]$ and $[Cu(\mathbf{LX})(\mathbf{LY})]$ reflect changes in the solution composition.

The work described in chapter 6 extends the study of solution phase speciation using mass spectrometry. When the Cu(II) and proton concentrations of solutions were varied distinct changes in the resulting electrospray mass spectra were observed and the resulting species were identified using CID and high resolution mass spectrometry. A novel, $[Cu_3(\mathbf{L}\text{-}H)_3\text{-}\mu_3\text{-}O/OH]^-$ species is determined to be a major component of solutions where Cu(II) concentrations are equal to/greater than the **LH** concentration. Various 3-X-2-hydroxybenzaldehyde oximes ($X = CH_2NR_2$) were synthesised. The incorporation of a protonatable arm in the 3-position enabled trinuclear complexes, $[Cu_3(\mathbf{L}\text{-}H)_3\text{-}\mu_3\text{-}OH]$, to be isolated and fully characterized, including two X-ray determined crystal structures.

Acknowledgements

I must thank first and foremost my supervisor, Prof. Peter Tasker, whose support, guidance, knowledge and enthusiasm has been a constant source of inspiration. I think he'd have to agree that this thesis has been a definite learning experience for us both. Thanks also go to Dr. Bridgette Duncombe for her patience, drive and knowledge over the initial period of my thesis.

Thanks go to my industrial sponsors CYTEC, in particular Eduardo Kamenetzky, John Campbell, Mike Piquette, Doug Harris and everyone else in the MEP group for their support and useful discussions during my time in Stamford

Special thanks go to Patricia Richardson for all her help battling against Gaussian and Fraser white for his unwavering tolerance of my crystals/crystal submission forms/constant emails.

I have to thank the Tasker group past and present for keeping me laughing over the years, with a special thanks to Dr. Dave Henderson who was always available to offer help and guidance and did appreciate a good moan. I've made too many friends here in Edinburgh to thank personally but thanks go to Robbos, who, although they aren't as cool as us, have always been up for a night out or a Julies at lunch and the Geology crew, whose wild parties, dinners, days out in Helmut and Balkanaramaring have made these last three years a lot of fun.

I have to thank Charlotte and Lynsey, who have kept me sane over the past three years.....or should that be making me *seem* sane in comparison ☺

I want to thank my Family, both blood and adoptive, for their support throughout the entirety of my studies. Even though for the most part they take immense pleasure in asking me when I'm going to get a *real* job!!! I want to especially thank my Mum as without her constant support (both emotionally and financially) I'd probably be a broken wreck somewhere.

And last but not least I need to thank Romain, without whom not only would i not be in Edinburgh, I probably wouldn't even be in research.

Table of Contents

CHAPTER 2

CHAPTER 3

CHAPTER 5

CHAPTER 6

Ligands

Ligand	X	R	Name
L1H	H	*t*-Bu	5-*t*-Butyl-2-hydroxybenzaldehyde oxime
L2H	Me	*t*-Bu	5-*t*-Butyl-2-hydroxy-3-methylbenzaldehyde oxime
L3H	*t*-Bu	*t*-Bu	3,5-di-*t*-Butyl-2-hydroxybenzaldehyde oxime
L4H	NO_2	*t*-Bu	5-*t*-Butyl-2-hydroxy-3-nitrobenzaldehyde oxime
L5H	Cl	*t*-Bu	5-*t*-Butyl-3-chloro-2-hydroxybenzaldehyde oxime
L6H	Br	*t*-Bu	3-Bromo-5-*t*-butyl-2-hydroxybenzaldehyde oxime
L7H	OMe	*t*-Bu	5-*t*-Butyl-2-hydroxy-3-methoxybenzaldehyde oxime
L8H	H	*t*-Oct	5-*t*-Octyl-2-hydroxybenzaldehyde oxime

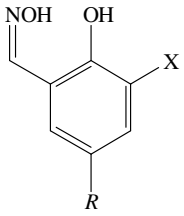

Ligand	X	Name
L9H	H	5-*t*-Butyl-2-hydroxybenzaldehyde methylhydrazone
L10H	OMe	5-*t*-Butyl-2-hydroxy-3-methoxybenzaldehyde methylhydrazone
L11H	Br	3-Bromo-5-*t*-butyl-2-hydroxybenzaldehyde methylhydrazone
L12H	NO_2	5-*t*-Butyl-2-hydroxy-3-nitrobenzaldehyde methylhydrazone

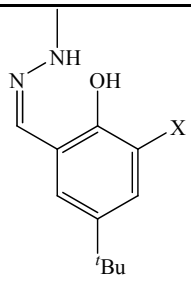

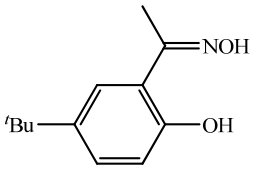

L1bH: 5-*t*-Butyl-2 -hydroxybenzaldehyde methylketoxime

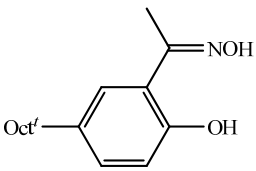

L8bH: 5-*t*-Octyl-2 -hydroxybenzaldehyde methylketoxime

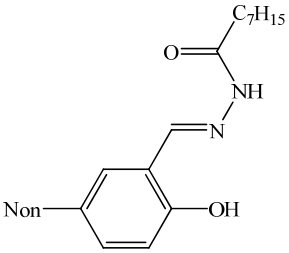

L13H: N-(5-nonyl-2-hydroxyphenyl)methylidene] heptane hydrazide

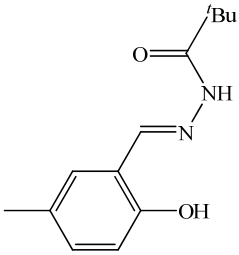

L14H: N-(5-methyl-2-hydroxyphenyl)methylide ne]iso-butane hydrazide

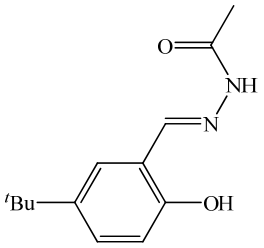

L15H: N-(5-*tert*-butyl-2-hydroxyphenyl)methylidene] methane hydrazide

L16H: 2-hydroxy-5-*t* -butyl-3-(piperidin-1 -ylmethyl)benzaldehyde oxime

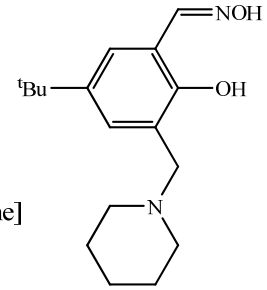

L17H: 2-hydroxy-5-*t* -butyl-3-(morpholin-1 -ylmethyl)benzaldehyde oxime

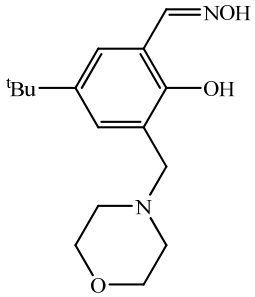

L18H: 2-hydroxy-5-*t* -butyl-3-(4-methyl-piperizin-1-ylmethyl) benzaldehyde oxime

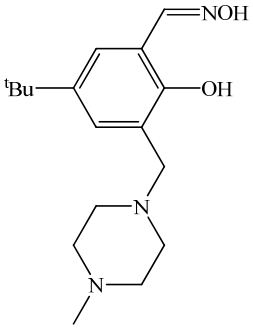

Abbreviations

Δ	change in
δ	chemical shift
°	Degrees
<	less than
≤	less than or equal to
>	greater than
≥	greater than or equal to
%	percent
±	plus or minus
~	approximately
√	square route
ν	wavenumber (IR)
λ	wavelength
Å	Angstrom
aq	aqueous phase
anal.	Analysis
AIC	analyte ion current
AGC	Automatic Gain Control
B3LYP	Becke's three parameter exchange functional and non-local correlation functional of Lee, Yang and Parr
br	broad (spectroscopy)
Br	Bromo-
BuOH	butan-1-ol
cf.	*Cofere*; see also
C_6H_5	phenyl
C_9H_{19}	nonyl
CID	Collision Induced Dissociation (MS)
Cl	Chloro-
cm^{-1}	wavenumber (IR)
d	doublet (NMR)

DFT	Density Functional Theory
ΔE	difference in energy
ed.	editor(s)
e.g.	for example
EPR	Electron Paramagnetic Resonance
ESI	electrospray (MS)
et al	*et alli* (and others)
EtO	ethoxy
EtOH	ethanol
FTICR	Fourier Transform ion cyclotron resonance (mass spectrometry)
FTIR	Fourier Transform Infrared
g	gram; gaseous;.
$\hat{H}$	Hamiltonian
ΔH	difference in enthalpy
HF	Hartree-Fock
hr	hour
ICP-OES	inductively coupled plasma optical emission spectroscopy
i.e.	that is
in situ	in the natural place
in vacuo	under vacuum
IR	infrared
K	degree Kelvin; equilibrium constant; formation constant.
kJ mol^{-1}	kilojoules per mole
∇	Laplacian operater
LCQ	Double octapole ion trap mass spectrometer
m	multiplet (NMR), metre
m	*meta*
M	molar
Me	methyl
MeO	methoxy
MeOH	methanol
MH^+	protonated parent ion
MHz	frequency (NMR)

MJ/kg	megajoules per kilogram
μL	microlitre
μM	micromolar
mg	milligram
ml	millilitre
mm	millimetre
mmol	millimole
MM	Molecular Mechanics
Mod	equilibrium modifier
MOF	metal-organic framework
mol	mole
mol dm^{-3}	mole per litre
MP2	truncated second order Moller Plesset
MS	mass spectrometry
MS/MS	tandem mass spectrometry
MS^n	mass spectrometry (multi-stage analysis)
m/z	mass to charge ratio
n	normal; number.
NCE	Normalised Collision Energy
NMR	nuclear magnetic resonance
NO_2	Nitro-
Ω	oscillating frequency
o	*ortho*
obs.	observed
org	organic phase
p	*para*
P50	5-nonyl-2-hydroxybenzaldehyde oxime
pH	$-\log_{10}[H^+]$
$pH_{0.5}$	pH when D = 0
pK_a	$-\log_{10}K_a$
pls	pregnant leach solution
POM	poly-oxometallate
ppm	parts per million

py	pyridine
q	quartet (NMR)
QIT	Quadrupole Ion Trap (mass spectrometer)
QM	Quantum Mechanics
Q-ToF	Quadrupole Timo-of-Flight (mass spectrometer)
r	ion trap radius
s	singlet (NMR); strong (IR); second; solid
SX	solvent extraction
t	triplet (NMR)
t	tertiary
T	temperature
tert	tertiary
^{t}Bu	tertiary butyl
^{t}Oct	tertiary octyl
TIC	total ion current
trans	transoid
TXIB	2,2,4-trimethyl-1,3-pentanediol diisobutyrate
U	amplitude
UV-Vis	ultraviolet-visible
V	voltage
via	by way of
vs.	versus
XRD	X-Ray Diffraction

Phenolic Oxime Copper Complexes:
A Gas Phase Investigation

CHAPTER 1:

Introduction

An introduction into metal extraction, mass spectrometry and the substitution of phenolic oximes

Table of Contents

1.1 Thesis Aims

Although hydrometallurgical recovery of copper using phenolic oxime ligands is responsible for up to a third of the worlds copper production,[1] understanding of the extraction process is still limited. This thesis provides an insight into the chemistry, gas phase speciation and the strength and selectivity of phenolic oxime ligands in extraction systems.

The principle theme of this thesis is the use of mass spectrometry to investigate the gas phase speciation and stability of copper complexes of salicylaldoxime based extractants and the effects of substituting in the 3 position (Figure 1.1)

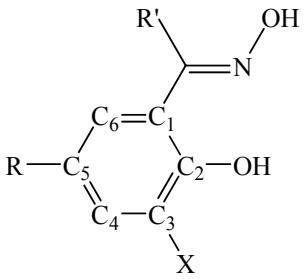

Figure 1.1: The basic phenolic oxime ligand indicating the substituted 3-position. X = Br, NO_2, Cl, OMe, Me, H, ^{t}Bu.[2]

This chapter gives an introduction into the chemistry of the recovery of copper from its constituent ores, in particular hydrometallurgical recovery of copper using phenolic oxime ligands. A brief introduction of mass spectrometry and its potential application in metal extraction systems is given, as is some background into the modification of phenolic oximes in previous studies.[2,3] The final Section of this chapter introduces molecular modelling and density functional theory as a means of investigating structure in the gas phase.

1.2 Copper Extraction

There are over two hundred known copper containing minerals, including malachite (copper carbonate hydroxide [$Cu_2(CO_3)(OH)_2$]), azurite (copper carbonate hydroxide, [$Cu_3(CO_3)_2(OH)_2$]) and azurite (hydrated copper aluminium phosphate, [$CuAl_6(PO_4)_4(OH)_8.5(H_2O)$]). Only a small number have any importance as copper ores such as cuprite (copper oxide, Cu_2O) and chalcopyrite (copper iron sulphide, $CuFeS_2$) due to their relatively high copper content. Copper has an extremely high affinity for sulphur which combined with the fact that the composition of early Earth's atmosphere had an abundance of SO_2 and CO_2 and fairly low levels of O_2 contributes directly to its occurrence in the earth's crust.[4,5] Consequently the principal minerals are sulphides, with chalcopyrite estimated to account for 50% of all copper deposits.[6] However, the purity and "quality" of the chalcopyrite ore is not always high as it is often contaminated by a variety of other transition elements such as Co, Ni, Mn and Zn as well as Sn which substitute both the Cu and Fe ions. Se, Fe and As are also found as substitutes for sulphur, and trace amounts of Ag, Au, Pt, Pd, Pb, V, Cr, In, Al and Sb have also been reported.[7]

1.3 Extractive Metallurgy

.

In order to purify the metals of value, four steps must be taken:

- *concentration* of the metals of value,
- *separation* from the unwanted metals of the ore,
- *reduction* of the oxidised metals of value, and
- *refinement* to a purity suitable for commercial use.

These four steps comprise the basis of extractive metallurgy.[8]

1.3.1 Pyrometallurgy

Pyrometallurgy is a type of extractive metallurgy. It consists of the thermal treatment of minerals, metallurgical ores and concentrates to induce physical and chemical transformations in the materials.[9] It is a technique that he been used for thousands of years with evidence suggesting that pyrometallurgical extraction of copper has been carried out since 4000BC.[10,11] It is therefore an extremely well developed process which can be carried out on extremely large scales and is a very profiTable extraction technique for high-grade ore bodies.

The major disadvantage of pyrometallurgy is an environmental one, as well as the high energy requirements, pyrometallurgical extraction of copper is a fairly polluting process. Arsenic and antimony are both by-products, with the milling and smelting of copper ores currently releasing an estimated 7×10^3 – 7×10^4 metric tons of toxic metals into the aquatic atmosphere.[12] Gaseous waste is also a major problem with the emission of toxic and greenhouse gases such as sulphur dioxide and carbon dioxide together with fine dusts (also known as particulate matter and defined as being under 10nm in diameter)[13] contributing to the 'enhanced greenhouse effect'. In 2000, 200,000 tonnes of sulphur and 60,000 tonnes of particulates were released by one Chilean smelter alone (Chuquicamata).[13] Another problem faced by the pyrometallurgical process is that it is not cost effective when applied to low-grade ores .[14]

Pyrometallurgy is still an important metal extraction technique but other methods are needed which are capable of processing the large stocks of low-grade ores with a higher level of selectivity at lower economic costs and which can comply with new environmental regulations.

1.3.2 Hydrometallurgy

Hydrometallurgy is the processing of an ore *via* dissolution, separation, purification and precipitation of the desired metal using an aqueous solution. It can be defined as "the use of wet (aqueous) chemistry for the recovery of metals".[14,15] The particular technology implemented depends on the target metal and its chemical composition in the source material. Hydrometallurgy is also applied in cleanup operations for the recovery of heavy metals from contaminated industrial wastelands and acid mining drainage systems.[16] Well established industrial processes include the recovery of aluminium, titanium, chromium, cobalt, nickel, copper, zinc, palladium, silver, cadmium, platinum, gold, lead, and uranium from their ores or pyrometallurgical wastes.[8,16,17]

In contrast to pyrometallurgy the technique is relatively modern, with the first major industrial application being the purification of gold by the cyanidation process dating from 1887.[15,18]

The massive increases in copper production in the late 20th and early 21st century have led to the necessity of processing lower grade ores, *i.e.* ores with less copper content, in order to satisfy demand. In medieval processing of copper, the copper content of exploited ores averaged around 8%, whereas in the mid 1990s this value had decreased to an average of 0.9%.[14] Since the world supplies of high-grade ores are decreasing rapidly, techniques are required for the recovery of metals from low grade ores, transition ores, dump stocks and other residues.

1.3.3 Solvent Extraction

Solvent extraction is the most efficiently applied method in the hydrometallurgical extraction of copper. Solvent extraction is typically defined as "the separation of materials of different chemical types and solubilities by selective solvent action" *i.e.* some materials are more soluble in one solvent than in another, hence a preferential

extractive action is observed. An idealised flow sheet for the recovery of copper *via* solvent extraction from oxidic ores can be divided into four key stages, leaching, extraction, stripping and electrowinning. (Figure 1.2)

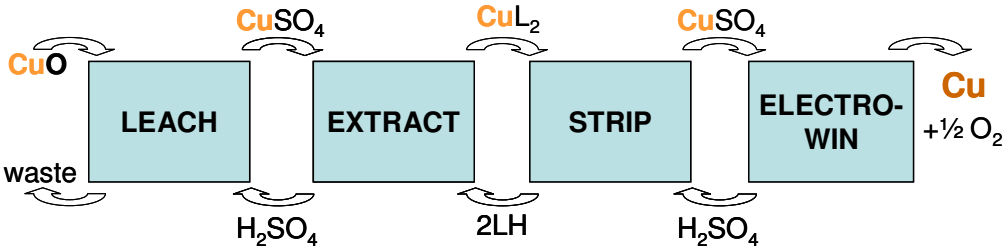

Figure 1.2: An idealised flow sheet for the recovery of copper *via* solvent extraction from oxidic ore

1.3.3.1 Leaching

Leaching refers to the process in which a crude metal ore is dissolved, generally into an acidic aqueous solution (**1.1**). The acid leaching step in hydrometallurgy is less energy intensive than the mining, crushing and grinding portions of the processing in pyrometallurgy, as the ore does not have to be crushed as finely as it is gradually dissolved and therefore "leached" of it's metal value. The dissolution of copper with sulphuric acid is achieved by passing the acid through a "heap pad" of oxidic ore. This transfers most of the metals in the ore into an aqueous Pregnant Leach Solution (PLS) in which Cu^{II} is present at concentrations of usually 3-10 gL^{-1}, along with high concentrations of Fe^{II} and Fe^{III}.[8]

$$CuO + H_2SO_4 \rightarrow CuSO_4 + H_2O \qquad \textbf{1.1}$$

1.3.3.2 Extraction

In the extraction stage, the PLS is brought into contact with an organic phase, usually kerosene,[15] containing the extractant. A cation exchange reagent is utilised, which forms a Cu^{II} complex with enhanced solubility in the organic phase (**1.2**):

$$Cu^{2+} + 2\mathbf{L}H_{(org)} \rightleftharpoons [Cu\mathbf{L}_2]_{(org)} + 2H^+ \qquad \mathbf{1.2}$$

The equilibrium is pH-dependent, with the acidic extractant **L**H complexing with Cu^{II} at higher pH. The formed Cu^{II} complex is subsequently stripped of its metal value at lower pH. Due to it's pH dependency this load-strip process is known as a "pH-swing" process.[19]

Almost all commercial solvent extraction of copper employs extractants based on phenolic oxime ligands.[20] (Figure 1.3, see also 1.4.1)

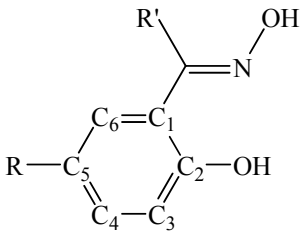

Figure 1.3: The basic structure of a phenolic oxime ligand

1.3.3.3 Stripping

During the stripping process, the copper-enriched organic phase is brought into contact with aqueous sulphuric acid. Under strongly acidic conditions, the Cu^{2+} ions are replaced by protons and the cation exchange process is reversed. This regenerates the extractant, which is recycled and the Cu^{2+} ion is released into an aqueous phase **1.3**.

$$CuL_{2\ (org)} + H_2SO_{4\ (aq)} \rightarrow CuSO_{4\ (aq)} + 2LH_{\ (org)} \qquad \mathbf{1.3}$$

One of the many environmental advantages of these extractants and of the hydrometallurgical process in general is that all reagents can be recycled and basic phenolic oxime ligands, for example, can have an active lifespan of around 2 years.

In practice the salicylaldoxime extractants forming the basis of this project are too strong for efficient stripping of Cu^{2+} back into the aqueous phase to occur simply under sulphuric acid conditions. They are used in conjunction with modifiers[14] such as alkyl phenols, ketoximes, esters or alcohols, which are known help promote stripping under stripping conditions but do not significantly affect loading under extraction conditions (see 1.5.1).

1.3.3.4 Electrowinning

The final stage of the solvent extraction process is electrowinning. This is used for obtaining copper metal of 99.99% purity from the pure aqueous copper sulphate stripping solution by electrolysis. The electrowinning of copper is one stage of the hydrometallurgical process that still requires a large amount of energy. This is due to the electrowinning process requiring considerably more electrical energy, - an average of about 8 MJ/kg vs. about 1.5 MJ/kg for electrorefining.[21] In electrowinning the copper must be reduced from the cupric form to metal; whereas, in electrorefining, the copper is already in metallic form and is merely transported from the anode to the cathode to purify it. The electrowinning energy consumption is, however, a problem for the pyrometallurgical process as well, and is due to the level of copper purity required for effective application. The electrorefined "crude" copper is therefore required to undergo further electrowinning to yield the desired purity. Recent patent applications show, however, that steps are being taken to reduce the energy requirement of electrowinning, one claiming to reduce the energy consumption by about 40% due to a modification of the anode reaction.[22] (Figure 1.4)

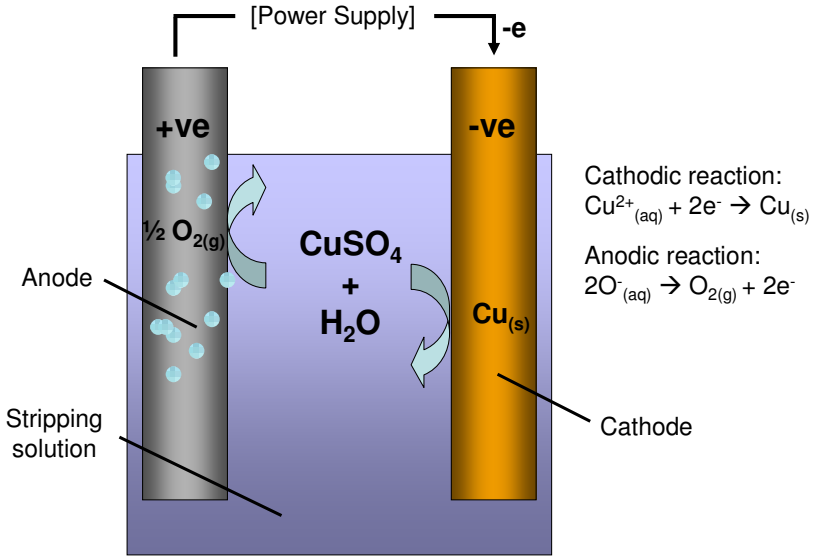

Figure 1.4: a schematic representation of the electrowinning process, showing the reduction of Cu^{2+} to Cu metal.

Deposition of copper occurs at stainless steel cathodes, which are immersed in the stripping solution, while oxygen is released at the anode, usually made of a lead-based alloy.[14] (**1.4**)

$$CuSO_{4\,(aq)} + H_2O_{\,(l)} \rightarrow Cu_{\,(s)} + \tfrac{1}{2}\,O_{2\,(g)} + H_2SO_{4\,(aq)} \qquad \textbf{1.4}$$

1.4 Copper(II) Recovery by Phenolic Oxime Extractants

1.4.1 Phenolic Oxime Extractants

These are currently used in solvent extraction plants all over the world, producing over 2 million tonnes of copper each year, around one quarter of the total world production.[1,20] In order to effectively carry out this role the phenolic oxime ligand must show a very high selectivity for Cu^{2+} over all other metals found in the PLS, in particular over Fe^{3+} ions which are usually present at equal or, sometimes, higher concentrations than Cu^{2+}.[8]

Phenolic oxime ligands have been shown to pre-organise in solution forming a *pseudo*-macrocyclic arrangement, stabilised by intra-complex hydrogen-bonding between the two ligands, and upon contact with the PLS these dimers undergo cation exchange with Cu^{2+} (**1.2**).

A proton is lost from each molecule and a charge neutral, square planar complex, with a 2:1 ligand to metal ratio is formed.[23] The protons released from the extractant pass into the aqueous phase, regenerating the acid used in the initial leaching process. The "selectivity" of complex formation with copper has been assumed[23] to arise from a very favourable "goodness-of-fit" of the Cu^{2+} ion within the ligand cavity formed over the other ions in solution. (see Figure 1.5)

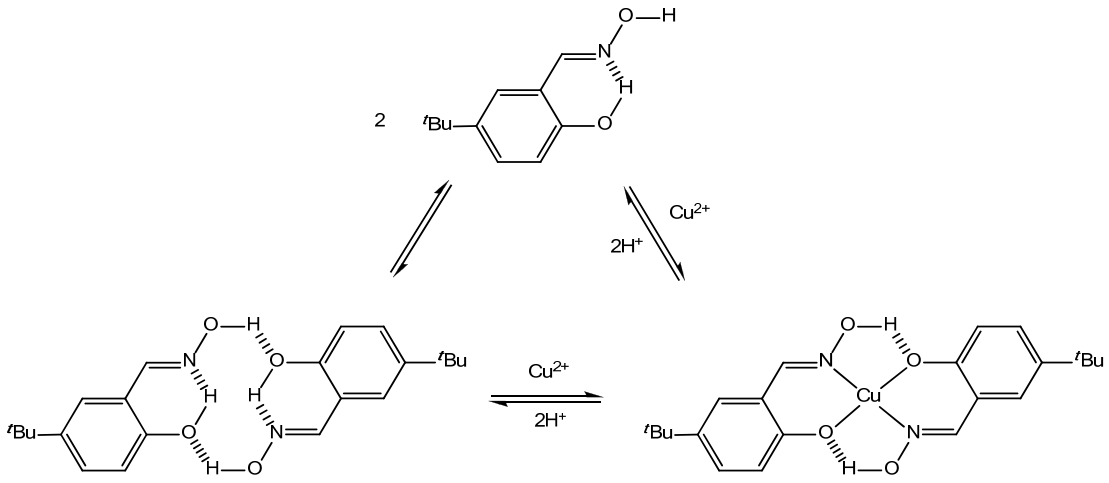

Figure 1.5: Reaction equilibria of phenolic oxime based extractants in the extraction of Copper.

1.5 Modification of Extractant Strength

Industrially, the modification of extractant strength and efficacy is carried out in three ways. The first is by use of equilibrium modifiers, hydrogen bond donor and/or acceptor molecules which, when present, improve the efficacy of the extractant. The second method of modification is by "blending" two or more extractants of differing strengths. The third, and least explored method is the modification of the extractant molecule itself.

1.5.1 Equilibrium Modifiers

The commercial salicylaldoxime extractant **P50** (2-hydroxy-5-nonylbenzaldehyde oxime), is used extensively in commercial solvent extraction processes for copper recovery and is extremely selective for copper in a conventional sulphuric acid extraction circuit (see Section 1.3). Its $pH_{0.5}$ value for copper extraction is *ca*. 0.5 in aliphatic hydrocarbon solvents.[14] The stripping of copper from the organic phase requires[14] a sulphuric acid solution of concentration 250-300 g L^{-1}. However, most plants[24] operate with sulphuric acid strip solution concentrations with a maximum of < 250 g L^{-1} as higher electrolyte acidities diminish the purity of the copper cathode.[14] Because copper cannot be efficiently stripped under these desired operating conditions, "equilibrium modifiers" are added to extractants at 5-10% concentration relative to that to that of the extractant to facilitate copper stripping in a more suitable pH range.[25]

Equilibrium modifiers have been shown to successfully enhance the mass transfer of copper in sulphate based solvent extraction circuits which employ salicylaldoxime reagents.[14,25] Although they do decrease the extraction capacity of the reagent, the overall mass transfer is greater than for unmodified systems.[23] Extraction modifiers are hydrogen bond donors and/or acceptors and have been shown to interact with the extractant molecules.[26,27] The intermolecular interaction between extractant and modifier lowers the concentration of the active extractant at the hydrocarbon/water interface and also affects the interfacial behaviour of the system and phase transfer kinteics.[25,28-30]

The first use of modifier molecules involved the 8-hydroxyquinoline-based extractant Kelex 100™, which contained isodecanol. Although never used commercially for copper extraction, the concept of extractant modification was subsequently developed by many companies.[14] The Acorga P5000™ series of reagents contained **P50** as the active component, with varying quantities of *para*-

nonylphenol to tune extractant strength.[31,32] Tridecanol was later introduced as a modifier, requiring only half the quantity compared with that of *para*-nonylphenol.[20] Further advances in modifier technology came with the introduction of Cytec Industries Inc.'s highly branched esters (*e.g.* Acorga M5640™) which can also increase Cu/Fe selectivity and oxime stability.[32-34] Esters, such as TXIB, have since become the SX industry's most commonly used modifier.[20]

Although the effects of modifiers have been quantified, the mode by which they interact with the extractant and copper complex is not fully understood.[30] The literature suggests a displacement of the phase distribution of copper by formation of adducts with the extractants (**LH**) and/or the copper complexes, [Cu(**L**)$_2$]. (see Figure 1.6)

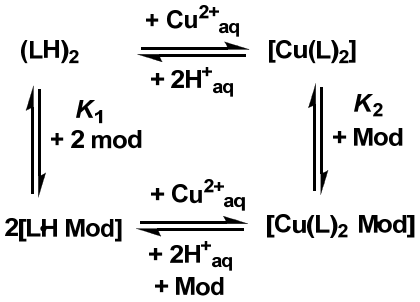

Figure 1.6: Equilibria involving the formation of possible adducts of an equilibrium modifier (Mod) with an extractant dimer (**LH**)$_2$ or with a copper complex ([Cu(**L**)$_2$]) in a water immiscible solvent.

1.5.2 Reagent Blends

Phenolic ketoximes are slightly weaker extractants for copper from sulphate leach solutions than aldoximes.[20] Structurally they differ from aldoximes by having an alkyl or aryl group in the R^1 position (see Figure 1.7).

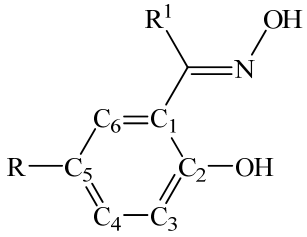

Figure 1.7: The structure of a phenolic ketoxime extractant, where the azomethine hydrogen atom of an aldoxime is replaced by an aryl or alkyl group.

Mixtures of strong aldoxime extractants such as LIX 860 with moderately strong ketoxime extractants such as LIX 64N and LIX 84, produce blends with the fast kinetics and good copper extraction performance of the ketoximes without the detrimental properties of modifiers which used to be added to pure aldoxime extractants to enhance stripping.[35] Aldoxime/ketoxime mixtures today produce more copper than any single reagent system.[36] (Figure 1.7) (see also Chapter 5 Section 5.2.2.1)

1.5.3 Reagent Modification

For commercial processes, the tuning of the extraction strength of a phenolic oxime formulation is achieved by reagent blending and "modification" as discussed above. The third possibility is to modify the extractant molecule itself. For phenolic oximes one means of modification is to introduce an X-substituent in the 3-position. (Figure 1.8)

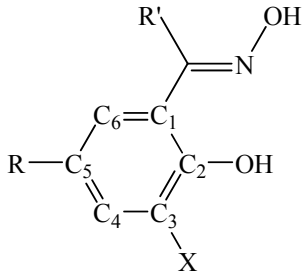

Figure 1.8: 5-Alkylsubstituted salicylaldoximes derivatives used in copper recovery, showing a X-substituent in the 3-position.

There have been few systematic studies on the effects of benzene-ring substitution on strength and selectivity of phenolic oxime extractants. In the mid 1960's Burger *et al* investigated the effect of substitution in the 5-position of a series of salicylaldoximes. This spectrophotomeric study showed that a nucleophilic substituent increases both the pK_a of the phenol group and overall complex formation constant in a single phase system.[37] This was attributed to the effect of the substituent on the ligands' σ-donating abilities. In a further study, Parrish *et al.* showed that 3-nitro-2-hydroxy-5-nonylbenzophenone oxime, operates in a lower pH range than its unsubstituted analogue but concluded that substituents affect ligand properties in many ways, making prediction of extractant strength difficult.[38]

In addition to influencing the electronic properties of the donor atoms substituents in the 3-position have been shown to have a significant effect on the interligand hydrogen bonding thought to contribute to the stability of resulting *pseudo*macrocyclic complexes.[39]

In 1971, General Mills introduced the LIX70™ extractant, with the active component being the 3-chloro-2-hydroxy-5-nonylbenzophenone oxime (R = C_9H_{19}, R' = C_6H_5, X = Cl in Figure 1.8). The 3-chloro group resulted in high extractant strength, providing a reagent for copper recovery from highly acidic and chloridic media.[40] In practise, the reagent has only been used as a component of extractant blends.[41-44]

This thesis will focus on a series of ligands investigated by Forgan *et. al.*[2,45], who showed that the strength of salicylaldoxime extractants can be significantly adjusted by introducing substituents (X) in the 3-position, (Figure 1.9) with the distribution coefficient for Cu-extraction varying by two orders of magnitude in the series: Br > NO_2 > Cl > OMe > Me ≥ H > ^{t}Bu.[2]

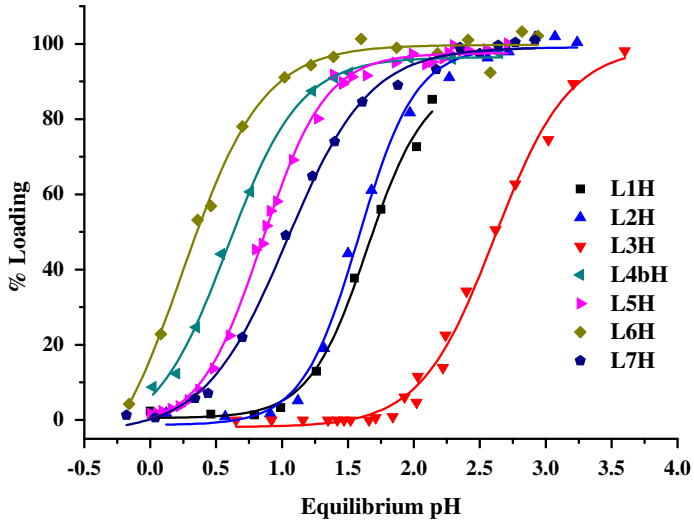

Figure 1.9: pH loading profiles and $pH_{0.5}$ values for loading of copper by 0.01 M chloroform solutions of **L1H-L7H** from equal volumes of 0.01 M aqueous solutions of copper sulphate. 100% copper loading based on a 1Cu:2**LH** ratio.[2,45]

The consensus in publications from industrial labs is that the electronic effect of a 3- or 5-substituent controls extractant strength; electron-withdrawing groups lower the pK_a of the phenol, allowing copper binding to occur at lower pH and thus increase the reagent strength. Forgan *et. al.* showed, however that The 3-OMe substituted ligand, although expected to be a weaker extractant as a consequence of the 3-methoxy group's electron-donating properties, is a better extractant than the unsubstituted ligand**.** Although the 3-X-substituents were shown to have an electronic effect on the ligand, the differences in extractant strength of the substituted phenolic oximes arose partially from the "buttressing" of the *intra*molecular H-bonding which defines the *pseudo*macrocyclic assembly, (Figure 1.10).

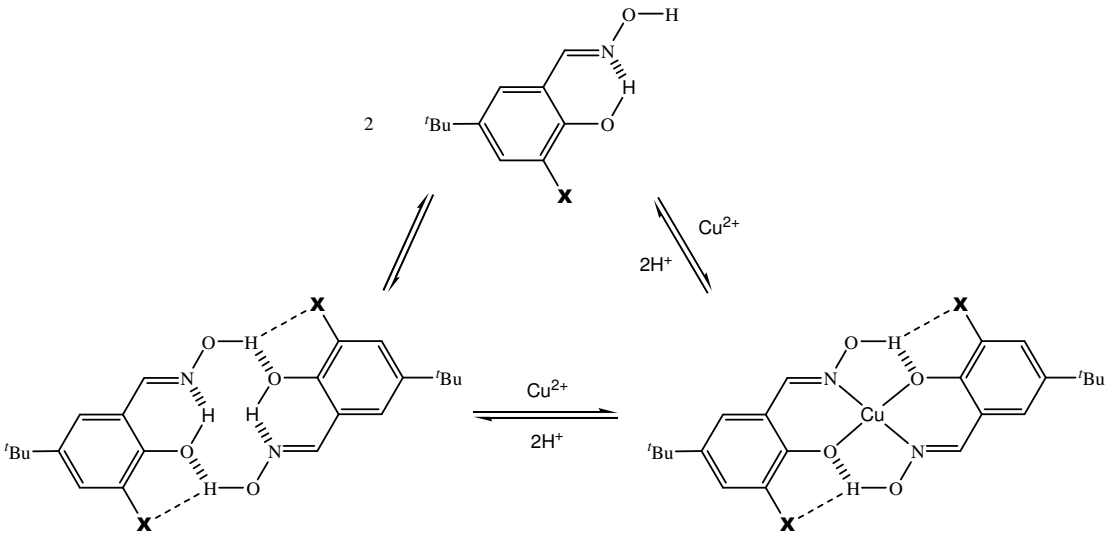

Figure 1.10: Key molecular components involved in the extraction of copper by salicylaldoxime-based ligands, indicating secondary H-bond buttressing.

The effect of the buttressing was also observed in both the solid state and in gas phase calculations of ligand dimer structures.[45]

In this thesis gas phase analysis will be used to understand how the nature of the 3-X-substituent affects the extraction strength of the phenolic oxime as an extractant for copper in an attempt to define what makes an effective extractant.

1.6 Mass Spectrometry

Mass spectrometry is a gas phase analytical technique that is used to determine the mass or masses of a sample. The components of a sample can be separated by their mass-to charge ratios using both electric and magnetic fields, depending on the instrument; the structure of the molecules in question can therefore be inferred. A mass spectrometer consists of 3 principal components: the ion source, the mass analyzer and the ion detector. The sample can be introduced into the ion source in the liquid, solid and vapour phase where it is ionized and fragmented. These ions are then passed to the mass analyzer where they are separated according to their mass-to-

charge ratios and then go to the ion detector where their presence is recorded and a mass spectrum is produced.

1.6.1 Tandem Mass Spectrometry

Tandem mass spectrometry,[46] generally abbreviated to MS/MS, refers to any method of mass spectrometry that has at least two stages of mass analysis. Generally, some form of mass selection or fragmentation occurs in between each stage.

Separation in tandem mass spectrometry can be achieved in space, by multiple instruments or in time with a single machine that incorporates MS/MS capabilities.[47,48]

In space-separation experiments, the two mass analysers are physically distinct and separated, although a connection between the elements is used to maintain high vacuum. Instruments of this kind generally use quadrupoles and mass analysers, but time-of-flight and sector instruments are also commonly used.

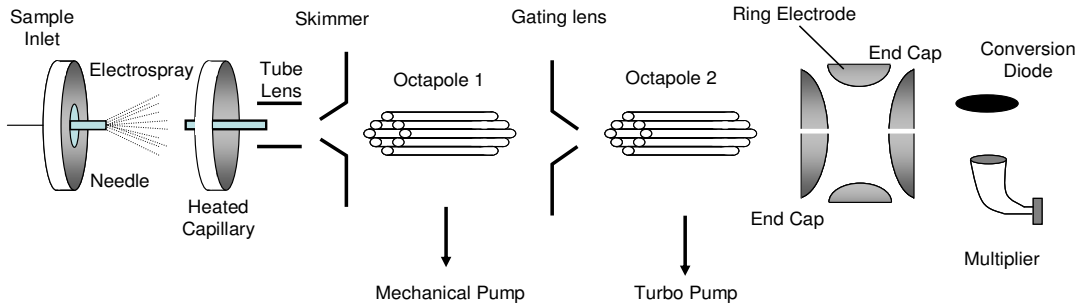

Figure 1.11: a schematic representation of a thermo-fisher LCQ, consisting of a double Octapole system and a Paul ion trap. Figure reproduced from Mass Spectrometry: principles and Applications by de Hoffmann and Stroobant.[48]

For time-separation instruments, separation is accomplished with ions trapped in the same place and the multiple separation steps occurring over time. The quadrupole ion trap,[49] LCQ[50] (double octapole ion trap) (Figure 1.11), FTICR[51] and the Orbitrap[52] instruments can all be used for such an analysis. These trapping instruments can

perform multiple steps of analysis, which are referred to as MS^n-studies[53] (*n* being the number of stages of analysis).

1.6.2 Electrospray Ionisation

Electrospray ionisation (ESI) is an ionisation technique that generates a very fine liquid aerosol through electrostatic charging. [54,55] In ESI the ions are generated whilst in solution by the application of an electric potential to the tip of a capillary (Figure 1.12).

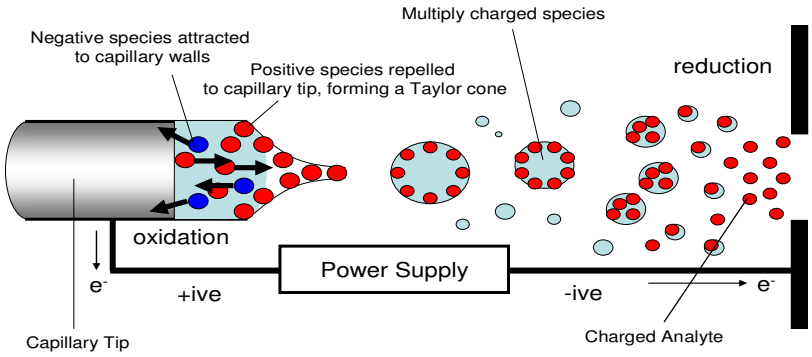

Figure 1.12: Formation of ions *via* the electrospray process

The applied electric potential leads to a partial separation of positive from negative electrolyte ions in the solution due to partial penetration of the field past the surface of the liquid at the tip of the capillary. Thus, in the positive ion mode, the applied field enriches positive ions at the surface of the liquid at the capillary tip whereas negative ions are drawn towards the inside of the capillary. The charge repulsion of the positive ions at the surface of the capillary tip increases and the pull of the electric field on the positive ions overcomes the surface tension of the solution and a Taylor cone forms (Figure 1.13).[56]

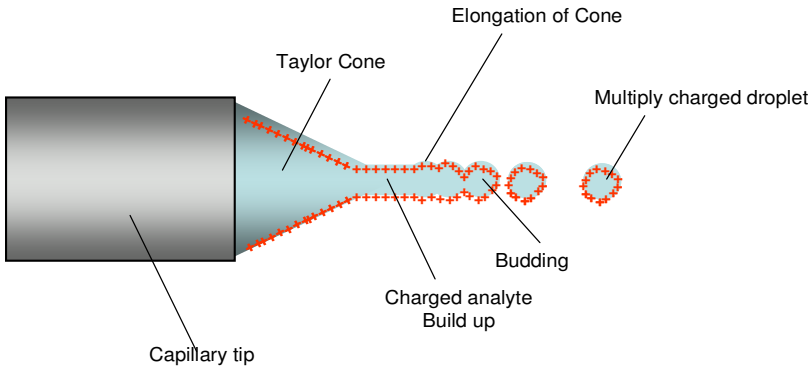

Figure 1.13: The formation of a Taylor Cone.

The tip of the Taylor cone is the least stable point and elongates into liquid filament. The increased repulsion and decreased stability leads to the formation of multiply-charged droplets; the point at which this occurs is known as the Rayleigh limit,[57] the point at which Coulombic repulsion of the surface charge is equal to the surface tension of the solution. The droplet formation process does not require any heating and the charged droplets are subsequently accelerated towards the analyser *via* a large charge potential. An uncharged sheath gas, usually oxygen free nitrogen, is used to help nebulize the liquid and desolvate the charged droplets.

1.6.3 Desolvation

Desolvation is thought to proceed *via* a mixture of two primary processes: The Charged Residue Model[58] (CRM) by Malcolm Dole (also known as the Coulombic explosion model) and The Ion Evaporation Model[59,60] (IEM) by Iribarne and Thomson.

1.6.3.1 The Charged Residue Model

With increasing charge on the surface of a droplet the repulsion between the charged species increases. When this limit becomes greater than the surface tension of the droplet (the Rayleigh limit) a Coulombic explosion occurs,[61] forming smaller

multiply charged droplets. Intervening periods of Coulombic explosions and solvent evaporation produces "ultimate" droplets, each of which contains only one molecule of solute.[62]

1.6.3.2 The Ion Evaporation Model

Iribarne and Thomson have worked on predictions for the rate of ion emission from a charged droplet. The model predicts the propensity of a charged species to be emitted from a multiply charged droplet and states the dependence of the rates of ion ejection on the chemical properties of the ions. The rate constant k_1 for emission of ions from droplets can be described as (**1.5**) where k_B is the Boltzmann constant, T is the temperature of the droplet, and h is the Planck constant.[48]

$$k_1 = \frac{k_B T}{h} \exp(-\Delta G / RT) \qquad \textbf{1.5}$$

The free energy of activation ΔG is based on the Iribarne transition state, although the transition state chosen resembles the final product more than the starting droplet as there is a large barrier to overcome.[63] The barrier in the Iribarne transition state is due to opposing electrostatic forces: 1) the repulsion of the escaping ion by the other charges of the droplet and 2) the attraction between the escaping ion and the droplet because of the polarizability of the solvent in the droplet. The attraction has been found to be larger at short distance between the ion and the droplet surface, but reduces a lot faster than the repulsive forces as the distance is increased. These emitted ions can be thought of as being similar to the "ultimate" droplets of the Charged Residue Model, containing only one molecule of solute per droplet. These droplets are generally desolvated, with the aid of the nitrogen carrier gas and the heated capillary, forming the charged analyte species.

ESI has many advantages; firstly it permits the detection of high-mass compounds at mass-to-charge ratios that are easily determined by most mass spectrometers; it is an

extremely effective method for analyzing multiply charged, polar or basic compounds. ESI also exhibits low chemical background noise which leads to excellent detection limits and it is especially useful in producing ions from macromolecules as it reduces the tendency of these molecules to fragment upon ionisation. ESI is often referred to as being 'softer' than other MS ionisation methods and, although the ions observed in the ESI mass spectra are not always the same as those present in the solution, it is one of the only widely used ionisation techniques that is able to give mass spectrometric information that may be relevant to solution-phase structures.[64] It is well known that this Mass Spectrometry technique is very suitable for the study of various metal complexes and allows some insight into their intrinsic properties.[65,66] The majority of the mass spectrometry studies discussed in this thesis will be performed using Thermo-Fischer LCQ double octapole ion trap which has an ESI source.

1.6.4 The quadrupole ion trap

The quadrupole ion trap (QIT) mass analyser was developed by physicist Wolfgang Paul.[67-69] Commercial QIT incorporating instruments are common, not only in chemical but also in biochemical and forensics laboratories; they are extremely diverse systems and can be easily coupled to various ionisation techniques such as ESI, SSI and MALDI as well as with liquid chromatography, LCMS.[70] A quadrupole ion trap is an instrument roughly the size of a tennis ball whose size is inversely proportional to its versatility. Three hyperbolic electrodes, consisting of a ring and two endcaps, form the core of this instrument (Figure 1.14). In the early 1950s, Paul and co-workers invented two instruments that could be used to determine mass-to-charge (*m/z*) ratios of ions.[67] The first was the quadrupole mass filter that was rapidly applied to a wide range of analytical problems.[71] The second was the quadrupole ion trap. A user of note was Hans Dehmelt at the University of Washington who won the Nobel Prize for employing the ion trap to investigate the physical properties of isolated ions.[72]

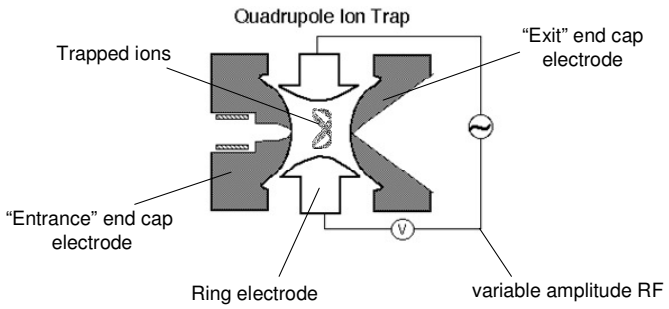

Figure 1.14: a diagrammatic representation of the QIT.

The chemistry community's general interest in the ion trap was confined to several research groups until 1983 when George Stafford and co-workers at Finnigan MAT made two major advances. The first was the development of the mass-selective instability mode of operation, in which the fundamental difference from previous methods was that all ions created over a given time period were trapped and then sequentially ejected from the ion trap into a conventional electron multiplier detector. The second breakthrough was the discovery that the incorporation of a helium buffer gas within the trapping volume greatly improved the mass resolution of the instrument by contracting the ion trajectories to the center of the trap and reducing the kinetic energy of the ions.[73] This allows ions of a given *m/z* to form a packet which is ejected more quickly and efficiently than a diffuse cloud of ions, thus improving resolution. Both these discoveries led to the successful development of a commercial ion trap mass spectrometer.

1.6.5 Ion Trapping

Ion trapping involves focusing ions into the ion trap using an electrostatic lensing system. An electrostatic ion gate pulses open and closed to inject ions into the ion trap. This differentiates ion traps from "beam" instruments such as quadrupoles, where ions continually enter the mass analyzer, as, with the ion trap, finite "packets" of ions are allowed into the trap. The time during which ions are allowed into the trap is generally set to maximize the signal-to-noise ratio while minimizing space-charge effects, where too many ions in the trap distort the electric fields, leading to

significantly impaired performance. The commercial ion trap is typically filled with helium to a pressure of about 1 mtorr. Collisions with the neutral helium atoms reduce the kinetic (translational) energy of the ions and serve to quickly contract trajectories toward the center of the ion trap, thermalising the injected ions. Trapped ions are further focused toward the center of the trap through the use of an oscillating potential, also known as the fundamental radial frequency (rf) voltage, typically a 1.1 MHz potential applied to the ring electrode[74] (Figure 1.15).

Figure 1.15: a SIMION[43] representation of a stable ion trajectory within the quadrupole ion trap

An ion will be stably trapped depending upon the values for the mass and charge of the ion, the size of the ion trap (r), the oscillating frequency of the fundamental *rf* (Ω), and the amplitude of the voltage on the ring electrode (*V*). The dependence of ion motion on these parameters is described by the dimensionless parameter q_z, given by the derived Equation **1.6**:[50]

$$q_z = -\frac{4eV}{mr_0^2\Omega^2} \qquad \textbf{1.6}$$

For the case of most existing commercial ion traps, r = 1 cm, Ω /2p = 1.1 MHz, and *V* ranges from 0 to 7,500 V. A DC potential, *U*, can be placed on the ring electrode and can also affect the stability of the ion trajectories *via* a parameter a_z that depends upon the amplitude of *U*. (**1.7**)[50]

$$a_z = -\frac{8eU}{mr_0^2\Omega^2} \qquad \textbf{1.7}$$

Figure 1.16 shows the "stability diagram", a region where radial and axial stability overlap. Depending upon the amplitude of the voltage placed on the ring electrode,

an ion of a given m/z will have a q_z value that will fall within the boundaries of the stability diagram, and the ion will be trapped. If the q_z value at that voltage falls outside of the boundaries of the stability diagram, the ion will hit the electrodes and be lost.

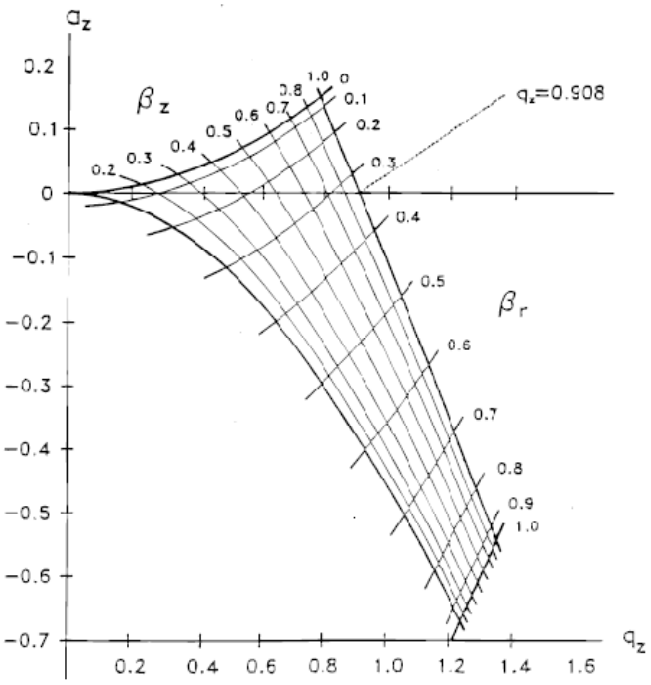

Figure 1.16: Diagram of the stability regions of a quadrupole ion trap according to the voltage and frequency applied to the ion trap elements.[50]

1.6.6 Activation and ejection

The trapped ions oscillate with a frequency, known as the secular frequency, a factor determined by the values for a_z and q_z and by the frequency of the fundamental rf. Resonance conditions are induced by matching the frequency of a supplementary potential applied to the endcap electrodes to the secular frequency of the ions. Structural information can be obtained by collision induced dissociation in which the application of a low-amplitude alternating current (ac) resonance signal across the endcap electrodes which leads to an increase in the ion kinetic energies and leads to ion dissociation due to many collisions with the helium collision gas. A mass spectrum is generated by sequentially ejecting fragment ions from low m/z to high m/z by choosing amplitudes of the fundamental rf potential that sequentially make

ion trajectories unstable. Ions are ejected through holes in the endcap electrode and are detected using an electron multiplier.

The very nature of trapping and ejecting makes a QIT especially suited to performing MS/MS experiments in structural elucidation studies. It is possible to selectively isolate a particular *m/z* in the trap by ejecting all the other ions from the trap. Fragmentation of this isolated precursor ion can then be induced by collision induced dissociation (CID) experiments. These isolation and fragmentation steps can be repeated a number of times, MS^n, and is generally limited only by the trapping efficiency of the instrument and the lifetime of the ions produced.

1.6.7 The application of electrospray mass spectrometry to inorganic systems

Since simple metal salts are the most fundamental inorganic substances known there have been many studies that have investigated metal salt solutions using ESI.[75,76] Simple copper(II) salts have been extensively studied[77-79] with studies showing the effect of solvents (e.g. the reductive stabilisation of Cu(I) in acetonitrile[80,81] and the adducts formed with methanol[82]) and reduction of Cu(II) to Cu(I) due to both high cone voltages[79] and negative mode ESI.[83]

The analysis of coordination complexes is generally done using a combination of Spectroscopy methods [nuclear magnetic resonance (NMR), Infrared (IR), UV/Vis etc.], but the application of these techniques is generally situation dependant, e.g. Cu(II) complexes are paramagnetic and analysis NMR is of little use. Single crystal X-ray crystallography is often used to define the structure of coordination complexes, but a single crystal can often misrepresent the bulk. FAB-MS has been used in complex analysis and has shown for example that the single crystal obtained from a sample of $[Cr_4(C_5Me_5)_4]$ did not represent the bulk sample.[84] There have been a number of detailed reviews on the application of ESI-MS to inorganic complexes and coordination complex systems.[85-88]

In 2005 Di Marco and Bombi published a review of studies that have used ESI to investigate metal-ligand solution equilibria with the majority dating from the late 90's to 2004, indicating the effect ESI has had on the recent analysis of inorganic systems.[89] ESI Mass spectrometry is an ideal tool to investigate large inorganic systems and has recently been used to investigate both polyoxometallate (POM) systems[90,91] and metal organic frameworks (MOF's).[92]

The following section introduces the background of the modelling of molecules and the origins and importance of Density Functional Theory.

1.7 Introduction to Molecular Modelling

In General there are two main methods used for calculating the structure of matter; one is based on classical Newtonian physics, and the other on quantum mechanics (QM). The former, classical approach, gives rise to molecular mechanics (MM) which works on the basis that atoms are large enough to be treated as objects (as defined by Newtonian physics). The problem encountered by chemist and physicists is that in molecular mechanics the electrons are ignored. This deficiency has fuelled the development of the quantum mechanical approaches of *ab initio* molecular orbital theory and density functional theory (DFT).

In quantum mechanics solutions to Schrödinger's equation are sought in order to obtain the ground state electronic configuration. From that point the forces between the atoms can be calculated and can be used to optimise the atomic positions. In QM methods the molecular orbital (MO) theory approach is used in finding solutions to Schrödinger's equation is used (**1.8**). The advantage of the MO approach is that with an explicit description of the properties of the electrons we can calculate any molecular property to within an impressive level of accuracy. The major drawback with QM methods is that they require a lot of computational power and, compared to

MM methods, are limited to "small" systems (50-100's atoms, instead of tens of 1000's by MM methods).

1.7.1 Solving Schrödinger's equation

In the molecular orbital (MO) theory approach to finding solutions to Schrödinger's equation (**1.8**)

$$\widehat{\boldsymbol{H}}\boldsymbol{\Psi} = \frac{-\hbar^2}{2\boldsymbol{m_e}}\boldsymbol{\nabla^2\Psi} + \boldsymbol{V\Psi} = \boldsymbol{E\Psi} \qquad \textbf{1.8}$$

The Hamiltonian operator, $\widehat{H}$, acts on the wavefunction, Ψ, to yield the energy levels, E, of the molecule using the kinetic energy term, $\frac{-\hbar^2}{2m_e}$, the Laplacian operator, ∇^2 ($\nabla^2 = \frac{\delta^2}{\delta X^2} + \frac{\delta^2}{\delta Y^2} + \frac{\delta^2}{\delta Z^2}$) and the potential energy term, V. The Hamiltonian operator is ultimately concerned with modelling the interactions (correlation and exchange) between electrons. There are a number of different ways to simplify it giving rise to different levels of theory.

1.8 Hartree Fock

Combining Hartree theory (which ignores electron correlation, by assuming that each electron moves in a uniform field generated by the other electrons present) and Fock theory (which provides an accurate account of electron exchange) gives Hartree-Fock (HF) theory. For a multi electron (*N*) system Schrödinger's equation is replaced with $N \times 1$ e- Hartree-Fock equations. For certain systems HF can account for up to 99% of the total energy. The missing correlation energy is significant for molecules that contain areas of high electron density, such as double bonds, aromatic rings, anionic species etc. as HF tends to calculate bond distances that are too short for these systems.

There are ways to improve on HF theory and these different techniques are known as different levels of theory. All methods take HF theory as their starting point and have

additional terms to try and capture the missing correlation energy. Names of such methods (in order of increasing complexity) are:

- Møller-Plesset (MP) series
- couple cluster (CC)
- configuration interaction (CI)

The above, higher, levels of theory do a better job of modelling electron correlation. However, all methods are based on 4 variables per electron: 3 positional (x,y and z) and 1 spin and are extremely computationally demanding.

1.9 Density Functional theory

Density functional theory (DFT) is an alternative methodology for constructing the Hamiltonian operator of a multi-electron system that relies on calculating the electron density, r, depending on just the three positional variables. As with *ab initio* methods Schrödinger's equation is still solved one electron at a time, but now the *N* equations are known as the Kohn-Sham equations. The major problem with using the Kohn-Sham equations is that the functional (known as the exchange/correlation functional) is not known. This results in a number of different approximations and a number of different functionals are used.

1.9.1 Hybrid DFT

Hybrid density functional theory is a result of the combination of Hartree Fock theory and DFT, to create hybrid DFT functionals. The two techniques are combined to effectively deal with correlation and exchange: e^-/e^- correlation e^-/e^- exchange. Hybrid DFT functionals offer computational accuracy similar to post HF methods (such as MP2), but as they are based on 3N variables instead of 4N variables and are therefore less computationally demanding.

1.9.2 B3LYP

The majority of the DFT calculations presented in this thesis use the hybrid DFT B3LYP[93-96] functional, formed by combining Becke's three-parameter exchange functional[93] and the nonlocal correlation functional of Lee, Yang, and Parr.[94] This functional was chosen as previous studies employing it have been found to yield reaction energies correlating to experimentally determined values for a wide range of processes and have been applied to a range of systems including macrocycles and transition metal complexes.[97] B3LYP has been used to investigate strong hydrogen bonds[98,99] and hydrogen bond dimers[100-103] including a recent study by Borisenko *et. al.* which considered the influence of methoxy- and nitro-substitution in an aromatic ring on proton donation ability in hydrogen bonding,[104] a theme which is relevant to the work in this chapter. Lozynski *et. al.* also suggested that B3LYP was a DFT method that could achieve similar results to the more widely used MP2 (commonly used for smaller hydrogen bonding systems) and other more computationally demanding *ab-initio* methods. The 6-31G basis set[105-111] was used for all of the calculations and for higher level calculations polarisation and diffuse functions were included.[112]

1.10 Gaussian

Gaussian is an electronic structure program used to predict the energies, molecular structures, vibrational frequencies and molecular properties of molecules and reactions, starting from the fundamental laws of quantum mechanics, in a wide variety of chemical environments. Although the newer Gaussian '09 became available for use during the latter stages of the work described in this chapter, for consistency the version used throughout the thesis is Gaussian '03.[113]

1.10.1 Basis Set Superposition Errors (BSSE)

Non-covalent interactions can be studied in a manner similar to covalent interactions, that is, by standard methods of quantum chemistry based either on perturbation or variation theory.[114] A problem often encountered when calculating the energies of non-covalent interactions is that they are susceptible to basis set superposition error (BSSE)[115,116] which can occur as, when the atoms of interacting molecules approach one another, their basis set functions overlap. This results in an overlap of the basis set functions, and in each monomer "sharing" functions from other nearby components. The overlap increases each monomer's basis set and improves the calculated properties such as its geometry optimised energy minimum. As will be seen for some of the systems described in Chapter 4, if the total energy is minimised as a function of the systems optimised geometry, the short-range energies from the "mixed" basis sets must be compared with the long-range energies from the unmixed sets as this mismatch introduces an error.

Boys and Bernardi introduced a solution to the BSSE problem and called the respective procedure the function counterpoise (CP) method.[115] The counterpoise correction is realised by introducing so-called ghost orbitals, *i.e.* upon calculation, the ghost subsystems have basis set functions placed at the position of the atoms but no electrons and protons, which results in the BSSE being geometry dependent. The final BSSE error is then subtracted *a posteriori* from the uncorrected energy.

1.10.2 Natural Bond Orbital (NBO) Program

Gaussian '03[113] contains version 3.1 of the Natural Bond Orbital or NBO program by F. Weinhold and coworkers.[117] and enables NBO analysis to be incorporated into geometry optimisation calculations using the Gaussian program. NBO analysis is based on a method for optimally transforming each wave function into localized form, which corresponds to the one-center *i.e.* lone pairs, and two-center *i.e.* bonds elements of the chemist's Lewis structure picture. In NBO analysis, the input atomic

orbital basis set is transformed via natural atomic orbitals (NAOs) and natural hybrid orbitals (NHOs) into natural bond orbitals (NBOs). The NBOs obtained with this method correspond to the widely used Lewis model, in which two-center bonds and lone pairs are localized. The NBO program searches over all possible ways of drawing the bonds and lone pairs for the variationally optimal bonding pattern that places the highest percentage of the total electron density in the leading "Lewis-type" natural bond orbitals which account for typically >99.9% in common organic molecules. The NBO analysis allows effective measuring of individual “Lewis-Type” interactions and the comparison of such interactions (bond strengths) in different calculated structures.

1.10.3 Calculating Enthalpies of Reactions using Gaussian

The usual way to calculate enthalpies of reaction is to calculate heats of formation, take the appropriate sums and difference according to equation **1.9**

$$\Delta_r H^\circ(\mathbf{298\ K}) = \sum_{products} \Delta_f H^\circ_{prod}(\mathbf{298\ K}) - \sum_{reactants} \Delta_f H^\circ_{react}(\mathbf{298\ K}) \qquad \mathbf{1.9}$$

where $\Delta_r H^\circ(298\ K)$ is the standard enthalpy of reaction at 298 K and $\Delta_f H^\circ$ is the heat of formation.

Gaussian, however, provides the sum of electronic and thermal enthalpies and by taking the *difference* of the sums of these values for the reactants and the products all the atomic information cancels out. Only the molecular data is then required to calculate enthalpies of reactions using Equation **1.10**.

$$\Delta_r H^\circ(\mathbf{298\ K}) = \sum(\boldsymbol{E_0} + \boldsymbol{H_{corr}})_{products} - \sum(\boldsymbol{E_0} + \boldsymbol{H_{corr}})_{reactants} \qquad \mathbf{1.10}$$

Where E_0 is the minimised energy and H_{corr} is the thermal correction for enthalpy calculated for each species in a frequency calculation. Equation **1.10** will be the basis for all calculated enthalpies of reaction within this thesis.

1.11 Thesis Outline

In addressing the main themes of this thesis (see Section 1.1), collision induced dissociation has been used in Chapter 2 to rank the relative gaseous stabilities of negative ions derived from solutions of copper complexes of phenolic oximes, **L1H**-**L7H**, which carry a range 3-X substituents and to compare this ranking with the strengths of the ligands in solvent extraction experiments. This work is extended in Chapter 3, applying the methodology to a comparison of the stabilities of aldoxime and ketoxime complexes and to a comparison of complexes with different metals in the gas phase including positively charged species.

Density functional theory computational methods are applied in Chapter 4 to interpret the origins of substituent effects on complex stabilities and to establish whether these apply in the inner or outer coordination spheres, or both. The results obtained were confirmed by extending the range of ligand structures to phenolic hydrazones, **L9H**-**L13H**, which have closely related structures to the phenolic oximes used elsewhere in the thesis.

Chapter 5 considers to what extent it is possible to use electrospray mass spectrometry to determine the relative concentrations of complexes of mixtures of ligands in solution and thus compare the relative strengths of the ligands. In a similar vein in Chapter 6, electrospray MS is used to follow the formation of oligomeric copper complexes in solution by varying ligand to copper stoichiometry, pH etc. An unexpected trinuclear complex detected as a dominant species by mass spectrometry was isolated and characterized by X-ray structure determination.

1.12 References

(1) Mackey, P. J. *CIM Magazine* **2007**, *2*, 35.

(2) Forgan, R. S.; Wood, P. A.; Campbell, J.; Henderson, D. K.; McAllister, F. E.; Parsons, S.; Pidcock, E.; Swart, R. M.; Tasker, P. A. *Chem. Commun.* **2007**, 4940.

(3) Forgan, R. S.; Henderson, D. K.; McAllister, F. E.; Tasker, P. A.; White, F. J.; Campbell, J.; Swart, R. M. *Canadian Metallurgical Quarterly* **2008**, *47*, 293.

(4) Hong, S.; Candelone, J.-P.; Patterson, C. C.; Boutron, C. F. *Science* **1996**, *272*, 246.

(5) Hong, S.; Candelone, J.-P.; Soutif, M.; Boutron, C. F. *Science of the Total Environment* **1996**, *188*, 183.

(6) Grayson, M.; Eckroth, D. *Kirk-Othmer Encyclopedia of Chemical Technology*; 3rd ed.; Wiley, 1978; Vol. 6.

(7) webmineral.com/chalcopyrite, 2005.

(8) Tasker, P. A.; Plieger, P. G.; West, L. C. *Comprehensive Coordination Chemistry II* **2004**, *9*, 759.

(9) Academic, H. *Principles of Extractive Metallurgy: Pyrometallurgy*; March 1985 ed.; Medical.

(10) Lambert, J. B. *Traces of the past; unravelling the secrets of archeology through chemistry*; Helix books: Reading, Mass., 1997.

(11) Lottermoser, B. G. *Mine wastes; characterisation, treatment and environmental impacts*; Springer, 2003.

(12) Moore, J. N.; Luoma, S. N. *Environmental Science & Technology* **1990**, *24*, 1278.

(13) Lagos, G.; Lehuede, J. M.; Andia, M. *Resources Policy* **2001**, *27*, 147.

(14) Szymanowski, J. *Hydroxyoximes and Copper Hydrometallurgy*; CRC Press: London 1993.

(15) Habashi, F. *A Textbook of Hydrometallurgy* Quebec, 1994; Vol. 7.

(16) Cerna, M. *Environmental Monitoring and Assessment* **1995**, *34*, 151.

(17) Brooks, C. S. *Sep. Sci. Technol.* **1993**, *28*, 579.

(18) Habashi, F. *Hydromet.* **2005**, *79*, 15.

(19) Galbraith, S. G., PhD Thesis, Edinburgh University, 2005.

(20) Kordosky, G. A. *Int. Solv. Ex. Conf., Cape Town, South Africa, Mar. 17-21* **2002**, 853.

(21) Velarde, F. J. S.; Siles, H. O.; de Namor, A. F. D. *Miner. Eng.* **2005**, *18*, 213.

(22) Hardee, K. L.; Ernes, L. M.; Brown Jr., C. W.; Corporation, E. S., Ed. 2004.

(23) Szymanowski, J. *Crit. Rev. Anal. Chem.* **1995**, *25*, 143.

(24) Casas, J. M.; Alvarez, F.; Cifuentes, L. *Chem. Eng. Sci.* **2000**, *55*, 6223.

(25) Prochaska, K.; Staszak, K. *J. Colloid Interface Sci.* **2005**, *285*, 1.

(26) Bogacki, M. B.; Szymanowski, J. *Solvent Extraction Research and Development, Japan* **1996**, *3*, 10.

(27) Majdan, M.; Sperline, R. P.; Gu, W. G.; Yu, W. H.; Freiser, H. *Solvent Extr. Ion Exch.* **1989**, *7*, 987.

(28) Szymanowski, J. *Solvent Extr. Ion Exch.* **2000**, *18*, 729.

(29) Bogacki, M. B. *Solvent Extr. Ion Exch.* **1997**, *15*, 731.

(30) Sastre, A. M., Szymanowski, J. *Solvent Extr. Ion Exch.* **2004**, *22*, 737.

(31) Dalton, R. F. *Canadian Institute of Mining and Metallurgy* **1979**, *21*, 40.

(32) Tumilty, J. A.; Dalton, R. F.; Massam, J. P. *Adv. Extr. Metall., Int. Symp., 3rd* **1977**, 123.

(33) Cupertino, D. C.; Sugarman, A. D.; (Avecia Limited, UK). WO Patent, 2001, p 22.

(34) Virnig, M. J.; Grinstein, R.; Sudderth, R. B.; Wolfe, G.; Olafson, S.; (Henkel Corp., USA). WO Patent, 2000, p 24 pp.

(35) Kordosky, G. A.; MacKay, K. D.; Sudderth, R. B.; Sierakoski, J. M.; (Henkel Corp., USA). European Patent, 1983, p 62 pp.

(36) Jergensen, G. V. *Copper Leaching, Solvent Extraction, and Electrowinning Technology*; Society for Mining Metallurgy & Exploration, 1999.

(37) Burger, K.; Egyed, I. *J. Inorg. Nucl. Chem.* **1965**, *27*, 2361.

(38) Parrish, J. R. *J. S. Afr. Chem. I.* **1970**, *23*, 129.

(39) Burger, K.; Egyed, I. *Magyar Kemiai Folyoirat* **1965**, *71*, 143.

(40) Lakshmanan, V. I.; Lawson, G. J. *J. Inorg. Nucl. Chem.* **1975**, *37*, 207.

(41) Agers, D. W.; Dement, R. *Solvent Extr. Met. Processes, Proc. Int. Symp.* **1972**, 31.

(42) Agers, D. W.; Dement, R. *Ingenieursblad* **1972**, *41*, 433.

(43) Mattison, P. L.; Swanson, R. R.; (General Mills, Inc., USA). USA Patent, 1976, p 8 pp.

(44) Mattison, P. L.; Swanson, R. R.; (General Mills, Inc.). USA Patent, 1972, p 7.

(45) Forgan, R. S., PhD Thesis, University of Edinburgh, 2008.

(46) McLafferty, F. W. *Accounts of Chemical Research* **1980**, *13*, 33.

(47) de Hoffman, E.; Stroobant, V. *Mass Spectrometry - Principles and Applications*; 2nd Edition ed.; John Wiley & Sons, Ltd: Chichester, 2001.

(48) de Hoffman, E.; Stroobant, V. *Mass Spectrometry: Principles and Applications*; 3rd ed.; Wiley, 2002.

(49) Morand, K. L.; Horning, S. R.; Cooks, R. G. *Int. J. Mass Spectrom. Ion Proc.* **1991**, *105*, 13.

(50) March, R. E. *J. Mass Spectrom.* **1997**, *32*, 351.

(51) Comisaro.Mb; Marshall, A. G. *Chem. Phys. Let.* **1974**, *25*, 282.

(52) Hu, Q. Z.; Noll, R. J.; Li, H. Y.; Makarov, A.; Hardman, M.; Cooks, R. G. *J. Mass Spectrom.* **2005**, *40*, 430.

(53) Gaskell, S. J. *J.Mass Spectrom.* **1997**, *32*, 677.

(54) Fenn, J. B.; Mann, M.; Meng, C. K.; Wong, S. F.; Whitehouse, C. M. *Mass Spectrom. Rev.* **1990**, *9*, 37.

(55) Gaskell, S. J.; Bolgar, M. S.; Riba, I.; Summerfield, S. G. *Selected Topics in Mass Spectrometry in the Biomolecular Sciences* **1997**, *504*, 3.

(56) Wilm, M. S.; Mann, M. *Int. J.Mass Spectrom Ion Proces.* **1994**, *136*, 167.

(57) Taflin, D. C.; Ward, T. L.; Davis, E. J. *Langmuir* **1989**, *5*, 376.

(58) Dole, M.; Mack, L. L.; Hines, R. L. *J. Chem. Phys.* **1968**, *49*, 2240.

(59) Iribarne, J. V.; Thomson, B. A. *J. Chem. Phys.* **1976**, *64*, 2287.

(60) Thomson, B. A.; Iribarne, J. V. *J. Chem. Phys.* **1979**, *71*, 4451.

(61) Oberacker, V. E.; Pinkston, W. T.; Kruse, H. G. W. *Reports on Progress in Physics* **1985**, *48*, 327.

(62) Hirabayashi, A. *Int. J. Mass Spectrom.* **1998**, *175*, 241.

(63) Tang, L.; Kebarle, P. *Anal. Chem.* **1993**, *65*, 3654.

(64) Takats, Z.; Nanita, S. C.; Cooks, R. G.; Schlosser, G.; Vekey, K. *Anal. Chem.* **2003**, *75*, 1514.

(65) Schalley, C. A. *Int. J.Mass Spectrom.* **2000**, *194*, 11.

(66) Schalley, C. A. *Mass Spectrom. Rev.* **2001**, *20*, 253.

(67) Paul, W. *Reviews of Modern Physics* **1990**, *62*, 531.

(68) Paul, W. *Angew. Chem. Int. Ed.* **1990**, *29*, 739.

(69) Paul, W.; Steinwedel, H. *Zeitschrift Fur Naturforschung Section a-a Journal of Physical Sciences* **1953**, *8*, 448.

(70) Lee, M. S.; Kerns, E. H. *Mass Spectrom. Rev.* **1999**, *18*, 187.

(71) Cooks, R. G.; Glish, G. L.; McLuckey, S. A.; Kaiser, R. E. *Chemical & Engineering News* **1991**, *69*, 26.

(72) Dehmelt, H. *Physica Scripta* **1995**, *T59*, 87.

(73) Stafford, G. C.; Kelley, P. E.; Syka, J. E. P.; Reynolds, W. E.; Todd, J. F. J. *Int. J. Mass Spectrom. Ion Proc.* **1984**, *60*, 85.

(74) Wilcox, B. E.; Hendrickson, C. L.; Marshall, A. G. *J. Am. Soc. Mass Spectrom.* **2002**, *13*, 1304.

(75) Agnes, R. G.; KHorlick, G. *Applied Spectroscopy* **1994**, *48*, 655.

(76) Cech, N. B.; Enke, C. G. *Anal. Atom. Spectrom.* **2001**, *20*, 362.

(77) Hao, C. Y.; March, R. E. *J. Mass Spectrom.* **2001**, *36*, 509.

(78) Lavanant, H.; Virelizier, H.; Hoppilliard, Y. *J. Am. Soc. Mass Spectrom.* **1998**, *9*, 1217.

(79) Gianelli, L.; Amendola, V.; Fabrizzi, L.; Pallavicini, P.; Mellerio, G. G. *Rapid Commun. Mass Spectrom.* **2001**, *15*, 2347.

(80) Deng, H.; Kebarle, P. *J. Am. Chem. Soc.* **1998**, *120*, 2925.

(81) Gatlin, C. L.; Turecek, F.; Vaisar, T. *Anal. Chem.* **1994**, *66*, 3950.

(82) Schramel, O.; Michalke, B.; Kettrup, A. *J. Chromatogr. A* **1998**, *819*, 231.

(83) Mollah, S.; Pris, A. D.; Johnson, S. K.; Gwizdala III, A. B.; Houk, R. S. *Anal. Chem.* **2000**, *72*, 985.

(84) Thomas, B. J.; Mitchell, J. F.; Theopold, K. H.; Leary, J. A. *J. Organomet. Chem.* **1988**, *348*, 333.

(85) Shepherd, R. E. *Coord. Chem. Rev.* **2003**, *247*, 147.

(86) Gatlin, C. L.; Turecek, F. *Electrospray Ion Mass Spectrom.* **1997**, 527.

(87) Gatlin, C. L.; Turecek, F. *Electrospray ionisation Mass Spectrometry: Fundamentals, Instrumentation and Applications*; Wiley, 1997.

(88) Stewart, I. I. *Spectrochem. Acta.* **1999**, *B54*, 1649.

(89) Di Marco, V. B.; Bombi, G. G. *Mass Spectrom. Rev.* **2006**, *35*, 347.

(90) Alyea, E. C.; Craig, D.; Dance, I.; Fisher, K.; Willett, G.; Scudder, M. *Cryst. Eng. Comm.* **2005**, *7*, 491.

(91) Miras, H. N.; Wilson, E. F.; Cronin, L. *Chem. commun.* **2009**, 1297.

(92) Garibay, S. J.; Wang, Z.; Cohen, S. M. *Inorg. chem.* **2010**, *49*, 8086.

(93) Becke, A. D. *J. Chem. Phys.* **1993**, *98*, 5648.

(94) Lee, C.; Yang, W.; Parr, R. G. *Phys. Rev. B* **1988**, *37*, 785.

(95) Stephens, P. J.; Devlin, F. J.; Chabalowski, C. F.; Frisch, M. J. *J. Phys. Chem.* **1994**, *98*, 11623.

(96) Vosko, S. H.; Wilk, L.; Nusair, M. *Can. J. Phys.* **1980**, *58*, 1200.

(97) Strassner, T.; Taige, M. A. *J. Chem. Theory. Comput.* **2005**, *1*, 848.

(98) Mariam, Y. H.; Musin, R. N. *J. Mol. Struc-Theochem.* **2001**, *549*, 123.

(99) Huang, Z. G.; Yu, L.; Dai, Y. M. *Struct. chem.* **2010**, *21*, 855.

(100) Ruangpornvisuti, V. *Int. J. Quantum Chem.* **2010**, *110*, 1019.

(101) Himmel, H. J. *Eur. J. Inorg. Chem.* **2003**, 2153.

(102) Lozynski, M.; Rusinska-Roszak *J. Phys. Chem. A* **1998**, *102*, 1899.

(103) Troitino, D.; Bailey, L.; Peral, F. *J. Mol. Struc-Theochem.* **2006**, *767*, 131.

(104) Borisenko, V. E.; Krekov, S. A.; Fomenko, M. Y.; Koll, A.; Lipkovski, P. **2008** *882*, 9.

(105) Ditchfield, R.; Hehre, W. J.; Pople, J. A. *J. Chem. Phys.* **1971**, *54*, 724.

(106) Hehre, W. J.; Ditchfield, R.; Pople, J. A. *J. Chem. Phys.* **1972**, *56*, 2257.

(107) Hariharan, P. C.; Pople, J. A. *Mol. Phys.* **1974**, *27*, 209.

(108) Hariharan, P. C.; Pople, J. A. *Theoretica Chimica Acta* **1973**, *28*, 213.

(109) Francl, M. M.; Pietro, W. J.; Hehre, W. J.; Binkley, J. S.; Gordon, M. S.; DeFrees, D. J.; Pople, J. A. *J. Chem. Phys.* **1982**, *77*, 3654.

(110) Gordon, M. S. *Chem. Phys. Let.* **1980**, *76*, 163.

(111) Blaudeau, J.-P.; McGrath, M. P.; Curtiss, L. A.; Radom, L. *J. Chem. Phys.* **1997**, *107*, 5016.

(112) Clark, T.; Chandrasekhar, J.; Spitznagel, G. W.; Schleyer, P. v. R. *J.Comp. Chem.* **1983**, *4*, 294.

(113) Frisch, M. J. T., G. W.; Schlegel, H. B.; Scuseria, G. E.; Robb, M. A.; Cheeseman, J. R.; Montgomery, Jr., J. A.; Vreven, T.; Kudin, K. N.; Burant, J. C.; Millam, J. M.; Iyengar, S. S.; Tomasi, J.; Barone, V.; Mennucci, B.; Cossi, M.; Scalmani, G.; Rega, N.; Petersson, G. A.; Nakatsuji, H.; Hada, M.; Ehara, M.; Toyota, K.; Fukuda, R.; Hasegawa, J.; Ishida, M.; Nakajima, T.; Honda, Y.; Kitao, O.; Nakai, H.; Klene, M.; Li, X.; Knox, J. E.; Hratchian, H. P.; Cross, J. B.; Bakken, V.; Adamo, C.; Jaramillo, J.; Gomperts, R.; Stratmann, R. E.; Yazyev, O.; Austin, A. J.; Cammi, R.; Pomelli, C.; Ochterski, J. W.; Ayala, P. Y.; Morokuma, K.; Voth, G. A.; Salvador, P.; Dannenberg, J. J.; Zakrzewski, V. G.; Dapprich, S.; Daniels, A. D.; Strain, M. C.; Farkas, O.; Malick, D. K.; Rabuck, A. D.; Raghavachari, K.;

Foresman, J. B.; Ortiz, J. V.; Cui, Q.; Baboul, A. G.; Clifford, S.; Cioslowski, J.; Stefanov, B. B.; Liu, G.; Liashenko, A.; Piskorz, P.; Komaromi, I.; Martin, R. L.; Fox, D. J.; Keith, T.; Al-Laham, M. A.; Peng, C. Y.; Nanayakkara, A.; Challacombe, M.; Gill, P. M. W.; Johnson, B.; Chen, W.; Wong, M. W.; Gonzalez, C.; and Pople, J. A; Gaussian, Inc.: Wallingford, CT, 2004.

(114) Fitzgerald, G.; Andzelm, J. *J. Phys. Chem.* **1991**, *95*, 10531.

(115) Boys, S. F.; Bernardi, F. *Mol. Phys.* **1970**, *19*, 553.

(116) Lipinski, J.; Chojnaki, H. *Int. J. quantum chem.* **1981**, *19*, 891.

(117) Glendening, E. D.; Reed, A. E.; Carpenter, J. E.; Weinhold, F. NBO Program.

CHAPTER 2: Collision Induced Dissociation of Substituted Phenolic Oxime Copper Complexes

A tandem mass spectrometry investigation of gas phase stability

Table of Contents

2.1 Introduction

2.1.1 Aims

This chapter considers the collision induced dissociation of ionised copper(II) complexes, [Cu(**L**)$_2$], of a series of 5-*tert*-butyl-3-X-substituted salicylaldoximes, where X = H, Me, ^{t}Bu, NO_2, Cl, Br, OMe. (Figure 2.1)

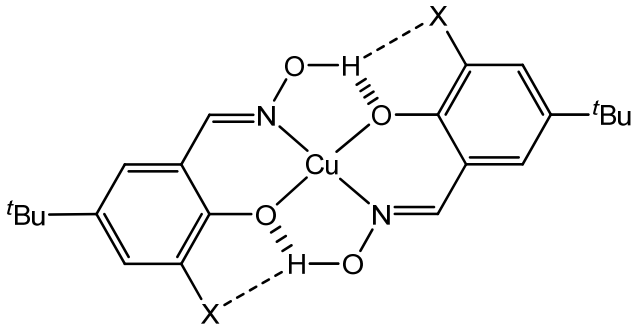

Figure 2.1: [Cu(L)$_2$], X = H, Me, ^{t}Bu, NO_2, Cl, Br, OMe

At the outset we aimed to

1. Determine the relative gas phase stabilities of ions derived from 5-*tert*-butyl-3-X-substituted [Cu(**L**)$_2$] series under resonance excitation conditions.
2. Investigate whether experimental conditions influence the gas phase stability of these complexes.
3. Establish whether there is a correlation between gas phase stabilities of the ion series and the extraction strength of the ligand (**L**H).
4. Evaluate the usefulness of CID methods in comparing the effects on the strength of inner and outer coordination sphere interactions in Cu(II) phenolic oxime complexes.

2.1.2 Collision Induced Dissociation (CID)

As discussed in Chapter 1, most tandem mass spectrometry systems, in particular systems incorporating an ion trap, can perform MS/MS and MS^n studies.[1] In such experiments, a selected precursor is trapped and fragmented in a collision cell or chamber, producing spectra of the product ions for that particular precursor ion. These data are usually used for structural elucidation and analyte identification through "fragment fingerprinting". The most common method of fragmentation is collision induced dissociation (CID)[2,3] which is also sometimes referred to as collisionally activated decomposition (CAD).

Three types of mass spectrometers are capable of performing CID experiments; quadrupole ion trap mass spectrometers,[4,5] triple quadrupole time-of-flight[6] mass spectrometers incorporating collision cells, and Fourier transform ion cyclotron resonance mass spectrometers (FT-ICR-MS).[7] For each of these, CID is carried out using the same basic approach. A mass/charge (m/z) range is isolated, an electrical potential is applied to the ions falling within this range, resulting in kinetically energetic ions. These ions are then allowed to collide with neutral gas molecules (often helium, nitrogen or argon), with each collision converting some of the kinetic energy is into internal energy which results in bond cleavage and the dissociation into smaller fragments. Both linear and quadrupole ion trap mass spectrometers were used in this research. Their means of measuring mass to charge ratios are detailed in chapter 1. Sections 2.1.3 and 2.1.4 below outline the use of CID with each of these machines.

2.1.3 Quadrupole Ion Trap

In CID using a quadrupole ion trap the precursor ion is selectively isolated and thermalised in the trap *via* collisional cooling with a chemically inert collision gas such as Ar, He, N_2, CO_2 etc., focussing the ions in the centre of the trap. The

precursor ion is resonantly excited by application of a tickle voltage which forces the ions out of the centre of the trap due to an increase in translational energy. The ions then undergo repeated collisions with the inert gas, which convert the applied translational energy into internal energy. The build up of potential energy within the molecule continues until the fragmentation threshold is reached, whereupon dissociation occurs and the product ions are formed.[8-10] The excited ions are subsequently re-focussed to the centre of the trap during a second collisional cooling event which reduces both their kinetic energy and the physical dimensions of their associated trajectories. The ion cloud remains vibrationally activated for some time after resonant excitation as a large number of collisions are required to dissipate the excess internal energy.[11](Figure 2.2)

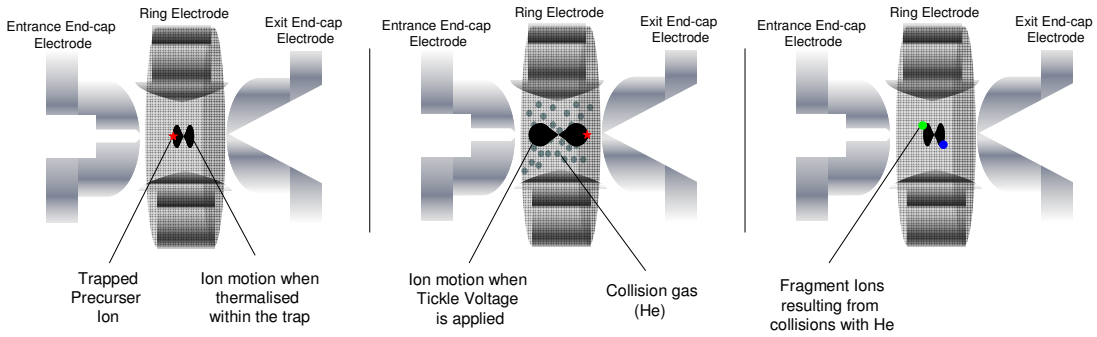

Figure 2.2: Application of tickle voltage to induce precursor ion dissociation within a quadrupole ion trap

2.1.4 Quadrupole Time-Of-Flight collision cell

The main difference between an ion-trap and a collision cell is that a collision cell generally has an applied RF on the ion guiding multipoles within the cell but no collision RF, *i.e.* the ions are excited before entering the collision cell. The "collision" energy is typically set to 10eV for non-CID TOF-MS experiments as the resultant collisional cooling has a beneficial effect of increased resolution[12-14] but when increased acts in a similar way to a tickle voltage, increasing the number of collisions, and resulting in fragmentation. (Figure 2.3)

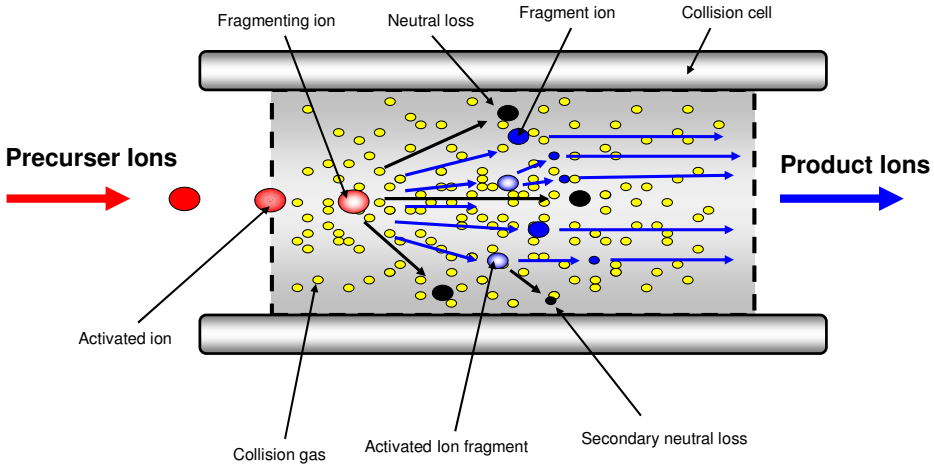

Figure 2.3: Fragmentation processes occurring in a collision cell during CID. Figure modified from the University of Bristol mass spectrometry resource web page.[15]

The fragmentation reactions that occur in CID vary considerably depending on the precursor ion, the type of product ion and the amount of energy involved. At lower energies, which are close to the fragmentation threshold, fragmentation reactions are often limited to neutral losses, depending on the nature of the precursor ion. At higher energies, retro-synthetic type reactions are often observed which are much more structurally significant, and often result in cleavage of the molecule at characteristic positions. At very high energies, C-C bond cleavage can occur which could lead to uncontrolled fragmentation.[16]

CID has been used extensively used to investigate biological samples, [17-20] but has already been applied to metal complexes[21] and used to determine the bond dissociation energies by measuring the kinetic energy dependence of reactions between solvated metal ions and the inert collision gas.[22]

2.1.5 Definition of Gas Phase Stability in CID

When describing "gas phase stability" with respect to collision induced dissociation of ions, it is the stability of ions under resonance excitation conditions. The resonance threshold in CID defines the "stability" of the trapped ion and is determined by the ease at which the ion can redistribute the increased energy

amongst its vibrational modes upon collision with a stationary collision gas (helium in this case).

CID has been shown to offer an easy way of probing the stability of bonding interactions in the gas phase. As will be discussed later, CID can be carried out on wide range of commercial mass spectrometers, including triple quadrupoles, quadrupole ion traps and ion cyclotron resonance instruments. The use of CID in quadrupole ion traps to estimate bonding strength was first reported by Hart and McLuckey.[23] Brodbelt *et. al.* further developed this idea and proposed a technique for quadrupole ion traps called "energy-variable CID".[24]

Similar experiments have since been carried out in an ion cyclotron resonance mass spectrometer.[25] Similar to the threshold CID experiments normally done on guided ion beam mass spectrometers, as discussed above,[26] energy variable CID has been shown to probe the kinetic stability of ions. Although it has not yet offered a route to quantitative binding strength measurements, correlations between the energy-variable CID results and bonding energy has been developed, and the use of CID to obtain *relative* strengths of bonds has been fairly extensive.[23-25,27]

Among the many factors that affect the stability of an ion under CID conditions in quadrupole ion traps,[28] the binding energy and overall number of vibrational degrees of freedom of the ion[29] play the most prominent role. When comparing chemically similar systems with the same number of degrees of freedom, differences in the binding energy can be observed. Brodbelt's group used this approach to compare the binding strengths in various systems such as drug–DNA/metal (CO^{2+}, $Ni^{2+,}$ or Zn^{2+}) complexes[30] and metal ion-pyridyl ligand complexes.[31]

The number of degrees of freedom-dependent stability of ions and ion–neutral non-covalent complexes under CID conditions was studied by Vinokur and Ryzhov. They showed that the stability of ions as probed by CID has a linear dependence on the total number of degrees of freedom for the ions with similar bonding energies.[32]

The groups of Brodbelt and O'Hair, amongst others, have extensively used energy-dependent CID and proposed schemes for the conversion of the apparent thresholds into threshold energies and discussed the most relevant effects, such as excitation time and amplitude, ion mass and ion density of states.[23,24,30-40] A study by O'Hair et. al. looking into the effects of chloride and acetate ligands on the reactivity of organomagnesates by determining relative gas phase stabilities of the ligated complexes.[37] In the previous approaches for the quantitative analysis of breakdown curves obtained with IT-CID, the energy to bring about a certain amount of fragmentation was considered, e.g. either a small amount (5% or 10%) or 50% parent-ion dissociation,[32,35,36] as used in this work, termed as X_c. Schröder *et. al.* suggested using the AE_{exp} value, *i.e.* the onset of fragmentation obtained by linear extrapolation of the slope of the breakdown curve at $E_{0.5}$ (X_c) to the baseline, to investigate substitution effects on the dissociation of benzylpyridinium ions.[38]

Most of the reported work using LCQ Ion traps to determine gas phase stabilities covert the Normalised Collision Energy, which takes into account the m/z of the sample being investigated (See Section 2.1.6), into the point-to-point potential applied upon CID. Recent work by Schröder *et. al.* used the unconverted NCE values to investigate relative binding energies of copper(II) complexes with chloride and pyridine ligands.[41]

Another factor that needs to be taken into account when defining stability under resonance excitation conditions is the efficiency with which the applied energy, E_{Lab}, increases the analyte ion's internal energy, E_{int}. This increase in internal energy can related to the laboratory frame interaction energy by Equation **2.1**;

$$\boldsymbol{E_{int} = E_{Lab}\left(\frac{M_a}{\langle M_a + M_c \rangle}\right)} \qquad \textbf{2.1}$$

where M_a is the mass of the analyte and M_c is the mass of the collision gas.[1]

2.1.6 Normalised Collision Energy

In the early nineties a number of groups reported energy resolved mass spectrometry experiments, examining the relative thermodynamic stability of a range of desolvated gaseous ions.[42-46] These investigations gave little consideration to the distribution of energy and its relationship with the properties of the analyte. Subsequent work described a linear relationship between *m/z* and fragmentation efficiency for a series of doubly protonated tryptic peptides.[47] The experiments were reproduced in a patent filed by the Finnigan Corporation and this development was incorporated into commercial software used to control this company's ion trap devices.

Normalised collision energy (NCE) was introduced by Finnigan as a means to standardise experimental results, allowing comparison between investigations of the same chemical system using the same type of instrument and to correct for the known mass dependency of energy distribution.[48,49]

In this work the energy required to dissociate trapped species contained within the trap was tuned using the NCE function of Xcalibur 1.2 during experiments performed using the Finnigan LCQ Classic. The amplitude of the NCE corresponds to the amplitude of the radiofrequency (RF) potential applied to the end-cap electrodes of the QIT during resonant excitation. NCE values (given in %) can be converted to RF amplitude (in volts) using Equation **2.2**, where, *m* and *c* are the respective gradient and intercept of the calibration curve obtained during calibration of the Finnigan LCQ Classic.

$$\boldsymbol{RF = \frac{NCE}{30} \times \left[\left(m\frac{m}{z}\right) + c\right]} \qquad \boldsymbol{NCE = \left(\frac{RF}{\left[\left(m\frac{m}{z}\right)+c\right]}\right) \times 30} \qquad \textbf{2.2}$$

The correction factor (equalling 30%) corresponds to the ratio between the *m/z* of the parent ion and the lowest *m/z* ion that can be simultaneously contained within the QIT (see Chapter 1 Section 1.6.4.).[49] Although consideration will be given to units of fragmentation energy (% or V) in the gas phase stability studies presented throughout this thesis, for the most part the normalised energy is reported.

2.1.7 The Use of Sigmoidal Curves

The method in this thesis to compare the stabilities of gaseous ions uses the ratio of the ion current of the trapped analyte ion (AIC) to the total current for all ions (TIC). These values are plotted against increasing collision energy (for the most part, NCE) yielding a sigmoidal curve which describes the dissociation of the analyte ion (see Figure 2.4).

The sigmoidal curves give a good visual representation of the dissociation process, the point of inflection (termed the X_c value) is defined as the point at which the sign of the curvature changes. This is a useful point to compare the relative positions of different sigmoidal curves and relates to the stability as it defines the point when 50% of the analyte has been dissociated.

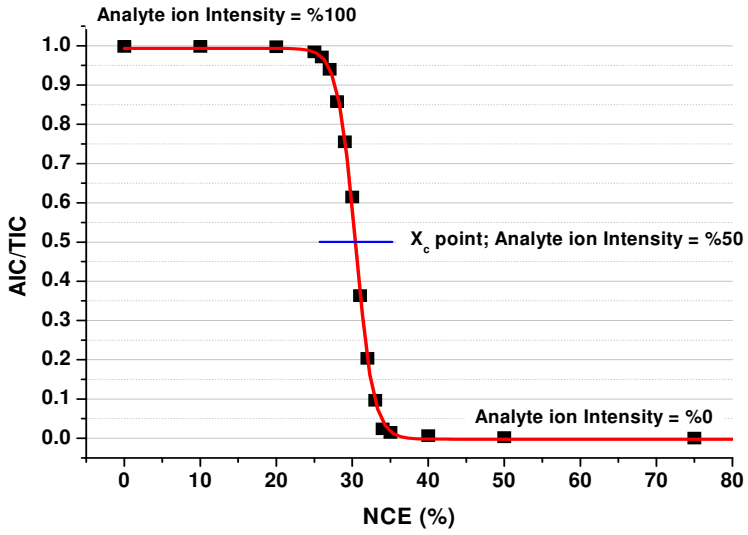

Figure 2.4: A CID dissociation curve (in black) with sigmoidal fit (in red). The minima and maxima of the data are highlighted as is the X_c value, where %50 of the analyte ions have been dissociated.

2.2 Results and Discussion

2.2.1 Mass spectrum of [Cu(L1)$_2$] complex

The mass negative mode ESI mass spectrum of a 20µM methanolic solution of [Cu(**L1**)$_2$] is shown in Figure 2.5. The base peak is the monodeprotonated complex, [Cu(**L1**)(**L1**-H)]$^-$, and has a m/z of 446.1. The remaining peaks observed in the spectrum represent species formed by both in-source fragmentation (labelled [**L1**-H_2O], [M-**L1**]$^-$ and [M-H_2O]$^-$ in Figure 2.5, see also Section 2.27) and solution aggregation of the [Cu(**L1**)$_2$] (labelled [M][Cu(**L1**-H)]$^-$ and [M][Cu(**L1**-H)]$_2^-$ in Figure 2.5, see also Chapter 6 for further information on aggregates).

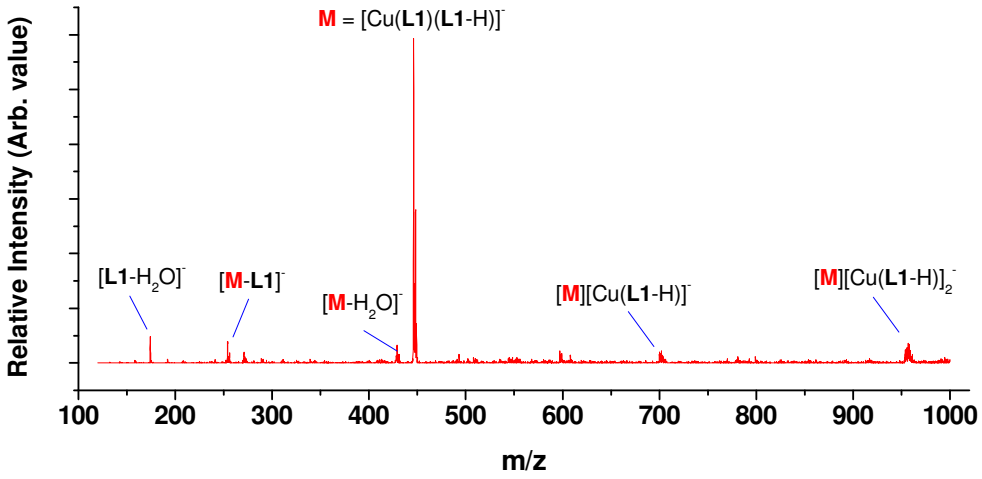

Figure 2.5: ESI mass spectrum of a 20µM methanolic solution of [Cu(**L1**)$_2$] as measured using a Thermo-Fisher LCQ. The major observed species have been labelled.

The machine settings were altered as to obtain the best signal intensity for each of the [Cu(**L**)(**L**-H]$^-$ species investigated, reducing in-source fragmentation and the formation of aggregate species . The [Cu(**L**)(**L**-H]$^-$ species were selected and isolated for collision induced dissociation studies using the MS/MS capabilities of the LCQ mass spectrometer.

2.2.2 Collision induced dissociation of monoanionic [Cu(L)(L-H)]⁻ species

The CID recorded for [Cu(**L1**)(**L1**-H)]⁻ (Figure 2.6) indicates the resonance threshold to be ≈ 27% NCE with dissociation occurring at 27-35% NCE.

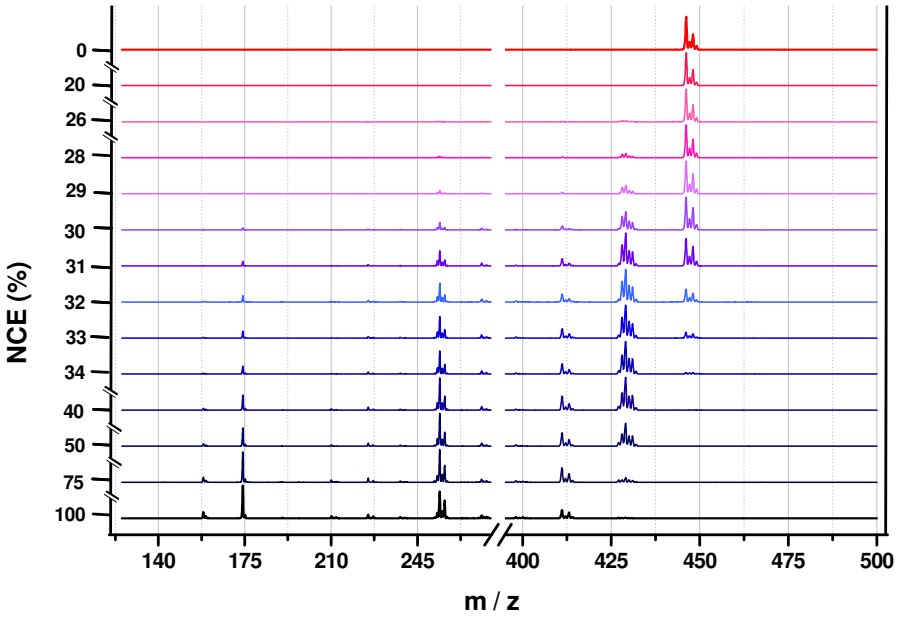

Figure 2.6: The relative intensities of parent [Cu(**L1**)(**L1**-H)]⁻ ion (m/z = 446) and fragment ions with variation of collision energies.(NCE)

As seen in Figure 2.6 numerous fragmentations occur simultaneously when the threshold is reached, suggesting that gas phase stability, in these cases, is not dependent on a single dissociation, as discussed previously, but proceeds *via* competing fragmentation processes.

2.2.3 Solvent effects on mass spectra and CID stability

The effects of solvent on condensed phase equilibria[50] and ionisation equilibrium constants[51] have been well documented, with the polarity, pH and nature (protic, aprotic, coordinating or non-coordinating) being amongst the most influential solvent

properties. These are reflected in the ESI mass spectra obtained for methanol and acetonitrile solutions of [Cu(**L7**)$_2$] shown in Figure 2.7.

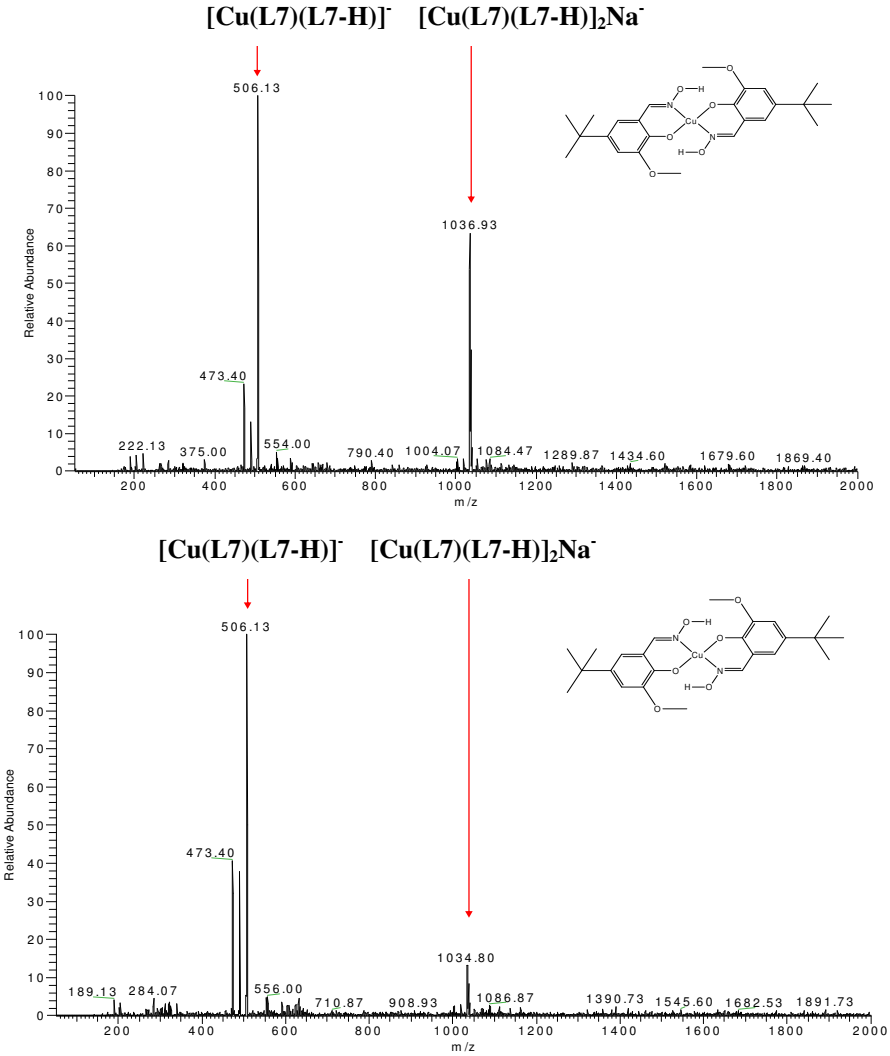

Figure 2.7: ESI negative ion mass spectra of 10μM solutions of [Cu(**L7**)$_2$] in MeOH (top) and MeCN (bottom).

The relative intensities of the major anion peaks [Cu(**L7**)(**L7**-H)]$^-$ and Na[Cu(**L7**)(**L7**-H)]$_2^-$ are solvent dependent. The sodium aggregate, Na[Cu(**L7**)(**L7**-H)]$_2^-$ is more prevalent in the ESI in methanol solutions probably as a consequence of sodium salt impurities being present in a higher concentration in methanol than in acetonitrile. It is also possible that the changes are not only due to a direct relationship between the solvent and the condensed phase equilibria, but the role the

solvent plays in the ionisation process as well *i.e.* polarity, the rate of desolvation, surface tension of the droplets *etc.*(see also Chapter 1 Section 1.6.3)

In extraction equilibria the polarity and chemical structure of the solvent can play a major role in determining the relative thermodynamic stability of the ligand monomers and dimers and of the copper complexes. The industrial processes use non-polar solvents such as kerosenes, generally defined by their aromatic : aliphatic content, which have been shown to facilitate the aggregation and dimerisation of these ligands.[52] The non-polar environment encourages the polar NOH groups to form intermolecular H-bonds.

When highly polar solvents are used for ESI (see Chapter 1 Section 1.6.3) they heavily influence solution phase speciation. The polarity of the solvent disfavours dimerisation and influences ionisation and desolvation processes. Methanol, for example, being both a polar and protic solvent, is not suited to deliver ligand dimers but has been proven to be an efficient and effective carrier solvent in ESI mass spectrometry.

In the CID of small molecules the ions are thermalised and, in theory, the solvent, mode of ionisation, and machine settings should not influence their gas phase stability. A study was carried out to ensure solvent effects did not affect the properties of the *trapped* [Cu(**L**)(**L**-H)]$^-$ species. 10 μM solutions of [Cu(**L1**)$_2$], [Cu(**L2**)$_2$] and [Cu(**L4**)$_2$] were prepared in methanol and acetonitrile. CID investigations were carried out as described in Section 2.1.7. S-curves of the gas phase stabilities of each anion in both solvents are plotted in Figure 2.8.

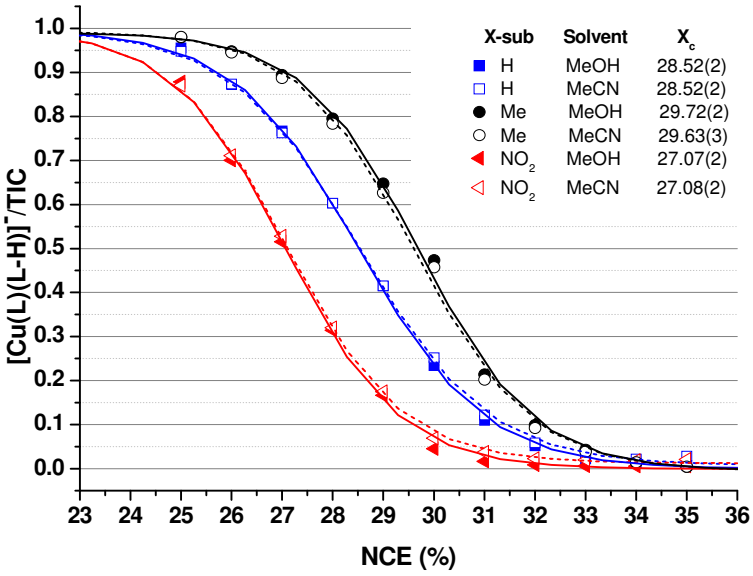

Figure 2.8: Comparison of the breakdown curves for [Cu(**L4**)(**L4**-H)]$^-$, [Cu(**L1**)(**L1**-H)]$^-$, and [Cu(**L2**)(**L2**-H)]$^-$ when delivered from methanol and acetonitrile.

The breakdown curves in Figure 2.8 show that the [Cu(**L**)(**L**-H)]$^-$ species generated from either acetonitrile or methanol solutions have the same X_c values within experimental error, indicating that solvent effects have little to no effect on the stability of the monoanions, [Cu(**L**)(**L**-H)]$^-$ under CID. In contrast it can be seen that the stability of the monoanions varies considerably with nature of the 3-X substituent in the order NO_2 < H < Me.

2.2.4 Effects of trapping parameters on stability

Another possible influence on the relative stabilities of ions within the trap is space charge effects.[53,54] These occur when the number of ions in the trap is too great resulting from the ions experiencing a degree of charge interaction. If a number of ions of the same m/z value are present, as is the case for CID, it can lead to mass shifts and delayed ion ejection.[55-57] When an appropriate number of ions are present in the trap ion motion occurs as calculated by the SIMION program[58] as discussed in Chapter 1. The existence of ghost peaks is due to discrete changes in the ion motion

within the trap and it has been reported that this could potentially lead to a variable stability of ions within the trap.

To determine whether the number of ions within the trap has an influence on stability under CID conditions a study was carried out exploiting the automatic gain control settings in the Xcalibur 2.0 interface suite.

2.2.4.1 Automatic Gain Control (AGC)

Automatic gain control (AGC)[59-61] was first developed by the Finnigan Corporation in the early nineties[60] and provides an automated regulation to a dynamic ion flux transmitted from the source of the instrument. This increased control results in a more constant ion population within the QIT, occurring *via* constant monitoring of the ion population using a pre-scan, providing continual adjustment to the ion accumulation time of the ion trap.

Using a single sample, and fixed machine settings, a series of CID dissociation experiments were carried out on the [Cu(**L1**)(**L1**-H)]$^-$ ion, varying the ion population within the trap using the AGC and set inject times. (Figure 2.9)

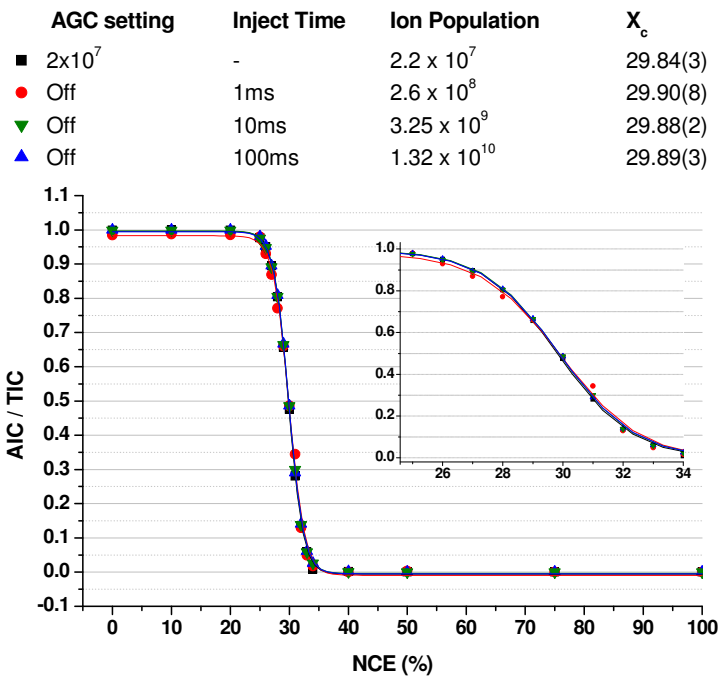

Figure 2.9: Sigmoidal dissociation curves of of [Cu(**L1**)(**L1**-H)]$^-$ when varying the inject time and hence ion populations within the trap.

Figure 2.9 shows that, within the ion population range 2.2 x 10^7 – 1.32 x 10^{10}, if space-charge effects are occurring they are having no noticeable effect on the gas phase stability of the trapped [Cu(**L1**)(**L1**-H)]$^-$ species under resonance excitation conditions. This is confirmed by the absence of any variation in the sigmoidal curves and the concordant X_c values with increasing ion populations.

2.2.5 Concentration Studies.

It has been shown[62] that concentration has a major effect on the number of analyte ions formed in the electrospray ionisation process. Such a dependence upon concentration has been seen in the case of this study, as a varying number of [Cu(**L**-H)(**L**-2H)]$^-$ ions are formed from solutions of different concentrations .

The two parameters of interest are the ion count (Figure 2.10), and the inject time (Figure 2.11) for the [Cu(**L**)(**L**-H)]$^-$ species. When using the AGC, in this case the stipulated number of ions was set at 2 x 10^7 and the inject time had a cut off set at

200 µs to avoid trap flooding. Solutions of [Cu(**L1**)$_2$], [Cu(**L3**)$_2$] and [Cu(**L4**)$_2$] of varying concentration (1-80 µM) in LCMS grade methanol were injected into the LCQ at 30 µL/min with constant machine parameters. The experiment was repeated three times and the average inject time times and ion counts were plotted against concentration.

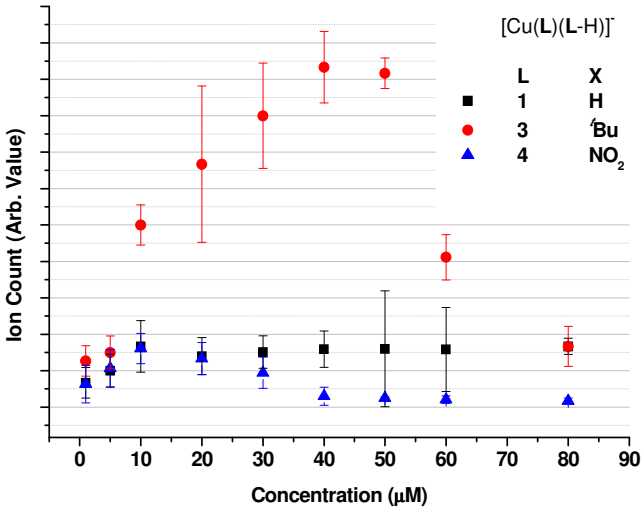

Figure 2.10: Dependence of ion count of [Cu(**L**)(**L**-H)]$^-$ on sample concentration in methanol.

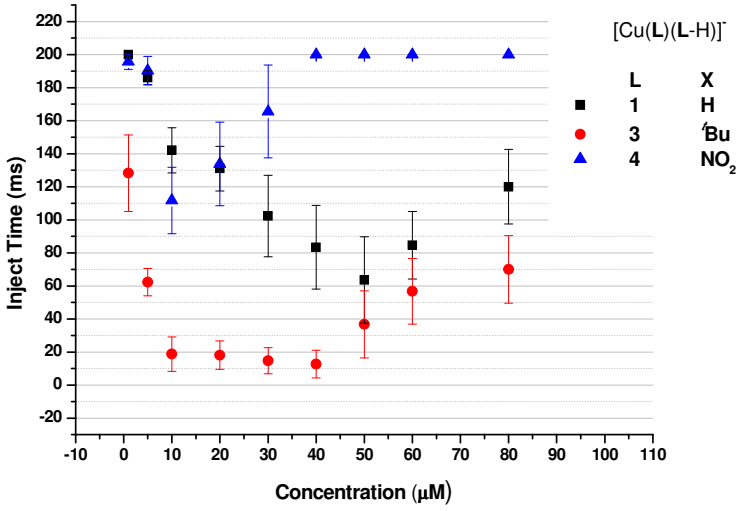

Figure 2.11: Dependence of inject time of [Cu(**L**)(**L**-H)]$^-$ on sample concentration in methanol.

Figure 2.10 shows that the ion count for the [Cu(**L**)(**L**-H)]$^-$ species varies with concentration and the nature of the X-substituent and these in turn affect the time required to attain the desired number of ions within the mass analyser (Figure 2.11). No systematic trend is observed for the three samples, which accentuates the difficulty in using non-automated spray ionisation methods for quantitative measurements.

2.2.5.1 CID study of 10 and 80µM solutions in MeOH.

To determine whether sample concentration has an effect on the gaseous stabilities of *trapped* monoanions, samples ([Cu(**L**-H)$_2$] (**L1**-**L7**)), at two concentrations, 10 and 80 µM, (Figure 2.12 and Figure 2.13 respectively) were subjected to CID. The AGC setting was implemented and trapping times never exceeded the 200 µs cut off, ensuring a constant number of ions within the trap throughout the study.

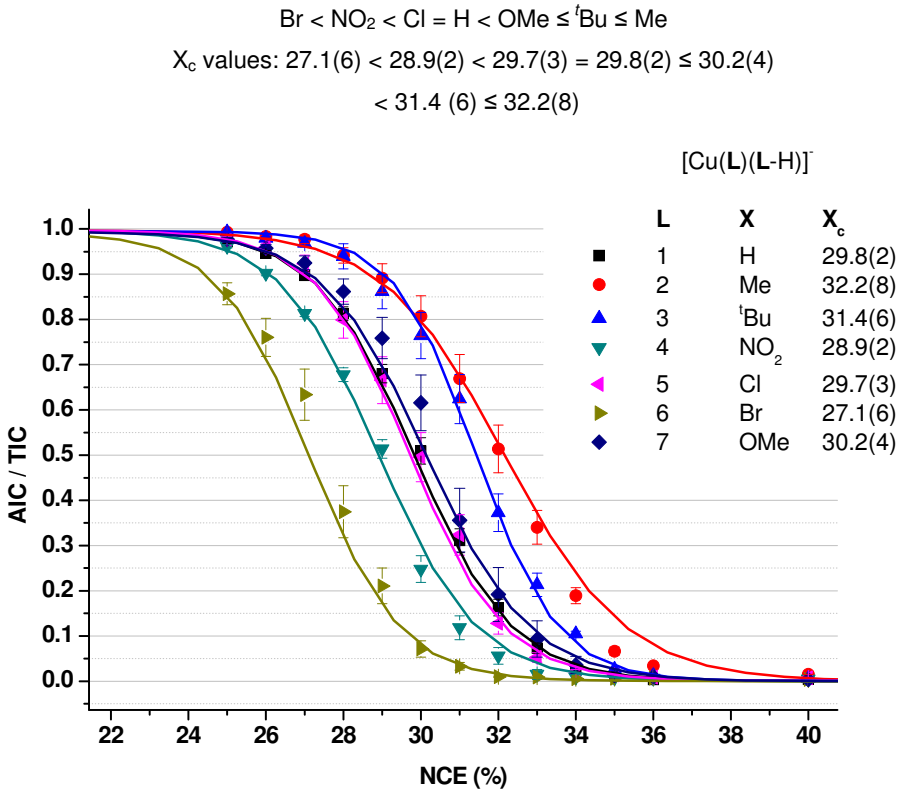

Figure 2.12: Sigmoidal breakdown curves for [Cu(**L**)(**L**-H)]$^-$ monoanions generated from 10µM solutions in MeOH. Errors given to a 2σ level based on 3 repeats. Each point represents 90 scans

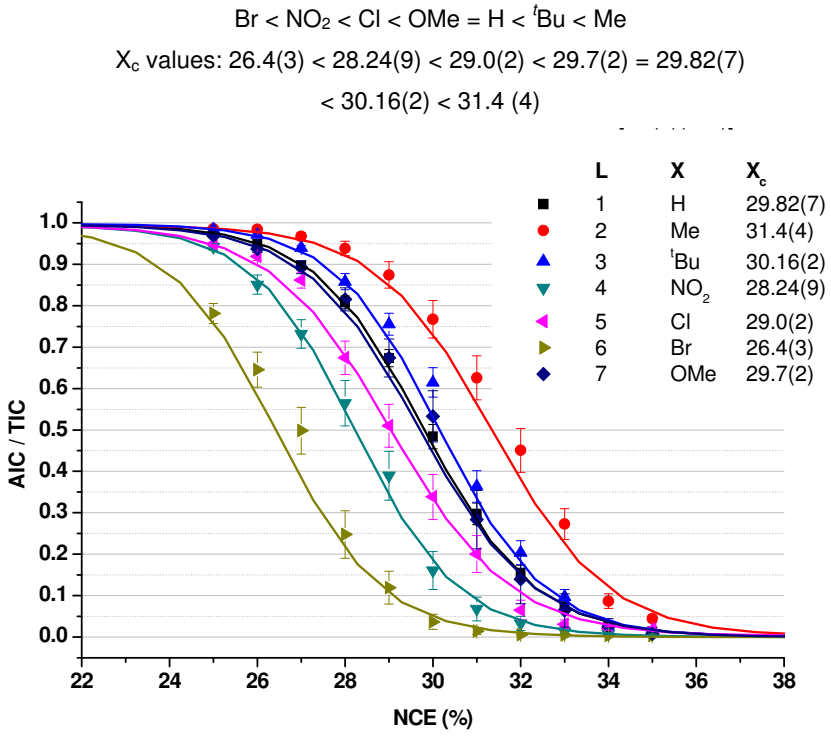

Figure 2.13: Sigmoidal breakdown curves for [Cu(**L**)(**L**-H)]$^-$ monoanions generated from 80μM solutions in MeOH. Errors given to a 2σ level based on 3 repeats. Each point represents 90 scans

Upon increasing the concentration the relative stability ordering changed slightly and a larger spread of X_c energies was observed. The observed changes were, however, within the errors of the experiment as is to be expected. The calculated errors were reduced when the concentration was increased, probably due to better scientific protocol, *i.e.* each of the samples was analysed on the same day and the repeats were performed with a week. Despite the errors of the experiment a definite difference is observed in the stability of the [Cu(**L**)(**L**-H)]$^-$ when the nature of the 3-X-substituent is varied.

2.2.6 Differences in gas phase energies of [Cu(L)(L-H)]$^-$ anions under CID

A comparison of the CID curves for the series of monoanions allows their gas phase stabilities to be ranked. The dependence of stability of [Cu(**L**)(**L**-H)]$^-$ on

the nature of the 3-X-substituent was observed to be Br < NO_2 < Cl < MeO ≈ H < *t*-Bu < Me. (Figures 2.12 and 2.13) This trend is consistent with large electronegative X-groups experiencing significant repulsion from the deprotonated oxime oxygen atom (shaded area in Figure 2.14) and this destabilising effect being larger than the beneficial effect of the hydrogen bond buttressing with the neutral oxime group. The electronegetivity of the X group will also reduce the basicity of the donor atoms in the inner coordination sphere and lead to a further decrease in the stability of the monoanion[Cu(**L**)(**L**-H)]$^-$.

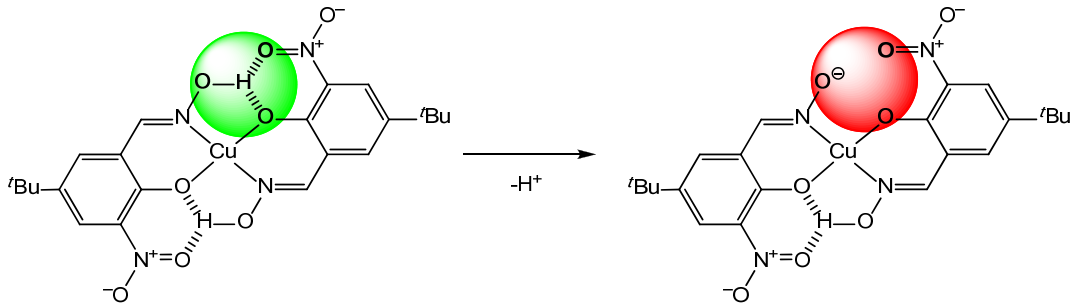

Figure 2.14: Deprotonation of [Cu(**L4**-H)$_2$], and resulting repulsion in the cavity of electronegative atoms (shaded area) destabilizes [Cu(**L4**)(**L4**-H)]$^-$.

The importance of outer sphere coordination interactions in determining stability of these monoanioic complexes is reflected by the position of the methoxy-substituted compound in the series. On the basis of its electron donating properties we would expect this substituent to give the greatest enhancement of bond strength to the *inner* coordination sphere, but in practice the methoxy-substituted anion, [Cu(**L**)(**L**-H)]$^-$, has a very similar gas phase stability to the unsubstituted complex where X=H. This is consistant with the destabilising interaction between the oximate oxygen ion and the methoxy oxygen atom being important.

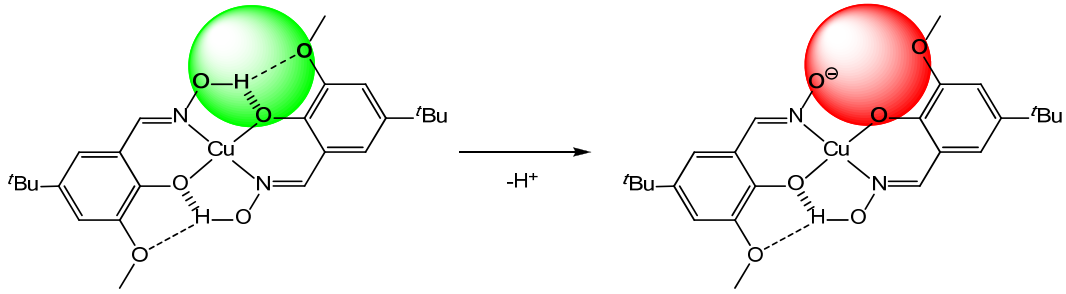

Figure 2.15: Deprotonation of [Cu(**L7**-H)$_2$], and the resulting electronegative "cavity" of oxygen atoms (shaded) which destabilises the [Cu(**L7**)(**L7**-H)]$^-$ anion.

When using CID sigmoidal plots of the type shown in Figure 2.12 and Figure 2.13, to compare the stabilities of ions, account must be taken of the ability of the ions to redistribute the energy acquired by collisions within differing vibrational modes, including those of the substituents. As described above, the "resonance threshold" for an ion in CID is determined by the ease at which it can redistribute the increased energy amongst its vibrational modes after making contact with a collision gas atom. It has previously been observed that the resonance threshold amplitude of gaseous ions is related to the critical energy required for ion dissociation.[63,64] As a consequence, the number of degrees of freedom in chemically related ions is expected to influence the relative stabilities, as derived from the sigmoidal plots. Data indicating how the normalised collision energies for dissociation vary with the number of bonds in the alkyl substituents (R) are presented in Figure 2.16. The six ligands used in this study are shown in Table 2.1 together with the numbers of covalently bonded atom pairs in their monoanionic copper complex [Cu(**L**)(**L**-H)]$^-$.

Table 2.1: The six ligands used together with the numbers of covalently bonded atom pairs in their monoanionic copper complex $[Cu(\mathbf{L})(\mathbf{L}\text{-}H)]^-$. And the resultant X_c values for $[Cu(\mathbf{L})(\mathbf{L}\text{-}H)]^-$.

Ligand	Bonds in $[Cu(\mathbf{L})(\mathbf{L}\text{-}H)]^-$	X_c value for $[Cu(\mathbf{L})(\mathbf{L}\text{-}H)]^-$
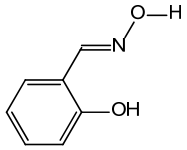	33	26.1(1)
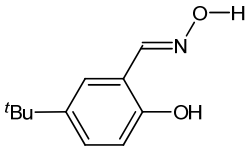	57	29.68(8)
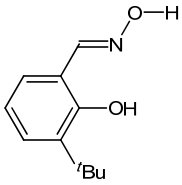	57	26.9(1)
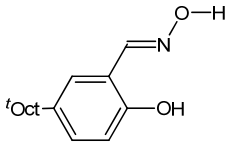	81	30.80(8)
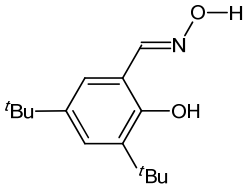	81	30.0(3)
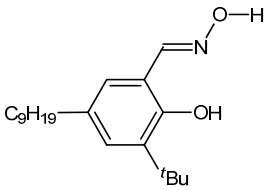	111	32.22(9)

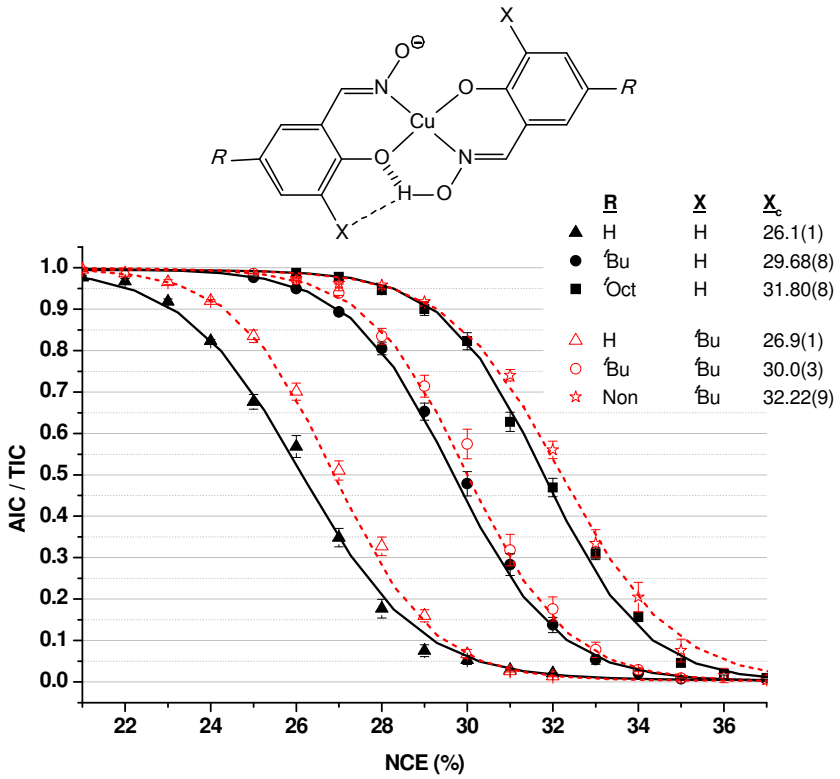

Figure 2.16: Influence of the variation of alkyl groups in the 5-position on collision induced dissociation energies of [Cu(**L**)(**L**-H)]$^-$. Errors given to a 2σ level based on 3 repeats. Each point represents 90 scans

For the anions with no substituent in the 3-position (X=H), the stability increases in the order R = H < ^{t}Bu < ^{t}Oct < Non as the number of vibrational modes associated with the substituent *para* to the phenolate increases. If the alkyl substitution is made in the 3-position then the beneficial effect of additional vibrational modes is offset by the bulk of the group leading to repulsion within the *outer* coordination sphere. Thus despite having identical masses (exact mass = 446.13 daltons) and number of bonds, 3-*t*-butyl salicylaldoximato anion [Cu**L**(**L**-H)]$^-$ has a considerably lower gas phase stability than it's 5-*t*-butyl isomer (X_c = 26.9(1) vs. 29.68(8))

The consistency of interpretation of these effects is supported by considering the series in which the 3-X –substituent is maintained as the *tert*-butyl group. We expect, and observe, the stability to increase as the number of bonds in the 5-substitutent increases *i.e.* R = H < ^{t}Bu < Non and the X_c values (26.9(1), 30.0(3)

and 32.22(9)) confirm this.

2.2.7 CID Fragmentation patterns of 3-X-substituted [Cu(L)(L-H)]⁻ series

In CID the stability of a trapped species is determined by a number of factors including the chemical nature of the species (Section 2.2.4) and the number of bonds (see Section 2.2.6). Another important issue to consider when comparing gas phase stabilities is the mechanism of fragmentation. The fragmentation of the [Cu(**L**)(**L**-H)]⁻ species was investigated to ensure dissociation proceeded using the same modes, *i.e*. ensuring analogous fragments were observed in each case. Figure 2.17 shows the CID spectra for each [Cu(**L**)(**L**-H)]⁻ where **LH** = 3-X-subsituted salicylaldoximes indicating three of the major fragments found.

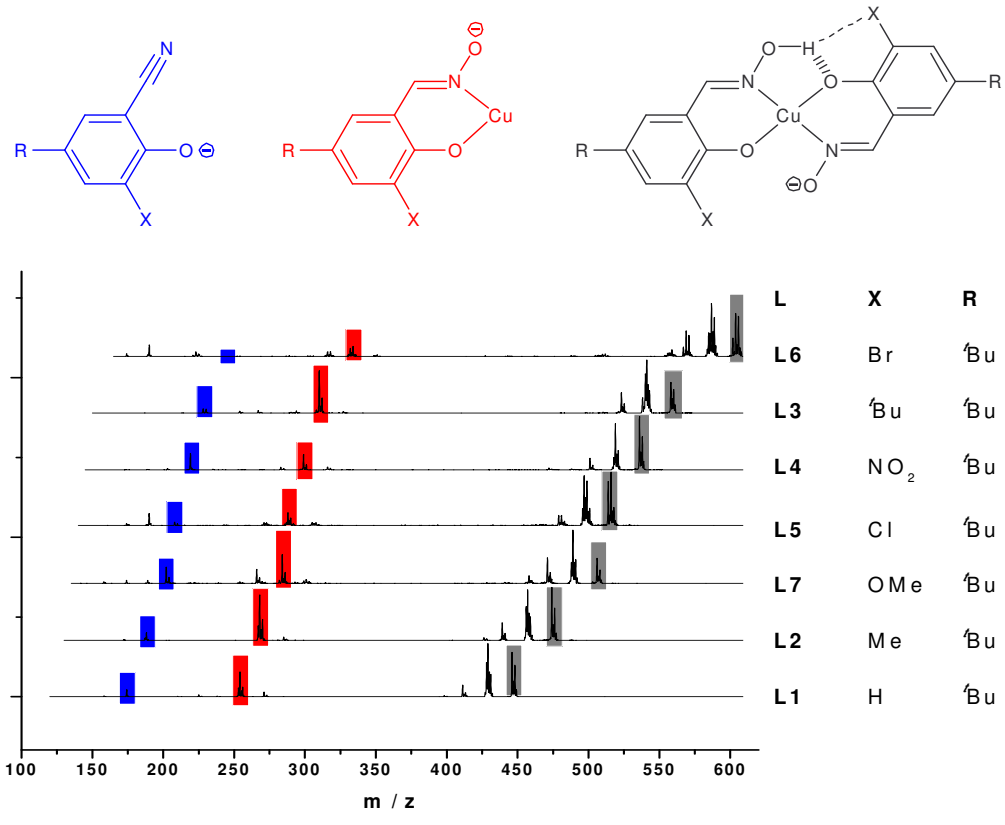

Figure 2.17: Fragmentation patterns of the 3-X-substituted anions. [Cu(**L**)(**L**-H)]⁻, [Cu(L-H)]⁻ and [L-OH_2]⁻ are shaded grey, red and blue respectively. Inset: Proposed structural formula for shaded fragments. For each species the CID spectrum was chosen where the AIC/TIC ratio is closest to the calculated X_c value.

As can be seen in Figure 2.17, the fragmentation patterns of the 3-X-substituted anions, $[Cu(\mathbf{L})(\mathbf{L}\text{-H})]^-$, are virtually identical varying only in minor fragments; for certain species, X=Br, X=Cl, an XH loss is observed, theses losses account for <2% of fragment loss upon dissociation of the $[Cu(\mathbf{L})(\mathbf{L}\text{-H})]^-$ anion and are further investigated in Section 2.2.11 The peaks highlighted are three of the major species. The peaks highlighted in grey represent the trapped ions. The three fragment peaks seen next to these are the initial fragment losses and are detailed more fully in Figure 2.18. The peaks highlighted in red show the major $[Cu(\mathbf{L}\text{-H})]^-$ species and the peaks highlighted in blue indicate the rearranged cyano- form of the deprotonated ligand. In this figure these peaks are minimal but at higher NCE's their intensities become more pronounced.

2.2.8 CID Fragmentation of the 5-R-substituted $[Cu(L)(L\text{-H})]^-$ anions

As for the 3-X-substituted series, the fragmentation profiles for the 5-R-substituted $[Cu(\mathbf{L})(\mathbf{L}\text{-H})]^-$ ions were first investigated to ensure that dissociation occurred in a similar manner within the series. Figure 2.18 shows the CID spectra for each species with AIC/TIC = 5-10%. The highlighted fragments are formed by the same pathways and their structures are shown if Figure 2.18 corresponding to the colours of the highlighted peaks.

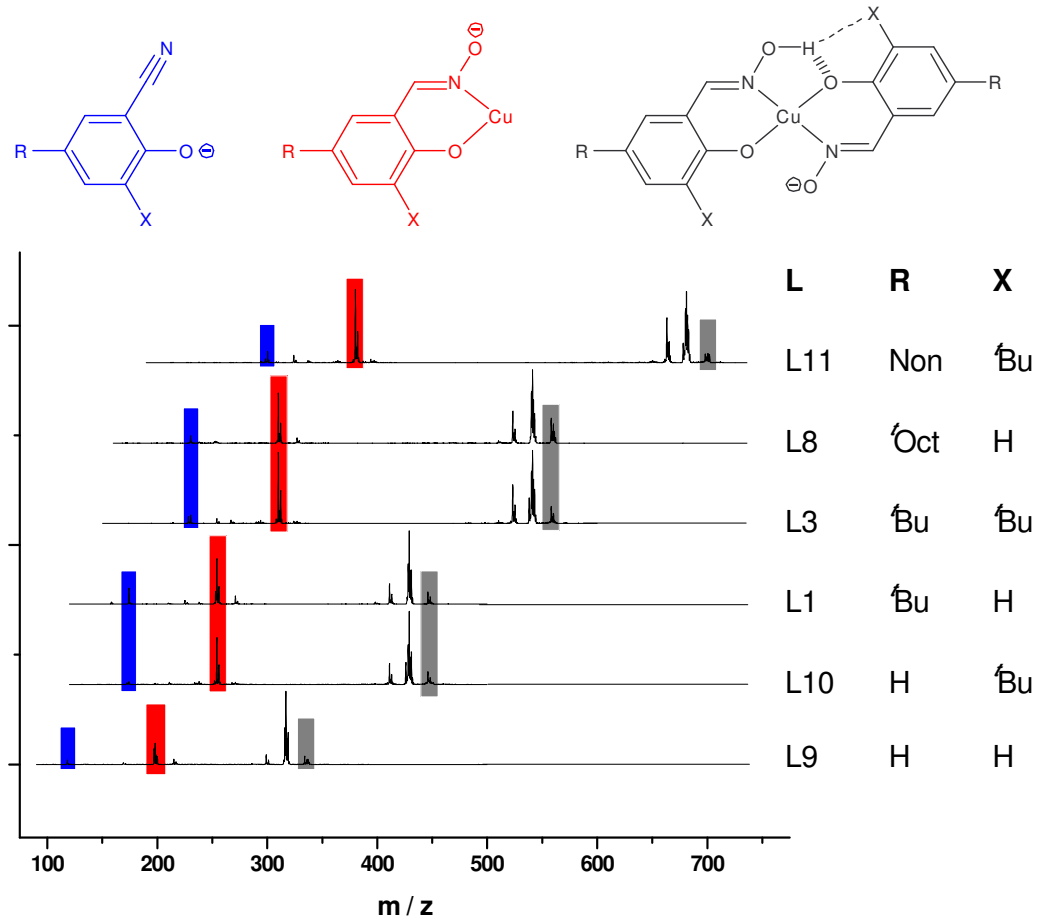

Figure 2.18: Fragmentation patterns of the 5-R-substituted anions. $[Cu(\mathbf{L})(\mathbf{L}\text{-H})]^-$, $[Cu(\mathbf{L}\text{-H})]^-$ and $[\mathbf{L}\text{-OH}_2]^-$ are shaded grey, red and blue respectively. Inset: Proposed structural formula for shaded fragments. For each species the CID spectrum was chosen where the AIC/TIC ratio =5-10%.

The fragments formed from each $[Cu(\mathbf{L})(\mathbf{L}\text{-H})]^-$ species are analogous suggesting that the gas phase stability of each species is not due to differing fragmentation profiles. The main influence on the gas phase stabilities of the 5-R-substituted $[Cu(\mathbf{L})(\mathbf{L}\text{-H})]^-$ anions is the total number of covalently bonded atoms (as defined in Table 2.1) and the influence of the 3-*t*-butyl-substituent on the outer coordination sphere.

2.2.8.1 Accurate CID Fragment masses for [Cu(**L1**)(**L1**-H)]$^-$

Accurate mass CID spectra were recorded using A Waters Quadrupole-Time-of-Flight (Q-ToF) mass spectrometer. The accurate masses of the fragments recorded for [Cu(**L1**)(**L1**-H)]$^-$ were compared to those recorded using the low resolution LCQ. The fragments were found to be the same for both the collision cell and the QIT suggesting that dissociation occurs similarly in both machines. Figure 2.19 contains the observed fragment accurate mass and a calculated mass for each of the major fragments in the CID spectrum of [Cu(**L1**)(**L1**-H)]$^-$ along with a proposed structural formula and possible dissociative mechanisms and pathways.

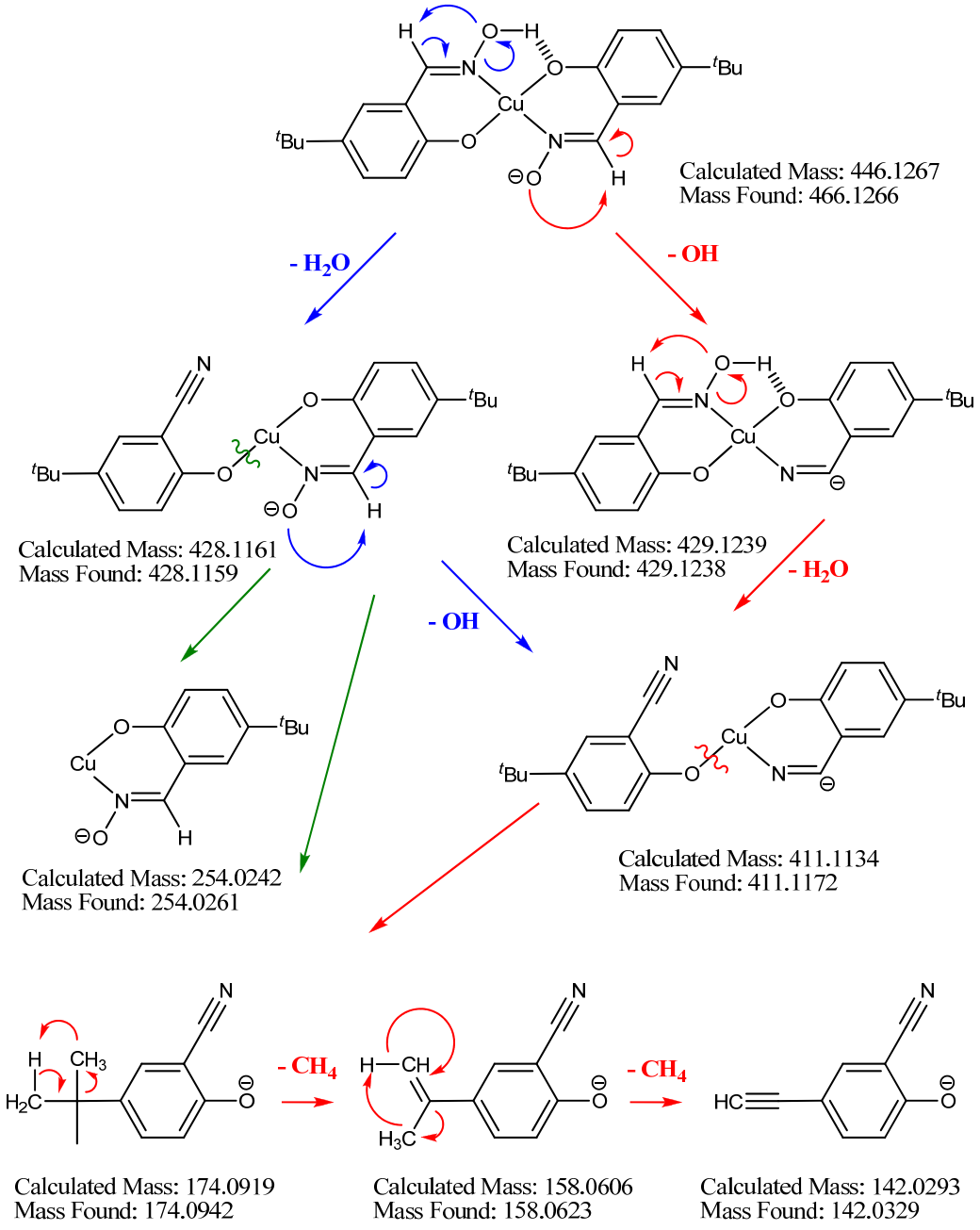

Figure 2.19: Major fragments observed in the CID spectrum for [Cu(**L1**)(**L1**-H)]$^-$. The observed mass is given with proposed structure for each fragment. Likely unimolecular dissociation mechanisms are also indicated.

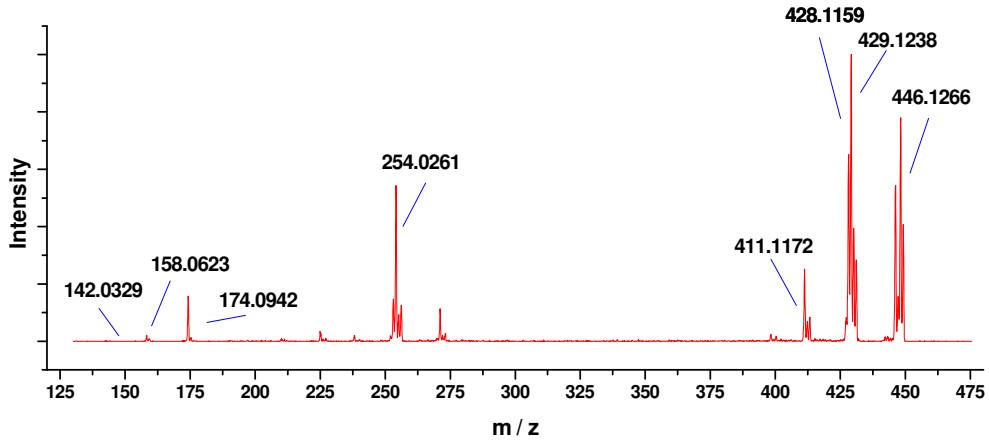

Figure 2.20: High resolution CID spectrum for [Cu(**L1**)(**L1**-H)]$^-$. The observed masses for the major fragments are indicated.

Dissociation of the [Cu(**L1**)(**L1**-H)]$^-$ ions proceeds via OH and H_2O losses, which occur simultaneously. These neutral losses are concordant with studies that have previously shown fragmentation under resonance excitation conditions proceeding *via* similar neutral losses at low collision energies.[38] When higher NCE is applied, the coordinating O-Cu and N-Cu bonds are broken and fragmentation proceeds via the loss of a ligand, forming a [Cu(**L**-H)]$^-$ fragment (highlighted red in Figure 2.19). The subsequent fragmentations occur at energies that enable C-C bond cleavage, again resulting in neutral losses. A fairly stable fragment appears to be the aforementioned cyano-derivative, [**L**-H_2O]$^-$. (highlighted blue in Figure 2.19)

2.2.9 Quantification of OH and H_2O losses in CID

From CID studies on bis ketoximate and mixed aldoximate/ketoximate copper complexes (see also Chapter 3 Section 3.2.2) the OH/H_2O losses were found to occur as shown in Figure 2.21, where OH fragment loss occurs from the deprotonated oxime (red arrow mechanism) and H_2O loss from the oximic OH and the N=C*H* as indicated by the blue arrow mechanism.

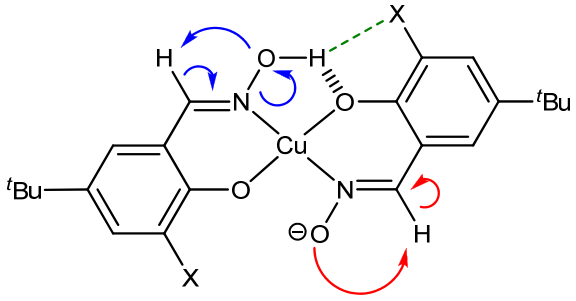

Figure 2.21: Proposed dissociation pathway for OH (red arrows) and OH_2 (blue arrows) losses.

These initial losses result in two fragment ions whose peaks overlap in the mass spectra. By looking at the CID spectrum at the X_c value for each species we can investigate the relationship between the nature of X and the relative occurrences of OH and H_2O losses and thus the importance of the H-bonding interactions with the X substituent. Figure 2.22 shows the two de-convoluted peaks for [Cu(**L1**)(**L1**-H)-OH]$^-$ (blue) and [Cu(**L1**)(**L1**-H)-H_2O]$^-$ (red).

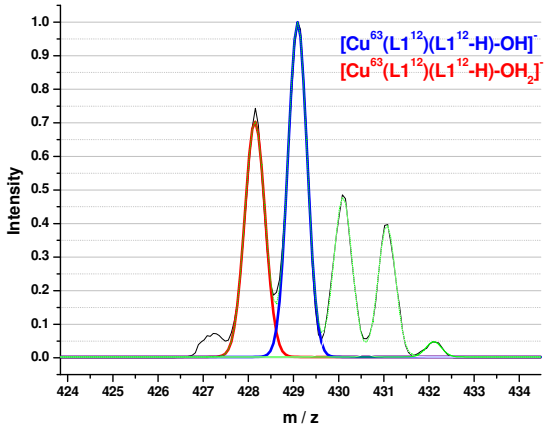

Figure 2.22: De-convoluted peaks for the monoisotopic masses of [Cu(**L1**)(**L1**-H)-OH]$^-$ and [Cu(**L1**)(**L1**-H)- H_2O]$^-$ with Gaussian fits for each monoisotopic mass (shown in blue and red respectively).

A comparison of the intensities of the monoisotopic masses ($Cu^{63}C^{12}$ isotopes) for [Cu(**L**)(**L**-H)- H_2O]$^-$ and [Cu(**L**)(**L**-H)-OH]$^-$ (Figure 2.23) reveals that the calculated relative area for [Cu(**L**)(**L**-H)-OH_2]$^-$ is smaller when the 3-X-substituent is a hydrogen bond acceptor such as NO_2 or OMe).

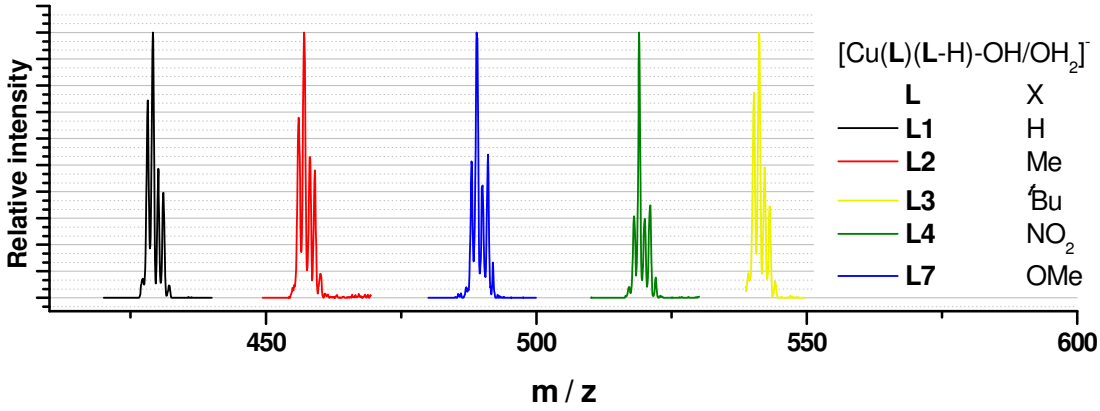

Figure 2.23: **P**eaks for [Cu(**L**)(**L**-H)-OH]$^-$ and [Cu(**L**)(**L**-H)-OH_2]$^-$ where **L** = **L1-4** and **L7**. Each peak is taken from its CID mass spectrum at the X_c value for [Cu(**L**)(**L**-H)]$^-$.

An area correction of the [Cu^{63}(**L**^{12})(**L**^{12}-H)-OH]$^-$ for the presence of the $Cu^{63}C^{13}$ isotope, [Cu^{63}(**L**^{13})(**L**^{13}-H)- H_2O]$^-$ (species yields corrected OH: H_2O loss ratios. (Table 2.2)

Table 2.2: The measured and corrected [Cu(**L**)(**L**-H)-OH]$^-$: [Cu(**L**)(**L**-H)-OH_2]$^-$ ratios for ligands **L1**-**L7**.

L	3-X-substituent	Area of [Cu(**L**)(**L**-H)-OH_2]$^-$ peak relative to that of $Cu^{63}C^{12}$ isotope	Area correction for $Cu^{63}C^{13}$ isotope	corrected OH: H_2O ratio
L1	H	0.72	26%	**1:0.88 (3)**
L2	Me	0.69	26%	**1:0.85 (3)**
L3	^{t}Bu	0.76	33%	**1:1.02 (2)**
L4	NO_2	0.32	27%	**1:0.35 (2)**
L5	Cl	0.35	27%	**1:0.39 (2)**
L6	Br	0.28	33%	**1:0.31 (6)**
L7	OMe	0.43	29%	**1:0.49 (1)**

The relative area of the $Cu^{63}C^{12}$ isotopes of the [Cu(**L**)(**L**-H)- H_2O]$^-$ peaks are plotted against the extraction strengths of the ligands **LH** yielding Figure 3.24

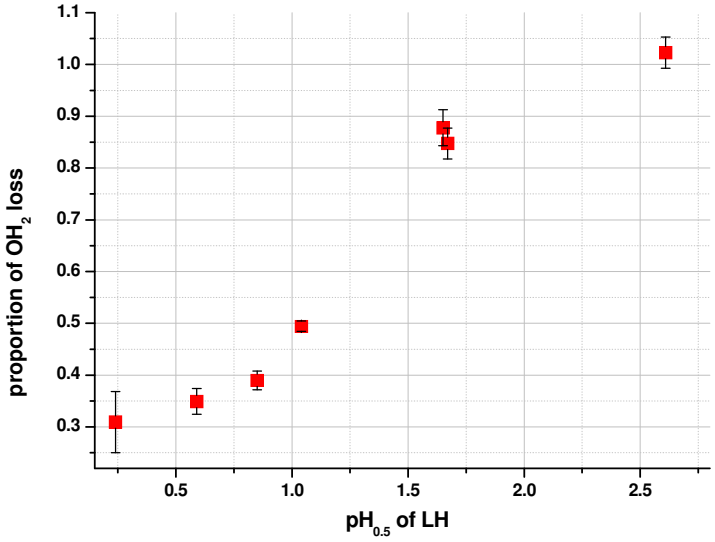

Figure 2.24: The proportion of H_2O loss for each [Cu(**L**)(**L**-H)]$^-$ species at the NCE closest to the X_c value.

Figure 2.24 shows a distinct trend between the nature of X and the relative amount of H_2O dissociation when X is hydrogen-bond accepting group, the stabilisation of the non-deprotonated oximic OH group is observed as the relative amount of OH_2 loss is reduced significantly. The proportion of OH to H_2O loss for the [Cu(**L**)(**L**-H)-H]$^-$ series increases in the order **L6** ≥ **L4** ≥ **L5** > **L7** > **L1** ≥ **L2** > **L3**. This trend again indicates the effects that the outer coordination sphere of the deprotonated complexes can influence gaseous stability under CID conditions.

2.2.10 Formation of [L-H_2O]$^-$ fragment.

The formation of the fragment ion [**L**-H_2O]$^-$ can be expected as the formation of the C-N triple bond makes the fragment thermodynamically stable, the neutral loss of H_2O also facilitates the rearrangement. The stability of this fragment was further validated by studies carried out to determine the stability of the [Cu(**L**)$_2$] complexes in a methanol, a protic solvent. The composition of the mass spectrum of a 10 µM solution of [Cu(**L1**)$_2$] was monitored over time. It showed the gradual decomposition of the [Cu(**L1**)(**L1**-H)]$^-$ peak and the appearance of a peak at 174, attributed to [L-H_2O]$^-$. (Figure 2.25)

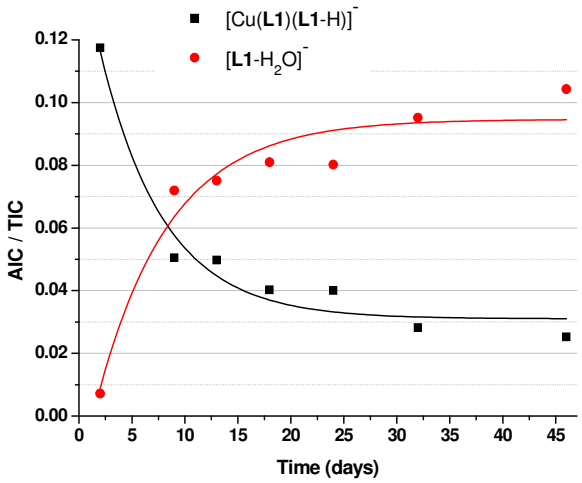

Figure 2.25: Graph showing the reduction over time of the [Cu(**L1**-(**L1**-H)]$^-$ peak and the closely correlating appearance of the peak at m/z 174, [**L1**-H_2O]$^-$.

The increased intensity of the [**L1**-OH_2]$^-$ over time suggests a degradation of the [Cu(**L**)$_2$] complexes in solution due to decomplexation by methanol, which could result in the release of ligands from the complex as shown in equation **2.7.**

$$[Cu(\mathbf{L})_2] + MeOH \rightarrow [Cu(\mathbf{L})]^+ + OMe^- + \mathbf{LH} \qquad \mathbf{2.7}$$

The oxime free-ligand could then feasibly be dehydrated forming the corresponding nitrile, the reaction being driven by the formation of the more thermodynamically stable product, [**L**-H_2O]. This type of reaction has been reported[65] with the use of a Lewis acid catalyst and in this case the Lewis acid catalyst could be the Cu^{2+} ions themselves.

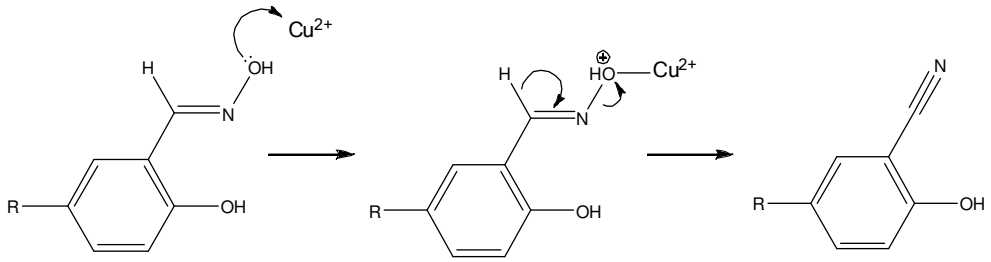

Figure 2.26: Possible dehydration of salicylaldoxime ligand.

2.2.11 Fragmentation of [Cu(L6)(L6-H)]$^-$: pathways involving X-substituent

The fragmentation profile of [Cu(**L6**)(**L6**-H)]$^-$ was examined in detail when high levels of NCE were applied, i.e. when the collision energy is sufficient to completely dissociate the trapped ion.

Figure 2.27 shows the major CID fragments of [Cu(**L6**)(**L6**-H)]$^-$ when subjected to 40% NCE. The black fragments are those analogous with the fragments found for [Cu(**L1**)(**L1**-H)]$^-$ and account for the majority of fragment ions formed. But, unlike for [Cu(**L1**)(**L1**-H)]$^-$, where the 3-X-substituent = H, the bromo-substituent in [Cu(**L6**)(**L6**-H)]$^-$ facilitates fragmentation by providing alternative pathways. The fragments highlighted in blue represent those that have lost the Br-substituent as HBr, HOBr or CuBr – losses that are not accessible when X = H. The presence of $[CuBr_2]^-$ at m/z 220.7 indicates a rearrangement pathways upon fragmentation which is shown in red in Figure 2.27.

Formation of the nitrile upon dehydration of the oxime (H_2O loss) results in the nitrogen not being coordinated to the copper, leaving the fourth equatorial coordination site open to possible coordination of the bromide X-substituent. The presence of the [Cu(**L-**H)Br]$^-$ fragment at m/z 410.8 and the [Cu(**L-O**H_2)Br]$^-$ at m/z 393.8 could also be generated by a similar rearrangement.

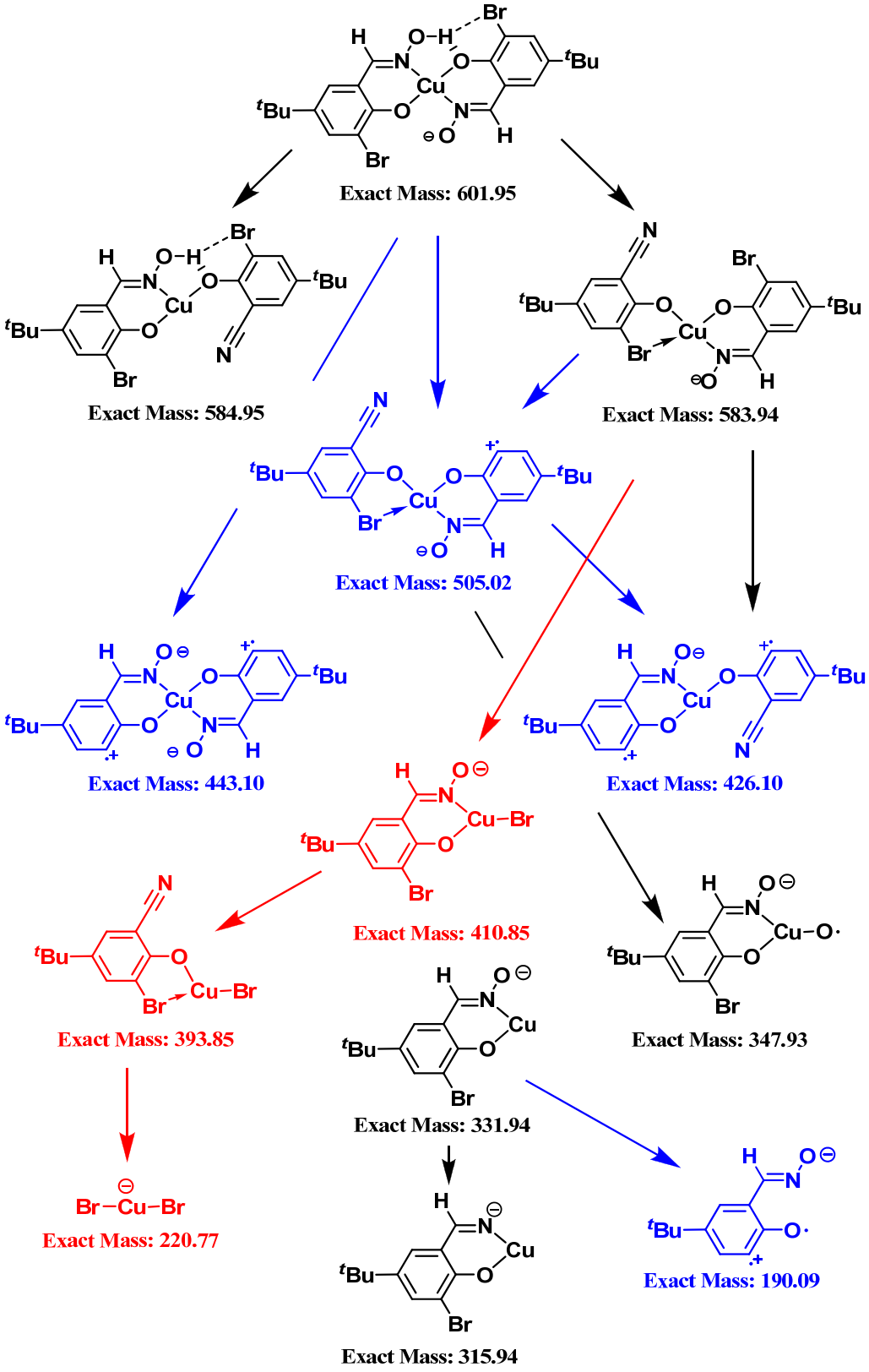

Figure 2.27: Proposed dissociation pathway for [Cu(**L6**)(**L6**-H)]$^-$ with calculated exact mass's for each fragment.

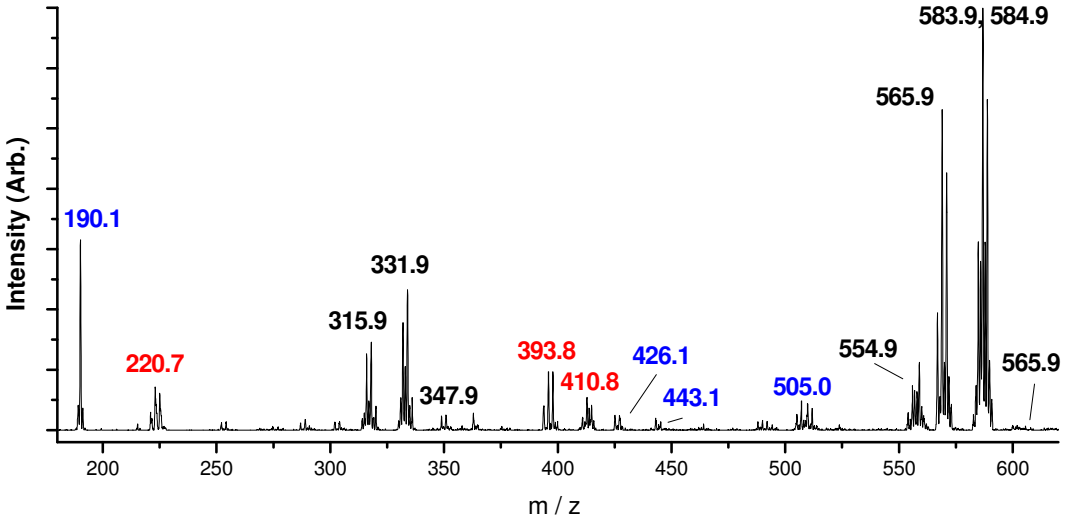

Figure 2.28: CID spectrum at 40% NCE for [Cu(**L6**)(**L6**-H)]$^-$ with the observed mass's for the most abundant isotopic peak for each fragment indicated. The peaks labelled black correspond to fragments that are analogous to those observed for [Cu(**L**)(**L**-H]$^-$. The peaks labelled blue correspond to fragments in which the Br-substituent influences the fragmentation/rearrangement and those labelled red invole the Br-substituent in neutral losses.

Although, when initially looking at the influence of fragmentation pathways on gas phase stability in Section 2.2.5, it was thought that the fragmentations involving the bromo-substituent were not thought to influence the stability of the [Cu(**L6**)(**L6**-H)]$^-$ anion. The is clearly not the case and, although the major fragments (black in Figure 2.27 and Figure 2.28 are analogous to those found for [Cu(**L1**)(**L1**-H)]$^-$, both the dissociation pathways facilitated by the bromo-substituent and the resultant fragments (red and blue in Figure 2.27) influence the gas phase stability of the [Cu(**L6**)(**L6**-H)]$^-$ anion.

[Cu(**L5**)(**L5**-H)]$^-$, where X=Cl, shows fragmentation where the neutral loss is HX, albeit not to the same extent as for [Cu(**L6**)(**L6**-H)]$^-$. Figure 2.29 shows the CID spectrum at 40% NCE for [Cu(**L5**)(**L5**-H)]$^-$ with a peak at m/z 190.1 highlighted in blue. This peak is analogous for the [**L**-HX]$^-$ peak observed in the CID spectrum for [Cu(**L6**)(**L6**-H)]$^-$. The remaining peaks, not highlighted, are analogous to the fragments observed for [Cu(**L1**)(**L1**-H)]$^-$.

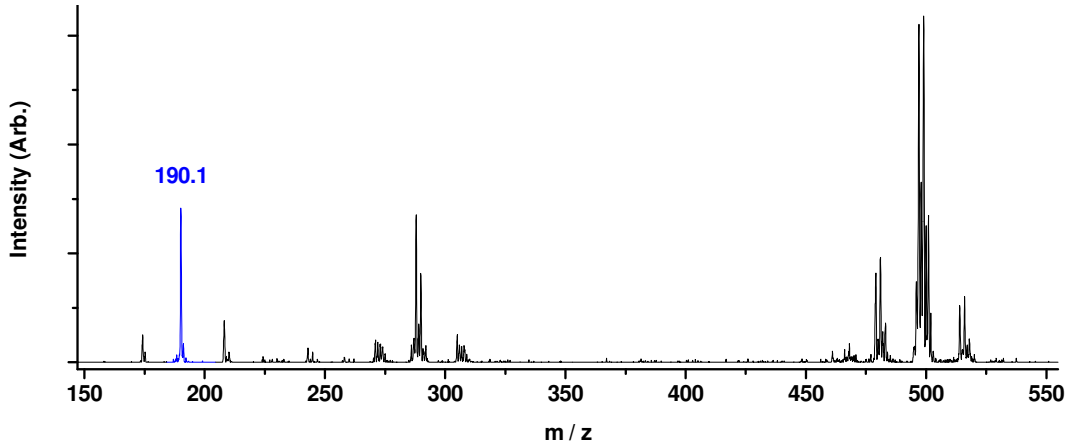

Figure 2.29: CID spectrum at 40% NCE for [Cu(**L5**)(**L5**-H)]$^-$ with [**L5**-XH]$^-$ fragment at 190.1 (highlighted blue)

2.2.12 Density Functional Theory Calculations

Density Functional Theory or DFT is computational modelling of matter using a quantum mechanical approach. Full calculation methodology and introduction are covered in Chapter 1 and Chapter 4: DFT Investigations of extractant systems. In this chapter cross referencing will be used to highlight the relevant sections of Chapter 1 and 4.

DFT calculations were carried out on the mono deprotonated copper complexes, [Cu(**L**)(**L**-H)]$^-$ to determine the influence of electronic repulsion between the X-substituent and the deprotonation site (oximate oxygen) on the order of the gas phase stabilities of the anions under CID conditions. It was thought that electronic repulsion between the X-substituent and the deprotonated oximate oxygen could partially explain the gas phase stability ordering shown in Figure 2.12 and Figure 2.13.

Initially the geometries of the deprotonated structures were optimised using B3LYP (see also Chapter 1 Section 1.9.2.) with the basis set 6-31G, resulting in 2 optimised forms; a distorted planar conformation ((a) in Figure 2.30) and a distorted tetrahedral conformation ((b) in Figure 2.30)

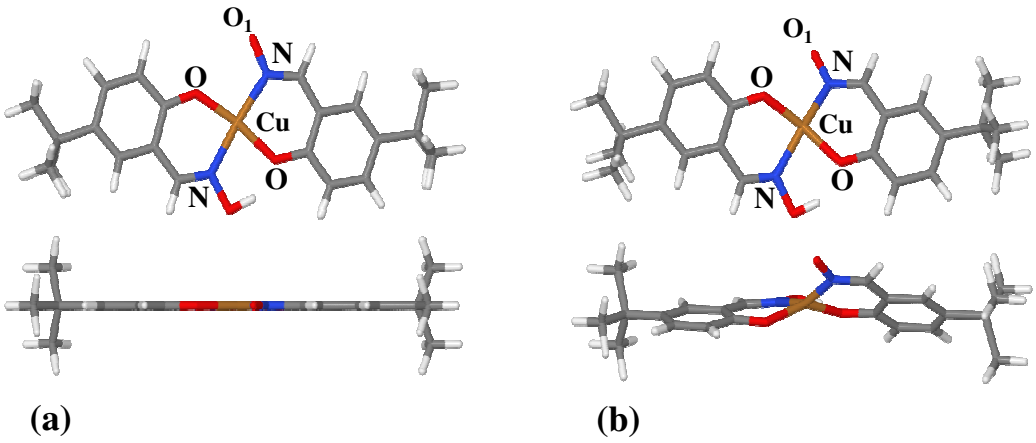

Figure 2.30: Energy minimised structures of [Cu(**L1**)(**L1**-H)]$^-$ using B3LYP/6-31G (a) a distorted planar conformation and (b) a distorted tetrahedral conformation. Atom labels correlate those presented in Table 2.3.

The extent of distortion is described in Table 2.3, in which the O···Cu···O angle, the N···Cu···N angle and the O···O_1 contact distances are reported for the energy minimised conformers of [Cu(**L**)(**L**-H)]$^-$, where **L** = **L1** (H), **L5** (Cl), **L6** (Br and **L7** (OMe)

Table 2.3: Energy minimised angles and contact distances for [Cu(**L**)(**L**-H)]$^-$ using B3LYP/6-31G in the distorted planar conformation and distorted tetrahedral conformations. Atom labels are taken from Figure 2.30.

L (X)	**Distorted planar conformation**			**Distorted tetrahedral conformation**		
	O···Cu···O (°)	N···Cu···N (°)	O···O_1 (Å)	O···Cu···O (°)	N···Cu···N (°)	O···O_1 (Å)
L1 (H)	170.28	176.35	2.8999	152.08	154.52	3.1507
L5 (Cl)*	-	-	-	151.50	154.54	3.1882
L6 (Br)	170.17	176.13	2.91	153.39	157.18	3.1605
L7 (OMe)	169.59	175.08	2.94	152.29	155.48	3.1795

* The [Cu(**L5**)(**L5**-H)]$^-$ anion did not geometry optimise in the planar distorted conformation at B3LYP/6-31G.

In DFT calculations the energies of the complexes are related to the number of electrons in each system and cannot be compared directly. As the number of electrons in the mono-deprotonated complex [Cu(**L**)(**L**-H)]$^-$ is the same as its parent

the difference in energy of the energy minimised structures represents the enthalpy of deprotonation in the gas phase as defined by equations **2.8** and **2.9**:

$$[Cu(\mathbf{L}_2)] \xrightarrow{\Delta H_{depro}} [Cu(\mathbf{L})(\mathbf{L}\text{-H})]^- + H^+ \qquad \textbf{2.8}$$

$$\Delta H_{depro} = (E_{[Cu(\boldsymbol{L})(\boldsymbol{L}-H)]^-} + E_{H^+}) - E_{[Cu(\boldsymbol{L})_2]} \qquad \textbf{2.9}$$

These deprotonation enthalpies are compared for complexes with X = H, OMe, Cl and Br in Table 2.4 for formation of both the planar and tetrahedral forms of the monoanions.

Table 2.4: Calculated energies from the geometry optimised structures of [Cu(**L**)$_2$] and the two conformations of the deprotonated anion, [Cu(**L**)(**L**-H)]$^-$ at B3LYP/6-31G. The calculated deprotonation energies for each anion conformation are also given.

L (X)	$E_{[Cu(\boldsymbol{L})_2]}$ (AU)	$E_{[Cu(\boldsymbol{L})(\boldsymbol{L}-H)]^-}$ (tetrahedral distortion AU)	$E_{[Cu(\boldsymbol{L})(\boldsymbol{L}-H)]^-}$ (planar distortion, AU)	ΔH_{depro} (planar distortion, kJ mol^{-1})	ΔH_{depro} (tetrahedral distortion, kJ mol^{-1})	Difference (tetrahedral distortion-planar distortion)
L1 (H)	-2905.5909	-2905.02697	-2905.03044	**+1480.547**	**+1471.426**	**-9.12065**
L7 (OMe)	-3134.5508	-3133.97774	-3133.98117	**+1504.644**	**+1495.646**	**-8.99866**
L5 (Cl)	-3824.7389	NA*	-3824.18646	**NA***	**+1450.546**	**NA***
L6 (Br)	-8047.5404	-8046.98074	-8046.98399	**+1469.498**	**+1460.941**	**-8.55776**

* The [Cu(**L5**)(**L5**-H)]$^-$ anion did not geometry optimise in the planar distorted conformation at B3LYP/6-31G.

For the complexes where X = H, OMe and Br the deprotonation energy to form the tetrahedrally distorted conformation was lower than that to form the distorted planar conformation by 8-9 kJ mol^{-1} (highlighted red in Table 2.4). The deprotonation energies showed no correlation with the gas phase stability of the [Cu(**L**)(**L**-H)]$^-$ anions or the extraction strength of the ligands **LH**. The deprotonation energy for the methoxy-substituted complex, [Cu(**L7**)$_2$] (1495.6 kJ mol^{-1}), was greater than that for the unsubstituted complex,[Cu(**L1**)$_2$] (1471.4 kJ mol^{-1}), whereas those for the chloro

and bromo analogues, [Cu(**L5**)$_2$] (1450.5kJ mol^{-1}) and [Cu(**L6**)$_2$] (1460.9 kJ mol^{-1}), were smaller.

The calculations shown in Table 2.4 were repeated using a higher level of theory, B3LYP/6-31+G(d,p). (details for the neutral species are given in Chapter 4 Section 4.2.2) The new basis set described the delocalisation of the electrons throughout the pi system more accurately (see Chapter 4 section 4.2.2.2.) and the planarity of the monoanions, [Cu(**L**)(**L**-H)]$^-$, was greater in their energy minimised structures. The distorted tetrahedral conformation of the [Cu(**L**)(**L**-H)]$^-$ anions observed in the lower level calculations (Table 2.4) was not associated with a minimised energy well as the level of theory was improved. Table 2.5 lists the energies of the neutral complexes and those of the anions obtained be deprotonation of one oximic OH group as found for the optimised geometries with the higher level of theory, together with the calculated deprotonation energies, ΔH_{depro} (bold in Table 2.5).

Table 2.5: Calculated energies from the geometry optimised structures of [Cu(**L**)$_2$] and the deprotonated anion, [Cu(**L**)(**L**-H)]$^-$ at B3LYP/6-31+G(d,p). The calculated deprotonation energy for each complex is also given.

L (X)	$E_{[Cu(\boldsymbol{L})_2]}$ (AU)	$E_{[Cu(\boldsymbol{L})(\boldsymbol{L}-H)]^-}$ (planar distortion, AU)	$\boldsymbol{\Delta H_{depro}}$ **(planar distortion, kJ mol^{-1})**	ΔH_{depro} relative to [Cu(**L1**)$_2$]
L1 (H)	-2906.0458	-2905.4956	**+1390.15**	0
L7 (OMe)	-3135.0972	-3134.5391	**+1410.06**	+19.91
L5 (Cl)	-3825.2323	-3824.6875	**+1376.53**	-13.62
L6 (Br)	-8048.3063	-8047.7614	**+1376.78**	-13.37

The deprotonation enthalpies follow a dependence on the nature of the 3-X-substituen, OMe (1410 kJ mol^{-1}) > H (1390 kJ mol^{-1}) > Br (1377 kJ mol^{-1}) ≥ Cl (1377 kJ mol^{-1}). This appears to follow the electron withdrawing properties of the 3-X-substituent suggesting that the cleavage of the NO-H bond contributes more to the ionisation enthalpies of the [Cu(**L**)$_2$] complexes than the stability of the conjugate ion which will be adversely affected by electronegative 3-X-substituents.

Bond lengths and angles for the deprotonated anions in the inner and outer coordination sphere were calculated and compared with those of the neutral complexes. Table 2.6 contains the selected bond lengths (1-4) and angles (α and β) shown in Figure 2.31.

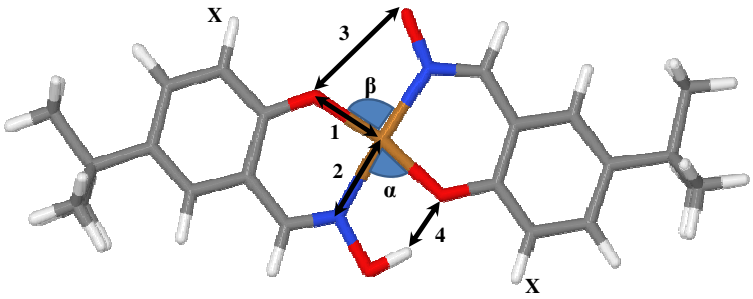

Figure 2.31: Geometry optimised structure for the deprotonated complex [Cu(**L1**)(**L1**-H)]$^-$. Bond lengths and angles indicated are contained in Table 2.6.

Table 2.6: Selected bond lengths (1-4) and angles (α and β) in the monoanions (see Figure 2.31) [Cu(**L**)(**L**-H)]$^-$ compared with those of the neutral complexes, [Cu(**L**)$_2$], (Chapter 4) differences in italics.

3-X-Substituent	O-Cu (1) (Å)	N-Cu (2) (Å)	O - O (3) (Å)	H - O (4) (Å)	O-Cu- N (α) (°)	O-Cu- N (β) (°)
H						
Neutral	1.9162	1.9639	2.6323	1.7787	88.05	88.05
Deprotonated	1.9406	2.0308	2.8987	1.6536	83.19	95.64
Difference	**+0.0247**	**+0.0669**	**+0.2664**	**-0.1251**	**-4.86**	**+7.59**
OMe						
Neutral	1.9001	1.9658	2.6336	1.7931	87.87	87.87
Deprotonated	1.9358	2.0330	2.9316	1.6678	82.67	96.63
Difference	**+0.0357**	**+0.0673**	**+0.2980**	**-0.1253**	**-5.20**	**+8.76**
Cl						
Neutral	1.9070	1.9666	2.6498	1.8165	88.11	88.11
Deprotonated	1.9451	2.0274	2.8979	1.7005	83.43	95.90
Difference	**+0.0381**	**+0.0609**	**+0.2481**	**-0.1160**	**-4.68**	**+7.79**
Br						
Neutral	1.8994	1.9704	2.6508	1.8230	87.97	87.97
Deprotonated	1.9376	2.0299	2.8799	1.7205	83.62	95.29
Difference	**+0.0382**	**+0.0595**	**+0.2291**	**-0.1025**	**-4.35**	**+7.32**

The same trend is observed for the differences between distances (2), (3) and (4) and bond angles (α) and (β) in the neutral and deprotonated complexes. For [Cu(**L5**)$_2$] and [Cu(**L6**)$_2$], when X = Cl and Br respectively, the change in bond lengths (2), (3) and (4) upon deprotonation is less than that observed for the unsubstituted complex, [Cu(**L1**)$_2$]. For [Cu(**L7**)$_2$], where X=OMe, we see the opposite; the bond lengths (2), (3) and (4) change to a greater extent upon deprotonation than those of [Cu(**L1**)$_2$]. The changes in bond angles (α) and (β) follow the same trends as observed for the changes in bond lengths. The trend further supports the lower stability of the deprotonated anion [Cu(**L7**)(**L7**-H)]$^-$ and the greater stabilities of the [Cu(**L5**)(**L5**-H)]$^-$ and [Cu(**L6**)(**L6**-H)]$^-$ anions relative to the **L1** analogue. This suggests that, contrary to previous suggestions that when X= electron withdrawing the [Cu(**L**)(**L**-H)]$^-$ is destabilised via electronic repulsion (see Section 2.2.6.), that, when the X substituent is electron withdrawing the [Cu(**L**)(**L**-H)]$^-$ is stabilised.

2.3 Conclusions

The experiments described in this chapter have shown that collision induced dissociation can be used to determine the relative gas phase stabilities of substituted phenolic oxime copper complex anions. The stabilities are, however, dependent on a number of variables including number of bonds and degrees of freedom in each complex, the influence of the 3-X-substituent on the inner and outer coordination spheres of the complex and the dissociation pathways.

The relative stability of the $[Cu(\mathbf{L})(\mathbf{L}\text{-H})]^-$ anion series under resonance excitation conditions was found to be **L6** (Br) < **L4** (NO_2) < **L5** (Cl) < **L1** (H) ≤ **L7** (OMe) < **L3** (^{t}Bu) < **L2** (Me) which is approximately the inverse of the extraction strengths of the ligands, **LH.** The ordering, however, seems to be coincidental, as the influences of the 3-X-substituent vary considerably and are difficult to quantify.

In an attempt to understand the CID process further and the aspects that affect the stability of ions in the gas phase Chapter 3 continues the investigation and examines the influences of charge, ligand type and metal on the stabilities under resonance excitation conditions of ions derived from $[M(\mathbf{L})_2]$ solutions.

2.4 Experimental

2.4.1 Chemicals and Instrumentation

All solvents and reagents were used as received from Aldrich, Fisher, Fluorochem and Acros. ^{1}H and ^{13}C NMR were obtained using a Bruker AC250 spectrometer at ambient temperature. Chemical shifts (δ) are reported in parts per million (ppm) relative to internal standards.

Aldoxime ligands **L1H**-**L5H** were synthesized by Dr. Ross S. Forgan during his PhD[66] at the University of Edinburgh 2005-2008. Aldoxime ligands **L6H**-**L8H** were synthesised according to the thesis of Dr. Ross S. Forgan.

2.4.2 Aldoxime Synthesis (L6H-L8H)

2.4.2.1 2-Bromo-4-*tert*-butylphenol (**1**)

4-*tert*-Butylphenol (5.140 g, 34 mmol) and tetra-*n*-butylammonium tribromide (16.50 g, 34 mmol) were dissolved in dichloromethane (100 ml) and methanol (60 ml) and stirred for 30 min. The solvent was removed *in vacuo* and the resulting orange oil partitioned between diethyl ether (100 ml) and water (100 ml). The organic phase was separated, washed with saturated brine (2 x 50 ml) and water (50 ml), dried over $MgSO_4$ and the solvent removed to give a slightly pink oil which was purified by silica-60 wet flash column chromatography (2% ethyl acetate in hexane eluent) to give a colourless oil (5.82 g, 75%). ^{1}H NMR (250 MHz, $CDCl_3$): δ_H (ppm) 1.13 (s, 9H, $C(CH_3)_3$), 6.83 (d, 1H, Ar*H*), 7.05 (dd, 1H, Ar*H*), 7.32 (d, 1H, Ar*H*); ^{13}C NMR (63 MHz, $CDCl_3$): δ_C (ppm) 31.9 (3C, $C(\mathbf{C}H_3)_3$), 34.6 (1C, $C(\mathbf{C}H_3)_3$), 110.4 (1C, aromatic **C**), 116.2 (1C, aromatic **C**H), 126.6 (1C, aromatic **C**H), 129.3 (1C, aromatic **C**H), 145.5 (1C, aromatic **C**), 150.4 (1C, aromatic **C**)

2.4.2.2 2-Hydroxy-5-*tert*-octylbenzaldehyde (**2**)

Magnesium turnings (20 g, 800 mmol), methanol (373 ml), toluene (160 ml) and magnesium methoxide (a few drops of 8% w/w methanol solution) were refluxed until all magnesium was dissolved and H_2 evolution stopped. 4-*tert*-Octylphenol (268.2 g, 1.3 mol) was added and refluxed for 1 hr. Toluene (333 ml) was added and the mixture distilled under vacuum to remove the methanol/toluene azeotrope. A slurry of paraformaldehyde (120 g, 4 mol) in toluene (200 ml) was added slowly with continuous distillation, and heated for a further 2 hrs. After cooling to room temperature, H_2SO_4 (20%, 800 ml) was added slowly with stirring and heated to 50 °C to dissolve all solids. The product was extracted with toluene (2 x 400 ml), washed with H_2SO_4 (10%, 2 x 150 ml) and water (150 ml), dried over $MgSO_4$ and the solvent removed *in vacuo*. Purification by silica-60 wet flash column chromatography (2% ethyl acetate in hexane eluent) yielded an off white solid (196.2 g, 64.5%) ^{1}H NMR (250 MHz, $CDCl_3$): δ_H (ppm) 0.68 (s, 9H, C(C*H*$_3$)$_3$), 1.30 (s, 6H, C(C*H*$_3$)$_2$), 1.66 (s, 2H, C*H*$_2$), 6.85 (d, 1H, Ar*H*), 7.42 (s, 1H, Ar*H*), 7.48 (dd, 1H, Ar*H*), 9.82 (s, 1H, ArC*H*O), 10.80 (s, 1H, ArO*H*); ^{13}C NMR (63 MHz, $CDCl_3$): δ_C (ppm) 30.4 (2C, C(**C**H$_3$)$_2$), 30.8 (3C, C(**C**H$_3$)$_3$), 31.3 (1C, **C**(CH$_3$)$_3$), 36.9 (1C, **C**(CH$_3$)$_2$), 55.6 (1C, **C**H$_2$) 116.0 (1C, aromatic **C**H), 119.0 (1C, aromatic **C**), 129.5 (1C, aromatic **C**H), 134.4 (1C, aromatic **C**H), 140.8 (1C, aromatic **C**), 158.4 (1C, aromatic **C**), 195.8 (1C, Ar**C**HO)

2.4.2.3 3-Bromo-5-*tert*-butyl-2-hydroxybenzaldehyde (**3**)

A mixture of hexamethylenetetramine (9.1 g, 65 mmol) and **(1)** (3.00 g, 13.1 mmol) was heated in trifluoroacetic acid (50 ml) to 90˚C for 16 h under reflux. The reaction mixture was poured still hot into 2 M HCl (150 ml) and stirred for 8 h. An off-white precipitate was filtered, washed with water (50 ml) and vacuum dried over P_2O_5 to yield an off white powder (3.039 g, 90%). ^{1}H NMR (250 MHz, $CDCl_3$): δ_H (ppm) 1.15 (s, 9H, C(C*H*$_3$)$_3$), 7.33 (d, 1H, Ar*H*), 7.63 (s, 1H, Ar*H*), 9.68 (s, 1H, C*H*O), 11.2 (br, 1H, O*H*); ^{13}C NMR (63 MHz, $CDCl_3$): δ_C (ppm) 31.6 (3C, C(**C**H$_3$)$_3$), 34.7, (1C, **C**(CH$_3$)$_3$), 111.2 (1C, aromatic **C**), 121.0 (1C, aromatic **C**), 129.8 (1C, aromatic **C**H),

138.0 (1C, aromatic **C**H), 144.6 (1C, aromatic **C**), 156.2 (1C, aromatic **C**), 196.7 (1C, Ar**C**HO)

2.4.2.4 Oximation General Procedure

Ca. 1.2 equivalents of KOH and $NH_2OH.HCl$ were dissolved separately in EtOH, mixed thoroughly and a white KCl precipitate removed by filtration. The filtrate was added to the precursor aldehyde, refluxed for 3 hr and the solvent removed *in vacuo*. The residue was redissolved in $CHCl_3$, washed with water 3 times, dried over $MgSO_4$ and the solvent removed *in vacuo* to yield the crude product.

2.4.2.5 3-Bromo-5-*tert*-butyl-2-hydroxybenzaldehyde oxime (**L6H**)

Hydroxylamine hydrochloride (0.709 g, 10.2 mmol), potassium hydroxide (0.674 g, 10.2 mmol) and **(8)** (2.00 g, 7.8 mmol) were reacted according to the general procedure to yield a white solid (2.00 g, 94%). ^{1}H NMR (250 MHz, $CDCl_3$): δ_H (ppm) 1.20 (s, 9H, C(C*H*$_3$)$_3$), 7.06 (d, 1H, Ar*H*), 7.48 (d, 1H, Ar*H*), 8.13 (s, 1H, C*H*N); ^{13}C NMR (63 MHz, $CDCl_3$): δ_C (ppm) 31.7 (3C, C(**C**H$_3$)$_3$), 34.6, (1C, **C**(CH$_3$)$_3$), 110.6 (1C, aromatic **C**), 117.3 (1C, aromatic **C**), 127.2 (1C, aromatic **C**H), 132.2 (1C, aromatic **C**H), 144.3 (1C, aromatic **C**), 151.7 (1C, aromatic **C**), 152.6 (1C, Ar**C**HN).

2.4.2.6 5-*tert*-Butyl-2-hydroxy-3-methoxybenzaldehyde oxime (**L7H**)

Hydroxylamine hydrochloride (0.348 g, 5 mmol), potassium hydroxide (0.280 g, 5 mmol) and 5-*tert*-butyl-2-hydroxy-3-methoxybenzaldehyde (0.501 g, 2.4 mmol) were reacted according to the general procedure to yield a white solid (0.51 g, 95%). Crystals suitable for XRD analysis were grown by slow evaporation of an acetone solution. ^{1}H NMR (250 MHz, $CDCl_3$): δ_H (ppm) 1.25 (s, 9H, C(C*H*$_3$)$_3$), 3.85 (s, 3H, OC*H*$_3$), 6.74 (d, 1H, Ar*H*), 6.89 (d, 1H, Ar*H*), 8.16 (s, 1H, C*H*N), 9.6 (br, 1H, O*H*); ^{13}C NMR (63 MHz, $CDCl_3$): δ_C (ppm) 31.8 (3C, C(**C**H$_3$)$_3$), 34.7, (1C, **C**(CH$_3$)$_3$), 56.7

(1C, O**C**H_3), 111.9 (1C, aromatic **C**H), 116.2 (1C, aromatic **C**), 119.1 (1C, aromatic **C**H), 143.0 (1C, aromatic **C**), 145.1 (1C, aromatic **C**), 148.5 (1C, aromatic **C**), 153.4 (1C, Ar**C**HN).

2.4.2.7 2-Hydroxy-5-*tert*-octylbenzaldehyde oxime (**L8H**)

Hydroxylamine hydrochloride (0.709 g, 10.2 mmol), potassium hydroxide (0.674 g, 10.2 mmol) and **(4)** (2.120 g, 9.1 mmol) were reacted according to the general procedure to give a yellow oil, which solidified overnight. This was recrystallised from hexane, yielding a white crystalline solid (1.375 g, 60%). ^{1}H NMR (250 MHz, $CDCl_3$): δ_H (ppm) 0.64 (s, 9H, C(C*H*$_3$)$_3$), 1.23 (s, 6H, C(C*H*$_3$)$_2$), 1.58 (s, 2H, C*H*$_2$), 6.80 (d, 1H, Ar*H*), 7.01 (s, 1H, Ar*H*), 7.20 (dd, 1H, Ar*H*), 8.12 (s, 1H, ArC*H*N); ^{13}C NMR (63 MHz, $CDCl_3$): δ_C (ppm) 31.2 (2C, C(**C**H$_3$)$_2$), 31.2 (2C, C(**C**H$_3$)$_3$), 32.7 (1C, **C**(CH$_3$)$_3$) 38.3, (1C, **C**(CH$_3$)$_2$), 57.3 (1C, **C**H$_2$), 115.9 (1C, aromatic **C**), 116.4 (1C, aromatic **C**H), 128.5 (1C, aromatic **C**H), 129.9 (1C, aromatic **C**H), 141.9 (1C, aromatic **C**), 153.9 (1C, Ar**C**HN), 155.1 (1C, aromatic **C**).

2.4.3 Copper(II) Complex Synthesis

All copper(II) complexes of the ligands were synthesised using the following general procedure. Stoichiometric amounts of the ligand and metal acetate (0.5 equivalents) were mixed in methanol (50 ml) for 24 h. Colour changes due to complex formation occurred immediately, along with precipitation. Complexes were isolated by filtration and dried under vacuum.

2.4.3.1 [Cu(**L6**)$_2$]

Cu(OAc)$_2$.H$_2$O (0.100 g, 0.50 mmol) and **L6** (0.270 g, 1.01 mmol) yielded a brown solid (0.284 g, 88%). (Anal. Calc. for $C_{22}H_{26}Br_2O_4N_2Cu$: C, 43.6; H, 4.3; N, 4.6. Found: C, 43.9; H, 4.1; N, 4.5%)

2.4.3.2 [Cu(**L7**)$_2$]

$Cu(OAc)_2.H_2O$ (22.4 mg, 0.11 mmol) and **L7** (50.0 mg, 0.22 mmol) yielded a brown solid (45.8 mg, 82%). (Anal. Calc. for $C_{24}H_{32}O_6N_2Cu$: C, 56.7; H, 6.4; N, 5.5. Found: C, 56.6; H, 6.1; N, 5.5%).

2.4.3.3 [Cu(**L8**)$_2$]

$Cu(OAc)_2.H_2O$ (40.0 mg, 0.20 mmol) and **L8** (99.5 mg, 0.40 mmol) yielded a brown powder (103.5 mg, 93%). (Anal. Calc. for $C_{30}H_{44}O_4N_2Cu$: C, 64.3; H, 7.9; N, 5.0. Found: C, 64.3; H, 8.0; N, 5.1%).

2.4.4 Machine parameters and settings for CID studies on Thermo LCQ

For each study mass spectra were taken with a mass range of 50-2000 Daltons, the selected precursor ion was then trapped with an isolation width of 8 Daltons for the negative and positive CID studies. The mass range minima were automatically limited according to the size of the trapped species (around 1/4 of the mass of the trapped species, e.g. for [Cu(**L1**-H)], which has a monoisotopic mass of 446.1, the mass range minimum is 120 Daltons) but this is dependent on the set Q value (which was kept at 0.25 for all experiments). The upper maxima for the scan range was set automatically for most of the studies at 1000 Daltons this prevented any major interference when extrapolating information from the spectra for data processing.

The selected ions were trapped, the isolation width and mass minima and maxima were set and a set of 30 scans were recorded with the activation energy set to 0%. The activation energy was increased gradually and for each increase another set of 30 scans were taken. This was done until the selected precursor ion had been fully dissociated. The general activation energy range was 0-100% normalised collision energy for the negative ion dissociations. Each sigmoidal dissociation curve presented in this chapter is the averaged data of three individual CID investigations.

2.4.4.1 CID machine parameters.

Sample flow rate:	2µL/min		
Sheath gas flow rate:	46 (Arb. Units)		
Aux. gas flow rate:	0 (Arb. Units)		
Capillary temperature	190°C		
RF amplitude	560V		
Spray Voltage	4.5kV	Capillary Voltage	-26.5V
Octapole 1 offset	6.8V	Lens Voltage	13V
Octapole 2 offset	10.5V	Tube lens offset	0V

2.5 References

(1) de Hoffman, E.; Stroobant, V. *Mass Spectrometry - Principles and Applications*; 2nd Edition ed.; John Wiley & Sons, Ltd: Chichester, 2001.

(2) Jennings, K. R. *Int. J. Mass Spectrom.* **2000**, *200*, 479.

(3) Shukla, A. K.; Futrell, J. H. *J. Mass Spectrom.* **2000**, *35*, 1069.

(4) Paul, W. *Angew. Chem. Int. Ed.* **1990**, *29*, 739.

(5) Paul, W.; Steinwedel, H. *Zeitschrift Fur Naturforschung Section a-a Journal of Physical Sciences* **1953**, *8*, 448.

(6) Stephens, W. E. *Phys. Rev. Lett.* **1946**, *69*, 691.

(7) Comisarow, M. B.; Marshall, A. G. *Chem. Phys. Lett.* **1974**, 282.

(8) Henderson, W.; McIndoe, S. *Mass Spectrometry of Inorganic and Organometallic Compounds*; Wiley, 2005.

(9) March, R. E. *J. Mass Spectrom.* **1997**, *32*, 351.

(10) March, R. E.; Todd, J. F. J.; Inc., J. W. S., Ed. Hobboken, 1997.

(11) March, R. E. *Rapid Commun. Mass Spectrom.* **1998**, *12*, 1543.

(12) Douglas, D. J.; French, J. B. *J. Am. Soc. Mass Spectrom.* **1992**, *3*, 398.

(13) Xu, H. J.; Wada, M.; Tanaka, J.; Kawakami, H.; Katayama, I.; Ohtani, S. *Nucl. Instrum. Methods, Phys. Res. A* **1993**, *333*, 274.

(14) Tolmachev, A. V.; Chernushevich, I. V.; Dodonov, A. F.; Standing, K. G. *Nucl. Instrum. Methods, Phys. Res. B* **1997**, *I24*, 112.

(15) Gates, P.; University of Bristol: Bristol, 2005.

(16) Bookwalter, C. W.; Zoller, D. L.; Ross, P. L.; Johnston, M. V. *J. Am. Soc. Mass Spectrom.* **1995**, *6*, 872.

(17) Mangrum, J. B.; Flora, J. F.; Muddiman, J. C. *J. Am. Soc. Mass Spectrom.* **2002**, *13*, 232.

(18) Wysocki, V. H.; Tsaprailis, G.; Smith, L. L.; A., B. L. *J. Mass Spectrom.* **2000**, *35*, 1399.

(19) Dongre, A. R.; Jones, J. L.; Somogyi, A.; Wysocki, V. H. *J. Am. Chem. Soc.* **1996**, *118*, 8365.

(20) Summerfield, S. G.; Gaskell, S. J. *Int. J. Mass Spectrom. Ion Processes* **1997**, *165/166*, 509.

(21) Anichina, J.; Zhao, X.; Bohme, D. K. *J. Phys. Chem. A.* **2006**, *110*, 10763.

(22) Armentrout, P. B. *Accounts of Chemical Research* **1995**, *28*, 430.

(23) Hart, K. J.; McLuckey, S. A. *J. Am. Soc. Mass Spectrom.* **1994**, *5*, 250.

(24) Colorado, A.; Brodbelt, J. *J. Am. Soc. Mass Spectrom.* **1996**, *7*, 1116.

(25) Penn, S. G.; He, F.; Green, M. K.; Lebrilla, C. B. *J. Am. Soc. Mass Spectrom.* **1997**, *8*, 244.

(26) Rodgers, M. T.; Armentrout, P. B. *Mass spec. rev.* **2000**, *19*, 215.

(27) Rogniaux, H.; Van Dorsselaer, A.; Barth, P.; Biellmann, J. F.; Barbanton, J. *J. Am. Soc. Mass Spectrom.* **1999**, *10*, 635.

(28) Wan, K. X.; Gross, M. L.; Shibue, T. *J. Am. Soc. Mass Spectrom.* **2000**, *10*, 635.

(29) Gabelica, V.; DePauw, E. *J. Mass Spectrom.* **2001**, *36*, 397.

(30) Reyzer, M. L.; Brodbelt, J. S.; Kerwin, S. M.; Kumar, D. *Nucleic Acids Res.* **2001**, *29*, E103.

(31) Satterfield, M.; Brodbelt, J. S. *Inorg. Chem.* **2001**, *40*, 5393.

(32) Vinokur, N.; Ryzhov, V. *J. Mass Spectrom.* **2004**, *39*, 1268.

(33) David, W. M.; Brodbelt, J. S. *J. Am. Soc. Mass Spectrom.* **2003**, *14*, 383.

(34) Crowe, M. C.; Brodbelt, J. S. *J. Am. Soc. Mass Spectrom.* **2003**, *14*, 1148.

(35) Zhang, J. M.; Brodbelt, J. S. *J. Am. Soc. Mass Spectrom.* **2005**, *16*, 139.

(36) Waters, T.; O'Hair, R. A. J.; Wedd, A. G. *J. Am. Chem. Soc.* **2003**, *125*, 3384.

(37) O'Hair, R. A. J.; Vrkic, A. K.; James, P. F. *J. Am. Chem. Soc.* **2004**, *126*, 12173.

(38) Zins, E.-L.; Pepe, C.; Schroeder, D. *J. Mass Spectrom.* **2010**.

(39) Gozet, T.; Huynh, L.; Bohme, D. K. *Int. J. Mass Spectrom.* **2009**, *279*, 113.

(40) Fernandes, A. M.; Coutinho, J. A. P.; Marrucho, I. M. *J. Mass Spectrom.* **2009**, *44*, 144.

(41) Revesz, A.; Milko, P.; Zabka, J.; Schroeder, D.; Roithova, J**.** *J. Mass Spectrom.* **2010**.

(42) Bordas-Nagy, J.; Jennings, K. R. *J. Mass Spectrom. Ion Processes* **1990**, *100*, 105.

(43) Curcuruto, O.; Hamdan, H. *Rapid Commun. Mass Spectrom.* **1993**, *7*, 989.

(44) Jones, J. L.; Dongre, A. R.; Somogyi, A.; Wysocki, V. H. **1994**, *J. Am. Chem. Soc.*, 8368.

(45) Morris, M.; Thibault, P.; Boyd, R. K. **1994**, *J. Am . Soc. Mass Spectrom.*, 1042.

(46) Thomson, B. A.; Douglas, D. J.; Corr, J. J.; Hager, J.; Joliffe, C. L. *Anal. Chem.* **1995**, 1696.

(47) Haller, I.; Mirza, U. A.; Chait, B. T. *Am. Soc. Mass Spectrom.* **1996**, *7*, 677.

(48) Schwartz, J. C.; Taylor, D. M.; Office, U. S. P., Ed. 2000; Vol. 6,124,591.

(49) Corporation, T. E. *Product Support Bulletin 104: Normalized Collision Energy.*

(50) Brownstein, S. *Can. J. Chem.* **1960**, *38*, 1590.

(51) Llor, J. *J. Solution Chem.* **2001**, *30*, 641.

(52) Szymanowski, J.; Borowiak-Resterna, A. *Crit. Rev. Anal. Chem.* **1991**, *22*, 519.

(53) Gill, E. W. B. *Philosophical Magazine* **1928**, *5*, 859.

(54) Schottky, W. *Z. Phys.* **1914**, *15*, 656.

(55) Kaiser, R. E.; Cooks, R. G.; Stafford, G. C.; Syka, J. E. P.; Hemberger, P. H. *Int. J. Mass Spectrom. Processes* **1991**, *106*, 79.

(56) Williams, J. D.; Cox, K. A.; Cooks, R. G.; McLuckey, S. A.; Hart, K. J.; Goeringer, D. E. *Anal. Chem.* **1994**, *66*, 725.

(57) Julien, R. K.; Reiser, H.-P.; Cooks, R. G. *Int. J. Mass Spectrom. Ion Process.* **1993**, *123*, 85.

(58) Dahl, D. A.; Delmore, J. E.; Appelhans, A. D. *Rev. Sci. Instrum.* **1990**, *61*, 607.

(59) Belov, M. E.; Zhang, R.; Strittmatter, E. F.; Prior, D. C.; Tang, K.; Smith, R. D. *Anal. Chem.* **2003**, *75*, 4195.

(60) Schwartz, J. C.; Zhou, X.-G.; Bier, M. E. In *US Patent* 1996; Vol. 5,572,022.

(61) Belov, M. E.; Rakov, V. S.; Nikolaev, E. N.; Goshe, M. B.; Anderson, G. A.; Smith, R. D. *Rapid Comm. Mass Spectrom.* **2003**, 627.

(62) Enke, C. G. *Analytical Chemistry* **1997**, *69*, 4885.

(63) Goeringer, D. E.; McLuckey, S. A. *Rapid Comm. Mass Spectrom.* **1996**, *10*, 328.

(64) Hart, K. J.; McLuckey, S. A. *J. Am. Soc. Mass Spectrom.* **1994**, *5*, 250.

(65) Xi, C. W.; Lei, L.; Zheng, J. Q.; Hai, P. G.; He, L. Y.; Xiao, F. C. *Chinese Chem. Let.* **2009**, *20*, 651.

(66) Forgan, R. S., PhD Thesis, University of Edinburgh, 2008.

CHAPTER 3: Further Studies of Collision Induced Dissociation of Phenolic Oxime Complexes

An investigation into the effects of charge, metal, and ligand type on gas phase stability

Table of Contents

3.1. Introduction

3.1.1. Aims

This chapter extends the work described in Chapter 2 on the collision induced dissociation of ionised copper(II) complexes, [M(**L**)$_2$], of a series of 5-*tert*-butyl-3-X-substituted salicylaldoximes, where M = Cu and X = H, Me, ^{t}Bu, NO_2, Cl, Br, OMe. Other factors that could affect the gas phase stability under CID conditions of ions derived from solutions of [M(**L**)$_2$] are investigated. These include:

1. Determining the relative gas phase stabilities of *protonated* ions derived from solutions of 5-*tert*-butyl-3-X-substituted copper complexes, [Cu(**L**)$_2$], under resonance excitation conditions.
2. Investigating the effect of the oxime on the fragmentation profile and hence the gas phase stability of the [Cu(**L**)(**L**-H)]$^-$ complexes using salicylketoxime ligands of the form shown in Figure 3.1.

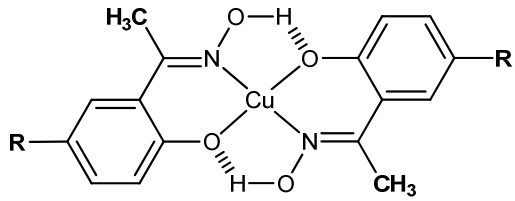

Figure 3.1 : Structure of bis-Ketoxime copper complex, where **R** = ^{t}Bu or ^{t}Oct.

3. Establishing whether the metal, M has an effect on the gas phase stability of deprotonated complexes derived from solutions of [M(**L1**)$_2$] and whether a connection can be made between the stability of [M(**L1**)(**L1**-H)]$^-$ and the selectivity for **L1H** for metal, M.
4. Investigating the gas phase stabilities of heteroleptic [Cu(**LX**)(**LY**)-H]$^-$ anions derived from solutions of Cu^{2+}mixed with **LXH** and **LYH.**

3.2. Results and Discussion

3.2.1. Effect of charge on gas phase stability

In Chapter 2 it was concluded that the inductive nature of the 3-X-substituent influences the stability of the $[Cu(\mathbf{L})(\mathbf{L}\text{-H})]^-$ anions. To investigate the validity of this argument further, this section uses CID to probe the gas phase stabilities of the cationic forms of the 3-X-substituted copper complexes.

There are three principle modes for complexes to obtain a positive charge for a neutral complex *via* electrospray ionisation. The first, and most common, is proton transfer from either the solvent or an added proton source, such as a weak acid (Equation **3.1**).

$$[Cu(\mathbf{L}\text{-H})_2] + H^+ \rightarrow [Cu(\mathbf{L})(\mathbf{L}\text{+H})]^+ \qquad \mathbf{3.1}$$

The second method is ionisation by the acquisition of an alkali metal such as sodium or potassium, yielding positively charged sodiated and potassiated species (Equation **3.2**). This often occurs spontaneously as these metal ions are easily picked up from both the glassware and the silica transfer capillaries. (See also Chapter 6 Section 2)

$$[Cu(\mathbf{L})_2] + Na^+ \rightarrow [Cu(\mathbf{L})_2\text{+Na}]^+ \qquad \mathbf{3.2}$$

The third, least common, method is the abstraction of an electron from the molecular species forming a radical cation (Equation **3.3**). This usually only happens if there is either a metal centre present that can be oxidised, or an aromatic system capable of delocalising the resultant charge and unpaired electron.

$$[Cu(\mathbf{L})_2] - e^- \rightarrow [Cu(\mathbf{L})_2]^{\bullet+} \qquad \mathbf{3.3}$$

For this study it is important that the positively charged species, investigated are the protonated cations, $[Cu(\mathbf{L})(\mathbf{L}\text{+H})]^+$. If the metallated (potassiated or sodiated)

versions were to be used it is difficult to quantify the effect they would have on the stability of the complexes. The radical cations, if present, are difficult to stabilise and would be heavily dependent on the electronic nature of the 3-X-substituent.

If electronic destabilisation *via* repulsion is a major influence on the stability of the 3-X-subtituted copper complex *anions* this will not be present in the protonated cations, as the oximic proton is still present and the secondary H-bond buttressing will not be disturbed. It was assumed (and later proven, see Chapter 2 Section 2.2.7.) that the oximic oxygen atom, being the most electronegative in the ligand, would be protonated to generate $[Cu(\mathbf{L})(\mathbf{L}+H)]^+$ cations. (Figure 3.2) The protonation site may, however, vary in the complexes where other oxygen-containing groups are present (NO_2, OMe).

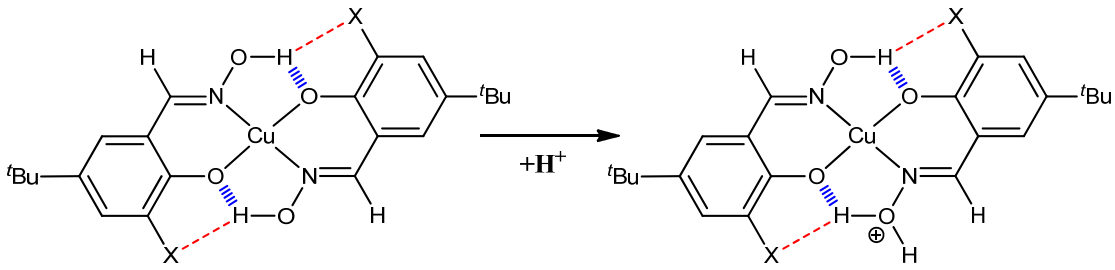

Figure 3.2: Protonation of the complex at the oximic oxygen upon ionisation in cationic mode.

To determine the gas phase cationic stability of the complex cations, 80 µM samples of $[Cu(\mathbf{L})_2]$ (**L1**-**L7**) were investigated. The protonated cations $[Cu(\mathbf{L})(\mathbf{L}+H)]^+$ (**L1**-**L7**) were subjected to CID. (Figure 3.3)

$$Br < Cl < H \leq OMe < NO_2 \leq Me < {}^{t}Bu$$

$$X_c \text{ values: } 24.95(5) < 26.69(2) < 27.26\ (2) \leq 27.22\ (2)$$

$$< 27.87\ (11) \leq 27.93\ (3) < 28.35(5)$$

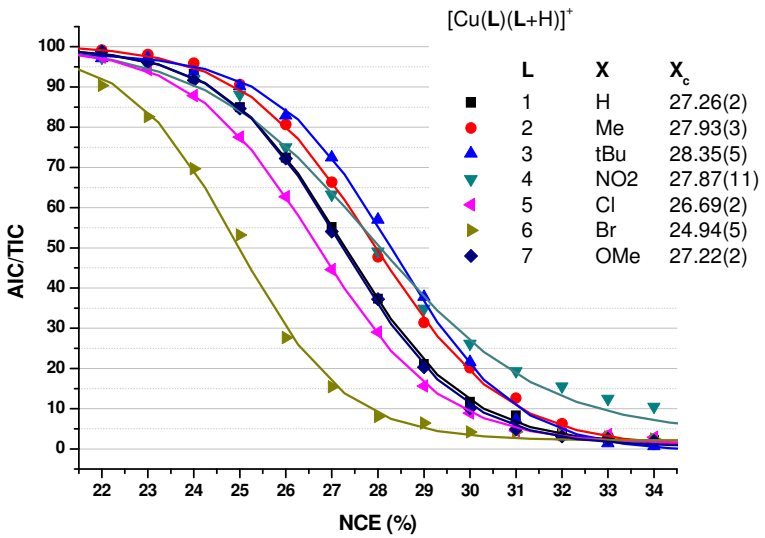

Figure 3.3: Sigmoidal breakdown curves and X_c values for $[Cu(\mathbf{L})(\mathbf{L}+H)]^+$ monocations generated from 80μM solutions in MeOH. Error bars omitted as repeats were not carried out.

A comparison of the CID curves for the series of monocations allows their gas phase stabilities to be ranked. Although only qualitative, the dependence of stability of $[Cu(\mathbf{L})(\mathbf{L}+H)]^+$ on the nature of the 3-X-substituent, Br < Cl < H ≤ MeO < NO_2 ≤ Me < *t*-Bu, does not differ significantly for that observed for the monoanionic series, $[Cu(\mathbf{L})(\mathbf{L}-H)]^-$ (Br < NO_2 < Cl < MeO ≤ H < *t*-Bu < Me). The overall stability of the $[Cu(\mathbf{L})(\mathbf{L}+H)]^+$ species (X_c = 24.9-28.3) are, however, lower than those of the anionic analogues (X_c = 26.4-31.4).

When the study of the cationic complexes, $[Cu(\mathbf{L})(\mathbf{L}+H)]^+$, was undertaken it was assumed that their relative stabilities might directly reflect the importance of the hydrogen bond buttressing by the 3-X-substituent; protonation at the oximic OH should enhance the attraction to the X-group (Figure 3.4) and, therefore increase the overall stability of the complex.

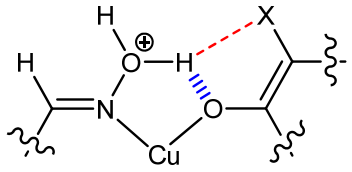

Figure 3.4: Protonation of the complex at the oximic oxygen should increase attraction to the 3-X-substituent.

In practice, for this to be observed using the CID experiment, the decomposition pathways for the series of 3-X-substituted cations must be identical. The relative stability positions of the $[Cu(\mathbf{L5})(\mathbf{L5}+H)]^+$ and $[Cu(\mathbf{L6})(\mathbf{L6}+H)]^+$ cations in this series are the same as for the deprotonated analogues, suggesting that electronic interactions between the large electronegative X-groups and the oxime oxygen atom *isn't* the overriding factor influencing their stability. The more likely explanation is that, as observed for the anionic series (see Chapter 2 Section 2.2), the decomposition pathways for $[Cu(\mathbf{L5})(\mathbf{L5}+H)]^+$ and $[Cu(\mathbf{L6})(\mathbf{L6}+H)]^+$ differ significantly from the unsubstituted analogue, $[Cu(\mathbf{L1})(\mathbf{L1}+H)]^+$.

The following section shows that electronic interactions could be important when comparing the stabilities of the unsubstituted and nitro-substituted complex cations, $[Cu(\mathbf{L1})(\mathbf{L1}+H)]^+$ and $[Cu(\mathbf{L4})(\mathbf{L4}+H)]^+$

3.2.1.1. Decomposition of the $[Cu(\mathbf{L4})(\mathbf{L4}+H)]^+$ cation.

The significantly improved stability of the $[Cu(\mathbf{L4})(\mathbf{L4}+H)]^+$ in Figure 3.4 (relative to the unsubstituted analogue, $[Cu(\mathbf{L1})(\mathbf{L1}+H)]^+$) suggests that the electronic effects between the nitro group and the oximic oxygen atom *are* affecting gas phase stability; the improved stability being due to enhanced outer-sphere interactions as shown in Figure 3.5.

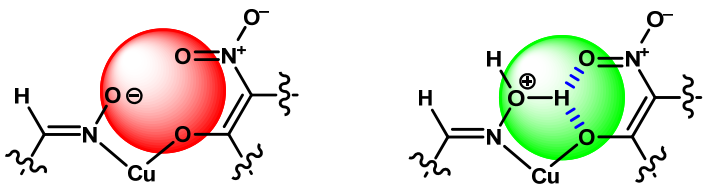

Figure 3.5: The negative and positive electronic effects when comparing the deprotonated (left) and protonated (right) forms of [Cu(**L4**)$_2$].

The shape and position of the dissociation curve for [Cu(**L4**)(**L4**+H)]$^+$ suggests that it behaves differently under CID conditions than the unsubstituted complex cation, [Cu(**L1**)(**L1**+H)]$^+$, with dissociation occurring over a larger range of NCE. (Figure 3.6)

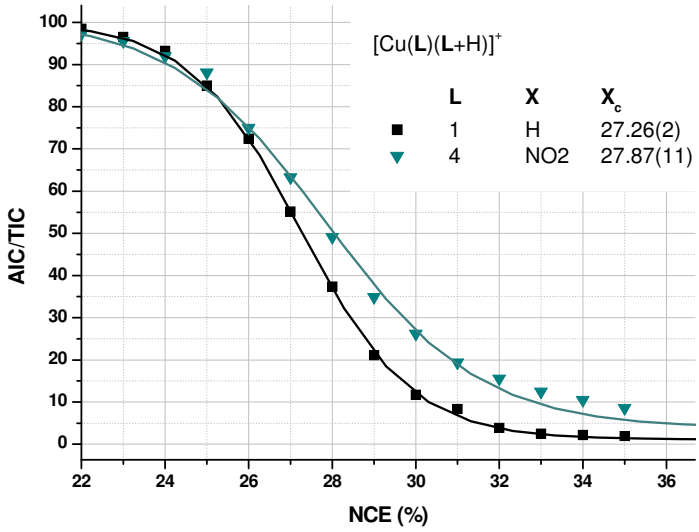

Figure 3.6: The sigmoidal breakdown curve for [Cu(**L4**)(**L4**+H)]$^+$ (turquoise) compared with the more typical profile for [Cu(**L1**)(**L1**+H)]$^+$ (black).

The dissociation pathway was investigated and compared with that of the [Cu(**L1**)(**L1**+H)]$^+$. Figure 3.7 shows the generic [Cu(**L**)(**L**+H)]$^+$ cation and three of the major fragments formed upon CID, [Cu(**L**)(**L**-OH)]$^+$, [Cu(**L**-OH$_2$)(**L**-OH)]$^+$ and [Cu(**L**+H)O]$^+$ with proposed structures and unimolecular fragmentation mechanisms. The observed m/z values for when **L** = **L1** (H) and **L6** (NO$_2$) are given. Fragmentation proceeds *via* H$_2$O loss which could occur either by the loss of the protonated oximic OH (red curly arrows in Figure 3.7) or by the loss of oximic OH with the oximic proton (as observed in the case of the [Cu(**L**)(**L**-H)$_2$] species, see Chapter 2 Section 2.2.7.) is also possible (blue curly arrows in Figure 3.7). The second loss of a water molecule occurs simultaneously but to a much lesser extent as does the formation of the mono-ligated [Cu(**L**+H)O]$^+$ fragment.

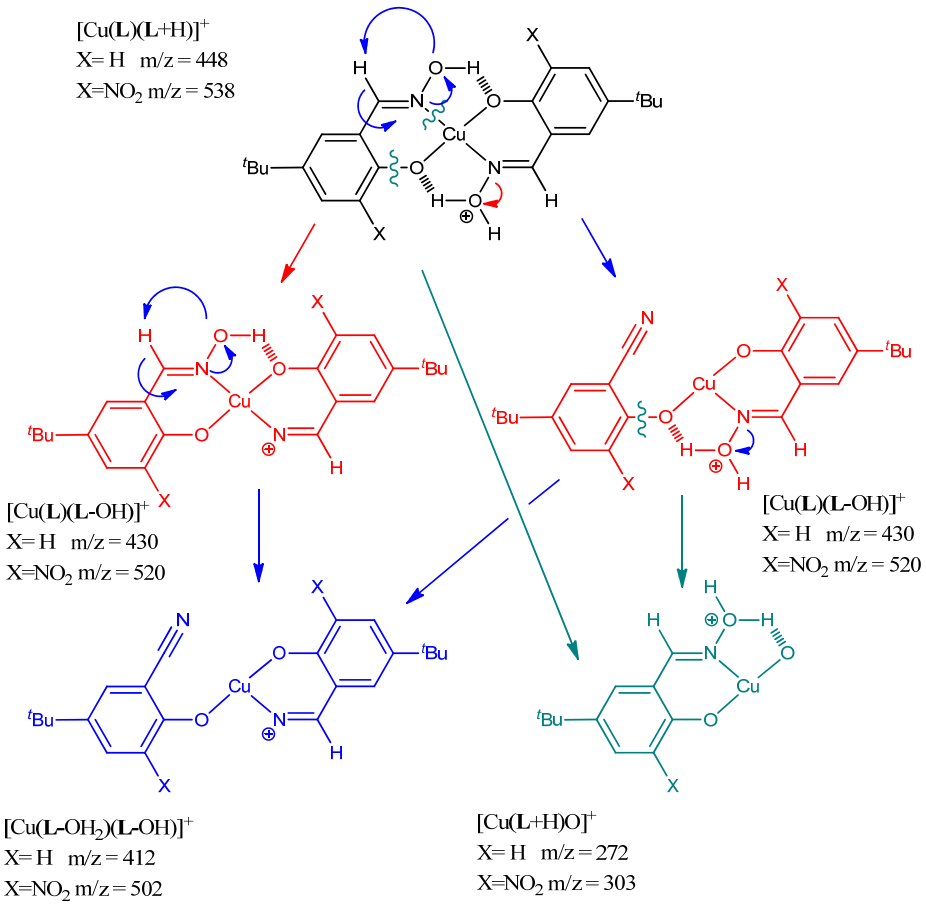

Figure 3.7: Typical fragmentation of [Cu(**L**)(**L**+H)]$^+$ (black) when subjected to CID to fragment ions [Cu(**L**)(**L**-OH)]$^+$ (red), [Cu(**L**-H_2O)(**L**-OH)]$^+$ (blue) and [Cu(**L**+H)O]$^+$ (turquoise). The m/z values for when **L** = **L1** and **L4** are shown.

3.2.1.2. CID fragmentation profiles for [Cu(**L4**)(**L4**+H)]$^+$ and [Cu(**L1**)(**L1**+H)]$^+$

The CID fragmentation profiles were investigated and the relative intensities of the [Cu(**L**)(**L**+H)]$^+$ cation and three of the major fragments [Cu(**L**)(**L**-OH)]$^+$, [Cu(**L**-OH_2)(**L**-OH)]$^+$ and [Cu(**L**+H)O]$^+$ were plotted against NCE for the complexes of the unsubstituted ligand (see Figure 3.8) and of the nitro-substituted ligand (see Figure 3.9). [Cu(**L1**)(**L1**+H)]$^+$ dissociates simultaneously to [Cu(**L1**)(**L1**-OH)]$^+$, [Cu(**L1**-OH_2)(**L1**-OH)]$^+$ and [Cu(**L1**+H)O]$^+$ upon CID. [Cu(**L1**)(**L1**-OH)]$^+$ is the preferred fragment with a relative intensity maximum of 0.48 at 26% NCE where [Cu(**L1**-

OH_2)(**L1**-OH)]$^+$ and [Cu(**L1**+H)O]$^+$ are formed consecutively to a lesser extent with relative intensity maxima of 0.15 (at 50% NCE) and 0.32 (at 100% NCE), see Figure 3.8.

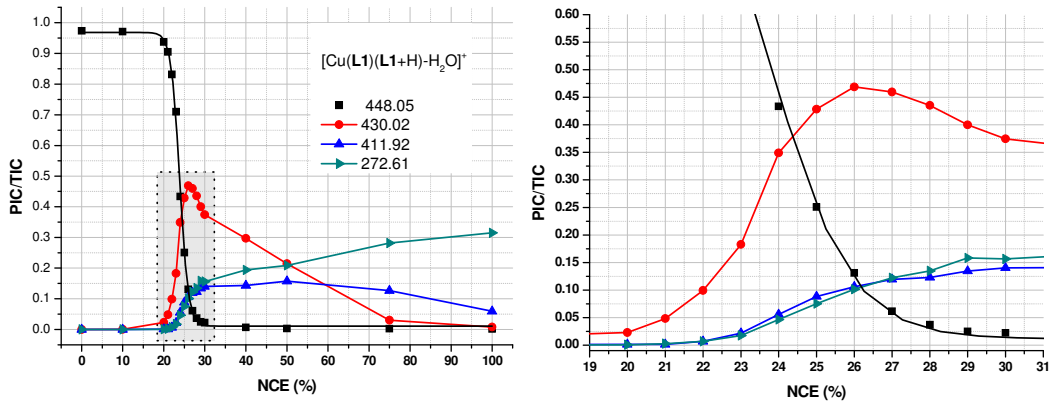

Figure 3.8: Sigmoidal breakdown curve (left) for [Cu(**L1**)(**L1**+H)]$^+$ (black) and relative fragment ion intensities with increasing NCE, with the highlighted area in grey enlarged (right).

[Cu(**L4**)(**L4**+H)]$^+$ also dissociates simultaneously to [Cu(**L4**)(**L4**-OH)]$^+$, [Cu(**L4**-OH_2)(**L4**-OH)]$^+$ and [Cu(**L4**+H)O]$^+$ upon CID but the relative amounts of the daughter ions varies considerably from that of the **L1** analogue. [Cu(**L4**)(**L4**-OH)]$^+$ is the most preferential fragment but the relative intensity maximum is only 0.25% at 27% NCE almost half that of the **L1** analogue. The [Cu(**L4**-OH_2)(**L4**-OH)]$^+$ and [Cu(**L4**+H)O]$^+$ fragments form to an even lesser extent with relative intensity maxima of 0.12 (at 50% NCE) and 0.22 (at 100% NCE) respectively.

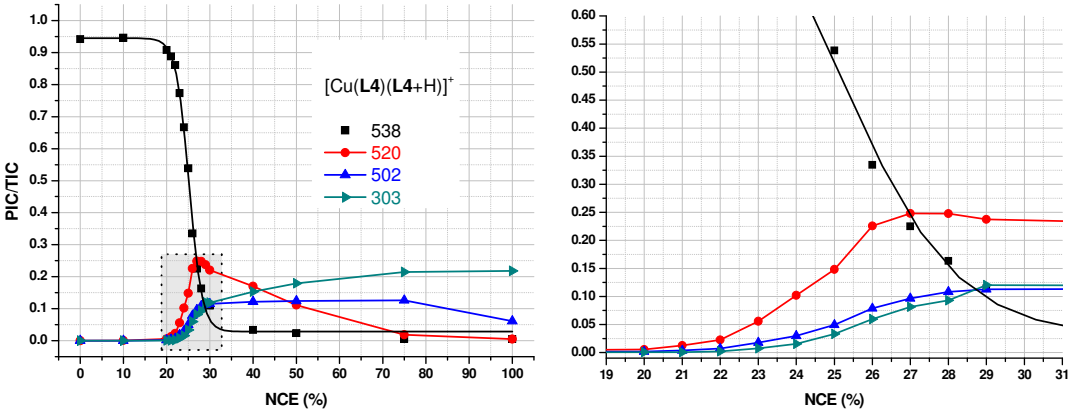

Figure 3.9: The sigmoidal breakdown curve (left) for [Cu(**L4**)(**L4**+H)]$^+$ (black) and relative fragment ion intensities with increasing NCE, with the highlighted area in grey enlarged (right).

When comparing the relative intensities of the major fragment ions of the [Cu(**L1**)(**L1**+H)]$^+$ and [Cu(**L4**)(**L4**+H)]$^+$ cations (Figure 3.8 and Figure 3.9) the shape of the [Cu(**L4**)(**L4**+H)]$^+$ dissociation curve (Figure 3.6) can be attributed to the reduced intensities of the major fragment [Cu(**L4**)(**L4**-OH)]$^+$ species. The relative intensities of [Cu(**L1**)(**L1**-OH)]$^+$ and [Cu(**L4**)(**L4**-OH)]$^+$ were normalised and plotted against NCE in Figure 3.10. A 1.5% difference in NCE maxima of each species is observed.

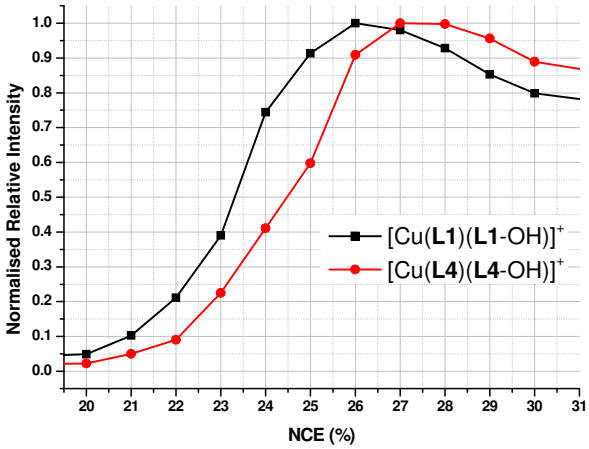

Figure 3.10: Normalised relative intensities of fragment ions [Cu(**L1**)(**L1**-OH)]$^+$ (black) and [Cu(**L4**)(**L4**-OH)]$^+$ (red).

The difference between both the NCE required for dissociation of the [Cu(**L4**)(**L4**+H)]$^+$ when compared with [Cu(**L1**)(**L1**+H)]$^+$ and the relative intensity maxima of the fragment ions is can explained by the effect the NO_2 group has on the *outer*-coordination sphere of the [Cu(**L4**)(**L4**+H)]$^+$ cation at both the protonated and unprotonated sides of the complex. As discussed in Chapters 1 and 2, the NO_2 groups in the copper complex [Cu(**L4**)$_2$] cause bifurcation of the already strong interligand hydrogen bonds and increase the extraction efficiency of the ligand **L4**. This bifurcation should be maintained in the gas phase when the [Cu(**L4**)$_2$] complex is protonated and it is this *increased* interligand interaction that increases the gas phase stability of the [Cu(**L4**)(**L4**+H)]$^+$ cation under CID conditions. (Figure 3.11)

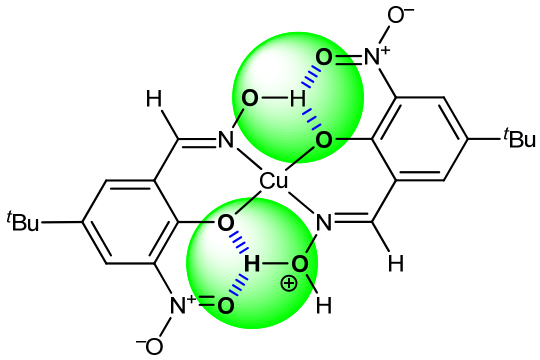

Figure 3.11: [Cu(**L4**)(**L4**+H)]$^+$ cation with highlighted interligand phenolate oxygen - oximic proton interactions (blue) and the nitro oxygen – oximic proton (red) interactions.

3.2.2. Gas phase stability of bis-ketoxime complexes

Ketoximes cover a group of extractants where R^1 is an alkyl or aromatic group. Ketoximes reagents are weaker extractants than aldoximes and blending of ketoxime and aldoxime reagents allows the metallurgist to tailor the properties of the extractant formulation.[1-3] The function and industrial importance of ketoxime reagents will be discussed more fully in Chapter 4. For the ketoximes used in this work, R^1 = Me and R^2 = ^{t}Bu (**L1bH**), ^{t}Oct (**L8bH**).

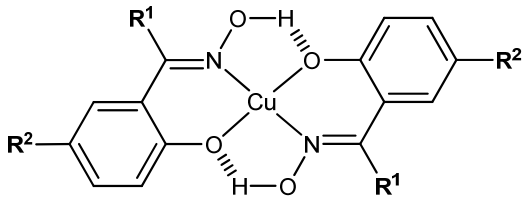

Figure 3.12: structure of bis-Ketoxime copper complex.

The application of CID to bis-ketoxime copper complexes is interesting for a number of reasons:

- CID-MS may help to develop an understanding of how the nature of R^1 affects the stabilities of complexes and, thus, the extraction ability of the ligands.

- The variation of R^1 is interesting fundamentally in the comparison of the gas phase stability of complexes.

- The fragmentation of a bis-ketoximato complex should be different as a consequence of the absence of the *HC*=N protons, which have been shown to be important in the initial stages of fragmentation of bis-aldoximato copper complexes by OH/H_2O losses. (See Section 3.2.2.1)

Figure 3.13 shows the sigmoidal dissociation curves of ^{t}Bu and ^{t}Oct-ketoxime complex anions, [Cu(**L1b**)(**L1b**-H)]$^-$ and [Cu(**L8b**)(**L8b**-H)]$^-$ comparing these with the aldoxime complexes [Cu(**L1**)(**L1**-H)]$^-$ and [Cu(**L8**)(**L8**-H)]$^-$.

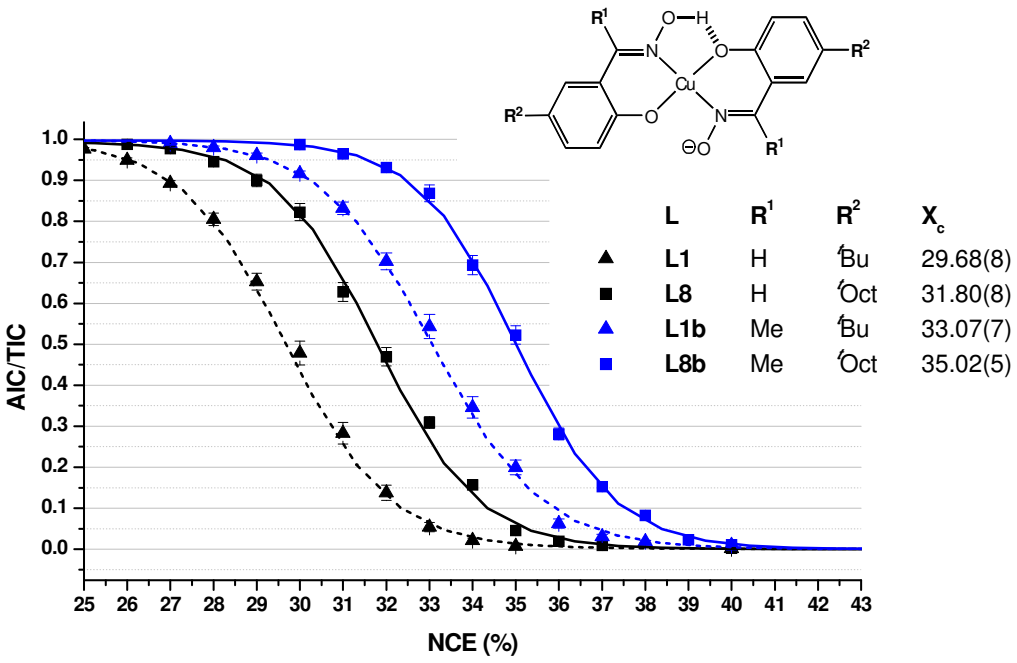

Figure 3.13: CID curves for bis-ketoximate anions [Cu(**L1b**)(**L1b**-H)]$^-$ and [Cu(**L8b**)(**L8b**-H)]$^-$ and bis-aldoximate anions [Cu(**L1**)(**L1**-H)]$^-$ and [Cu(**L8**)(**L8**-H)]$^-$. Errors given to a 2σ level based on 3 repeats. Each point represents 90 scans.

The bis-ketoximate complex anions [Cu(**L1b**)(**L1b**-H)]$^-$ and [Cu(**L8b**)(**L8b**-H)]$^-$ (X_c 33.07(7) and 35.02(5)) are more stable under resonance excitation conditions than their aldoxime derivatives, [Cu(**L1**)(**L1**-H)]$^-$ and [Cu(**L8**)(**L8**-H)]$^-$ (X_c 29.68(8) and

31.80(8)).The difference in stabilities between the analogous bis-ketoximate and bis aldoximate complex anions ≈ 3.3% NCE.

The increased stability of the bis-ketoximate complex anions arises as the first fragmentation has a higher threshold than that observed for the bis aldoximate complex anions. Figure 3.14 shows the CID fragments of [Cu(**L1**)(**L1**-H)]$^-$ and [Cu(**L1b**)(**L1b**-H)]$^-$.

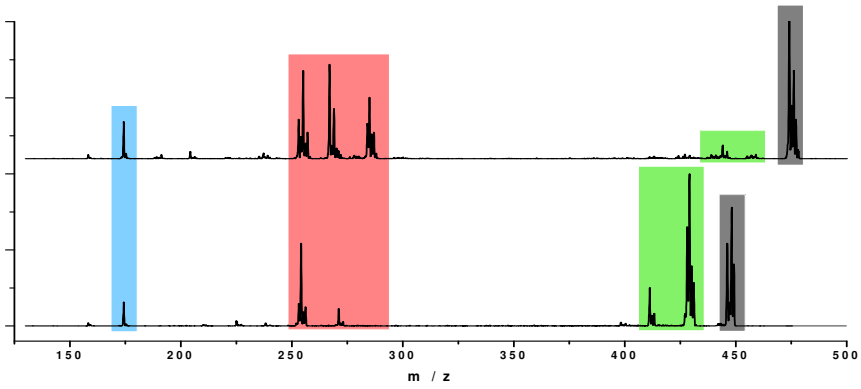

Figure 3.14: The CID spectra for [Cu(**L1**)(**L1**-H)]$^-$ (below) and [Cu(**L1b**)(**L1b**-H)]$^-$ (above) closest to their respective X_c values with analogous fragments highlighted for clarity.

The absence of the *H*C=N protons in the ketoximate [Cu(**L1b**)(**L1b**-H)]$^-$ greatly reduced OH/OH_2 losses (highlighted green in Figure 3.14) as abstraction of proton from the methyl group of the bis ketoximate complex anion requires more energy. The bis-ketoximate complex anion generates more mono-ligated fragments (highlighted red in Figure 3.14) compared to the bis-aldoximate complex anion. Both the [Cu(**L1**)(**L1**-H)]$^-$ and [Cu(**L1b**)(**L1b**-H)]$^-$ anions show a fragment ion at m/z 174.3 (highlighted blue in Figure 3.14) which corresponds to the [**L1**-OH_2]$^-$ and [**L1b**-MeOH]$^-$ fragments.

3.2.2.1. Accurate CID fragment masses for [Cu(**L1b**)(**L1b**-H)]$^-$

Accurate mass CID spectra for [Cu(**L1b**)(**L1b**-H)]$^-$, measured using a Waters Quadrupole-Time-of-Flight (Q-ToF) mass spectrometer, are shown in Figure 3.15. Accurate masses along with a proposed structural formula and possible dissociative mechanisms and pathways are shown.

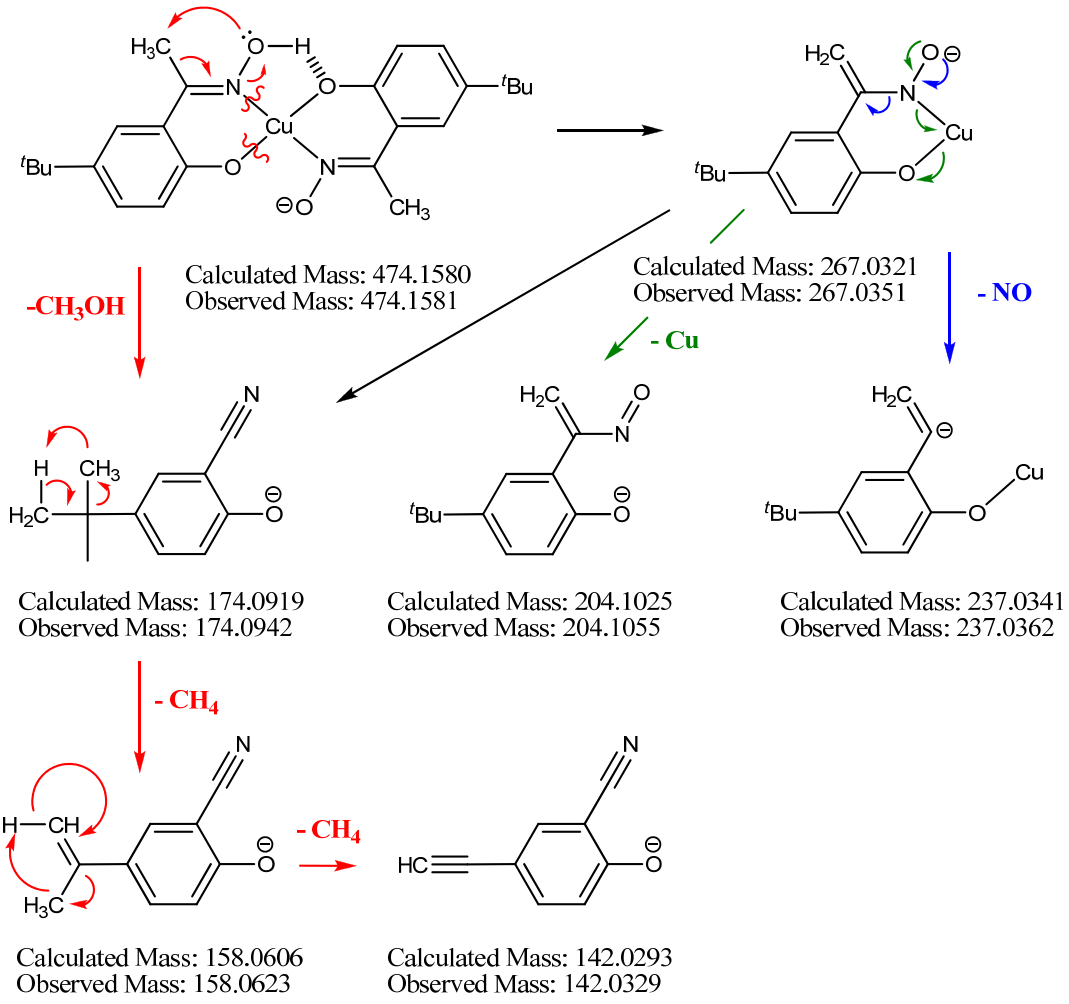

Figure 3.15: Proposed dissociation pathways of [Cu(**L1b**)(**L1b**-H)]$^-$ (m/z 474.16) with accurate observed and calculated fragment ion masses and their proposed structures.

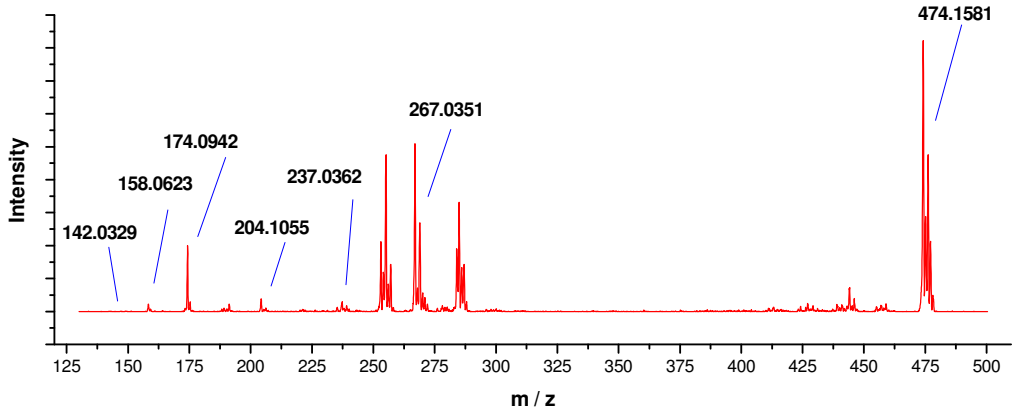

Figure 3.16: CID mass spectrum of [Cu(**L1b**)(**L1b**-H)]$^-$ with important monoisotopic fragment m/z ratios highlighted.

Unlike [Cu(**L1**)(**L1**-H)]$^-$, the initial neutral losses from [Cu(**L1b**)(**L1b**-H)]$^-$ arise from cleavage of the coordination bonds and loss of one of the ligands, resulting primarily in the [Cu(**L1b**-H_2O)]$^-$ fragment at m/z 267.0. This infers that, in order to undergo neutral losses upon fragmentation, unlike for [Cu(**L1**)(**L1**-H)]$^-$, substantial rearrangement occurs which results in ligand loss. The energy required for such a rearrangement in [Cu(**L1b**)(**L1b**-H)]$^-$ is likely to be higher than that for H_2O loss from [Cu(**L1**)(**L1**-H)]$^-$, resulting in a higher fragmentation threshold and a higher gas phase stability under resonance excitation conditions.

3.2.3. Mixed Ligand Complexes

3.2.3.1. Heteroleptic 3-X-substituted phenolic oxime copper complexes

When two ligands, **LXH** and **LYH**, are mixed with Cu^{2+} ions three possible species can form; [Cu(**LX**)$_2$], [Cu(**LY**)$_2$] and [Cu(**LX**)(**LY**)]. The formation of such species along with solution phase equilibria are discussed in detail in Chapter 5. In this chapter the gas phase stabilities of mixed ligand anionic complexes, [Cu(**LX**)(**LY**)-H]$^-$, are discussed and compared with those of ions derived from the [Cu(**LX**)$_2$] and [Cu(**LY**)$_2$] complexes. 80μM solutions of copper acetate in MeCN were mixed with

160µM solution of 1:1 **LXH**:**LYH**. The resultant deprotonated complexes; [Cu(**LX**)(**LX**-H)]$^-$ [Cu(**LY**)(**LY**-H)]$^-$ and [Cu(**LX**)(**LY**)-H]$^-$ were subjected to CID as described in Chapter 2. Results comparing the stabilities of the homoleptic complex anions of the unsubstituted, the 3-nitro-substituted and 3-bromo-substituted ligands, [Cu(**L1**)(**L1**-H)]$^-$, [Cu(**L4**)(**L4**-H)]$^-$ and [Cu(**L6**)(**L6**-H)]$^-$ with the heteroleptic analogues [Cu(**L1**)(**L4**)-H)]$^-$ and [Cu(**L1**)(**L6**)-H)]$^-$ are presented in Figure 3.17

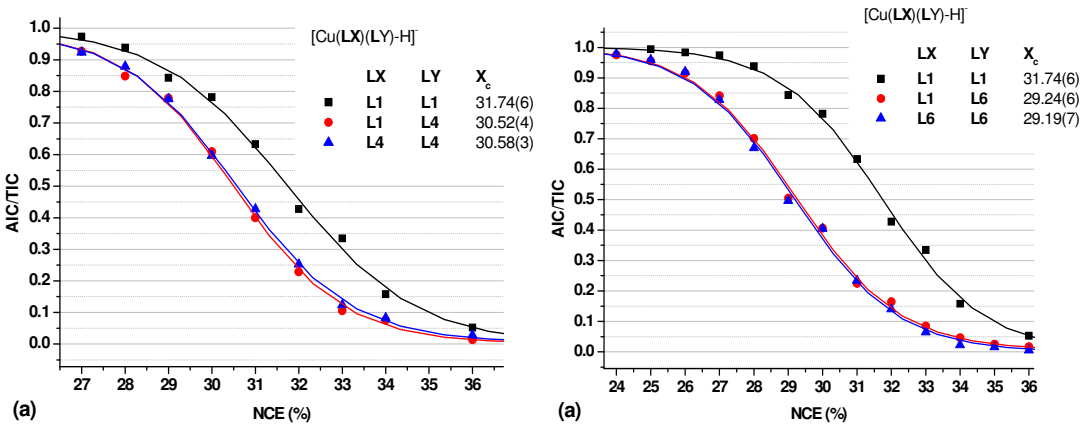

Figure 3.17: CID dissociation curves for (a) the homoleptic complexes [Cu(**L1**)(**L1**-H)]$^-$ and [Cu(**L4**)(**L4**-H)]$^-$ and the heteroleptic analogue [Cu(**L1**)(**L4**)-H)]$^-$ and for (b) the homoleptic complexes Cu(**L1**)(**L1**-H)]$^-$ and [Cu(**L6**)(**L6**-H)]$^-$ and the heteroleptic analogue [Cu(**L1**)(**L6**)-H)]$^-$.

In both cases the gas phase stability of the heteroleptic deprotonated complexes, [Cu(**LX**)(**LY**)-H]$^-$ ([Cu(**L1**)(**L4**)-H]$^-$ in figure (a), and [Cu(**L1**)(**L6**)-H]$^-$ in figure (b)), corresponds with the gas phase stability of the less stable deprotonated homoleptic complex ([Cu(**L4**)(**L4**-H)]$^-$ in figure (a), and [Cu(**L6**)(**L6**-H)]$^-$ in figure (b)) with their X_c values being within experimental error. The equality of the X_c values suggests that the stability of the [Cu(**LX**)(**LY**)-H]$^-$ anions is determined by which ligand provides the lower fragmentation threshold.

3.2.3.2. **Heteroleptic aldoxime/ketoxime copper complexes**

As for the the 3-X-substituted aldoxime investigation discussed in section 3.2.4.1, an 80µM solution equimolar solution of copper acetate, **L1H** and **L1bH** in MeCN was introduced into the mass spectrometer *via* ESI. The reultant deprotonated complexes;

[Cu(**L1**)(**L1**-H)]$^-$, [Cu(**L1b**)(**L1b**-H)]$^-$ and [Cu(**L1**)(**L1b**)-H]$^-$ were subjected to CID as described above and the resultant dissociation S-curves are shown in Figure 3.18.

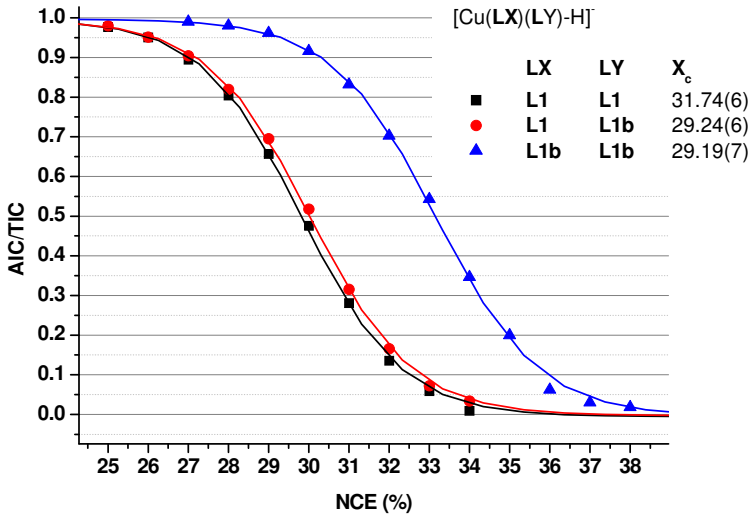

Figure 3.18: Sigmoidal dissociation curves for the homoleptic complexes, Cu(**L1**)(**L1**-H)]$^-$ and [Cu(**L4**)(**L4**-H)]$^-$ and for the heteroleptic complex, [Cu(**L1**)(**L4**)-H)]$^-$.

The stability of the heteroleptic aldoxime/ketoxime anion, [Cu(**L1**)(**L1b**)-H]$^-$ is identical (within experimental error) with that of the less stable homoleptic anion, that of the aldoxime, [Cu(**L1**)$_2$-H]$^-$ (X_c values of 29.24(6) and 29.19(7) respectively). This suggests that, as observed for the 3-X-substituted heteroleptic complex anions, that it is the coordinated ligand with the lower fragmentation threshold, which defines the stability of the [Cu(**L1**)(**L1b**)-H]$^-$ anion. High resolution CID of the [Cu(**L1**)(**L1b**)-H]$^-$ anion was investigated to confirm this. (Figure 3.19)

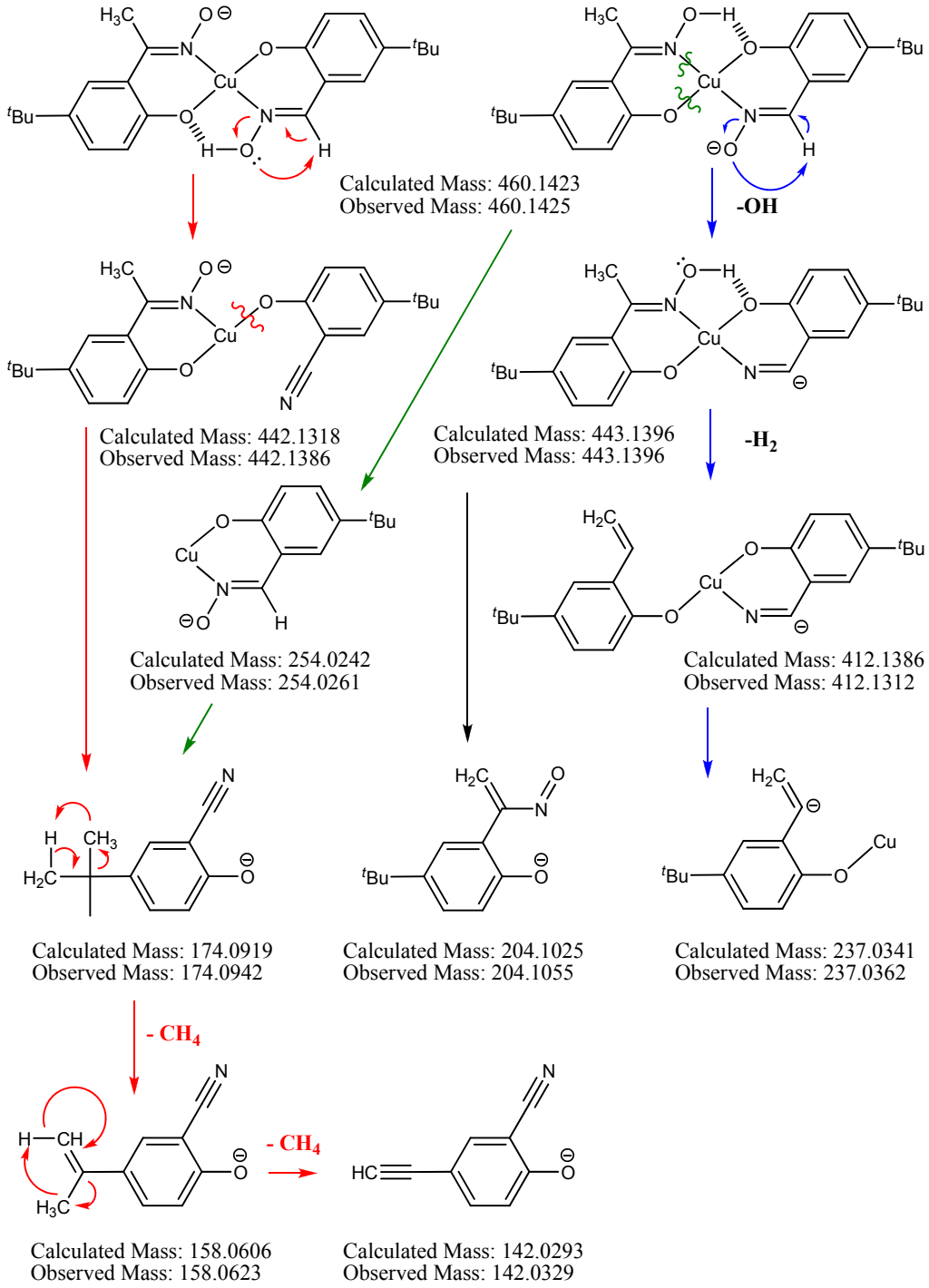

Figure 3.19: Proposed dissociation pathways of [Cu(**L1**)(**L1b**)-H)]$^-$ (m/z 460.14) with accurate observed and calculated fragment ion monoisotopic masses and their proposed structures.

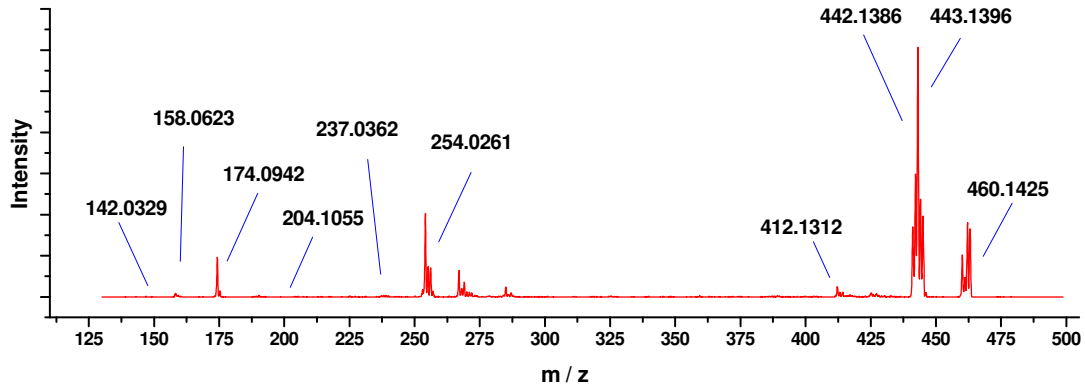

Figure 3.20: CID mass spectrum of [Cu(**L1**)(**L1b**)-H)]$^-$ with important fragment monoisotopic m/z ratios highlighted. (See also Figure 3.19)

The CID mass spectrum in Figure 3.20 shows the relative intensities of the [Cu(**L1**)(**L1b**)-H]$^-$ anion at m/z 460.1 and of the fragment ions resulting from CID. The dissociation pathways shown in Figure 3.19 show two plausable [Cu(**L1**)(**L1b**)-H]$^-$ structures where deprotonation occurs at at ketoximic or aldoximic OH. The initial losses of OH (red pathway in Figure 3.19) or H_2O (blue pathway in Figure 3.19) occur at the aldoxime ligand and the dominating fragments at m/z 442.14, 443.14 and 254.03 result from these. The fragmentation pathways are consistent with H_2O dissociation occurring *via* the aldoximate ligand.

3.2.4. The Influence of CID technique on gas phase stability

As discussed in Chapter 2 Sections 2.1.4-2.1.5 a collision cell can also be used for collision induced dissociation studies. CID studies were carried out using a Waters Micromass Q-ToF in order to determine whether the trends measured using an ion trap also occur in a collision cell. 80μM solution equimolar solution of copper acetate, **L1H** and **L1bH** in MeCN was introduced into the mass spectrometer *via* ESI using an autosampler. The resultant deprotonated complexes; [Cu(**L1**)(**L1**-H)]$^-$, [Cu(**L1b**)(**L1b**-H)]$^-$ and [Cu(**L1**)(**L1b**)-H]$^-$ were subjected to CID using increasing amounts of collision cell collision energy (in volts). The resultant dissociation S-curves are shown in Figure 3.21 (a).

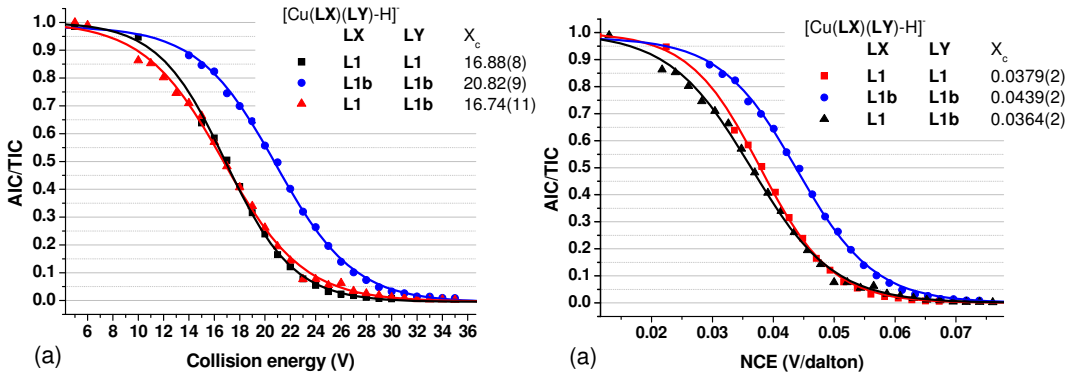

Figure 3.21: Sigmoidal dissociation curves for deprotonated homoleptic complexes [Cu(**L1**)(**L1**-H)]$^-$ and [Cu(**L1b**)(**L1b**-H)]$^-$ and heteroleptic complex [Cu(**L1**)(**L1b**)-H]$^-$ as measured using a collision cell shown as a function of (a) measured collision energy (in volts) and (b) calculated normalised collision energy (in volts/Dalton).

An identical trend is observed as seen in section 3.2.4.2, with the gas phase stability of the heteroleptic [Cu(**L1**)(**L1b**)-H]$^-$ anion being within experimental error of thatthe homoleptic aldoxime anion, [Cu(**L1**)$_2$-H]$^-$ (X_c values of 16.74(11) V and 16.88(8) V respectively). The homoleptic [Cu(**L1b**)$_2$-H]$^-$ complex has a considerably higher observed gas phase stability (X_c = 20.82(9) V).

Unlike with the LCQ, the Q-ToF does not have a collision energy that is normalised with respect to the mass of the ion being investigated. Figure 3.21 (b) shows the relative intensities of the 3 species being investigated with respect to a calculated normalised collision energy, $NCE_{Q\text{-}ToF}$ (given in V/Dalton), using equation **3.1**

$$NCE_{Q\text{-}ToF} = E_{Q\text{-}ToF} / M_{ion} \qquad \textbf{3.1}$$

where $E_{Q\text{-}ToF}$ is the measured collision energy and M_{ion} is the molecular mass of the species being investigated. This conversion does not affect the overall trend where the gas phase stability of [Cu(**L1b**)$_2$-H]$^-$ > [Cu(**L1**)(**L1b**)-H]$^-$ ≈ [Cu(**L1**)$_2$-H]$^-$.

3.2.5. Dependence of the gas phase stabilities of [M(L1)(L1-H)]$^-$ anions

As mentioned in Chapter 1, the selectivity of salicylaldoxime extractants for Cu(II) over other first row transition dications is thought to arise from the goodness-of-fit of the cavity size for the Cu^{II} ion. The selectivity of extractants can be determined achieved by measurement of the $pH_{0.5}$; the pH at which half the ligand in the organic phase is loaded with the appropriate metal ion.[2] Figure 3.22 contains plots of metal loading of the industrial extractant **P50** (2-hydroxy-5-nonylbenzaldehyde oxime) as a function of pH, showing that the higher $pH_{0.5}$ value is lower for Cu(II) than for other base metal cations.[2]

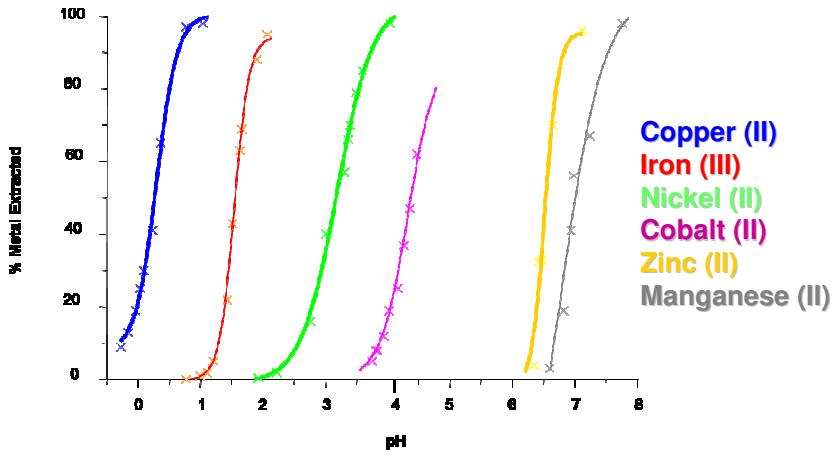

Figure 3.22: pH loading profiles for a range of metals for a solution of **P50** in kerosene.[2] Loading profiles for copper, zinc and nickel in bold.

CID studies were performed on nickel and zinc derivatives of [M(**L1**)(**L1**-H)]$^-$ to see whether the relative stabilities and fragmentation under resonance excitation conditions relate to the stabilities of the neutral complexes, [M(**L**)$_2$], formed by commercial extractants. Nickel and zinc were chosen because they exhibit a stable M^{2+} oxidation state which will lead to the neutral 2:1 **LH**:M complex. Fe, Co and Mn all have easily accessible M^{3+} oxidation states ($Fe^{3+} + e^- \rightarrow Fe^{2+} = +0.77$ E^0/V, $Co^{3+} + e^- \rightarrow Co^{2+} = +1.92$ E^0/V, $Mn^{3+} + e^- \rightarrow Mn^{2+} = +1.54$ E^0/V)[4] and are likely to lead to more complicated solution speciation.

The relative stability of the monoanions under resonance excitation conditions was found to be [Zn(**L1**)(**L1**-H)]$^-$ < [Cu(**L1**)(**L1**-H)]$^-$< [Ni(**L1**)(**L1**-H)]$^-$ (X_c = 25.42(4), 29.76(4), 33.27(26) respectively). The shape of the sigmoidal curves for the Zn and Ni complexes differ considerably from that of the Cu complex which indicates that different modes of fragmentation apply.

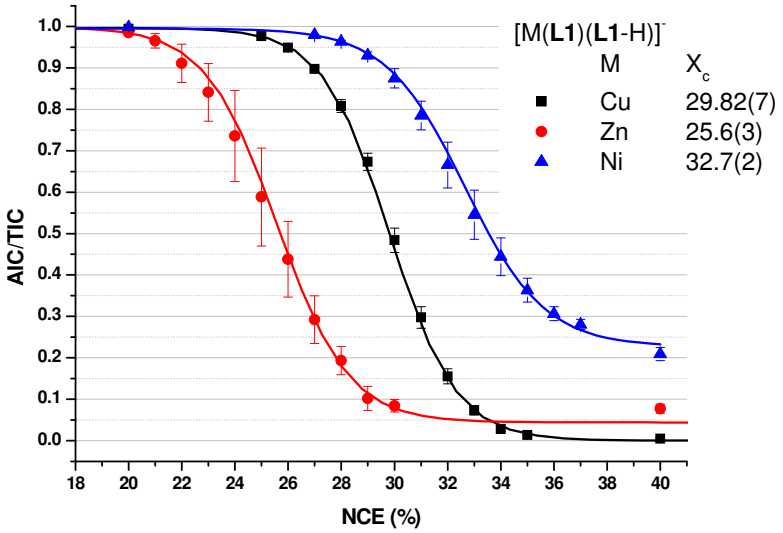

Figure 3.23: Dissociation curves of [M(**L1**)(**L1**-H)]$^-$ where M = Zn, Cu, Ni; X_c values 25.42(7), 29.78(4) and 33.27(26) respectively. Errors given to a 2σ level based on 3 repeats. Each point represents 90 scans.

The modes of dissociation for the [Ni(**L1**)(**L1**-H)]$^-$ and [Zn(**L1**)(**L1**-H)]$^-$ anions were compared with that established for the [Cu(**L1**)(**L1**-H)]$^-$ anion. (see also Chapter 2 Section 2.2.12) The dissociation pathways for the [Cu(**L1**)(**L1**-H)]$^-$ anion include OH/H_2O losses, a [Cu(**L1**-H)]$^-$ peak at m/z 254 and a nitrile form of the oxime ligand, [**L1**-H_2O]$^-$, at m/z 174. Figure 3.23 shows the relative intensities of the [Cu(**L1**)(**L1**-H)]$^-$, [Cu(**L1**)(**L1**-H)-OH/OH_2]$^-$, and [**L1**-H_2O]$^-$ peaks with increasing amounts of collision energy.

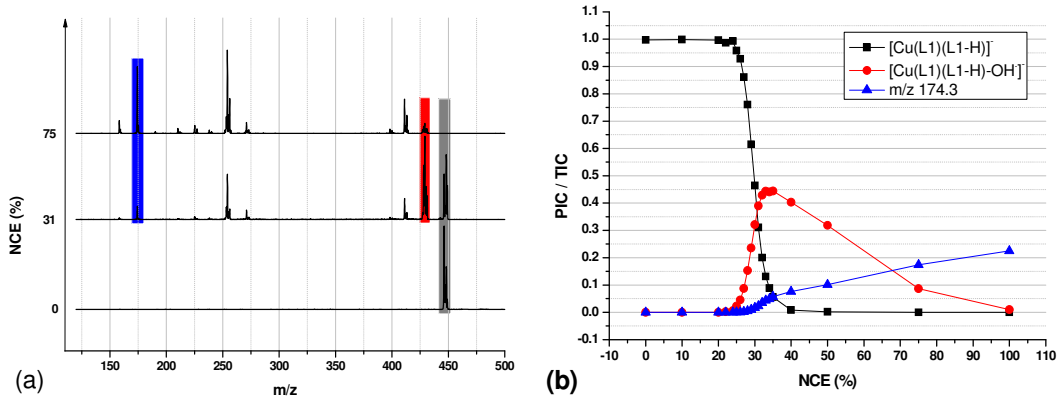

Figure 3.24: (a) CID mass spectra for [Cu(**L1**)(**L1**-H)]$^-$ at 0%, 31% and 75% NCE and (b) relative intensities of [Cu(**L1**)(**L1**-H)]$^-$, [Cu(**L1**)(**L1**-H)-OH/OH$_2$]$^-$ and [**L1**-H$_2$O]$^-$ with increasing NCE.

The OH/H$_2$O loss is shown to be the major fragmentation pathway with a relative intensity maximum of 45% at 34 % NCE, whereas the [**L1**-H$_2$O]$^-$ species only reaches a maximum of 23% at 100% NCE. The increased formation of the [**L1**-H$_2$O]$^-$ species at higher NCE will be a result of increased fragmentation of [Cu(**L1**)(**L1**-H)-OH/H$_2$O]$^-$ fragments to [**L1**-OH$_2$]$^-$ as indicated be the reduction in intensity of the [Cu(**L1**)(**L1**-H)-OH/H$_2$O]$^-$ peak after around 35% NCE.

The dissociation pathway for [Ni(**L1**)(**L1**-H)]$^-$ (Figure 3.25) is distinctly different from that observed for [Cu(**L1**)(**L1**-H)]$^-$.

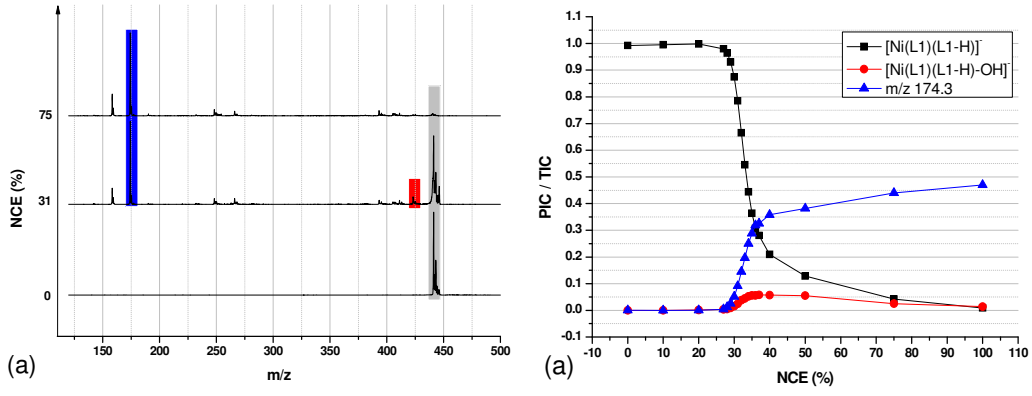

Figure 3.25: (a) CID mass spectra for [Ni(**L1**)(**L1**-H)]$^-$ at 0%, 31% and 75% NCE and (b) relative intensities of [Ni(**L1**)(**L1**-H)]$^-$, [Ni(**L1**)(**L1**-H)-OH/OH$_2$]$^-$ and [**L1**-H$_2$O]$^-$ with increasing NCE.

The observed OH/H_2O losses from [Ni(**L1**)(**L1**-H)]$^-$ are significantly reduced when compared with those for [Cu(**L1**)(**L1**-H)]$^-$, reaching a relative intensity maximum of only 6% at 35% NCE. This could indicate an increased strength the inter ligand H-Bonds, which would, in turn, increase the energy required for OH and H_2O losses. The formation of the [**L1**-H_2O]$^-$ directly upon dissociation of the [Ni(**L1**)(**L1**-H)]$^-$ ion suggests that the fragmentation pathways are distinctly different than those observed for [Cu(**L1**)(**L1**-H)]$^-$, which resulted in a higher X_c value.

The dissociation of [Zn(**L1**)(**L1**-H)]$^-$,again, shows fragments analogous to those observed for [Cu(**L1**)(**L1**-H)]$^-$ but the relative intensities of the major fragments, as seen for [Ni(**L1**)(**L1**-H)]$^-$, indicates a difference in the dissociation mechanisms. (Figure 3.26)

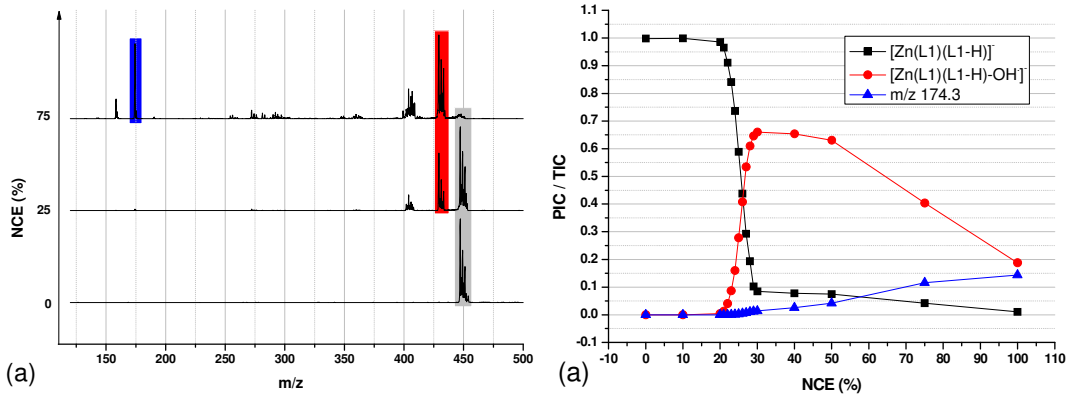

Figure 3.26: (a) CID mass spectra for [Zn(**L1**)(**L1**-H)]$^-$ at 0%, 31% and 75% NCE and (b) relative intensities of [Zn(**L1**)(**L1**-H)]$^-$, [Zn(**L1**)(**L1**-H)-OH/OH_2]$^-$ and [**L1**-H_2O]$^-$ with increasing NCE.

The formation of the [Zn(**L1**)(**L1**-H)-OH/H_2O]$^-$ fragments occurs at lower levels of NCE and to a much greater extent with a maximum of 67% at 30% NCE. This indicates a possible weakening of the interligand hydrogen bonding which facilitates the losses of OH and H_2O and leads to a lower X_c. The [Zn(**L1**-H)]$^-$ peak is also observed but its relative intensity maximum never exceeds 6%. The formation of the [**L1**-H_2O]$^-$ fragment does occur but only upon application of larger amounts of NCE.

Here the study has shown that the metal influences the dissociation mechanisms of the [M(**L1**)(**L1**-H)]$^-$ anions and, thus, their stabilities under resonance excitation

conditions. The following section uses DFT calculations to investigate the relationship between the geometry of the [M(**L1**)(**L1**-H)]$^-$ anions and the nature of the metals, M.

3.2.5.1. DFT calculations for [M(**L1**)(**L1**-H)]$^-$ gaseous anions

In order to understand the arising differences in the gas phase stabilities of the complex anions, [M(**L1**)(**L1**-H)]$^-$, density functional theory calculations were carried using B3LYP/6-31G+(d,p). Energy minimised structures for both the neutral complexes, [M(**L1**)$_2$], and the singly deprotonated monoanions, [M(**L1**)(**L1**-H)]$^-$ were calculated. The energy minimised structures for the neutral copper, nickel and zinc complexes were planar and are discussed in detail in Chapter 4 Section 4.4. Table 3.1 shows the calculated minimised energies of the [M(**L1**)$_2$] and [M(**L1**)(**L1**-H)]$^-$ species, from which the deprotonation energies for the [M(**L1**)$_2$] complexes are calculated to be 1451.9 kJ mol^{-1}, 1444.6 kJ mol^{-1} and 1441.8 kJ mol^{-1}, for Ni, Cu and Zn respectively.

Table 3.1: Calculated minimised energies of the [M(**L1**)$_2$] and [M(**L1**)(**L1**-H)]$^-$ species and the deprotonation energies.

M	Energy [M(**L**)$_2$]/au	Energy [M(**L**)(**L**-H)]$^-$/au	Deprotonation energy/kJ mol^{-1}	Deprotonation energy *cf.* Copper/kJ mol^{-1}
Ni	-2773.9210	-2773.3680	+1451.9	+7.3
Cu	-2906.0459	-2905.4956	+1444.6	0
Zn	-3044.8781	-3044.3289	+1441.8	-2.8

The deprotonation enthalpy is 7 kJ mol^{-1} larger for [Ni(**L1**)$_2$] than for [Cu(**L1**)$_2$] suggesting that the inter-ligand H-bonding is stronger for [Ni(**L1**)$_2$]. This is consistent with the [Ni(**L1**)$_2$] complex having a smaller cavity size, *i.e.* Shorter Cu-O

and Cu-N bonds in both the energy minimised structure (see Table 3.2) and X-ray determined crystal structures.[5] (See Chapter 4 Section 4.2.4.)

Bond lengths and angles in the inner coordination spheres and contact distances in the outer coordination spheres for the energy minimised neutral complexes, [M(**L1**)$_2$], and the monoanions, [M(**L1**)(**L1**-H)]$^-$, are presented in Table 3.2. the atom labelling scheme shown in Figure 3.27 is similar to that used for the discussion of the neutral complexes (see Chapter 4 Section 4.2.2.). In the discussion below the labels containing "m" and "d" refer to atoms in the monoanionic and dianionic ligands respectively (see Figure 3.27)

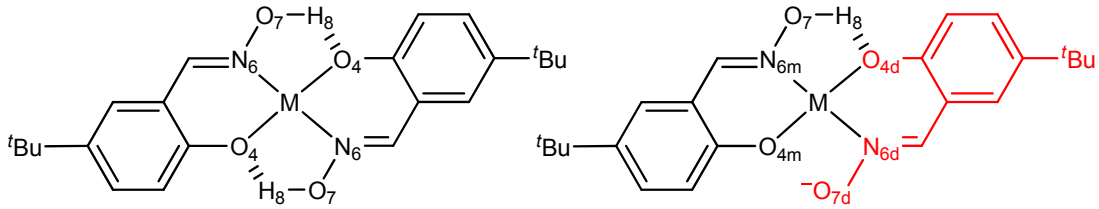

Figure 3.27: Atom labelling scheme for [M(**L1**)$_2$] complexes (left) and [M(**L1**)(**L1**-H)]$^-$ anions (right) presented in Table 3.2.

Table 3.2: Calculated bond distances/Å and bond angles/° for the [M(**L1**)$_2$] complexes and [M(**L1**)(**L1**-H)]$^-$ anions. The calculated differences are highlighted in red.

Species	$O_{4/4d}$-M/Å	$N_{6/6d}$-M/Å	$O_{7/7d}\cdots O_{4/4m}$ /Å	$O_{4/4d}$-H_8/Å	$O_{4/4d}$-M-$N_{6/6m}$/°	O_{4m}-M-N_{6d}/°
[Ni(**L1**)$_2$]	1.8477	1.8935	2.5297	1.6841	87.2239	-
[Ni(**L1**)(**L1**-H)]$^-$	1.8608	1.9312	2.6458	1.6036	84.7830	90.0811
difference	0.0131	0.0377	0.1161	-0.0805	-2.4409	2.8573
[Cu(**L1**)$_2$]	1.9162	1.9639	2.6323	1.7787	88.0498	-
[Cu(**L1**)(**L1**-H)]$^-$	1.9406	2.0308	2.8987	1.6536	83.1935	95.6412
difference	0.02437	0.0669	0.2664	-0.1251	-4.8563	7.5915
[Zn(**L1**)$_2$]	1.9587	2.027	2.7483	1.9005	88.97819	-
[Zn(**L1**)(**L1**-H)]$^-$	1.9807	2.1050	3.2150	1.6299	78.75201	104.7877
difference	0.0220	0.0780	0.4667	-0.2706	-10.2262	15.8095

The bond lengths in the inner coordination sphere, M-O_4 and M-N_6, increase in the order Ni < Cu < Zn as would be expected from the covalent radii of Ni(II) (low spin – as would be expected in a neutral square planar complex with no axial coordinating solvents), Cu(II) (4 coordinate, planar) and Zn(II) (4 coordinate) as revealed by X-ray structure determination of neutral salicylald -iminato and –oximato complexes.[6-8]

In all cases the M-N_6 bonds in [M(**L1**)$_2$] are shorter than the M-N_{6d} bonds calculated for the *di*anionic chelate unit. A similar trend is observed for the M-O_4 and M-O_{4d} bonds. These differences arise, in part, from the repulsion between the anionic oximate oxygen, O_{7d}, and neighbouring atoms; leading to an widening of the N_6-M-O_7 angle and an increase in the O_{4m}-O_{6d} contact distance. (Figure 3.28) This also appears to result in a compression of the bite angle in the *di*anionic chelate unit O_{4d}-M-N_{6d} compared with the *mono*anionic unit, O_4-M-N_6, in the neutral complex, [M(**L1**)$_2$].

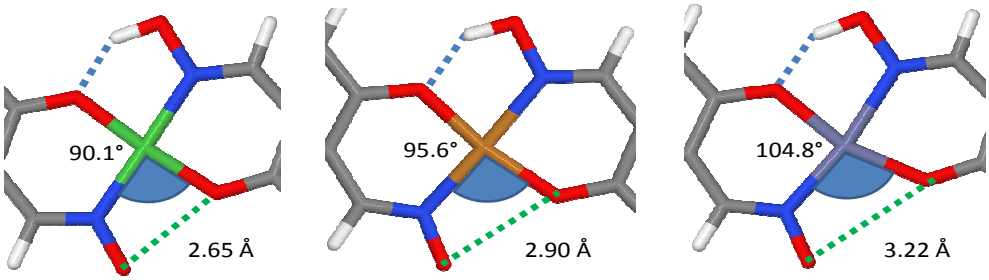

Figure 3.28: View of coordination for geometry optimised structures of [M(**L1**)(**L1**-H)]$^-$ complexes where M = (a) Ni, (b) Cu and (c) Zn. The O_{4m}-M-N_{6d} bond angles for the *di*anionic chelate are highlighted.

The distortion of the coordination geometry from a "square" plan in the neutral complexes [M(**L1**)$_2$] upon formation of the [M(**L1**)(**L1**-H)]$^-$ anions is much greater for the d^{10} cation, Zn(II), than for the d^8 cation, Ni(II).

When comparing the experimentally determined gas phase stabilities of the [M(**L1**)(**L1**-H)]$^-$ anions with the geometries of their energy minimised structures, it can be seen that the [Zn(**L1**)(**L1**-H)]$^-$ species has the lowest X_c value (25.42, see Figure 3.23 and Figure 3.26) and the largest distortion of the O_{4m}-M-N_{6d} bond angle.

This suggests that the nature of M influences the gas phase stability via the mode of fragmentation.

Ni(II), being d^8 and low spin, will form strictly square planar complexes with phenolic oximes, which is reflected in the square planar coordination geometries for both the [Ni(**L1**)$_2$] and the [Ni(**L1**)(**L1**-H)]$^-$ species. Loss of OH/H_2O should also not affect the coordination geometry of the nickel and would, therefore, not result in stable [Ni(**L1-H**)(**L1**-OH/H_2O)]$^-$ fragments. The first stable fragment is shown to be a result of cleavage of the coordinating bonds.

Cu(II), having 9 d-electrons, does form planar complexes with phenolic oximes, but can also form Jahn-Teller distorted octahedral complexes. This extra "flexibility" in coordination could be seen to allow the opening of the O_{4m}-M-N_{6d} angle and could also be responsible in facilitating the formation of the [Cu(**L1**-H)(**L1**-OH/H_2O)]$^-$ fragments and in turn affecting the X_c value.

Zn(II), being d^{10}, will generally form tetrahedral complexes in order to separate the donor set as much as possible. In the case of phenolic oximes a planar arrangement is observed as the energy gained due to the inter-ligand hydrogen bonding outweighs the energy lost due to donor set repulsion. Upon deprotonation the favourable energy is reduced as a hydrogen bond is removed, resulting in repulsion in the outer-coordination sphere and a large distortion of the O_{4m}-M-N_{6d} angle. The H_2O loss is the dominant fragmentation pathway probably due to the resultant [Zn(**L1**-H)(**L1**-OH_2)]$^-$ anion adopting a tetrahedral geometry, lowering its energy by separating the donor atoms.

3.3. Conclusions

The aims defined at the beginning of the chapter have largely been achieved.

An investigation of the dependence of the relative gas phase stabilities of the protonated copper(II) complexes, $[Cu(\mathbf{L})(\mathbf{L}+H)]^+$, on the nature of the 3-X-substituent in the ligand series **L1H** – **L7H** revealed the order of stability Br < Cl < H ≤ OMe < NO_2 ≤ Me < ^{t}Bu. As shown for the complex anions, $[Cu(\mathbf{L})(\mathbf{L}-H)]^-$, (see Chapter 2) the stability order for the $[Cu(\mathbf{L})(\mathbf{L}+H)]^+$ series differs from that for the neutral complexes, $[Cu(\mathbf{L})_2]$, as judged by extraction data.

A detailed CID fragment study of $[Cu(\mathbf{L4})(\mathbf{L4}+H)]^+$, similar to that described for $[Cu(\mathbf{L6})(\mathbf{L6}-H)]^-$ (X=Br) in Chapter 2, suggests that the dissociation is influenced by the H-bond accepting 3-nitro-substituent. The gas phase stability of the $[Cu(\mathbf{L4})(\mathbf{L4}+H)]^+$ cation, unlike in the anionic $[Cu(\mathbf{L})(\mathbf{L}-H)]^-$ series, is greater than that of the unsubstituted $[Cu(\mathbf{L1})(\mathbf{L1}+H)]^+$ analogue due to hiderence of H_2O loss.

Whilst this further emphises the difficulty of using mass spectrometry, which involves the use of *charged* species to predict the relative stability of related *neutral* complexes, the observed differences is gaseous ionic stability can still be rationalised by considering the effects of substituents on the inner- and outer-coordination spheres. In particular the effects the 3-X-substituents have on fragmentation pathways, e.g. on the elimination of H_2O or OH radicals, will directly influence the stability of ions in the gas phase.

Further studies in this chapter have lead to the following conclusions:

- the presence of a methyl substituent on the azomethine carbon of the ligands again affects the gas phase stability of the resultant $[Cu(\mathbf{L})(\mathbf{L}-H)]^-$ anionic complexes under CID conditions. This change in stability is, again, ascribed to the influence that substitution has on the fragmentation processes of the $[Cu(\mathbf{L})(\mathbf{L}-H)]^-$ anions. Substitution of the azomethine hydrogen atom of an

aldoxime ligand (**L1H** or **L8H)** with a methyl group, forming a ketoxime ligand (**L1bH** and **L8bH** respectively), hinders H_2O and OH radical loss. The removal of the fragmentation pathways requiring "lower" energies results in an increase in relative gas phase stability of the resultant $[Cu(\mathbf{L})(\mathbf{L}\text{-H})]^-$ anionic complex.

- when anions derived from mixed ligand complexes of the type $[Cu(\mathbf{LX})(\mathbf{LY})]$ are subjected to CID, their relative gas phase stability is the same as that observed for the least stable homoleptic complex anion ($[Cu(\mathbf{LX})(\mathbf{LX}\text{-H})]^-$ or $[Cu(\mathbf{LY})(\mathbf{LY}\text{-H})]^-$). This suggests that the stability of the anionic complex $[Cu(\mathbf{LX})(\mathbf{LY})\text{-H}]^-$ is determined by the fragmentations of the "least stable" chelate, i.e. that which has "lower energy" fragmentations (e.g. H_2O or OH radical loss in the case of aldoxime/ketoxime chelates) or that provides multiple fragmentation pathways (e.g. H_2O, OH radical, HBr or HOBr loss in the case of complex anions with **L6** chelates).

- that the nature of the metal, M, in $[M(\mathbf{L1})_2]$ complexes greatly influences the gas phase stabilities of the resultant monoanions, $[M(\mathbf{L1})(\mathbf{L1}\text{-H})]^-$. Here the nature of the metal affects *both* the inner- and outer coordination spheres of the $[M(\mathbf{L1})(\mathbf{L1}\text{-H})]^-$ anions *and* those of the resultant fragments upon CID. The stabilities of the resultant fragment ions in turn define the fragmentation mechanisms and, thus, the fragmentation threshold, *i.e.* the gas phase stability of the $[M(\mathbf{L1})(\mathbf{L1}\text{-H})]^-$ anion.

3.4. Experimental

3.4.1. Chemicals and Instrumentation

All solvents and reagents were used as received from Aldrich, Fisher, Fluorochem and Acros. ^{1}H and ^{13}C NMR were obtained using a Bruker av400 spectrometer at ambient temperature. Chemical shifts (δ) are reported in parts per million (ppm) relative to internal standards. Analytical data was obtained on a CE-440 Elemental Analyser by the University of St. Andrews Microanalytical Service.

Aldoxime ligands **L1H**-**L5H** were synthesised by R. S. Forgan[9] **L6H**-**L8H** were synthesized according to procedures given in Chapter 2 Section 2.4.2.

3.4.2. Ketoxime Synthesis

Ligands **L1B** and **L8B** were synthesized at CYTEC Ind. Blakeley, Manchester, UK according to the industrial protocol defined by CYTEC.

3.4.2.1. 5-*tert*-Butyl-2-hydroxyphenyl)ethanone oxime (**L1bH**)

4-*tert*-Butylphenol (135.2 g, 0.9 mol, 1.0 eq.) was dissolved in toluene (600 ml) and acetyl chloride (78.5 g, 1.0 mol, 1.1 eq.) was added dropwise. The resulting solution was refluxed for 4 hours and stirred overnight. Aluminium chloride (120.0 g, 0.9 mol, 1.0 eq.) was added portion-wise (48 portions) to the stirring solution of ester over 4 hours. The reaction mixture was then heated to reflux for 3 hours and stirred overnight at RT. The reaction was quenched with excess HCl (20%, 500 ml) which was added dropwise over 1h. The organic was separated from the aqueous, washed with distilled water (2 x 250 ml) and filtered using phase separation paper. The solvent was removed *in vacuo* yielding a viscous orange oil (190 g) 69% pure by GC. Hydroxylamine sulphate (221.5 g, 1.35 mol, 1.5 eq.) and sodium acetate (221.4

g, 2.7 mol, 3.0 eq.) was added to a solution of crude methylketone (230.2g, 0.9 mol, 1.0 eq) in ethanol (600 ml). The resulting suspension was refluxed for 2h, allowed to cool, and poured onto Toluene (500 ml) and distilled water (300 ml). The organic layer was separated, washed with distilled water (2 x 100 ml) and brine (100 ml) and filtered through phase separation paper. The solvent was removed *in vacuo* and the resulting orange solid was recrystallised from heptane yielding an off white powder (119.2 g, 0.57 mol, 69.9% yield). Crystals suitable for XRD analysis were grown by slow cooling and evaporation of a saturated hexane/diethyl ether solution (crystal structure analysis available in appendix). Anal. Calc. for $C_{12}H_{17}NO_2$: C, 69.54; H, 8.27; N, 6.76 % Found: C, 68.94; H, 8.57; N, 6.40 %; ν_{max}/cm^{-1} ($CHCl_3$) 3573 (free NOH), 3400br (H-bonded NOH), 3219br (PhOH), 2960 (C-H), 1620 (C=N); ^1H NMR (400 MHz, $CDCl_3$): δ_H (ppm) 1.32 (s, 9H, $C(CH_3)_3$), 2.41(s, 3H, $ArCNCH_3$), 6.95 (d, 1H, Ar*H*), 7.38 (dd, 1H, Ar*H*), 7.45 (d, 1H, Ar*H*); ^{13}C NMR (63 MHz, $CDCl_3$): δ_C (ppm) 10.84 (1C, $ArCN\mathbf{C}H_3$) 31.52 (3C, $C(\mathbf{C}H_3)_3$), 31.61, (1C, $\mathbf{C}(CH_3)_3$), 116.82 (1C, aromatic **C**), 117.72 (1C, aromatic **C**H), 124.07 (1C, aromatic **C**H), 128.09 (1C, aromatic **C**H), 141.75 (1C, aromatic **C**), 155.17 (1C, aromatic **C**); 159.86 (1C, Ar**C**HN).

3.4.2.2. 5-*tert*-Octyl-2-hydroxyphenyl)ethanone oxime (**L8bH**).

4-*tert*-octylphenol (206.3 g, 1 mol, 1.0 eq.) was dissolved in toluene (600 ml) and acetyl chloride (86.3 g, 1.1 mol, 1.1 eq.) was added dropwise. The resulting solution was refluxed for 4 hours and stirred overnight. Aluminium chloride (, 133.3 g, 1.0 mol 1.0 eq.) was added portion-wise (48 portions) to the stirring solution of ester over 4 hours. The reaction mixture was then heated to reflux for 3 hours and stirred overnight at RT. The reaction was quenched with excess HCl (20%, 500 ml) which was added dropwise over 1h. The organic was separated from the aqueous, washed with distilled water (2 x 250 ml) and filtered using phase separation paper. The solvent was removed *in vacuo* yielding a viscous yellow oil (230.2 g) 67% pure by GC. Hydroxylamine sulphate (221.5 g, 1.35 mol, 1.5 eq.) and sodium acetate (221.4 g, 2.7 mol, 3.0 eq.) was added to a solution of crude methoxyketone (230.2g, 0.9

mol, 1.0 eq) in ethanol (600 ml). The resulting suspension was refluxed for 2h, allowed to cool, and poured onto toluene (500 ml) and distilled water (300 ml). The organic layer was separated, washed with distilled water (2 x 100 ml) and brine (100 ml) and filtered through phase separation paper. The solvent was removed *in vacuo* and the resulting yellow solid was purified via complexation with copper. The complex was washed with methanol (2 x 100 ml) and the resulting dark brown crystals were dissolved in toluene (500 ml). The complex solution was stripped using sulphuric acid solution (0.1 Molar, 3 x 200 ml), washed with distilled water (200 ml) and filtered through phase separation paper. The solvent was removed in vacuo and the resulting off-yellow solid was recrystallised from hexane yielding an off white solid (135.2 g, 0.51 mol, 51.3% yield). Crystals suitable for XRD analysis were grown by slow cooling and evaporation of a saturated diethyl ether solution (crystal structure analysis available in appendix). (Anal. Calc. for $C_{16}H_{25}NO_2$: C, 72.96; H, 9.57; N, 5.32 % Found: C, 73.01; H, 10.06; N, 5.49 %; ν_{max}/cm^{-1} ($CHCl_3$) 3570 (free NOH), 3390br (H-bonded NOH), 3219br (PhOH), 2947 (C-H), 1602 (C=N); ^1H NMR (400 MHz, $CDCl_3$): δ_H (ppm) 0.75 (s, 9H, $C(CH_3)_3$), 1.39 (s, 6H, $C(CH_3)_2$), 1.76 (s, 2H, CH_2), 2.41 (s, 3H,$ArCNCH_3$) 6.93 (dd, 1H, Ar*H*), 7.31 (dd, 1H, Ar*H*), 7.42 (d, 1H, Ar*H*),11.10 (s, 1H, O*H*), 11.30 (s, 1H, O*H*); ^{13}C NMR (400 MHz, $CDCl_3$): δ_C (ppm) 10.90 (1C, $ArCN(\mathbf{C}H_3)$), 31.68 (2C, $C(\mathbf{C}H_3)_2$), 31.84 (2C, $C(\mathbf{C}H_3)_3$), 32.36 (1C, $\mathbf{C}(CH_3)_3$) 38.02, (1C, $\mathbf{C}(CH_3)_2$), 56.96 (1C, $\mathbf{C}H_2$), 116.57 (1C, aromatic **C**), 117.50 (1C, aromatic **C**H), 124.94 (1C, aromatic **C**H), 128.97 (1C, aromatic **C**H), 140.52 (1C, aromatic **C**), 155.14 (1C, $Ar\mathbf{C}N(CH_3)$), 155.1 (1C, aromatic **C**);

3.4.3. $[M(L)_2]$ complex synthesis

All copper(II) complexes of the ketoxime ligands were synthesised using the following general procedure. Stoichiometric amounts of the ligand and copper acetate (0.5 equivalents) were mixed in methanol (50 ml) for 24 h. Colour changes due to complex formation occurred immediately, along with precipitation. Complexes were isolated by filtration and dried under vacuum.

3.4.3.1. [Cu(**L1b**)$_2$]

$Cu(OAc)_2.H_2O$ (0.100 g, 0.50 mmol) and **L1bH** (0.210 g, 1.01 mmol) yielded a brown solid (0.401 g, 84%). (Anal. Calc. for $C_{24}H_{32}CuN_2O_4$: C, 60.55; H, 6.78; N, 5.88%. Found: C, 60.48; H, 6.73; N, 5.97%; ν_{max}/cm^{-1} ($CHCl_3$) 3167br (NOH), 2964 (C-H), 1609 (C=N); ESIMS: m/z 822.02

3.4.3.2. [Cu(**L8b**)$_2$]

$Cu(OAc)_2.H_2O$ (0.100 g, 0.50 mmol) and **L8bH** (0.260 g, 1.00 mmol) yielded a brown solid (0.514 g, 87%). Crystals suitable for X-ray diffraction analysis were grown by slow evaporation of a hexane/DCM solution. (for crystal structure and interpretation see Chapter 4) Anal. Calc. for $C_{32}H_{48}CuN_2O_4$ C, 65.33; H, 8.22; N, 4.76%. Found: C, 64.93; H, 8.30; N, 4.89%; ν_{max}/cm^{-1} ($CHCl_3$) 3175br (NOH), 2959 (C-H), 1606 (C=N); ESIMS: m/z 990.01

The [Ni(**L1**)$_2$] and [Zn(**L1**)$_2$] complexes were synthesised *in situ* by mixing 2 equivalents of **L1H** with the corresponding acetate salt.

3.4.3.3. [Ni(**L1**)$_2$]

$Ni(OAc)_2.4H_2O$ (0.125 g, 0.50 mmol) and **L1H** (0.193 g, 1.00 mmol) were mixed in MeCN (20 ml) and the resultant solution was diluted accordingly for CID analysis.

3.4.3.4. [Zn(**L1**)$_2$]

$Zn(OAc)_2.2H_2O$ (0.105 g, 0.50 mmol) and **L1H** (0.193 g, 1.00 mmol) were mixed in MeCN (20 ml) and the resultant solution was diluted accordingly for CID analysis.

3.4.4. X-Ray Structure Determinations

All crystal structures were solved by Fraser White or Simon Patterson at the University of Edinburgh Crystallography Service. The appropriate .cif files for **L1bH** and **L8bH**, along with figures and discussion are located in appendix 8.3.3.

3.4.5. General procedure for sample preparation.

All samples were prepared using LCMS analytical grade acetonitrile. Stock solutions of each ligand, **LH,** and metal acetate (Aldrich) or of the [Cu(**L**)$_2$] complex were prepared (10 mM in acetonitrile) and diluted to the required concentrations. Unless otherwise stated the concentrations used in each study was dependent on the copper concentration which was maintained at 80 μM, determined *via* weight of Copper(II) acetate used.

3.4.6. Machine settings for CID analysis.

CID analysis was carried out on a thermo-fisher LCQ double octapole ion trap mass spectrometer. Detailed machine settings and calibration information as well as data extrapolation and manipulation for both positive and negative mode experiments can be found in appendix 8.2.3. The general operating procedure is described in Chapter 2 Section 2.4.4 unless stated otherwise.

3.4.6.1. Machine settings for high resolution CID analysis.

High resolution CID analysis was carried out on a Waters micromass Q-ToF mass spectrometer coupled with an autosampler. Detailed machine settings used along with calibration information for both positive and negative mode experiments can be found in appendix 8.2.3. Unless otherwise stated the general operating conditions for each CID experiment carried out in this chapter are given in Chapter 2 Section 2.4.4.

3.5. References

(1) Kordosky, G. A.; MacKay, K. D.; Sudderth, R. B.; Sierakoski, J. M.; (Henkel Corp., USA). European Patent, 1983, p 62 pp.

(2) Szymanowski, J. *Hydroxyoximes and Copper Hydrometallurgy*; CRC Press: Boca Raton, USA, 1993.

(3) Szymanowski, J. *Crit. Rev. Anal. Chem.* **1995**, *25*, 143.

(4) Lide, D. R. *Handbook of Chemistry and Physics* 88th ed. ed.; CRC Press taylor and francis, 2007.

(5) Smith, A. G.; Tasker, P. A.; White, D. J. *Coord. Chem. Rev.* **2003**, *241*, 61.

(6) White, F. J., PhD Thesis, University of Edinburgh, 2008.

(7) Davidson, J. E., PhD Thesis, University of Edinburgh, 2005.

(8) Parkin, A., PhD Thesis, University of Edinburgh, 2002.

(9) Forgan, R. S., PhD Thesis, University of Edinburgh, 2008.

Chapter 4:
A DFT investigation into the Strength and Selectivity of Metal Extractants

A theoretical study of the strength and selectivity of substituted phenolic oximes and hydrazones.

Table of Contents

4.1. Introduction

4.1.1. Aims

The research in Chapters 2 and 3 used mass spectrometry to assess whether the gas phase stability of ions derived from copper complexes of substituted phenolic oxime ligands could give an insight into the strength and selectivity of the ligands as copper extractants. It was concluded in Chapter 3 that looking at ionic complexes in the gas phase made direct comparisons with solution based extraction processes, involving neutral complexes, difficult. In this chapter density functional (DFT) theory will be used as a theoretical approach to understanding the relationship between structure and extraction strength. The chapter is split into two sections; the first section uses DFT to investigate the 3-X- and 5-R-substituted phenolic aldoximes and ketoximes, **LH**, their ligands dimers, [(**LH**)$_2$], and their copper(II) complexes, [Cu(**L**)$_2$]. In the second section the ligand series is extended to include 3-X-substituted hydrazones (Figure 4.1) and investigates the relationship between structure and extraction strength.

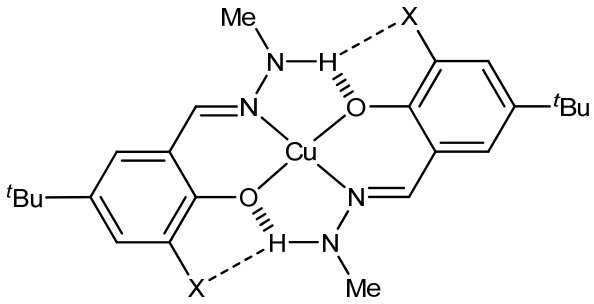

Figure 4.1: [Cu(**L**)$_2$], X = H, NO_2, Br and OMe

This Chapter deals with:

- Free ligand structure and dimerisation energies and the relation of the latter to extraction strength.

- The calculation of "deprotonation" energies relating these to the pKa of substituted ligands.
- An investigation into the electronic effects of substitution on structure of $[M(\mathbf{L})_2]$ complexes, in which close attention is paid to the effects of substitution on bond lengths and bonding energies.
- The calculation of the energies of $[M(\mathbf{L})_2]$ complex formation in the gas phase relating these values to both the strengths of the extractants **LH** and their selectivity for copper over other divalent transition metals.

4.2. Results and Discussion for 3-X-Substituted phenolic oximes and their copper(II) complexes

4.2.1. DFT calculations for 3-X-substituted phenolic oximes

Forgan *et. al.* have previously shown that 3-X-substituents greatly influence the extractant strength of phenolic oxime ligands for copper.[1,2] The influence in strength was thought to be due to H-bonding interactions in the outer coordination sphere of the [Cu(**L**)$_2$] complexes.[3] (see also Chapter 1 Section 1.5.3) Previous work described in this thesis (see for example Chapter 2 Section 2.2.4) show that the 3-X-substituents also influence the gas phase stability under collision induced dissociation conditions of the mono-anionic species', [Cu(**L**)(**L**-H)]$^-$.

DFT calculations were carried out on four of the 3-X-substituted phenolic oximes, **L1H**, **L5H**, **L6H** and **L7H** to determine whether the intramolecular hydrogen bonding occurs between the phenolic hydrogen and the oximic nitrogen atoms observed in the solid state structures as determined by XRD crystallography[3] is also present in the energy-minimised gas phase structures. Full geometry optimisations were performed using B3LYP[2-4]/6-31+G[5-14](d,p) and the resultant structures are shown in Figure 4.2.

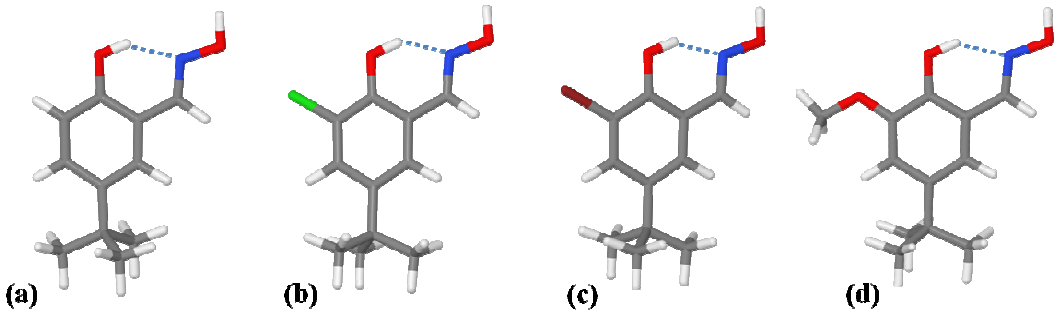

Figure 4.2: Energy minimised structures of the 3-X-substituted phenolic oximes (a) **L1H**, (b) **L5H**, (c) **L6H** and (d) **L7H** (X = H, Cl, Br and OMe respectively), with the hydrogen bonds between phenolic proton and oximic nitrogen marked in each case.

As observed in the solid state[3] the gas phase calculations confirmed the hydrogen bonding interaction between the phenolic hydrogen and the oximic nitrogen in each of the cases.

4.2.1.1. Deprotonation energies (ΔH_{depro}) for 3-X-substituted phenolic oximes

As described in Chapter 1, the acidity of salicylaldoximes has an important impact on their extractive efficacy with the more acidic ligands found to be stronger extractants.[3-5] The gas phase DFT calculations allow the calculation of deprotonation energies (ΔH°_{depro}) as described in Equations **4.4** and **4.5**.

$$LH \xrightarrow{\Delta H^{\circ}_{depro}} L^{-} + H^{+} \qquad \textbf{4.1}$$

Using Equation **4.2** and with H^+ having no electrons $(E_0 + H_{corr})_{H^+} = 0$, therefore:

$$\Delta H^{\circ}_{depro} = (E_0 + H_{corr})_{L^-} - (E_0 + H_{corr})_{LH} \qquad \textbf{4.2}$$

where E_0 is the minimised energy and H_{corr} is the thermal correction.

Full geometry optimisations were performed using B3LYP[2-4]/6-31+G[5-14](d,p). The ΔH°_{depro} values were calculated using equation **4.5** are given in Table 4.1.

Table 4.1: DFT energies for **LH** and $\mathbf{L}^-$ for **L1H**, **L5H**, **L6H** and **L7H** with calculated deprotonation enthalpies, ΔH°_{depro}. Calculated ligand pK_a values[3] and experimentally determined $pH_{0.5}$ values[2] are also given.

LH (X)	**L1H** (H)	**L5H** (Cl)	**L6H** (Br)	**L7H** (OMe)
$(E_0 + H_{corr})_{LH}$/au	-633.1518	-1092.7513	-3204.2859	-747.6399
$(E_0 + H_{corr})_{L}$-/au	-632.5989	-1092.2091	-3203.7444	-747.0864
ΔH°_{depro}/kJ mol^{-1}	1452.3	1423.6	1421.8	1453.2
ΔH°_{depro}/kJ mol^{-1} relative to **L1H**	0	-28.7	-30.5	0.9
Calculated pK_a of **LH**[3]	9.32 ± 0.48	7.84 ± 0.50	7.77 ± 0.50	9.31 ± 0.50
Calculated pK_a of **LH**[3] *cf.* **L1H**	0 ± 0.48	-1.48 ± 0.50	-1.55 ± 0.50	-0.01 ± 0.50
$pH_{0.5}$ **LH**[2]	1.68	0.91	0.42	1.09

The ΔH_{depro} values for the stronger extractants **L5H** (1421.8 kJ mol^{-1}) and **L6H** (1423.6 kJ mol^{-1}) are lower than those for **L1H** (1452.3 kJ mol^{-1}) and **L7H** (1453.2 kJ mol^{-1}) which is consistent with the acidity of the phenol as judged by the pK_a values (equation **4.6**) calculated by Daniel Tackley at Intertek ASG on behalf of Cytec Industries UK Ltd, using ACD/Labs pK_a predictor v10.01.

$$\boldsymbol{LH \rightleftharpoons L^- + H^+} \qquad \boldsymbol{K_a = \frac{[L^-][H^+]}{[LH]}} \qquad \textbf{4.3}$$

Whilst the ΔH°_{depro} values and pK_a values, see below) for **L1H**, **L5H** and **L6H** correlate well with the observed strengths as Cu-extractants ($pH_{0.5}$ values are given in Table 4.1 the values for the methoxy substituted ligand (**L7H**) do not. This is a stronger extractant than the unsubstituted ligand ($pH_{0.5}$ 1.09 *cf.* 1.68) and it is possible that this arises from favourable buttressing of the inter molecular hydrogen bond between the oximic OH group and the phenolic oxygen atom by the methoxy

group. The importance of interligand association should be revealed by a comparison of dimerisation enthalpies and is considered below.

4.2.1.2. Dimerisation enthalpies (ΔH_{dimer}) for 3-X-Substituted phenolic oximes

As described in Chapter 1, the phenolic oximes readily dimerise in non-polar media and the dimerisation ability has been assumed to contribute to their extraction efficacies. Energy minimization of the dimeric assembly leads to very nearly planar structures. (Figure 4.3)

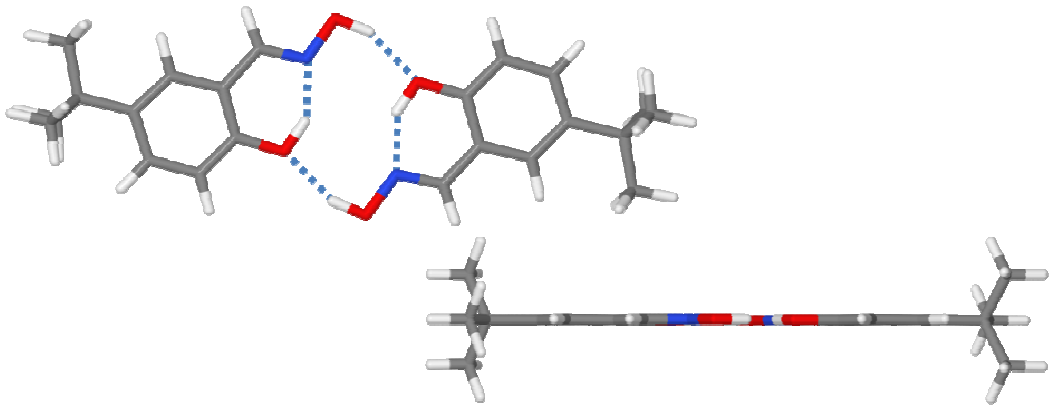

Figure 4.3: An energy minimised structure for **L1H** dimer with intra- and inter-molecular hydrogen bonding highlighted (blue) and, below a side view showing the planarity of $(\mathbf{L1H})_2$ unit.

The dimerisation enthalpy (ΔH°_{dimer}), defined in equation **4.7** was calculated using equation **4.8**,

$$\mathbf{2LH} \xrightarrow{\Delta H_{dimer}} \mathbf{[LH]_2} \qquad \mathbf{4.4}$$

$$\Delta \boldsymbol{H}^{\circ}_{\boldsymbol{dimer}} = (\boldsymbol{E_0} + \boldsymbol{H_{corr}})_{[LH]_2} - \mathbf{2}(\boldsymbol{E_0} + \boldsymbol{H_{corr}})_{\boldsymbol{LH}} \qquad \mathbf{4.5}$$

i.e. ΔH°_{dimer} is equal to the calculated energy of the ligand dimer, $E_{[LH]_2}$ minus twice the energy of the monomer E_{LH}. Full geometry optimisation of the ligand dimers was performed using B3LYP[2-4]/6-31+G[5-14](d,p) and the counterpoise correction was used

to estimate basis set superposition errors (BSSE). The minimised energy for the ligands, $(E_0)_{\boldsymbol{LH}}$, the ligand dimers, $(E_0)_{[\boldsymbol{LH}]_2}$, with thermal corrections and the ΔH°_{dimer} values for each ligand can be found in Table 4.2. The BSSE uncorrected dimerisation enthalpies are also given for comparison.

Table 4.2: Minimised energies, $\boldsymbol{E_0}$, for the ligand dimers, for **L1H**, **L5H**, **L6H** and **L7H,** calculated dimerisation enthalpies, $\Delta \boldsymbol{H^{\circ}_{dimer}}$ and $\Delta \boldsymbol{H^{\circ}_{dimer}}$ values relative to **L1H.**

LH (X)	**L1H** (H)	**L5H** (Cl)	**L6H** (Br)	**L7H** (OMe)
$2(E_0+H_{corr})_{\boldsymbol{LH}}$/au	-1266.3037	-2185.5025	-6408.5719	-1495.2799
$(E_0 + H_{corr})_{[\boldsymbol{LH}]_2}$/au	-1266.3192	-2185.5189	-6408.5900	-1495.2981
$[(E_0 + H_{corr})_{[\boldsymbol{LH}]_2}]_{BSSE}$/au	-1266.3190	-2185.5189	-6408.5878	-1495.2981
ΔH°_{dimer}/kJ mol^{-1}	-40.6	-43.1	-47.4	-47.9
$[\Delta H^{\circ}_{dimer}]_{BSSE}$/au	-40.1	-43.0	-46.9	-47.8
ΔH°_{dimer} *cf.* **L1H**/kJ mol^{-1}	0	-2.9	-6.8	-7.7

Dimerisation is favourable in all cases and becomes more exothermic in the order **L1H** (H) < **L5H** (Cl) < **L6H** (Br) < **L7H** (OMe). The energy minimised structure for (**L7H**)$_2$ is shown in Figure 4.4. The BSSE correction applied made little difference to the dimerisation enthalpy for **L5H** and **L7H** (<0.1 kJ mol^{-1} in both cases) and only a slight change to those for **L1H** and **L6H** (<0.5 kJ mol^{-1} in both cases).

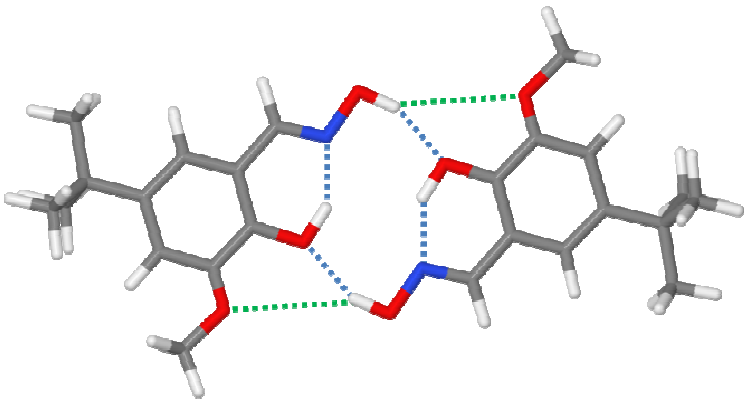

Figure 4.4: Energy minimised structure for **L7H** dimer with hydrogen bond buttressing indicated between oximic proton and methoxy oxygen (green) H···O.

4.2.2. Computational Studies on 3-X-substituted copper (II) complexes.

DFT was used to investigate the gas phase structures of the 3-X-substituted copper complexes [Cu(L)$_2$] where **L = L1-L7**, **L9-L12** in order to understand how the nature of the X-group influences the structure and bonding in the copper complexes in the gas phase. The 3-X-substituent has been shown to influence the strength of ligands as copper extractants (see Chapters 1-3) and also affects on the structure, acidity, and hydrogen bonding of the ligands and ligand dimers, (Sections 4.2.1.1. And 4.2.1.2). Calculations were carried out to understand the effects the nature of X has on both the *inner-sphere* coordination sphere of the copper complexes and the *outer-sphere* hydrogen bonding interactions.

4.2.2.1. Preliminary DFT calculations on copper(II) complexes of the 3-X-substituted phenolic oximes, L1H-L7H

Full structural optimizations were undertaken using B3LYP[2-4]/6-31G[5-14] for each of the [Cu(**L**)$_2$] complexes (**L1H**-**L7H**) and frequency calculations were carried out on all optimized structures to verify their nature. Bond lengths and angles in both the *inner*- and *outer*-coordination sphere of the complexes are listed in Table 4.3 using the atom numbering scheme shown in Figure 4.5. Variations of these structural parameters are also compared with the $pH_{0.5}$ values of the ligands in Table 4.3.

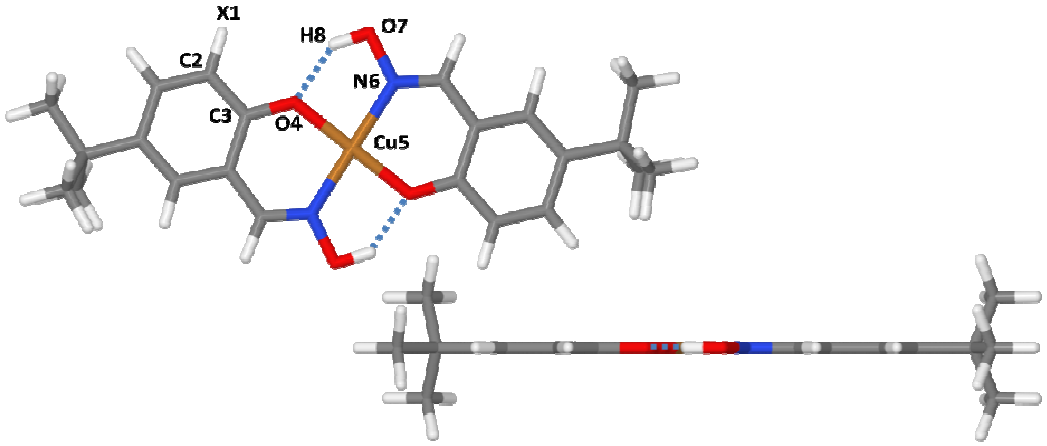

Figure 4.5: The calculated structure of [Cu(**L1**)$_2$] showing the atom numbering used in comparisons of inner- and outer-sphere coordination geometry.

The numbering scheme in Figure 4.5 is used for the majority of the Tables in this section with the 3-X-substituent in L1H etc. termed "X1" etc.

Table 4.3: Bond distances/Å and angles/° for energy minimised structures of copper(II) complexes [Cu(**L**)$_2$] complexes for ligands **L1H-L7H** using the B3LYP/6-31G level of theory. Atom labels are defined in Figure 4.5.

L (X)	**L1** (H)	**L2** (Me)	**L3** (^{t}Bu)	**L4** (NO_2)	**L5** (Cl)	**L6** (Br)	**L7** (OMe)
O4-Cu5/Å	1.9070	1.9069	1.9281	1.8855	1.9243	1.9097	1.8891
N6-Cu5/Å	1.9301	1.9276	1.9138	1.9374	1.9264	1.9297	1.9323
X1-C2/Å	1.0844	1.5085	1.5474	1.4539	1.8488	1.9688	1.3924
O4-H8/Å	**1.7140**	**1.7172**	**1.7446**	**1.8743**	**1.7419**	**1.7528**	**1.7325**
N6-O7-H8/°	101.37	101.28	101.35	105.93	101.60	102.14	102.36
Cu5-N6-O7/°	116.56	116.58	116.93	119.13	117.48	117.68	116.99
Cavity radius[a]	1.9186	1.9173	1.9210	1.9115	1.9254	1.9197	1.9107
$pH_{0.5}$ of **LH**	**1.68**	**1.67**	**2.64**	**0.70**	**0.91**	**0.42**	**1.09**

[a] Cavity radius is the mean distance of N and O donors from their centroid. Whilst no symmetry was imposed during energy minimisation, the central copper atom lies very close to the centroid and, thus, the cavity radius is taken as the mean of the Cu-O and Cu-N bond lengths.

The variations in cavity radius across the series of complexes are quite small but there are some significant variations in the *relative* lengths of the Cu-O and Cu-N bond lengths. In contrast to the other complexes, the Cu-O bond is longer than the Cu-N bond in the complex of **L3H**, which has a bulky *t*-butyl substituted in the 3-position. Outer coordination sphere interactions, and particularly hydrogen-bond buttressing, appear to influence structure of the [Cu(**L**)$_2$]. For the [Cu(**L**)$_2$] complexes show a hydrogen bond buttressing interaction via the atom directly bonded in the 3 position (see (a) in Figure 4.6) there is a strong correlation between extractant strength and the O4···H8 contact distance. Formation of the bifurcated hydrogen bond and the associated stabilisation of the copper complex involves the X atom "pulling" the oximic hydrogen atom away from the phenolate oxygen atom, lengthening the O4···H8 contact distance. Formation of a six-membered ring to achieve this bifurcation (see (b) in Figure 4.6) exacerbates this effect.

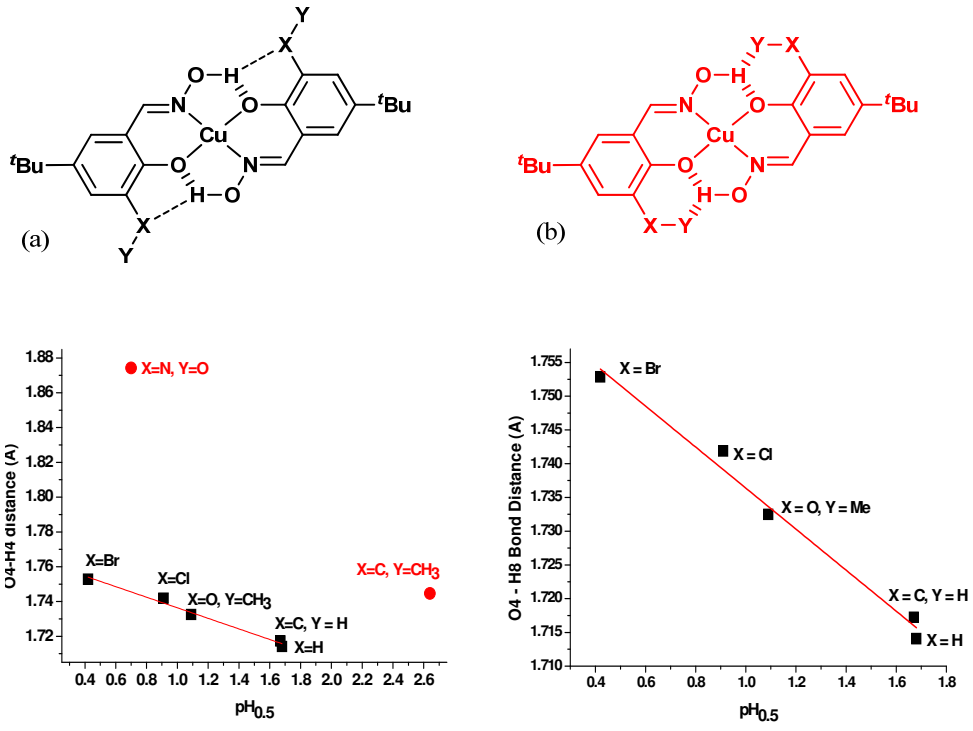

Figure 4.6: O4···H8 contact distances in the energy minimised structures of [Cu(**L**)$_2$] complexes plotted against the $pH_{0.5}$ value of the ligand **LH.**

When X is a single atom hydrogen bond acceptor and a five membered ring is formed as in (a) in Figure 4.6 there is some correlation between the C2-X1 bond length and extraction strength (see (a) Figure 4.7). This suggests that the efficiency of the buttressing interaction relates to the size of the X atom (and its van der Waals radius, see (b) Figure 4.7)

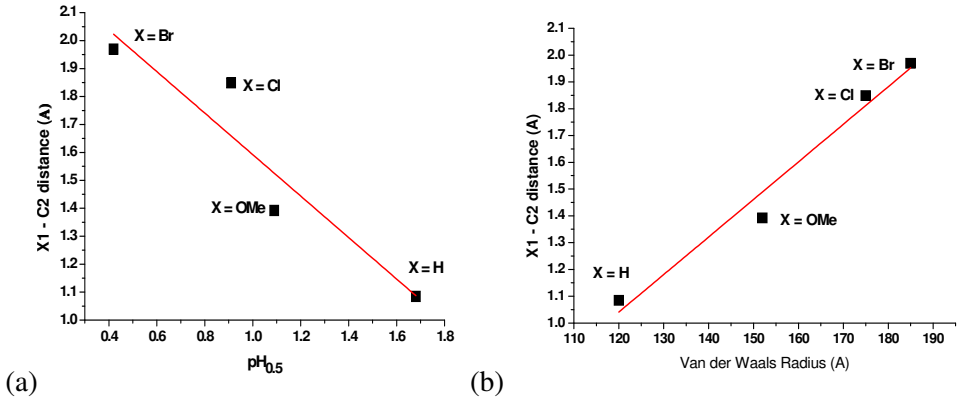

(a) (b)

Figure 4.7: X1-C2 bond distances in energy minimised structures of [Cu(**L**)$_2$] complexes against (a) the $pH_{0.5}$ value of the **LH** ligand and (b) the Van der Waals radii of the X substituents.

4.2.2.2. Geometries of 3-X-substituted phenolic oxime copper complexes calculated using B3LYP/6-31+G(d,p)

The preliminary calculations described above reveal that buttressing effects are fundamentally different when the substituent in the 3-position generates a six-membered bifurcated hydrogen bonded unit, as in the copper(II) complex formed by the nitro-substituted ligand (**L4H**). In order to probe the factors which contribute to buttressing in systems forming five-membered bifurcated units, calculated structures of complexes of the chloro, bromo and methoxy substituted ligands, [Cu(**L5**)$_2$], [Cu(**L6**)$_2$], and [Cu(**L7**)$_2$], were compared with that [Cu(**L1**)$_2$], of the unsubstituted ligand using a higher level of theory, B3LYP[2-4]/6-31+G[5-14](d,p) (see below).

Table 4.4: Bond distances and angles for geometry optimised structures of 3-X-substituted [Cu(**L**)$_2$] complexes where **L** = **L1**, **L7**, **L5** and **L6** using B3LYP/6-31+G(d,p) level of theory.

LH (*X*)	**L1** (*H*)	**L5** (*Cl*)	**L6** (*Br*)	**L7** (*OMe*)
Cu5-O4/Å	1.9168	1.9070	1.8994	1.9001
Cu5-N6/Å	1.9645	1.9666	1.9704	1.9658
O4-H8/Å	1.7787	1.8165	1.8230	1.7931
X1-H8/Å	2.9898	2.9364	2.9012	2.8015
N6-O7-H8/°	101.8047	102.8921	103.0911	102.5255
Cu5-N6-O7/°	117.5985	118.2661	118.4136	117.9278
O4-Cu5-N6/°	88.0498	88.1077	87.9743	87.8682
Cavity size/Å^2	11.8300	11.7819	11.7576	11.7345
Cavity size *cf.* [Cu(**L1**)$_2$]/Å^2	0	-0.048	-0.072	-0.095

The bond lengths of the inner coordination sphere, *i.e.* the Cu5-N6 and Cu5-O4 bonds, depend on the nature of X. A good correlation is seen between the lengths of the Cu5-N6 bonds and the $pH_{0.5}$ of the ligand **LH**, and the stronger extractants **L5H**, **L6H** and **L7H** all form complexes with calculated cavities smaller than that for **L1H** (X=H). The cavity size for [Cu(**L7**)$_2$] is, however, smaller that of the complexes of the stronger extractants **L5H** and **L6H.**

In the outer coordination sphere, the O4···H8 contact distance is shorter in the [Cu(**L**)$_2$] complexes of the stronger ligand, **LH**. This in turn causes the H8-O7-N6 and Cu5-N6-O7 angles and the Cu5-N6 bond lengths in the [Cu(**L**)$_2$] complexes to increase. (Figure 4.8)

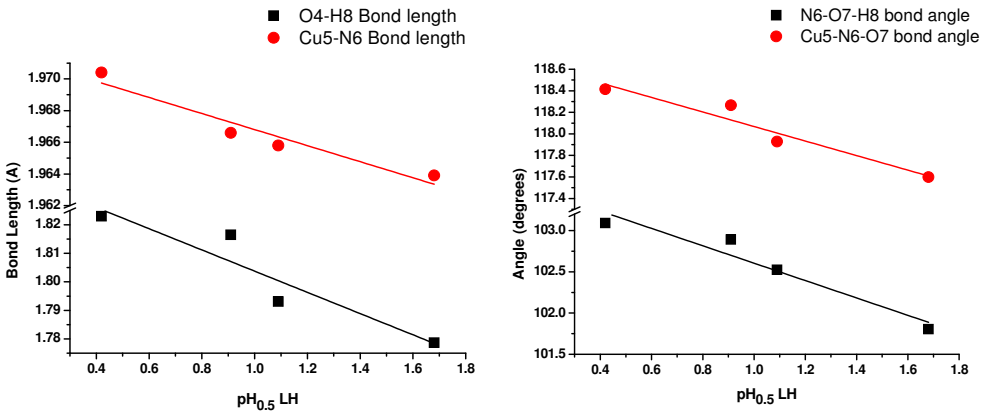

Figure 4.8: The O4···H8 contact and the Cu5-N6 bond distances and (right) the N6-O7-H8 and Cu5-N6-O7 bond angles of energy minimised structures of [Cu(**L**)$_2$] complexes plotted against the pH$_{0.5}$ value of **LH**.

4.2.2.3. Natural bond orbital interpretation for 3-X substituted phenolic oxime copper complexes

Weinhold's natural bond orbital (NBO) method [15-17] was used to compare the strength and nature of bonding interactions for the inner- and outer-coordination sphere and to explore the atomic charge distribution in each of the complexes. Table 4.5 shows the individual bonding energies (in kJ mol^{-1}) for the geometry optimised structures of 3-X-substituted [Cu(**L**)$_2$] complexes where L = **L1**, **L5**, **L6** and **L7**.

Table 4.5: Individual bonding energies for geometry optimised structures of 3-X-substituted [Cu(**L**)$_2$] complexes where X = H, OMe, Cl and Br using B3LYP/6-31+G(d,p) level of theory.

LH (*X*)	**L1 (*H*)**	**L5 (*Cl*)**	**L6 (*Br*)**	**L7 (*OMe*)**
O4-Cu5/kJ mol^{-1}	209.6	218.2	220.2	223.3
N6–Cu5/kJ mol^{-1}	198.2	196.9	195.2	193.0
$\Sigma_{O4\text{-}Cu5,\ N6\text{-}Cu5}$/kJ mol^{-1})	407.8	415.1	415.4	416.3
O4···H8/kJ mol^{-1}	48.2*	32.0	33.9	32.7
X1···H8/kJ mol^{-1}	**0**	2.7	5.1	0.9
$\Sigma_{O4\cdots H8,\ X1\cdots H8}$/kJ mol^{-1}	48.2*	34.7	39.0	33.5
pH$_{0.5}$ **LH**	1.68	0.91	0.42	1.09

*H8 described as separate unit in NBO calculation for Cu(**L1**)$_2$ (see appendix)

The oximic N-Cu and phenolic O-Cu bonding energies show no correlation with ligand extraction strength or with the electronic inductive properties of the X-substituent. We see a correlation between the $pH_{0.5}$ of the ligands and the X-substituent···oximic proton interaction energies in the complexes, where H < OMe < Cl < Br. Comparison of the NBO energies for [Cu(**L1**)$_2$] is difficult as the oximic H is described as a separate unit and not as part of the ligand this in turn alters the way the energies involved in bonding are described. The sums of the O4···H8 and X1···H8 energies for [Cu(**L7**)$_2$] (33.5 kJ mol^{-1}), [Cu(**L5**)$_2$] (34.7 kJ mol^{-1}), [Cu(**L6**)$_2$] (39.0 kJ mol^{-1}) correlate well with $pH_{0.5}$ of the corresponding ligands, giving weight to the argument that bifurcation of the oximic OH results in increased extraction strength.

The NBO calculation can also be used to look at the charge density. In the case for the [Cu(**L**)$_2$] complexes, the charge densities are determined for the copper atom and for each chelate unit, **L**, and are given in Table 4.6.

Table 4.6: Charge densities for Cu and **L** taken from geometry optimised structures of 3-X-substituted [Cu(**L**)$_2$] complexes where X = H, OMe, Cl and Br using B3LYP/6-31+G(d,p).

[Cu(L)$_2$] (X)	**L1 (H)**	**L5 (Cl)**	**L6 (Br)**	**L7 (OMe)**
Charge density on **L** (average)	-0.3571	-0.3577	-0.3580	-0.3563
Charge density on **L** *cf.* to **L1**	0	-0.0006	-0.0009	0.0008
Charge density on **Cu**	0.2142	0.2155	0.2160	0.2126
Charge density on **Cu** *cf.* to **L1**	0	0.0013	0.0018	-0.0016

There is no correlation between the charge densities on the copper atoms in the [Cu(**L**)$_2$] complexes and the $pH_{0.5}$ of the **LH** ligands. As might be expected when the X-substituent is electron donating (OMe), the positive charge density on the copper decreases and the average negative charge density on the chelate, **L**, increases. Conversely, when the X-substituent is an electron withdrawing substituent (Cl or Br) the charge density on the copper increases and that on the ligand decreases.

The calculated structural and electronic information for the copper complexes [Cu(**L1**)$_2$], [Cu(**L5**)$_2$] and [Cu(**L6**)$_2$] corresponds well with the pre-existing theory[3] of extractant modification, that the acidity of the phenol is more important than the basicity of the phenolate in determining extraction strength.

4.2.3. Homoleptic and heteroleptic [Cu(L)$_2$] complexes with aldoxime and ketoxime ligands

As described in Chapters 1, 3 and 4, ketoxime ligands of the type shown in Figure 4.9, where R = Me, have been shown to be weaker extractants than the aldoxime analogues, where R = H. In this section the effect of the R group on extraction strength is investigated by looking at both the homoleptic and heteroleptic complexes of copper with aldoxime **L1H** and ketoxime **L1bH** using DFT calculations.

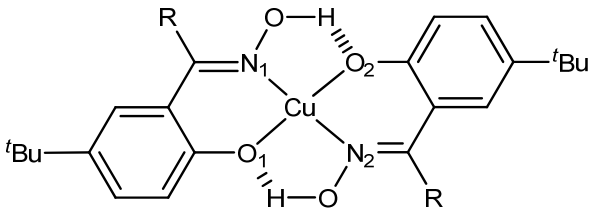

Figure 4.9: Structure of [Cu(**L1b**)$_2$], R = Me. Labelling scheme shown for bond lengths and angles shown in Table 4.7.

Full structural optimizations were done with B3LYP[2-4]/6-31+G[5-14] for [Cu(**L1**)$_2$], [Cu(**L1**)(**L1b**)], and [Cu(**L1b**)$_2$]. Bond lengths and angles of both the *inner*- and *outer*-coordination sphere were measured and are listed in table along with calculated cavity sizes (calculated as above). X-ray determined structural information for [Cu(**L8**)$_2$], a 5-tert-octyl analogue copper complex of [Cu(**L1**)$_2$] is also presented in Table 4.7.

Table 4.7: Bond lengths/Å and angles/° for the energy minimised structures of [Cu(**L1**)$_2$], [Cu(**L1**)(**L1b**)] and [Cu(**L1b**)$_2$] compared with single crystal X-ray diffraction data for two polymorphs of [Cu(**L8b**)$_2$] and [Cu(**L0**)$_2$].

[Cu(**L**)$_2$]	[Cu(**L1**)$_2$]	[Cu(**L1**)(**L1b**)]	[Cu(**L1b**)$_2$]	[Cu(**L8b**)$_2$]*		[Cu(**L0**)$_2$]
Cu-O distance/Å	1.9168	1.9052	1.8930	1.867(1)[a]	1.885(1)[b]	1.902(7)
Cu-N distance/Å	1.9646	1.9742	1.9846	1.961(2)[a]	1.955(2)[b]	1.964(7)
H···O$_1$ distance/Å	1.7786	1.7380	1.6978	1.85(3)[a]	1.88(1)[b]	1.92(1)
N$_1$-Cu-O$_1$/	88.032	88.516	88.955	88.97(7)[a]	88.68(7)[b]	88.8(3)
N$_1$-Cu-O$_2$/°	91.968	91.484	91.045	91.03(7)[a]	91.32(7)[b]	91.2(3)
Cavity/Å^2	11.830	11.816	11.802	11.502(13)[a]	11.577(13)[b]	11.736(3)
Cavity *cf.* [Cu(**L**)$_2$]/Å^2	0	-0.0136	-0.0275	-0.3[a]	-0.25[b]	-0.094
pH$_{0.5}$ **LH**	1.68	1.83*	2.07*‡	-	-	-

*determined experimentally in this work, ‡extrapolated pH$_{0.5}$ (see Chapter 5 Section 5.2.2.1) [a] and [b] are two independently determined polymorphs of [Cu(**L8b**)$_2$] (see Chapter 6 Section 6.2.7.1.)

The average Cu-O bond length is shorter for the homoleptic ketoxime complex than for the analogous aldoxime complex but the average Cu-N bond length is larger. A reduction in the calculated cavity size for the ketoxime complex is observed compared with the aldoxime analogue suggesting that a more stable complex is formed, however the pH$_{0.5}$ value is significantly greater indicating a weaker extractant. The X-ray determined Cu-O, Cu-N bond distances and the N$_1$-Cu-O$_1$ and N$_1$-Cu-O$_2$ bond angles of both polymorphs of [Cu(**L8b**)$_2$] show good correlation with the calculated analogues for [Cu(**L1b**)$_2$]. The variation between the bond lengths and angles between the two crystal structures of [Cu(**L8b**)$_2$] demonstrate well the effects of crystal packing on structure. It also confirms the difficulty faced when comparing X-ray determined structural information with theoretical values. (see also Chapter 6)

The charge densities and bond strengths were also calculated using the Weinhold's natural bond orbital (NBO) method as described in chapter.

Table 4.8: NBO calculated charge densities for Cu and **L** for the energy minimised structures of [Cu(**L1**)$_2$], [Cu(**L1**)(**L1b**)] and [Cu(**L1b**)$_2$].

[Cu(**L**)$_2$]	[Cu(**L1**)$_2$]	[Cu(**L1**)(**L1b**)]	[Cu(**L1b**)$_2$]
Charge density on **L** (average)	-0.3571	-0.35752	-0.35793
Charge density on **L** *cf.* [Cu(**L1**)$_2$]	0	-0.00042	-0.00083
Charge density on Cu	0.2142	0.21504	0.21585
Charge density on Cu *cf.* [Cu(**L1**)$_2$]	0	0.00084	0.00165

The positive charge on the metal increases in the order [Cu(**L1**)$_2$] < [Cu(**L1**)(**L1b**)] < [Cu(**L1b**)$_2$]. This indicates that the azomethine-methyl group of the ketoxime chelate **L1b** is having an electronic effect on the system similar to that observed for the 3-Br-substituent in [Cu(**L6**)$_2$] (Charge density on Cu *cf.* [Cu(**L1**)$_2$] being 0.00165 and 0.0018 for [Cu(**L1b**)$_2$] and [Cu(**L6**)$_2$] respectively). This again suggests that the ketoxime complex, [Cu(**L1b**)$_2$], is more stable than the aldoxime complex [Cu(**L1**)$_2$] and will be discussed further in Section 4.2.5.2.

4.2.4. Looking at different [M(L1)$_2$] complexes using DFT

Density functional calculations were carried out on the neutral [M(**L1**)$_2$] species (where M = Ni, Cu and Zn) with the Gaussian03 program using the B3LYP functional. Geometry optimizations were carried out at the 6-31g+(d,p) level, followed by frequency calculations, at the same level, to confirm structures were minima on the potential energy surface. The nickel and zinc structures were both square planar complexes analogous to that shown for [Cu(**L1**)$_2$]. The cavity areas for each species were calculated an ellipse (Figure 4.15) using the energy minimized structure and are given in Table 4.9. To check the validity of these structures cavity sizes were calculated for a similar series of complexes, [M(**L0**)$_2$], using crystallographic data.

Table 4.9: Theoretical Calculation data for [M(**L1**)$_2$] at B3LYP/6-31G+(d,p) and X-ray diffraction determined date for [M(**L0**)$_2$] with calculated cavity areas.

[M(**L**)$_2$]	**Ni**	**#Ni**[6]	**Cu**	**#Cu**[7]	**Zn**	**#Zn**[8*]
Average M-O distance/Å	1.8477	1.843	1.9168	1.902	1.9587	2.041
Average M-N distance/Å	1.8935	1.855	1.9646	1.964	2.0270	2.044
Cavity Area†/Å^2	10.9911	10.7403	11.830	11.7355	12.473	13.1061

X-ray determined data for [M(**L0**)$_2$] complexes. † calculated as an ellipse. *Zn(L0)$_2$.H$_2$O five co-ordinate complex

The area of the calculated cavities for the [M(**L1**)$_2$] species increases in the order Ni (10.99 Å^2) < Cu (11.83 Å^2) < Zn (12.47 Å^2) and correlates with the ionic radii of the M^{2+} ions which increase in the order Ni (69 pm) < Cu (73 pm) < Zn (74 pm).

There is a strong correlation between the cavity area of the gas phase calculated structures and the cavity calculated from the bond lengths determined by single crystal x-ray diffraction with cavity sizes for [M(**L1**)$_2$] increasing where M = Ni < Cu < Zn. There are, however, distinct differences between the cavity areas for the energy-minimized [M(**L1**)$_2$] complexes in the gas phase and the solid state structures for the [M(**L0**)$_2$] complexes determined by single crystal X-ray diffraction.. These differences (Ni (2.3% difference), Cu (0.8% difference) and Zn (4.9% difference)) can be accounted for as 1; the ligands used in each series are not the same and 2; crystal packing will have a slight affect on bond lengths. A larger difference in cavity area can be seen for [Zn(**L0**)$_2$] as it was crystallized as a five coordinate species which will have elongated the Zn-O and Zn-N bond lengths.

4.2.5. Calculated Enthalpies of Formation

4.2.5.1. Enthalpies of formation for $[Cu(L)_2]$ oxime complexes

Enthalpies of $[Cu(\mathbf{L})_2]$ complex formation in the gas phase were calculated using DFT to establish whether they are related to the copper extraction strengths shown by 3-X-substituted phenolic oximes. The energy minimised 3-X-substituted structure of a phenolic oxime dimer, $(\mathbf{LH})_2$, and the Cu^{2+} ion were calculated and the sum of the energies were compared with that of the corresponding complex $[Cu(\mathbf{L})_2]$. (Figure 4.10)

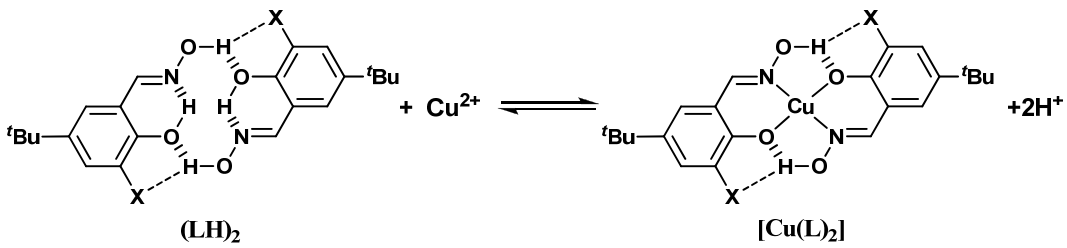

Figure 4.10: Cation exchange reaction for complex formation of 3-X-substituted phenolic oxime copper complexes.

The enthalpy of formation, ΔH_f, was calculated according to equation **4.9**,

$$\Delta H_f^\circ = [(E_0 + H_{corr})_{[Cu(\boldsymbol{L})_2]} + 2(E_0 + H_{corr})_{[H^+]}] - [(E_0 + H_{corr})_{[\boldsymbol{LH}]_2} + (E_0 + H_{corr})_{[Cu^{2+}]}] \quad \textbf{4. 6}$$

where E_0 is the gas phase minimised energy and H_{corr} is the thermal correction. (Table 4.10) The calculated gas phase enthalpies of formation are all positive which is not unexpected as the replacement of a Cu^{2+} ion by two H^+ ions in the gas phase; $Cu^{2+}_{(g)} + [(\boldsymbol{LH})_2]_{(g)} \xrightarrow{\Delta} [Cu(\boldsymbol{L})_2]_{(g)} + 2H^+_{(g)}$, is an unfavourable process. This is in contrast with what is seen in the solvent extraction experiments where the free

energy of solvation of two protons in aqueous media is much greater than that observed for a single Cu^{2+} ion, $Cu^{2+}_{(aq)} + [(\boldsymbol{LH})_2]_{(org)} \xrightarrow{\Delta} [Cu(\boldsymbol{L})_2]_{(org)} + 2H^{+}_{(aq)}$ (enthalpy of hydration is 2100 and 2260 kJ mol^{-1} for Cu^{2+} and $[2H^{+}]$ respectively[9]).

Table 4.10: E_0 values for each of the species in equation and the calculated ΔH_f for each $[Cu(\mathbf{L})_2]$ complex.

LH	L1H	L5H	L6H	L7H
$(E_0 + H_{corr})_{[\boldsymbol{LH}]_2}$/au)	-1266.3190	-2185.5189	-6408.5898	-1495.2981
$(E_0 + H_{corr})_{[Cu^{2+}]}$/au	-1639.2494	-1639.2494	-1639.2494	-1639.2494
$[(E_0 + H_{corr})_{[\boldsymbol{LH}]_2} + (E_0 + H_{corr})_{[Cu^{2+}]}]$/au	-2905.5684	-3824.7683	-8047.8392	-3134.5475
$[(E_0 + H_{corr})_{[Cu(\boldsymbol{L})_2]}$/au	-2905.5483	-3824.7514	-8047.8244	-3134.5293
ΔH_f° /kJ mol^{-1})	+52.8	+44.4	+39.0	+48.0

The calculated gas phase enthalpies of formation of the $[Cu(\mathbf{L})_2]$ complexes show a strong correlation with the strength of phenolic oxime extractants. (see Figure 4.11)

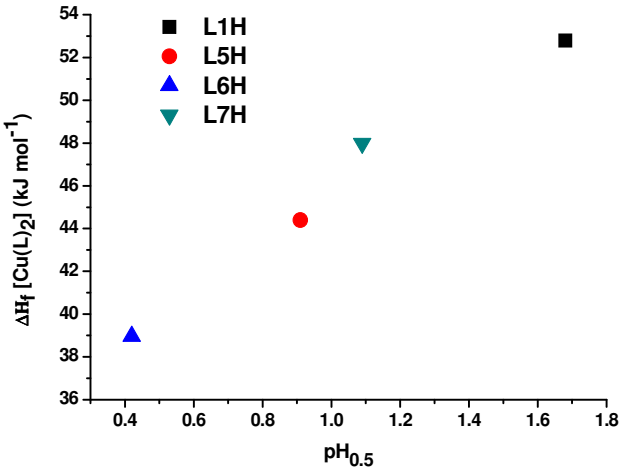

Figure 4.11: Calculated ΔH_f for each of the $[Cu(\mathbf{L})_2]$ complexes (**L** = **L1**, **L5**, **L6** and **L7**) compared with the $pH_{0.5}$ value of the corresponding ligands, **L1H**, **L5H**, **L6H** and **L7H**.[3]

At first sight it is surprising that there is an approximately linear relationship between the gas phase calculated ΔH_f values for [Cu(**L**)$_2$] and the $pH_{0.5}$ values determined for **LH** in the solvent extraction process. For this to be true free energies of solvation for the reaction $Cu^{2+}_{(aq)} + [(\boldsymbol{LH})_2]_{(org)} \rightleftharpoons [Cu(\boldsymbol{L})_2]_{(org)} + 2H^{+}_{(aq)}$ cannot be dependent on variations of the 3-X-substituents in the ligands. The relative free energies of hydration will be independent of the nature of the ligands and complexes in the organic phase. For each free ligand in the form of [(**LH**)$_2$] and its copper complex [Cu(**L**)$_2$] there are likely to be only minor differences in the free energies of solvation in non-polar solvents which do not coordinate to the copper atom.

4.2.5.2. Enthalpies of formation for homoleptic [Cu(L1)$_2$] aldoxime, homoleptic [Cu(L1b)$_2$] ketoxime and heteroleptic [Cu(L1)(L1b)] complexes.

The possibility of forming heteroleptic copper complexes is an important question posed by industry as aldoxime/ketoxime extractant blends are used extensively to tailor extraction strength. (see also Chapter 5 Section 5.2.2) DFT calculations were undertaken to determine the gas phase enthalpies of ligand dimerisation, $\Delta H_{dimer,}$ of ketoxime **L1bH** and of a mixed aldoxime/ketoxime ligand dimer, [(**L1H**)(**L1bH**)], which were compared with that calculated for the aldoxime ligand, **L1H.** Enthalpies of complex formation, ΔH_f, of the homoleptic complex [Cu(**L1b**)$_2$] of the ketoxime ligand **L1bH** (see Chapter 5 Section 5.2.2.1) and the heteroleptic complex [Cu(**L1**)(**L1b**)] were also calculated and compared with the ΔH_f for [Cu(**L1**)$_2$]. (Table 4.12)

The ΔH_{dimer} values show an inverse relationship the the $pH_{0.5}$ value of the corresponding ligands or the ligand blend, **L1H** (1.68) > **L1H/L1bH** (1.83) > **L1bH** (2.07). The electronic effect of the azomethine-methyl substituent on the ketoxime ligand could be increasing the inter-ligand hydrogen bond strength, making dimerisation more favourable.

The ΔH_f values, however, show an approximately linear relationship with the $pH_{0.5}$ value of the corresponding ligands or the ligand blend. This infers that the increased ΔH_f values for **L1bH** and the mixed **L1H/L1bH** blend makes complex formation of [Cu(**L1b**)$_2$] and [Cu(**L1**)(**L1b**)] less favourable relative to [Cu(**L1**)].

Again, such a relationship implies that *differences* in solvation enthalpies of ligands and complexes are not greatly dependant on the presence or absence of a methyl group on the azomethine carbon atoms and that the equilibrium is largely determined by the relative stabilities of the [(**LH**)$_2$] and [Cu(**L**)$_2$] species which are in turn dependent on subtle differences in the inner and outer coordination spheres.

Table 4.11: The $(\boldsymbol{E_0 + H_{corr}})$ values for each species are given with the calculated $\Delta \boldsymbol{H^\circ_{dimer}}$ for each [(**LH**)$_2$] and $\Delta \boldsymbol{H^\circ_f}$ for each [Cu(**L**)$_2$] complex.

LH	**L1H**	**L1H/L1bH**	**L1bH**
$2(E_0 + H_{corr})_{\boldsymbol{LH}}$/au)	-1266.3037	-1305.5954	-1344.8870
$(E_0 + H_{corr})_{[\boldsymbol{LH}]_2}$/au)	-1266.3192	-1305.6113	-1344.9036
ΔH°_{dimer} /kJ mol^{-1}	-40.6	-42.0	-43.5
$(E_0 + H_{corr})_{[Cu^{2+}]}$/au	-1639.2494	-1639.2494	-1639.2494
$[(E_0 + H_{corr})_{[\boldsymbol{LH}]_2} + (E_0 + H_{corr})_{[Cu^{2+}]}]$/au	-2905.5686	-2944.8608	-2984.1531
$[(E_0 + H_{corr})_{[Cu(\boldsymbol{L})_2]}$/au	-2905.5483	-2944.8374	-2984.1266
ΔH°_f /kJ mol^{-1}	+53.3	+61.3	+69.4
$pH_{0.5}$ **LH**	1.68	1.83*	2.07*‡

*determined experimentally in this work, ‡extrapolated $pH_{0.5}$ (see Chapter 5 Section 5.2.2.1.1.)

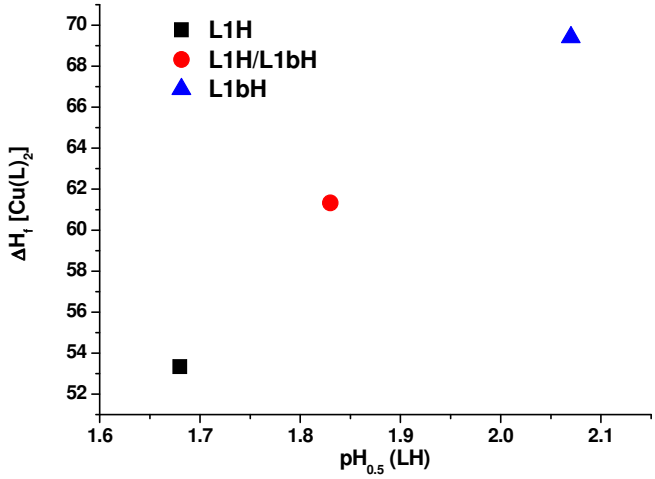

Figure 4.12: ΔH_f for each of the $[Cu(\mathbf{L})_2]$ complexes (where **L** = **L1**, **L1b**, and **L1/L1b**) compared to the $pH_{0.5}$ value of the corresponding ligands **L1H**, **L1bH** and **L1H/L1bH**.

4.2.5.3. Enthalpies of formation for $[M(L1)_2]$ complexes (M = Co, Ni, Cu or Zn)

Enthalpies of $[M(\mathbf{L1})_2]$ complex formation, where M = Co, Ni, Cu or Zn were also calculated in order to determine whether the selectivity of phenolic oximes for copper over nickel, cobalt and zinc can be explained in terms of relative thermodynamic stabilities of the complexes. The energy minimised structure of a phenolic oxime dimer, $[(\mathbf{L1H})_2]$, and M^{2+} ion were calculated and the sum of the energies was compared with that of the corresponding complex $[M(\mathbf{L})_2]$. (Figure 4.13)

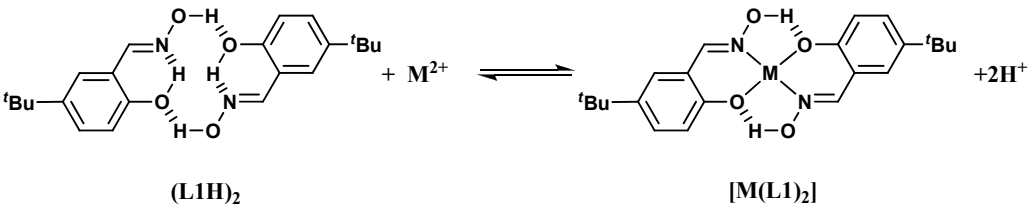

Figure 4.13: Cation exchange reaction for complex formation of $[M(\mathbf{L1})_2]$, where M = Cu, Zn, Ni and Co.

The enthalpy of formation, ΔH_f, for [M(**L1**)$_2$], where M = Cu, Zn, Co and Ni was calculated, using equation **4.10,**

$$\Delta H_f^\circ = [(E_0 + H_{corr})_{[M(\mathbf{L1})_2]} + 2(E_0 + H_{corr})_{[H^+]}] - [(\boldsymbol{E_0 + H_{corr}})_{[\mathbf{L1H}]_2} + (\boldsymbol{E_0 + H_{corr}})_{[M^{2+}]}] \quad \textbf{4.7}$$

where H_g is the gas phase calculated energy. (see Table 4.12)

Table 4.12: Calculated $(\boldsymbol{E_0 + H_{corr}})$ values for each species and the calculated $\Delta \boldsymbol{H_f^\circ}$ for each [M(**L1**)$_2$] complex.

M	Copper	Nickel	Cobalt	Zinc
$(E_0 + H_{corr})_{[LH]_2}$/au	-1266.3192	-1266.3192	-1266.3192	-1266.3192
$(E_0 + H_{corr})_{[M^{2+}]}$/au	-1639.2494	-1507.1477	-1381.6619	-1778.1537
$[(E_0 + H_{corr})_{[LH]_2} + (E_0 + H_{corr})_{[M^{2+}]}]$/au	-2905.5686	-2773.4669	-2647.9810	-3044.4729
$[(E_0 + H_{corr})_{[M(L)_2]}$/au	-2905.5483	-2773.4225	-2647.9023	-3044.3809
ΔH_f° /kJ mol^{-1}	53.3	116.6	206.8	241.5
$pH_{0.5}$ **P50**[4]	0.5	3	4.5	6

The calculated gas phase enthalpies of formation are positive for all complexes, as might be expected with the various hydration enthalpies of the M^{2+} and H^+ species are not included. (The enthalpies of formation of the complexes correlate with the reported selectivity of phenolic oxime-type ligands for these metals in solvent extraction processes. This is illustrated in Figure 4.14 in which the calculated ΔH_f values for 5-*t*-butylsalicylaldoxime (**L1H**) against the $pH_{0.5}$ values of 5-nonyl-salicylaldoxime, the commercial extractant **P50**. The ΔH_f increases in the order [Cu(**L1**)$_2$] < [Ni(**L1**)$_2$] < [Co(**L1**)$_2$] < [Zn(**L1**)$_2$] and correspond to the selectivity for these metals shown by the commercial extractant.

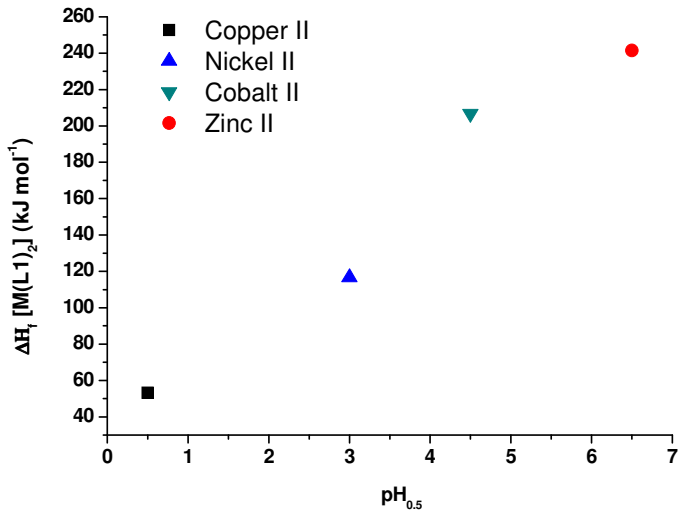

Figure 4.14: A plot of ΔH_f for the 5-*t*-butylsalicylaldoxime complexes, [M(**L1**)$_2$] (M = copper, zinc, nickel and cobalt) against the $pH_{0.5}$ values[4] at which each metal is extracted using the industrial extractant **P50.**

The electronic configuration of the metal is an important factor in calculating the ΔH_f [M(**L1**)$_2$] values as the spin state of the metal can change upon complexation. The zinc is straightforward, with Zn^{2+} being d^{10} and having a closed shell. Cu^{2+}, having a d^9 electronic, has an open shell and exhibits Jahn-Tellar distortion upon complexation (see Chapter 1) which enables the system to reduce its energy by lowering its symmetry. The systems for nickel and cobalt are more complicated as the spin state of M^{2+} can change upon complexation. Ni^{2+}, being d^8, and Co^{2+}, being d^7, exist as high spin complexes when hydrated in aqueous media but can spin pair upon complexation and extraction into apolar organic media. This was taken into account when calculating ΔH_f values for the [Ni(**L1**)$_2$] and [Co(**L1**)$_2$] complexes with the M^{2+} being energy minimised in its high spin state and the complex, [M(**L1**)$_2$], with the corresponding metals in their low spin state.

4.2.5.4. The Relationship between the calculated ΔH_f values of $[M(L)_2]$ and the observed $pH_{0.5}$ for extraction

As each of the calculations carried out in Sections 4.2.5.1-3 were performed at the same level of theory, the enthalpies of formation of the $[M(\mathbf{L1})_2]$ and the various $[Cu(\mathbf{L})_2]$ are comparable. A plot of the calculated gas phase enthalpies of formation of copper complexes of **L1H**, **L5H**, **L6H** and **L7H** and those of the cobalt, nickel and zinc complexes of **L1H** against the $pH_{0.5}$ values for extraction is given in Figure 4.15.

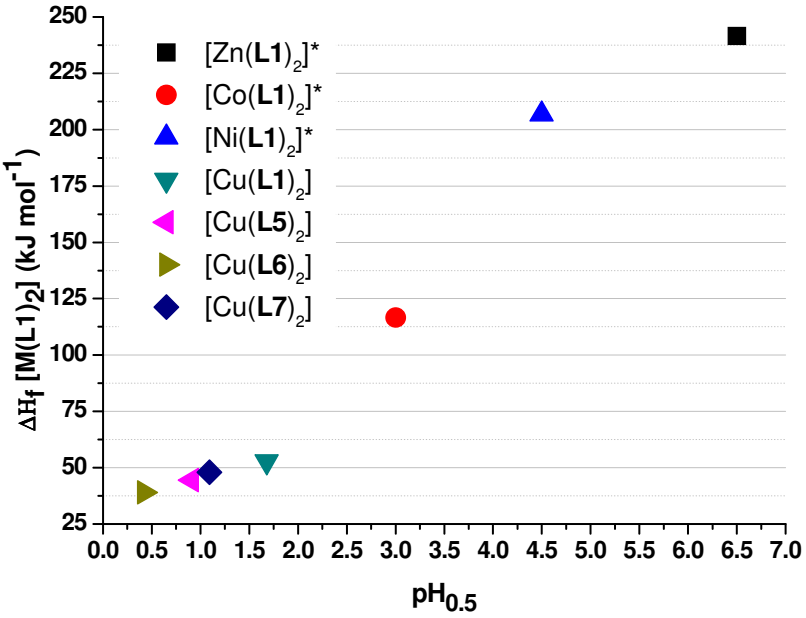

Figure 4.15: A plot of calculated enthalpies of formation of $[M(\mathbf{L})_2]$ aldoxime complexes against the $pH_{0.5}$ values for extraction by the same ligands (with the exception of the Co, Ni and Zn complexes where the $pH_{0.5}$ values[4] were determined using the 5-nonyl analogue of **L1H**.

The monotonic variation of $pH_{0.5}$ values with calculated gas phase enthalpies of formation of their complexes is remarkable given that the distribution coefficients for extraction vary by six orders of magnitude. The unexpectedly good correlation between the ΔH_f and $pH_{0.5}$ values implies that it is the thermodynamic stability of the complex relative to that of the free ligand dimer, $[(\mathbf{LH})_2]$, in the organic phase which largely controls the extractant strength. A corollary is that the free energies of

solvation of the ligand and its complexes in the organic phase do not differ greatly when different 3-X-substituents are present or when the azomethine hydrogen atom is replaced by a methyl group.

Given the good correlation between the ΔH_f and $pH_{0.5}$, it might be possible to predict the $pH_{0.5}$ values for different metals and for variants of the standard ligands. The data in Figure 4.15 show a sigmoidal distribution and when fitted the error is <1% with an extrapolated minimum and maximum of around 96.5 and 306.4 kJ mol^{-1}. This graph could potentially be used as a basis to predict approximate $pH_{0.5}$ values and may prove especially useful in designing stronger ligands for extraction of Ni(II) and Co(II).

In all the cases described in the above sections, in which the $pH_{0.5}$ values for metal extraction were compared with the calculated gas phase enthalpies of formation of the metal complexes, a monotonic variation has been observed. It seems that the conditions which are necessary for the approximately linear relationship between $pH_{0.5}$ and ΔH_f, notably that differences in solvation energy between the ligand dimer, $[(\mathbf{LH})_2]$, and its metal complex, $[M(\mathbf{L})_2]$, does not vary significantly when the 3-X-substituent or the azomethane substituent or the nature of the metal is varied.

Other results presented in this section allow us to conclude that:

- the introduction of substituents in the 3-position, that have previously been shown to greatly influence extraction strength, effects both the inner-coordination sphere due to their electronic properties and the outer-coordination sphere via their hydrogen bond accepting and steric properties. Electron withdrawing and good hydrogen bond accepting 3-X-substituents, e.g. NO_2 or Br, are the most effective in enhancing strength of copper extraction.

The DFT calculations support other evidence to suggest that:

- consecutive substitutions at the azomethane carbon considerably affects both the hydrogen bonding in the free ligand dimer, [(**LH**)$_2$] and the inner-coordination sphere of the resultant copper complex, [Cu(**L**)$_2$].

- that the nature of the metal greatly affects bond distances and angles in the inner-coordination sphere of the [M(**L**)$_2$] complexes and that these differences correspond well to data determined via single crystal X-ray diffraction.

The next section expands the study of 3-X-substituted phenolic oximes using DFT to 3-X-substituted phenolic hydrazones.

4.3. 3-X-substituted salicyl hydrazones and their copper(II) complexes

When the N-OH group of an oxime is replaced by an N-NHR group the resulting species is known as a hydrazone. It has been suggested that salicylaldehyde hydrazones could form N-H···O hydrogen bonds to generate dimers[10] and thus yield *pseudo*macrocyclic complexes (Figure 4.16) similar to those formed by the analogous oximes.

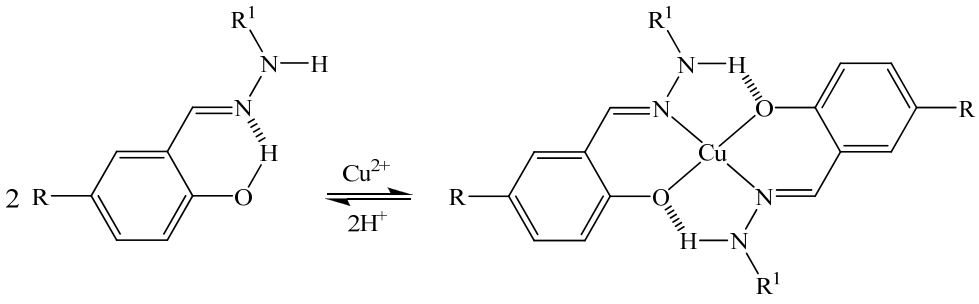

Figure 4.16: Formation of inter-ligand H-bonds in copper(II) complexes of salicylaldehyde hydrazones.

Salicylaldehyde benzoylhydrazone (R_1 = C_6H_5 in Figure 4.16) and analogous aroyl hydrazones have been studied as chelating agents to mobilize iron for iron-overload therapy,[11,12] and their transition metal complexes possess antitumour properties.[13,14] Many hydrazones and their transition metal complexes are used as antibacterial, antiviral and antifungal agents,[15,16] and in industry they are employed as plasticizers[17] and catalysts.[18-20]

N-acyl and N-aroyl hydrazones of salicylaldehyde[21-25] can form 2:2 copper(II) : **LH** complexes as tridentate ligands with the phenolate oxygen, azomethine nitrogen and enolimide oxygen atoms defining the binding site.[21-25].

After the ability of 3-x-substituents to tune the strength of salicylaldoximes as copper extractants had been established,[26,27] an investigation into similar effects with salicylaldehyde hydrazones was carried out by Dr. Tai Lin.[28] It was shown that these salicylaldehyde hydrazones formed copper(II) complexes with a similar *pseudo*macrocyclic H-bonding arrangement (Figure 4.17), and that the substituents tuned the strength of the extractants by buttressing the resultant copper complex. The hydrazone extractants **L9H**-**L12H** discussed in the work below are also shown in Figure 4.17.

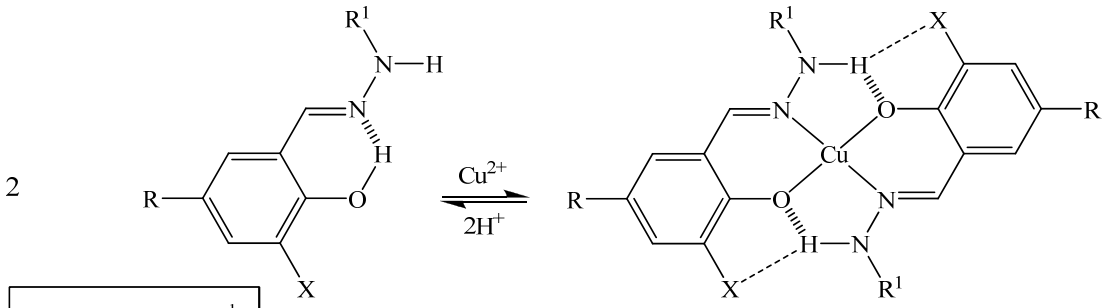

LH	X	R	R^1
L9H	H	^{t}Bu	Me
L10H	OMe	^{t}Bu	Me
L11H	Br	^{t}Bu	Me
L12H	NO_2	^{t}Bu	Me

Figure 4.17: Potential buttressing of H-bonds in copper(II) complexes of salicylaldehyde hydrazones. R = ^{t}Bu, R^1 = Me and X = H, OMe, Br, NO_2.[28]

An investigation of the strength of the hydrazones as solvent extractants, carried out by studying the pH dependence of the reaction,

$$CuSO_{4\,(aq)} + 2\boldsymbol{LH}_{(CHCl_3)} \rightleftharpoons [Cu(\boldsymbol{L})_2]_{(CHCl_3)} + H_2SO_{4\,(aq)}$$

indicated that they are intrinsically much weaker extractants than their oxime analogues and two problems were encountered. For some of the weaker extractants loading only occurred at pH values at which precipitation of copper(II) hydroxide occurred and several of the ligands and their Cu(II) complexes were insufficiently soluble in chloroform to allow extraction experiment to be conducted. To solve these problems strength data were obtained by determining the pH values for 50% loading of copper from stripping experiments in which chloroform solutions of preformed [Cu(**L**)$_2$] were contacted with aqueous solutions having different acidities but a constant sulphate (0.01M) concentration.[28]

The stripping curves and $pH_{1/2}$ values are shown in Figure 4.18.

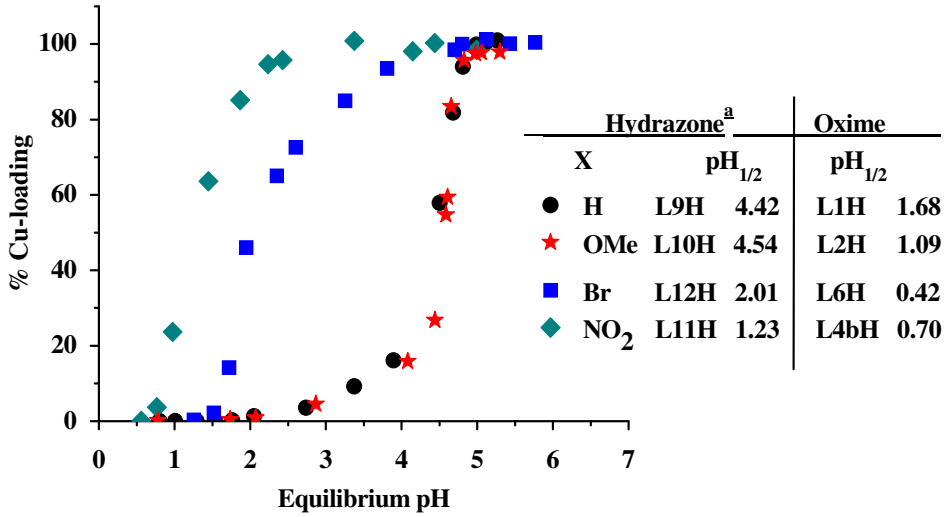

Figure 4.18: Copper loading of **L9H**-**L12H** after contacting 0.005 M chloroform solutions of [Cu(**L**)$_2$] with equal volume 0.01 M Na_2SO_4 aqueous solutions of various acidities. The $pH_{1/2}$ values of the oxime analogues (**L1H**, **L2H**, **L4bH** and **L6H**) are also listed.

3-Substitution of phenolic hydrazones significantly affects their extraction strength for copper(II). The distribution coefficient for copper transfer varies by more than three orders of magnitude across the series: NO_2 > Br > H ≥ OMe. It is apparent that the hydrazones are intrinsically weaker extractants than their oxime analogues ($pH_{1/2}$ data for the oximes[29] are included for comparison in the table in Figure 4.18).

Whilst the unsubstituted and methoxy-substituted hydrazones, **L9H** and **L10H**, are much weaker extractants than their oxime analogues, the differences in strength between the bromo- and nitro-substituted hydrazones **L11H** and **L12H** and their oxime analogues (**L6H** and **L4H**) are much smaller.

In an attempt to define to what extent the electronic, steric and hydrogen bond buttressing properties of the 3-X substituents determine the relative strengths of the extractants DFT calculations were carried out on the hydrazone ligands, **LH**, (**L9H**-**L12H**) their dimers, [(**LH**)$_2$], and their copper(II) complexes, [Cu(**L**)$_2$].

4.3.1. DFT Calculations for 3-X-substituted salicylaldehyde hydrazones

The energy minimised structures of the 3-X-substituted salicylaldehyde hydrazones were calculated using B3LYP[2-4]/6-31+G[5-14](d,p). To investigate the energy involved in the intramolecular hydrogen bonding in the monomeric forms of **L9H** (X = H), **L10H** (X = OMe) and **L11H** (X = Br) two conformers of the ligand shown as (a) and (b) in Figure 4.19 with OH···N and OH···X hydrogen bonds were investigated.

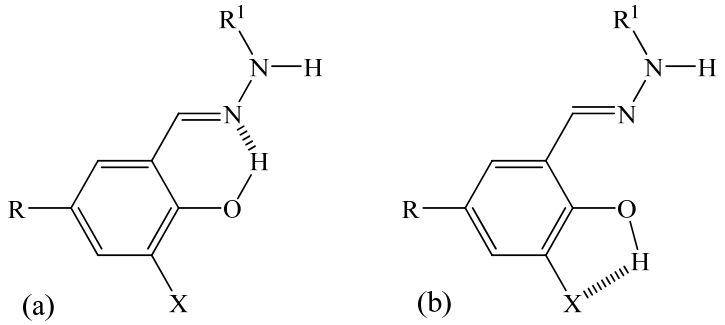

Figure 4.19: Intramolecular H-bonds in monomer forms of the salicylaldehyde hydrazones **L9H**-**L12H.**

For **L9H**, **L10H** and **L11H** the conformer with the phenolic hydrogen atom making contact with the hydrazone nitrogen atom (OH···N, (a) in Figure 4.19) was more favourable. (Table 4.13)

Table 4.13: Minimised conformation energies for **L9H, L10H** and **L11H**, where the phenolic OH is either coordinated to the hydrazone nitrogen atom, $\boldsymbol{E_{OH\cdots N}}$, or to the 3-X-substituent, $\boldsymbol{E_{OH\cdots X}}$.

LH (*X*)	**L9H** (*H*)	**L10H** (*OMe*)	**L11H** (*Br*)
$E_{OH\cdots X}$/au	-652.8549	-767.3851	-3223.9863
$E_{OH\cdots N}$/au	-652.8727	-767.3950	-3223.9994
ΔE/kJ mol^{-1}	46.8788	25.9781	34.4164

As might be expected the difference in energy between the two conformers varies in the order **L9H** (46.9 kJ mol^{-1}) > **L10H** (34.4 kJ mol^{-1}) > **L11H** (26.0 kJ mol^{-1}) in accordance with the hydrogen bonding properties of the 3-X-substituent. X groups with H-bond accepting properties make the OH···X conformer increasingly more favourable.

Calculations revealed that the influence of X on the H-bonding for **L12H,** where X = NO_2, is greater than that observed for **L9H** and **L10H** as the NO_2 group is a strong H-bond acceptor. The **L12H** geometry showing interaction between the NO_2 group

and the phenolic hydrogen atom is more favourable than for ligands with single atom 3-X-substituents, see Figure 4.20.

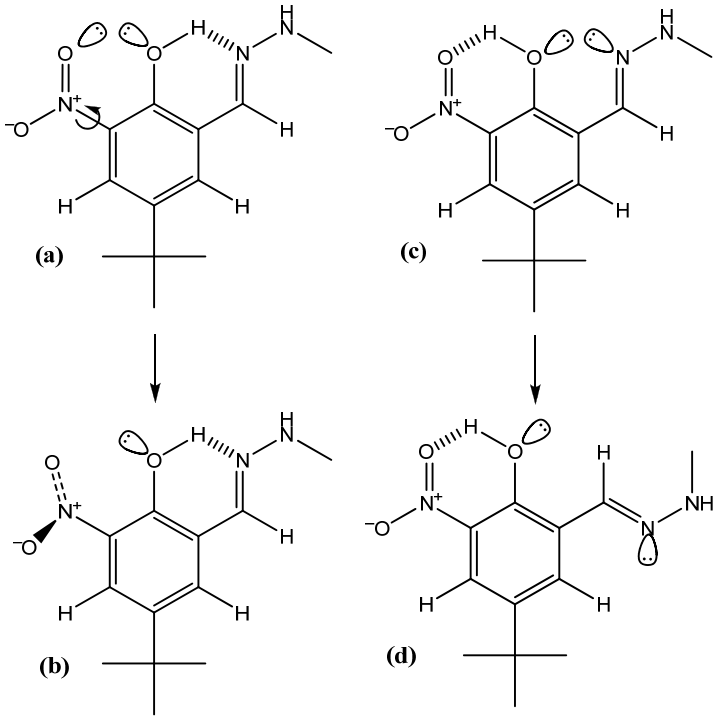

Figure 4.20: Possible conformers of **L12H** with resultant lone pair interactions and structural effects.

For the OH···N conformer, (a) in Figure 4.20, lone pair repulsion results in twisting of the NO_2 group out of the plane of the benzene ring (b in Figure 4.20) which reduces the electronic delocalisation in the ligand, increasing its energy. A similar interaction is observed in the OH···NO_2 conformer, (c) in Figure 4.20, which causes flipping of the hydrazone group resulting in the E-isomer of the ligand (d in Figure 4.20). Figure 4.21 provides an energy diagram with energy minimised structures of the conformer (a) and the E and Z-isomers of (c)

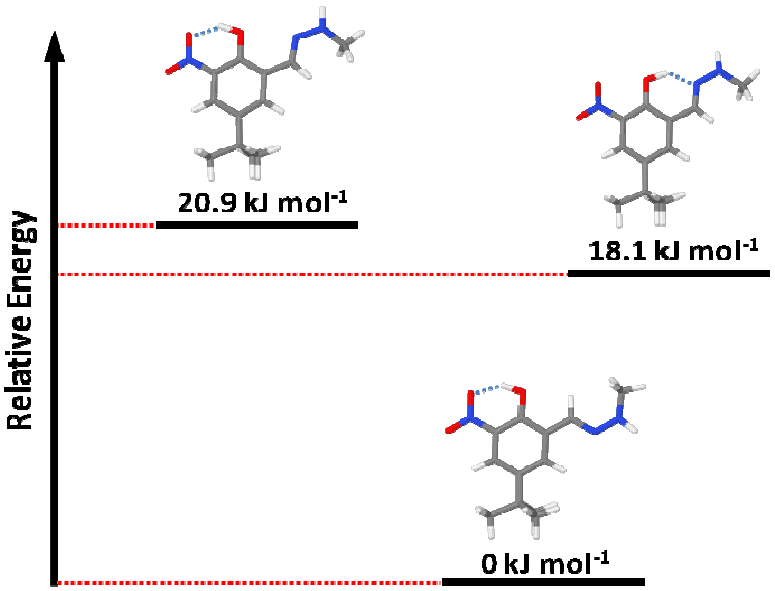

Figure 4.21: Energies of energy minimised conformers of **L12H** relative to the E-isomer (d) shown in Figure 4.19.

The E-isomer ((d) in Figure 4.19), where the H-bond interaction is OH···NO_2, has the lowest energy, 21 kJ mol^{-1} less than the Z-form. This is consistent with the x-ray structure of the oxime analogue **L4H**¸ which also exists (Figure 4.22) as the E-isomer.[3]

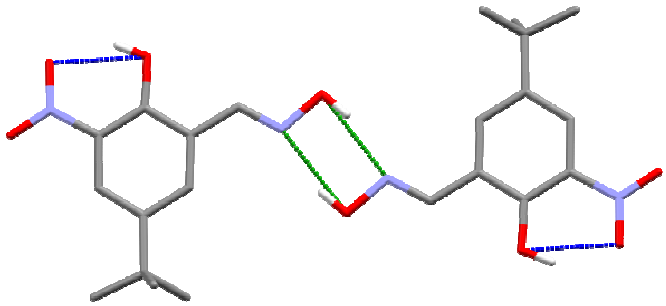

Figure 4.22: The solid state structure of the 3-nitro-substituted oxime, **L4H**, which exists as the E-isomer conformation and not the Z-form as observed for all other phenolic oximes studied.[3] Intra-molecular OH···NO_2 contacts (blue) and inter-molecular NOH···NOH contacts (green) are highlighted.

The main difference between the calculated structures of the oximes and hydrazones is that the N-OH group is coplanar ((a) in Figure 4.23) with the azomethine CH and the benzene ring whereas the N-NHMe group is not and has a geometry where hybridisation on the terminal nitrogen atom is an intermediate between sp^2 and sp^3.

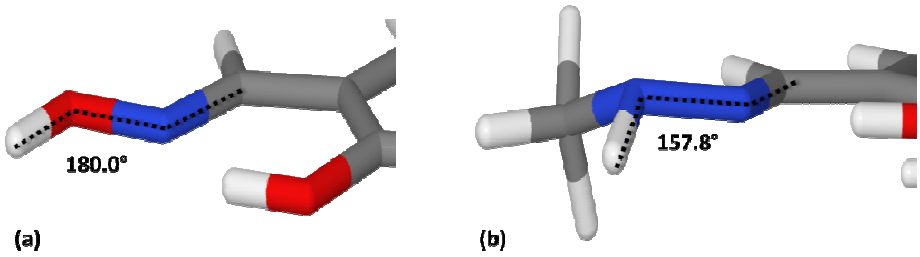

Figure 4.23: Calculated structures of (a) oxime group of **L1H** and (b) hydrazone group of **L11H** with C-N-X-H dihedral angles shown.

The C-N-O-H dihedral angle in all the calculated structures of the oximes is close to 180.0° whereas that for the C-N-N-H angle in the hydrazones is approximately 160°: (**L10H;** 157.7° < **L9H;** 157.8° < **L11H;** 158.4° < **L12H;** 162.0°). The degree of sp^3 hybridization of the hydrazone NHMe group seems to be dependent on the electron withdrawing nature of X, with electron withdrawing substituent NO_2 causing the smallest deviation from sp^2 hybridization.

4.3.1.1. Deprotonation energies (ΔH_{depro}) for 3-X-substituted salicylaldehyde hydrazones

To understand the effect X has on the electronic properties of the 3-X-substituted hydrazones full geometry optimisations were performed using B3LYP[2-4]/6-31+G[5-14](d,p). The ΔH_{depro} for each ligand was calculated according to equation **4.5** and these values are compared with the C-N-N-H torsion angle in Table 4.5.

Table 4.14: The minimised energies of the ligand $\boldsymbol{E_{LH}}$ and the corresponding deprotonated ligand $\boldsymbol{E_{L^-}}$ with calculated deprotonation energies, $\Delta \boldsymbol{H_{depro}}$ for **L9H**, **L10H**, **L11H** and **L12H**.

LH (X)	**L9H** (H)	**L10H** (OMe)	**L11H** (Br)	**L12H** (NO_2)
$(E_0 + H_{corr})_{\boldsymbol{LH}}$/au	-652.5719	-767.0592	-3223.7067	-857.0757
$(E_0 + H_{corr})_{\boldsymbol{L^-}}$/au	-652.0062	-766.4926	-3223.1524	-856.5304
ΔH°_{depro}/kJ mol^{-1}	1485.5	1487.6	1455.4	1431.4
ΔH°_{depro}/kJ mol^{-1} *cf.* **L9H**	0	-2.1	30.1	54.1
C-N-N-H dihedral angle /°	157.8	157.7	158.4	162.0

The deprotonation enthalpies for the methoxy and bromo substituted hydrazones, (**L10H** and **L11H**) relative to the unsubstituted ligand, **L9H**, correspond closely with the oxime analogues (**L7H** and **L6H** relative to **L1H**). As expected the ΔH_{depro} for the nitro-substituted hydrazone, **L12H**, is significantly smaller due to the NO_2 group activating the phenolic OH via electron withdrawal. A correlation is seen between the The deprotonation enthalpy and C-N-N-H dihedral angle for each of the ligands with **L11H** and **L12H** having smaller ΔH_{depro} and larger C-N-N-H dihedral angles.

4.3.1.2. Dimerisation enthalpies ($\Delta \boldsymbol{H_{dimer}}$) for 3-X-substituted salicylaldehyde hydrazones

Despite there being few data to suggest that the salicylaldehyde hydrazones dimerise in condensed media, gas phase calculations were carried out to determine the dimerisation enthalpies for the 3-X-substituted hydrazones because this process is involved in the forming copper(II) complexes with the pseudo-macrocyclic assembly of ligands as shown in Figure 4.16. Figure 4.24 shows the energy minimised structure of the phenolic hydrazone dimer, [(**L9H**)$_2$]. From the side view it can be seen that the terminal nitrogen atoms of the hydrazone groups appear to be sp^3 hybridised, as in the monomer units (Figure 4.24).

The dimerisation enthalpy (ΔH_{dimer}) was calculated using DFT as described by equations (**4.7**) and (**4.8**)

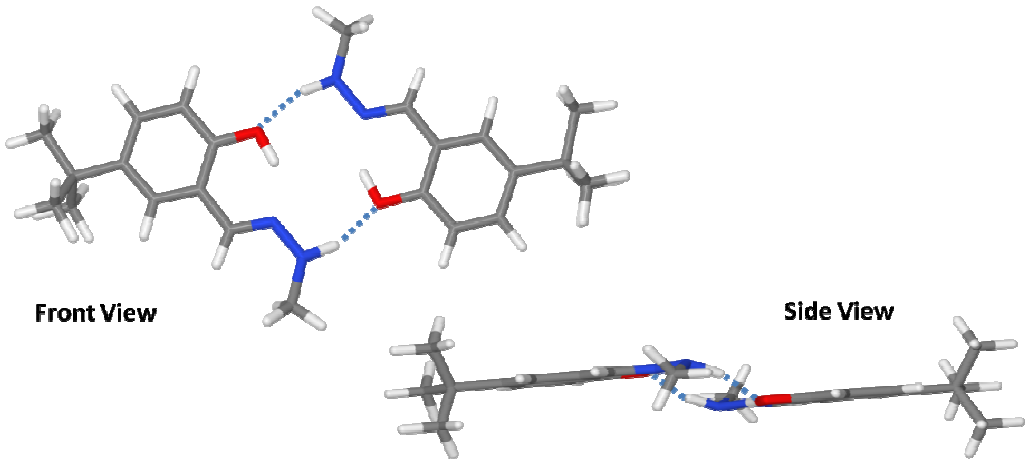

Figure 4.24: Energy minimised structure for **L9H** dimer with intra- and inter-molecular hydrogen bonding highlighted (blue).

Full geometry optimisations of the ligand dimers were performed using B3LYP[2-4]/6-31+G[5-14](d,p). As the counterpoise correction to estimate basis set superposition errors (BSSE) did not significantly change the relative dimerisation enthalpies for the 3-X-substituted phenolic oximes (**L1H**, **L5H**, **L6H** and **L7H**) it was omitted in this study and the uncorrected minimised energy for the ligand dimer, $E_{[LH]_2}$, was used to calculate ΔH_{dimer} for each ligand. (Table 4.15)

Table 4.15: Calculated formation enthalpies for the ligand dimers, ΔH°_{dimer}, ([(**L9H**)$_2$] – [(**L12H**)$_2$]) compared with that for [(**L9H**)$_2$].

LH	**L9H**	**L10H**	**L11H**	**L12H(*Z*)**	**L12H(*E*)**
$2(E_0+H_{corr})_{LH}$/au	-1305.1439	-1534.1184	-6447.4134	-1714.1513	-1714.1359
$(E_0 + H_{corr})_{[LH]_2}$/au	-1305.1560	-1534.1343	-6447.4316	-1714.1629	-1714.1629
ΔH°_{dimer}/kJ mol^{-1}	-31.8	-41.7	-47.6	-30.5	-71.0
ΔH°_{dimer} *cf.* **L1H**/kJ mol^{-1}	0	-9.9	-15.8	1.3	-39.2

Dimerisation is exothermic for each ligand with the least exothermic being that for the weakest extractant **L9H** (-31.8 kJ mol^{-1}). The dimerisation enthalpy for **L10H** (X= OMe, 41.7 kJ mol^{-1}) is relatively not as favourable as the oxime analogue **L7H.** This may be a result of the reduced orbital overlap and planarity of the dimer due to the non-planarity of the hydrazone group. The larger van der waals radii of the Br atoms of **L11H** could account for its increased ΔH_{dimer} relative to the oxime analogue **L6H** as the lack of planarity in the dimer will affect the orbital overlap to a lesser extent than for **L9H** and **L10H**. Two ΔH_{dimer} values have been calculated for **L12H** one using the energy of the E-isomer (conformer with the lowest energy) and the second using the Z-isomer with phenolic hydrogen bonded to the oximic nitrogen (as the minimised energy of the dimer is calculated with the monomers in this conformation, Figure 4.25).

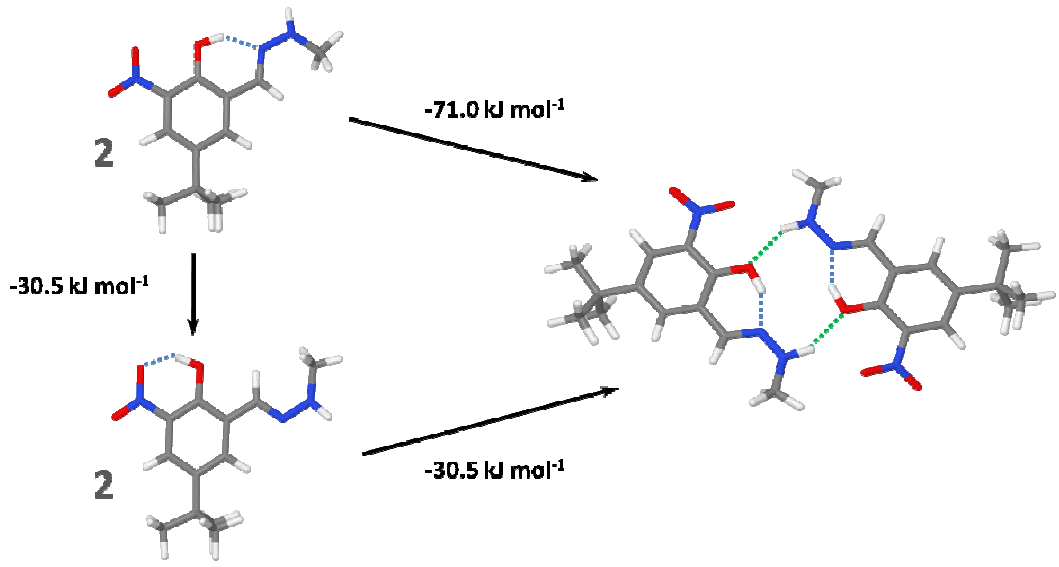

Figure 4.25: The value of ΔH_{dimer} and conformation energy differences for the Z (top) and E (bottom) forms of **L12H**.

Even though **L12H***E* is lower in energy the formation of the **L12H***Z* dimer from this conformer is still favourable (-30.5 kJ mol^{-1}). From these data it can be concluded that the hydrazones are likely to dimerise in apolar media in a similar manner previously observed for oximes.

4.3.2. DFT calculations on the 3-X-substituted salicylaldehyde hydrazone copper complexes

The energy minimised gas phase structures of the substituted salicylaldehyde hydrazones were calculated using DFT in a similar manner to that described (see Section 4.2.2.2.). The hydrazone groups of the energy minimised [Cu(**L**)$_2$] complexes (where **L** = **L9**-**L12**) exhibit non-planarity (Figure 4.26) in a similar manner to that observed in the free ligand monomers and dimers.

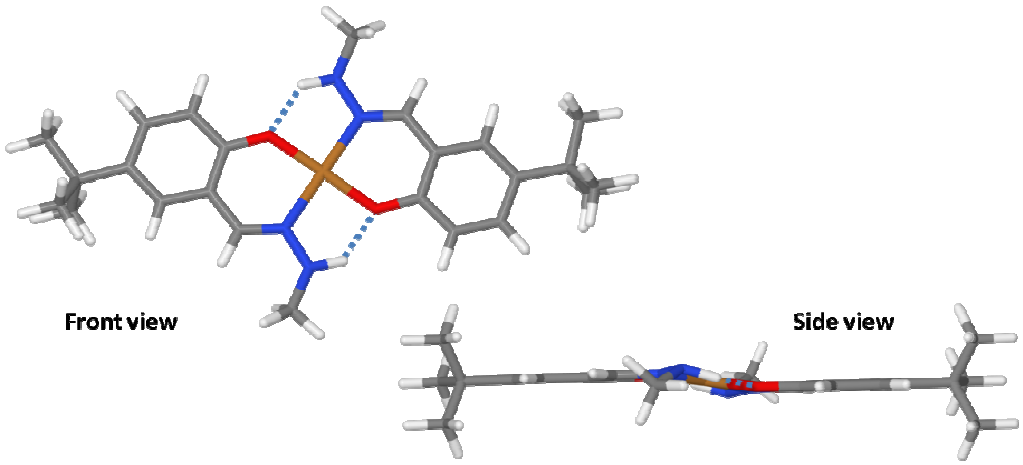

Figure 4.26: Energy minimised structure for the complex [Cu(**L9**)$_2$] with inter-molecular hydrogen bonding highlighted (blue). The side view illustrates reduced planarity of the complex (with respect to oxime analogues) arising from its non planar N-NHMe groups.

B3LYP/6-31+G(d,p) was used for geometry optimisation of the hydrazone copper complexes and Table 4.16 lists the calculated bond lengths and torsion angles for copper complexes of four hydrazone ligands **L9H**-**L12H.** Details of the copper complex for the unsubstituted oxime **L1H** is also given for reference. Distances of the Y atoms (N for hydrazones, O for the oxime) from the calculated least squares mean plane CuN_2O_2 as illustrated in Figure 4.27 are also presented.

Table 4.16: Results of B3LYP/6-31+G(d,p)-calculations for the copper complexes of hydrazones **L9H**-**L12H** and the oxime **L1H.**

LH	**L9H**	**L10H**	**L11H**	**L12H**	**L1H**
Cu-N/Å	2.0358	2.036	2.0409	2.0276	1.9168
Cu-O/Å	1.9070	1.8922	1.8938	1.9042	1.9645
Y-H···O/Å	1.8588	1.8591	1.8821	1.9085	1.7786
Y-H···X/Å	2.9109	2.7177	2.8139	2.0163	2.9883
Torsion angle O-Cu-N-Y/^{o}	170.53	171.90	174.16	172.52	179.98
Torsion angle O'-Cu-N-Y/^{o}	9.47	8.10	5.84	7.48	0.01
Distance of Y from the least squares mean plane CuN_2O_2/Å	0.205	0.175	0.126	0.159	0.001

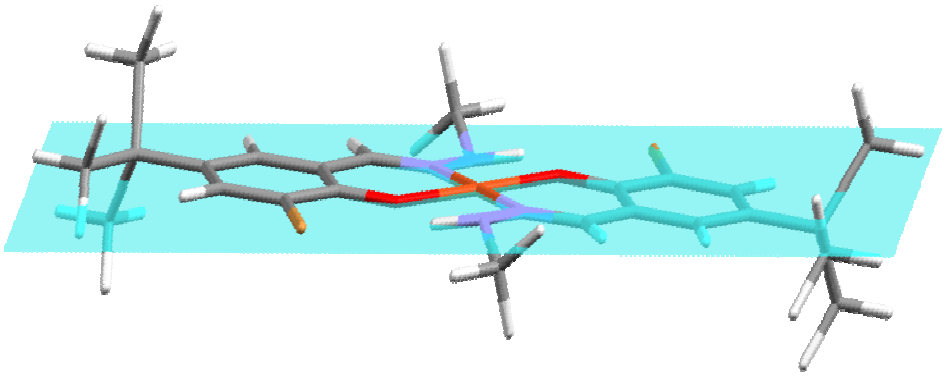

Figure 4.27: Geometry optimised structure of [Cu(**L11**)$_2$] with calculated least squares mean plane (blue) through CuN_2O_2 emphasising reduced complex planarity for hydrazone ligands.

Table 4.17: Interaction energies for the hydrazone copper (II) complexes compared with those for the oxime complex, [Cu(**L1**)$_2$].

LH	**L9H**	**L10H**	**L11H**	**L12H**	**L1H**
E/kJ mol^{-1}, Cu-O	214.3463	228.8648	220.434	217.6098	209.6184
E/kJ mol^{-1}, Cu-N	153.5946	155.8749	150.8332	155.1009	198.1961
O$^{\cdots}$H/kJ mol^{-1}	*	25.4387	25.0203	24.1417	*
X$^{\cdots}$H/kJ mol^{-1}	0	1.10876	9.3094	26.27552	0
$\Sigma_{O\cdots H,\ X\cdots H}$/kJ mol^{-1}	*	26.5475	34.3297	50.4172	*
$pH_{0.5}$ **LH**	4.42	4.54	2.01	1.23	**1.68**

*NY-*H* described as separate unit (see Appendix)

The hydrazone N-Cu and phenolic O-Cu bonding energies show no correlation with ligand extraction strength or with the electronic inductive properties of the X-substituent. A correlation is seen between the $pH_{0.5}$ of the ligands and the X-substituent$^{\cdots}$oximic proton interaction energies for the resultant complexes, where H < OMe < Br < NO_2. As experienced for [Cu(**L1**)$_2$], comparison of the NBO energies for [Cu(**L9**)$_2$] is not possible as the hydrazone N*H* is described as a separate unit. The sums of the O4$^{\cdots}$H8 and X1$^{\cdots}$H8 energies for [Cu(**L10**)$_2$] (26.5 kJ mol^{-1}), [Cu(**L11**)$_2$] (34.3 kJ mol^{-1}), [Cu(**L12**)$_2$] (50.4 kJ mol^{-1}) correlate well with $pH_{0.5}$ of the corresponding ligands. The O-Cu bonds are stronger for the hydrazones than the oximes with [Cu(**L9**)$_2$] being 214.3 kJ mol^{-1} compared to 209.6 kJ mol^{-1} for [Cu(**L1**)$_2$] but the N-Cu bonds are ≈ 40 kJ mol^{-1} weaker. The resultant total energy involved in the inner coordination sphere of the oxime complex [Cu(**L1**)$_2$] (816 kJ mol^{-1}) is 80 kJ mol^{-1} greater than that for the corresponding hydrazone (736 kJ mol^{-1}) which is consistent with the large difference in the strengths of these two extractants; $pH_{0.5}$ for **L1H** = 1.68 and that for **L9H** = 4.42.

4.3.2.1. Crystal structures for hydrazone copper (II) complexes; further proof of hybridization

Single crystal X-ray structure determinations of [Cu(**L9**)$_2$] and [Cu(**L10**)$_2$] were carried out to confirm that the hydrazones yield Cu(II) complexes with *pseudo*-macrocyclic structures similar to their oxime analogues and that the non-planarity of the hydrazone units in the gas phase structures obtained for the DFT calculations was observed in the condensed phase

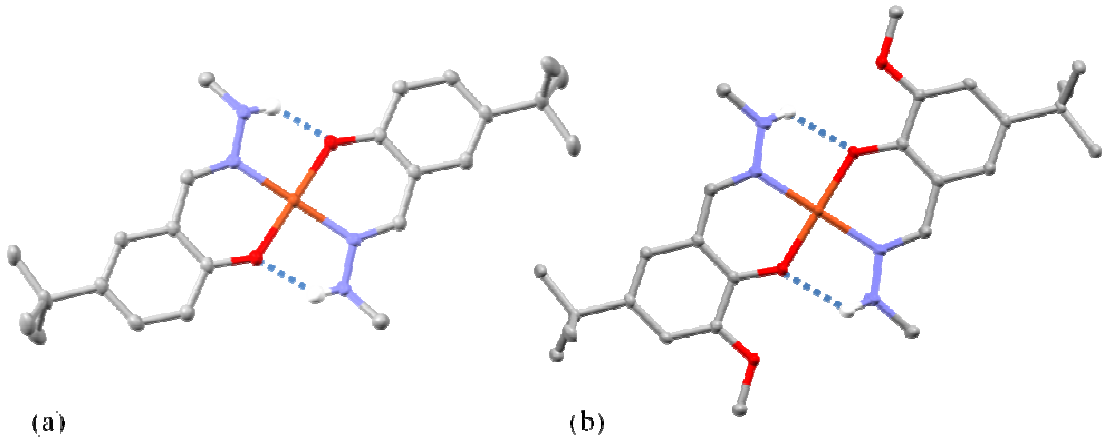

Figure 4.28: The solid state structures of (a) [Cu(**L9**)$_2$] and (b) [Cu(**L10**)$_2$]

The solid state structures of [Cu(**L9**)$_2$] and [Cu(**L10**)$_2$] reveal that the hydrazone N-N bonds bend away from the central CuO_2N_2 in contrast to the N-O bonds in the related oxime complexes and the determined structures correspond closely with the energy minimised structures obtained for the DFT calculations. The implications of this are that inter-ligand hydrogen bonding will be weaker in the hydrazones and will reduce complex stability and extractant strength.

The bond length and angles and the contact distances in the inner- and outer-coordination sphere of the unsubstituted and 3-methoxy substituted hydrazones copper complexes, [Cu(**L9**)$_2$] and [Cu(**L10**)$_2$], are compared with those in the oxime complex [Cu(**L1**)$_2$] in Table 4.18 using the labelling scheme described in Figure 4.29.

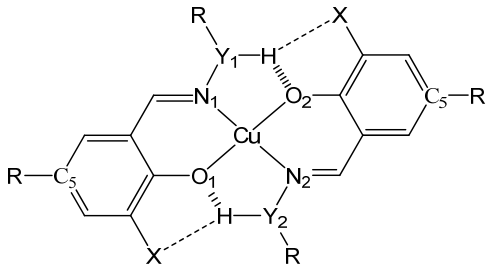

Compound	X	Y	R
[Cu(**L9**)$_2$]	H	N	Me
[Cu(**L1**)$_2$]	H	O	-
[Cu(**L10**)$_2$]	OMe	N	Me

Figure 4.29: Atom labelling scheme used in Table 4.18.

Table 4.18: Bond lengths (Å) and angles (°) in the inner coordination spheres of the [Cu(**L9**)$_2$] compared with those in the oxime analogue, [Cu(**L1**)$_2$], and methoxy-substituted [Cu(**L10**)$_2$]. [a]In all complexes the Cu^{II} atom lies on an inversion centre. [b]The mean distance of the donor N and O atoms from the centroid.

Bond lengths /Å and angles/°[a]	[Cu(**L9**)$_2$]	[Cu(**L1**)$_2$]			[Cu(**L10**)$_2$]	
Cu-O_1	1.9244(11)	1.905(2)	1.900(2)	1.907(2)	1.8658(10)	
Cu-N_1	1.9986(13)	1.941(2)	1.945(2)	1.943(2)	2.0020(13)	
O_1-Cu-O_2	180.0	180.0	180.0	180.0	180.0	
N_1-Cu-N_2	180.0	180.0	180.0	180.0	180.0	
O_1-Cu-N_1	91.03(5)	92.26(8)	92.13(8)	91.76(8)	92.24(5)	
O_2-Cu-N_1	88.97(5)	87.74(8)	87.87(8)	88.24(8)	87.76(5)	
$Y_1\cdots O_2$	2.7005(18)	2.581(2)	2.583(5)	2.584(3)	2.604(4)	2.614(4)
Cavity radius[b]	1.962(2)	1.923(3)	1.923(3)	1.925(3)	1.934(2)	
O_1-Cu-N_1-Y_1	160.55(10)	173.80(16)	177.88(16)	175.46(16)	168.7(2)	162.8(2)
O_2-Cu-N_1-Y_1	19.45(10)	6.20(16)	2.12(16)	4.54(16)	11.27(18)	17.2(2)
Distance of Y from the least squares mean plane CuN_2O_2	0.418(1)	0.135(2)	0.046(2)	0.099(2)	0.247(4)	0.380(4)

The Cu-N and Cu-O bond lengths are fairly similar in the hydrazone complexes [Cu(**L9**)$_2$] and [Cu(**L10**)$_2$] (Table 4.18) and do not differ greatly from those found in

the related oxime complex [Cu(**L1**)$_2$]. As the structures all have the copper atom at a crystallographic inversion centre the *bonding cavity radius*[30] defined by the N_2O_2 set is the mean of the Cu-O and Cu-N lengths. The smaller value for the oxime complex [Cu(**L1**)$_2$] implies tighter binding than in the hydrazone complexes but caution needs to be exercised in using cavity radii determined from solid state structures to compare the equatorial planar fields defined by the N_2O_2 donor sets because axial contacts vary considerably between structures.[30] The phenolate oxygen atoms of an adjacent complex make close contacts in the structure of [Cu(**L9**)$_2$] (as can be seen in the crystal packing diagram shown in Figure 4.30) but not in the solid state structure of [Cu(**L10**)$_2$].

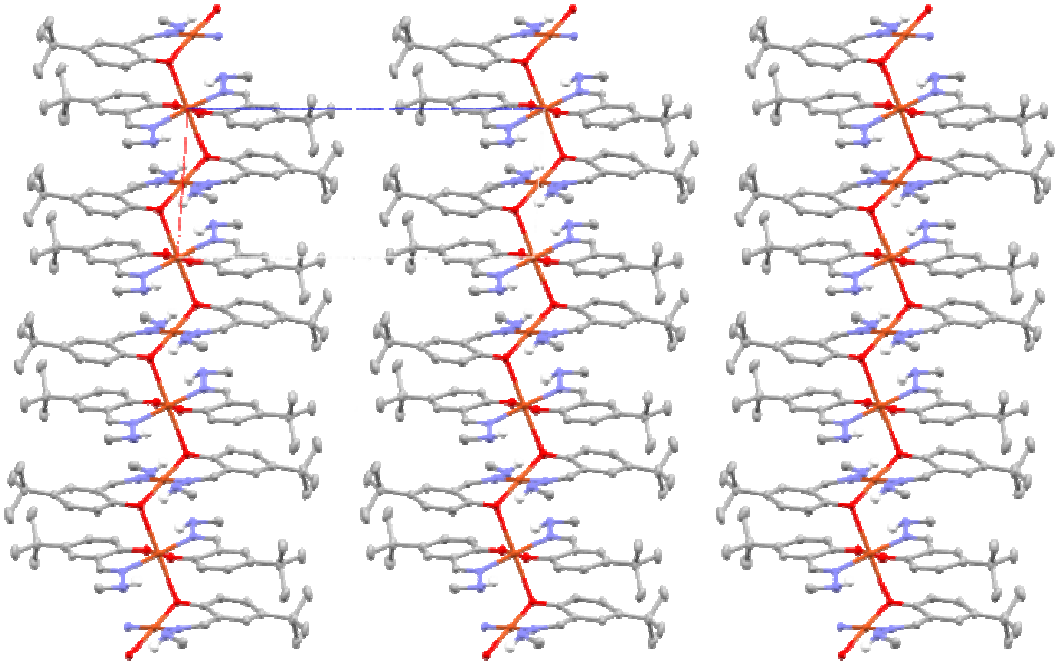

Figure 4.30: The solid state packing of [Cu(**L9**)$_2$], Hydrogen atoms not involved in hydrogen bonding omitted for clarity.

The axial coordination of phenolate oxygen atoms in neighbouring [Cu(**L9**)$_2$] units results in a Cu-O-Cu chain as can be seen in Figure 4.30.

Deviations from planarity of the hydrazone group revealed by the distances of the terminal nitrogen atom (Y) from the least square plane containing the CuN_2O_2 coordination sphere and the values for the O_1-Cu-N_1-Y_1 and O_2-Cu-N_1-Y_1 torsion angles (Table 4.18), are significantly greater than those for the oxime groups in [Cu(**L1**)$_2$].

Whilst the calculated structures of [Cu(**L9**)$_2$] and [Cu(**L10**)$_2$] show fairly similar deviations from planarity (Table 4.19) in the solid state [Cu(**L10**)$_2$] appears more nearly planar (see Figure 4.31). This is probably an artefact of the X-ray structure determination in that two conformers of the complex exist with 0.5 occupancy which results in nearly planar N-NHR groups in the observed, averaged structure (see Figure 4.32). The structure of [Cu(**L10**)$_2$] shows evidence of disorder of an unusual type. The atoms at the periphery of the structure e.g. C_5 (see Figure 4.29) have smaller thermal parameters, whereas those for the donor atoms O_1, O_2, N_1, N_2 are much larger with ellipsoids with their largest axes perpendicular to the CuO_2N_2 plane. Two resolved regions of electron density are found for the terminal nitrogen atoms of the hydrazone units (Y_1 and Y_2 in Figure 4.32) on either side of the CuO_2N_2. The higher thermal parameters in the centre of the complex and the disorder of the terminal nitrogen atoms of the hydrazone groups suggest that [Cu(**L10**)$_2$] also has a stepped structure similar to that of [Cu(**L9**)$_2$] but that this is disordered over two sites. As a consequence the deviation from planarity of the hydrazone unit appear smaller (see (b) in Figure 4.31) and are, in fact, probably similar to those in DFT calculated structure (see (c) in Figure 4.31)

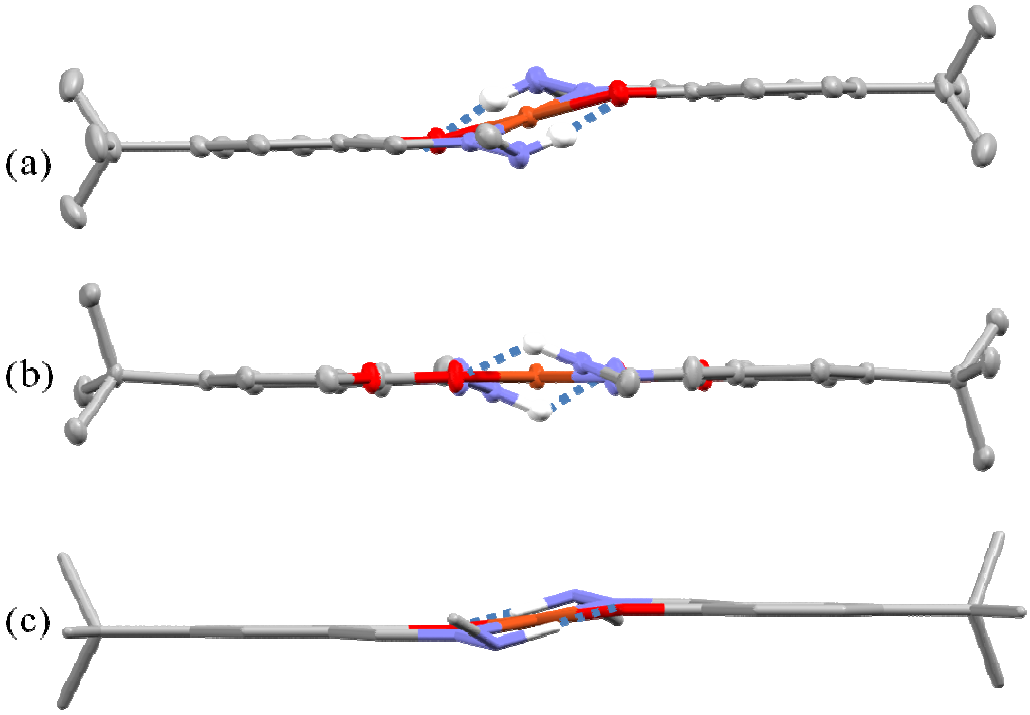

Figure 4.31: Side view of (a) the crystal structure for [Cu(**L9**)$_2$], (b) the crystal structure for [Cu(**L10**)$_2$] and (c) the energy minimised structure for [Cu(**L9**)$_2$]. Hydrogen atoms not involved in hydrogen bonding omitted for clarity.

Table 4.19: Selected bond lengths (Å) and angles (°) of the crystal structures for [Cu(**L9**)$_2$] and the methoxy-substituted [Cu(**L10**)$_2$] compared with those of the analogous energy minimised gaseous structures.

Bond lengths /Å and angles/°[a]	Solid state structures				Energy minimised structures	
	[Cu(**L9**)$_2$]		[Cu(**L10**)$_2$]		[Cu(**L9**)$_2$]	[Cu(**L10**)$_2$]
M-O_1	1.9244(11)		1.8658(10)		1.907	1.892
M-N_1	1.9986(13)		2.0020(13)		2.035	2.035
O_1-M-O_2	180.0		180.0		179.8	179.8
N_1-M-N_2	180.0		180.0		179.9	179.9
O_1-M-N_1	91.03(5)		92.24(5)		91.20	91.42
O_2-M-N_1	88.97(5)		87.76(5)		88.79	88.57
Y_1···O_2	2.7005(18)		2.604(4)	2.614(4)	2.677	2.665
O_1-M-N_1-Y_1	160.55(10)		168.7(2)	162.8(2)	170.52	171.88
R-H-N_1-Y_1	132(1)	131(1)	179.92	180.00	136.80	137.44
N_1-Y_1-H	106(1)		121.5(4)	120.8(4)	107.12	108.11
C_5-$O_1O_2N_1N_2$ plane	1.368	2.598	0.0	0.0	0.675	0.555
Y-$O_1O_2N_1N_2$ plane	0.418	0.627	0.238	0.374	0.205	0.175

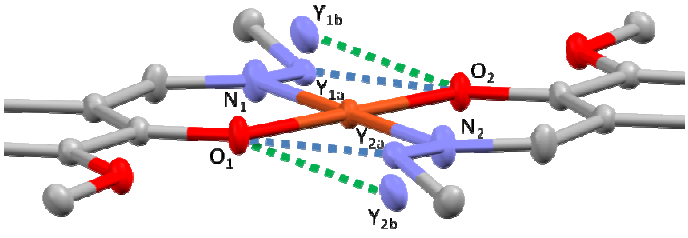

Figure 4.32: Partial structure of [Cu(**L10**)$_2$] with the disordered terminal nitrogen atoms, labelled Y_1 and Y_2, and the corresponding close contacts with the phenolate oxygen atoms, O_1 and O_2.

4.3.3. The effects of hybridisation and planarity on extraction strength

The large decrease in extraction strength observed when the oximic OH group is replaced by an NHR unit[28] appears to be related to the reduced planarity of the N-NHR unit which provides the inter-ligand hydrogen bonding (see Sections 4.3.1 and 4.3.2). The significance of this reduction in planarity was examined further by considering the structures of a related class of ligands, the phenolic semicarbazones as shown in Figure 4.33 (c), which has an acyl group instead of a hydrocarbon group at the terminal nitrogen atom of the hydrazone. Such semicarbazone ligands have been previously investigated at the University of Edinburgh and have been shown to have a lower $pH_{0.5}$ value for copper extraction than the hydrazone ligands.[31,32] Figure 4.33 shows the structures of the three semicarbazone ligands, **L13H**-**L15H**, used in this section to compare extraction strengths, solid state structures and energy minimised structures (calculated using DFT) with the unsubstituted oxime and hydrazone ligands **L1H** and **L9H.**

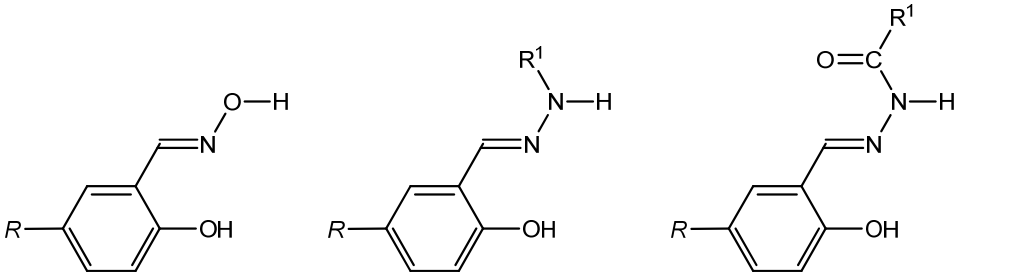

(a)

	R
LH	
L1H	^{t}Bu

(b)

	R	R^1
LH		
L9H	^{t}Bu	Me

(c)

	R	R^1
LH		
L13H	C_9H_{19}	C_7H_{15}
L14H	Me	^{t}Bu
L15H	^{t}Bu	Me

Figure 4.33: Ligand structures for (a) phenolic aldoximes, (b) phenolic hydrazones and (c) phenolic semicarbazones and the specific structures of the three semicarbazones **L13H**-**L15H** compared with the oxime and hydrazone analogues **L1H** and **L9H**.

The semicarbazone equivalent to **L1H** and **L9H**, **L13H**, with sufficient solubility to allow solvent extraction of copper to be performed was shown to have a $pH_{0.5}$ value significantly lower than the hydrazone **L9H**. Work of R. S. Forgan,[1] T. Lin[28] and J. Wood[32] at the University of Edinburgh has shown the copper extraction strengths of the ligands to vary in the order **L1H** > **L13H** > **L9H** ($pH_{0.5}$ = 1.68 < 2.10 < 4.42).

A crystal structure[31] of the semicarbazone ligand, **L14H** (Figure 4.34 (c)) indicates that the semicarbazone unit is much more nearly planar than that of the the "simple" hydrazones. Parts of the X-ray determined structures of [Cu(**L1**)$_2$] and [Cu(**L9**)$_2$] are included in Figure 4.34 for comparison.

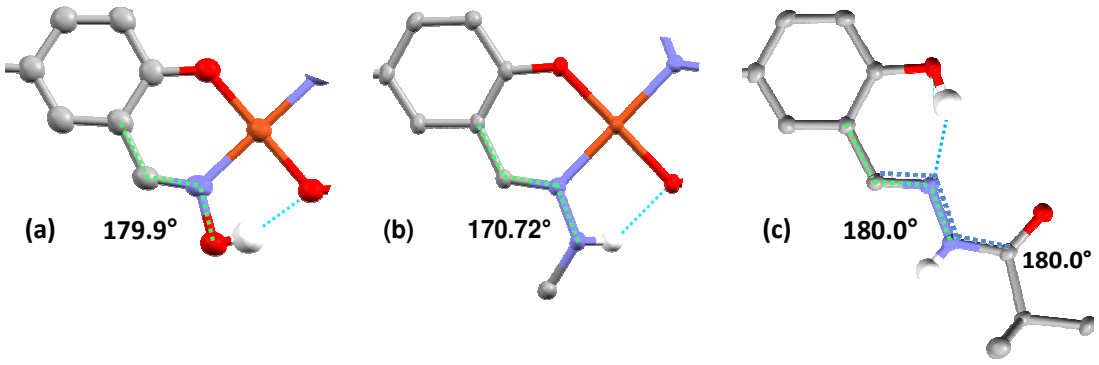

Figure 4.34: Parts of the crystal structures of (a) [Cu(**L1**)$_2$], (b) [Cu(**L9**)$_2$] and (c) the semicarbazone ligand **L14H.** The torsion angle C-C=N-X, where X = O for [Cu(**L1**)$_2$] and N for [Cu(**L9**)$_2$] and **L14H**, is also highlighted. Together with the C=N-N-C torsion angle for **L14H**.

The energy minimised structure of [Cu(**L1**)$_2$], [Cu(**L9**)$_2$] (see Sections 4.2.2.2 and 4.3.2.) are compared with that of [Cu(**L15**)$_2$] in Figure 4.35.

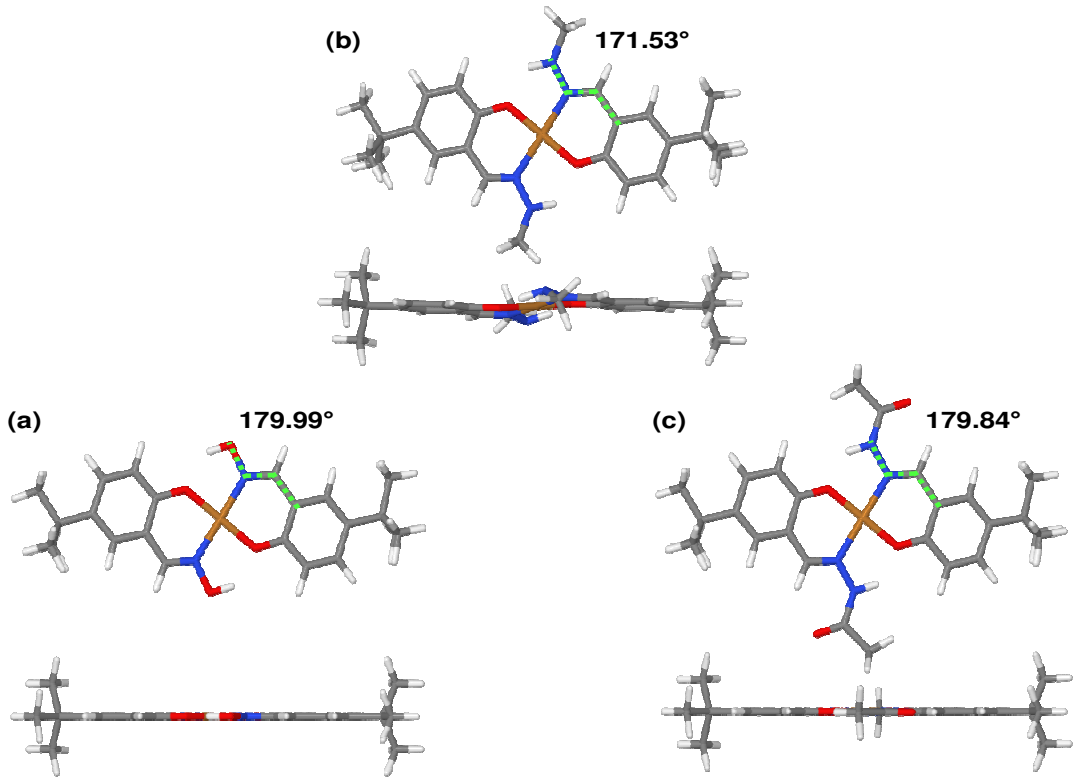

Figure 4.35: The energy minimised structures for (a) [Cu(**L1**)$_2$], (b) [Cu(**L9**)$_2$] and (c) semicarbazone complex [Cu(**L15**)$_2$] calculated at B3LYP/6-31+G(d,p). The torsion angle C-C=N-X, where X = O for [Cu(**L1**)$_2$] and N for [Cu(**L9**)$_2$] and [Cu(**L15**)$_2$], is also highlighted.

As reported in Section 4.2.2.2., the energy minimised structure of [Cu(**L1**)$_2$] (a in Figure 4.35) has an almost perfectly planar C-C=N-O unit associated with the oxime group (torsion angle, 179.99°). The planarity of the C-C=N-N unit in the [Cu(**L9**)$_2$] complex (b in Figure 4.35) is reduced due with a torsion angle of 171.53°. The energy minimised structure of the semicarbazone complex [Cu(**L15**)$_2$] confirms what was noted with the crystal structure for **L14H** that the carbonyl group increases planarity of the unit and the terminal nitrogen atom in C=N-*N*H(CO)R appears to be sp^2 hybridised.

4.3.3.1. Enthalpies of formation for $[Cu(L)_2]$ hydrazone complexes

Enthalpies of formation were calculated for the hydrazone copper complexes $[Cu(\mathbf{L9})_2]$-$[Cu(\mathbf{L12})_2]$ as described in Section 4.2.5.1. for the oxime complexes. The energy minimised 3-X-substituted structure of a phenolic hydrazone dimer, $[(\mathbf{LH})_2]$, and the Cu^{2+} ion were calculated and the sum of the energies were compared with that of the corresponding complex $[Cu(\mathbf{L})_2]$, Figure 4.36.

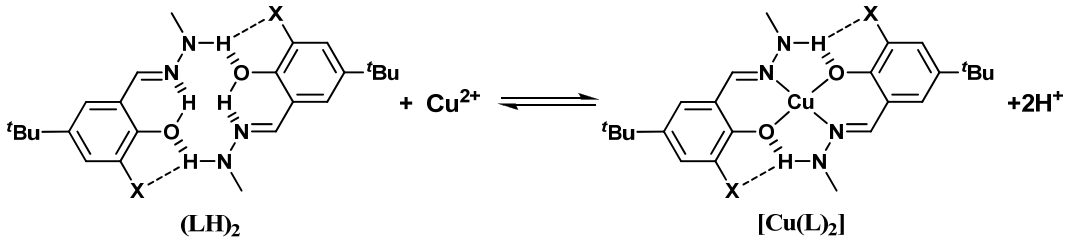

Figure 4.36: Cation exchange reaction for complex formation of 3-X-substituted phenolic hydrazone copper complexes.

The enthalpy of formation, ΔH_f, was calculated for $[Cu(\mathbf{L})_2]$ according to equation **4.9** and the individual H_g values for each species and the calculated ΔH_f for each hydrazone complex are given in Table 4.20.

Table 4.20: The minimised energies, $\boldsymbol{E_0}$, with thermal corrections, $\boldsymbol{H_{corr}}$, for each species highlighted in equation **4.9** and the calculated $\Delta \boldsymbol{H_f^\circ}$ for each $[Cu(\mathbf{L})_2]$ complex.

LH	**L9H**	**L10H**	**L11H**	**L12H**
$(E_0 + H_{corr})_{[\boldsymbol{LH}]_2}$/au	-1305.1560	-1534.1343	-6447.4316	-1714.1629
$(E_0 + H_{corr})_{[Cu^{2+}]}$/au	-1639.2494	-1639.2494	-1639.2494	-1639.2494
$[(E_0 + H_{corr})_{[\boldsymbol{LH}]_2} + (E_0 + H_{corr})_{[Cu^{2+}]}]$/au	-2944.4055	-3173.3838	-8086.6810	-3353.4124
$[(E_0 + H_{corr})_{[Cu(\boldsymbol{L})_2]}$/au	-2944.3740	-3173.3552	-8086.6544	-3353.3879
ΔH_f° /kJ mol^{-1}	82.7	75.1	69.9	64.2
$pH_{0.5}$ **LH**	4.42	4.54	1.23	2.01

The correlation between the enthalpies of formation of the hydrazone complexes, [Cu(**L9**)$_2$]-[Cu(**L12**)$_2$] with the strength of the hydrazones as copper extractants (Figure 4.37) is not as well defined as for the oxime extractants (Figure 4.11).

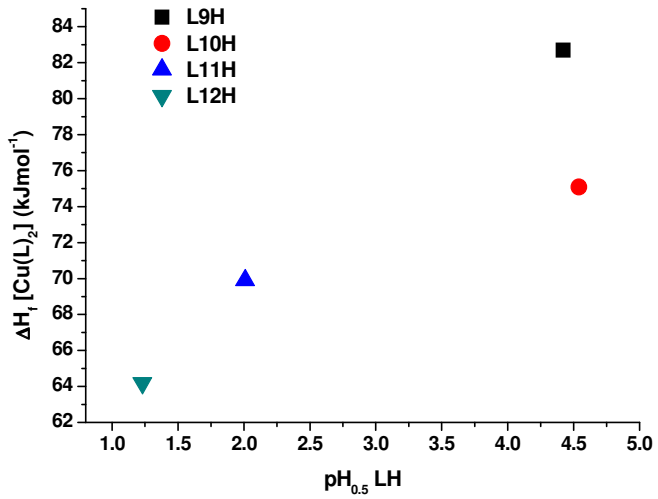

Figure 4.37: A plot of ΔH_f values for each of the [Cu(**L**)$_2$] complexes (where **L** = **L9**, **L10**, **L11** and **L12**) compared to the $pH_{0.5}$ value of the corresponding ligands **L9H**, **L10H**, **L11H** and **L12H** as copper extractants.[28]

The ΔH_f values become less favourable in the order [Cu(**L11**)$_2$] < [Cu(**L12**)$_2$] < [Cu(**L10**)$_2$] < [Cu(**L9**)$_2$]. Whilst this order is similar to that observed for the oximes **L1H** and **L5H**-**L7H** in which the hydrogen bond accepting groups X=Br, NO_2 and OMe stabilise the complex, unlike the oximes, it does not relate to the *observed* order of strength of copper extraction, **L10H < L9H < L11H < L12H** respectively. The possible reasons for this observation are discussed at the end of the next section.

4.3.3.2. The ΔH_f of [M(L)$_2$] for Oximes and Hydrazones.

Figure 4.38 shows the relationship between ΔH_f of [M(**L**)$_2$] and $pH_{0.5}$ of the corresponding extractant, **LH** for metal M. The substituted phenolic oximes are compared with the 3-X-substituted hydrazones.

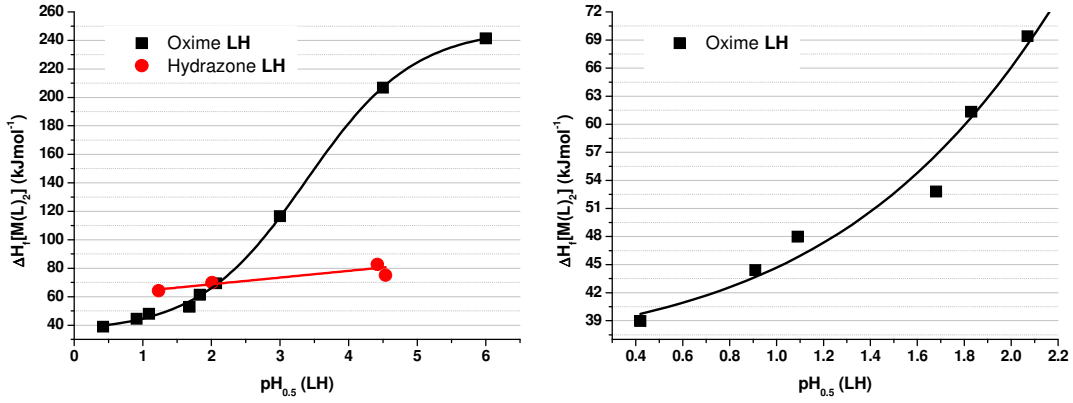

Figure 4.38: (a) Calculated enthalpies of formation for [M(**L**)$_2$] complexes compared to the pH$_{0.5}$ value at which metal, M is extracted by ligand **LH**. Values for the hydrazone ligands are shown in red. (b) The Calculated enthalpies of formation for [Cu(**L**)$_2$] oxime complexes compared to the pH$_{0.5}$ value of oxime, **LH**

A strong correlation is observed between the ΔH_f for [M(**L**)$_2$] and the pH$_{0.5}$of the extractant for the oxime ligands. The Hydrazone ligands do not, however, follow the same trend; a possible indication of the differences in the extraction mechanisms between the oxime and hydrazone ligands.

In all the previous cases described in this chapter, in which the pH$_{0.5}$ values for metal extraction were compared with the calculated gas phase enthalpies of formation of the metal complexes, a monotonic variation has been observed. The methoxy-substituted hydrazone **L10H** provides the only exception. It is possible that the conditions which are necessary for the approximately linear relationship between pH$_{0.5}$ and ΔH_f, notably that differences in solvation energy between the ligand dimer, [(**LH**)$_2$], and its metal complex, [M(**L**)$_2$], does not vary significantly when the 3-X-substituent or the azomethane substituent or the nature of the metal is varied, do not apply for **L10H**. This is unlikely because the 3-methoxy oxime, (**L7H**), does not fall out of line in the pH$_{0.5}$ vs. ΔH_f plot for the 3-X-substituted oxime ligands (see Figure 4.11).

The method used to determine the $pH_{0.5}$ values for **L9H** and **L10H** was anomalous. The high $pH_{0.5}$ value for copper loading by these extractants means that the copper precipitated from the aqueous feed solution when it was raised high enough for complete copper loading. Consequently solutions of preformed [Cu(**L9**)$_2$] and [Cu(**L10**)$_2$] were contacted with aqueous sulphate solutions of varying acidity to establish the pH at which copper transfer to the aqueous phase. The resulting "S-curves" (see Figure 4.18) are anomalously steep and thus it is possible that the derived $pH_{0.5}$ value (the pH at which the ligand shows a 50% loading by copper) cannot be compared with the conventionally determined values of **L11H** and **L12H**.

Despite the concerns over the anomalous $pH_{0.5}$ for the methoxy-substituted hydrazone, **L10H**, the results presented in this section allow us to conclude that:

- replacement of the oxime C=N-O-H in salicylaldoximes by an alkylated hydrazone C=N-N-R greatly reduces the strength as a copper extractant.
- the introduction of substituents in the 3-position greatly influence extraction strength and, like the salicylaldoximes, groups which are both electron withdrawing and good hydrogen bond acceptors, e.g. NO_2 or Br, are the most effective in enhancing strength of copper extraction.

The DFT calculations support other evidence to suggest that

- the 3-nitro-substituent in **L12H** results in the free ligand showing an unusual tautomeric form where the phenolic hydrogen atom is hydrogen bonding to the nitro-substituent and not the oximic nitrogen, resulting in the E-form of the oxime group.
- the hybridization of the terminal nitrogen atom in the free ligands and hydrazone complexes are not "pure" sp^2 resulting in the non-planar hydrazone unit. This may partly account for these ligands being weaker extractants than the oximes because the inter-ligand hydrogen bonding is weaker.

4.4. Conclusions and Future Work

The DFT calculations described in this chapter have provided an insight into the origin of structure/activity relationships associated with salicylaldoxime and phenolic oxime-based copper extractants. The calculated gas phase structures of the free ligands and, in particular, the hole-sizes in the dimeric *pseudo*-macrocycle correspond closely to those determined by single crystal X-ray structure determination, and calculated enthalpies of dimerisation are consistent with the buttressing effects of hydrogen bonding shown by 3-X-substituents.

The calculations are particularly useful dealing with the copper complexes because solid state structure determinations have been shown not to be useful in interpreting the influence of the 3-X-substituents as subtle differences in the inner- and outer-coordination spheres of the copper complex structures, due to the influence of intermolecular interactions with the axial sites of the copper atoms. It seemed the variations of structure in the energy minimised structures in the gaseous state can be ascribed to the electron-withdrawing/accepting, the hydrogen bond accepter properties and the steric nature of the 3-X-substituent.

The use of DFT in determining $[M(\mathbf{L})_2]$ formation enthalpies has been of particular use in understanding the relationship between the relative stabilities of the free ligand dimers of an extractant, $[(\mathbf{LH})_2]$, and that of its metal complex. This method could, in theory, also be applied to a wide range of metal extraction systems in the effective development of ligand efficacy and selectivity.

4.5. References

(1) Forgan, R. S.; Henderson, D. K.; McAllister, F. E.; Tasker, P. A.; White, F. J.; Campbell, J.; Swart, R. M. *Canadian Metallurgical Quarterly* **2008**, *47*, 293.

(2) Forgan, R. S.; Wood, P. A.; Campbell, J.; Henderson, D. K.; McAllister, F. E.; Parsons, S.; Pidcock, E.; Swart, R. M.; Tasker, P. A. *Chem. Commun.* **2007**, 4940.

(3) Forgan, R. S., PhD Thesis, University of Edinburgh, 2008.

(4) Szymanowski, J. *Hydroxyoximes and Copper Hydrometallurgy*; CRC Press: Boca Raton, USA, 1993.

(5) Szymanowski, J.; Borowiak-Resterna, A. *Crit. Rev. Anal Chem* **1991**, *22*, 519.

(6) K.Mereiter *Private Communication* **2002**.

(7) Wan, J.; Wang, S.-y.; Wen, Y.-h.; Ye, S.-j.; Ouyang, P.-k.; Zhang, S.-S. *Chem. Res. Chin. Univ.* **2005**, *21*, 415.

(8) Potocnak, I.; Heinemann, F. W.; Rausch, M.; Steinborn, D. *Acta Crystallogr., Sect. C: Cryst. Struct. Commun.* **1997**, *53*, 54.

(9) Lide, D. R. *Handbook of Chemistry and Physics* 88th ed. ed.; CRC Press taylor and francis, 2007.

(10) Bernstein, J.; Davis, R. E.; Shimoni, L.; Chang, N.-L. *Angew. Chem. Int. Ed.* **1995**, *34*, 1555.

(11) Johnson, D. K.; Murphy, T. B.; Rose, N. J.; Goodwin, W. H.; Pickart, L. *Inorg. Chim. Acta* **1982**, *67*, 159.

(12) Dubois, J. E.; Fakhrayan, H.; Doucet, J. P.; El Hage Chahine, J. M. *Inorg. Chem.* **1992**, *31*, 853.

(13) Mohan, M.; Kumar, A.; Kumar, M.; Jha, N. K. *Inorg. Chim. Acta* **1987**, *136*, 65.

(14) Ainscough, E. W.; Brodie, A. M.; Dobbs, A. J.; Ranford, J. D.; Waters, J. M. *Inorg. Chim. Acta* **1998**, *267*, 27.

(15) Massarani, E.; Nardi, D.; Tajana, A.; Degen, L. *J. Med. Chem.* **1971**, *14*, 633.

(16) Sreeja, P. B.; Kurup, M. R. P.; Kishore, A.; Jasmin, C. *Polyhedron* **2004**, *23*, 575.

(17) Sears, J. K.; Darby, J. R. *The Technology of Plasticizers*; John Wiley and Sons: New York, 1982.

(18) El-Hendawy, A. M.; Al-Kubaisi, A. H.; Shoair, A. F. *Monatshefte fuer Chemie* **1995**, *126*, 1291.

(19) Mino, T.; Ogawa, T.; Yamashita, M. *Heterocycles* **2001**, *55*, 453.

(20) Mino, T.; Shirae, Y.; Sakamoto, M.; Fujita, T. *J. Org. Chem.* **2005**, *70*, 2191.

(21) Iskander, M. F.; Khalil, T. E.; Werner, R.; Haase, W.; Svoboda, I.; Fuess, H. *Polyhedron* **2000**, *19*, 949.

(22) Samus, N. M.; Tsapkov, V. I.; Kerner, A. V. *Rus. J. General Chem. (Translation of Zhurnal Obshchei Khimii)* **2003**, *73*, 1611.

(23) Samus, N. M.; Prisakar, V. I.; Tsapkov, V. I.; Buracheva, S. A.; Gulya, A. P. *Pharmaceutical Chemistry Journal (Translation of Khimiko-Farmatsevticheskii Zhurnal)* **2004**, *38*, 373.

(24) Das, S.; Pal, S. *J. Mol. Struc.* **2005**, *753*, 68.

(25) Wu, L.-M.; Teng, H.-B.; Feng, X.-C.; Ke, X.-B.; Zhu, Q.-F.; Su, J.-T.; Xu, W.-J.; Hu, X.-M. *Crystal Growth & Design* **2007**, *7*, 1337.

(26) Forgan, R. S.; Davidson, J. E.; Galbraith, S. G.; Henderson, D. K.; Parsons, S.; Tasker, P. A.; White, F. J. *Chem. Commun.* **2008**, 4049.

(27) Forgan, R. S. PhD Thesis, University of Edinburgh, 2008.

(28) Lin, T., PhD Thesis, University of Edinburgh, 2009.

(29) Forgan, R. S.; Wood, P. A.; Campbell, J.; Henderson, D. K.; McAllister, F. E.; Parsons, S.; Pidcock, E.; Swart, R. M.; Tasker, P. A. *Chem. Commun.* **2007**, 4940.

(30) Smith, A. G.; Tasker, P. A.; White, D. J. *Coordination Chemistry Reviews* **2003**, *241*, 61.

(31) Gordon, R. J., PhD Thesis, University of Edinburgh, 2008.

(32) Wood, J. L., PhD Thesis, University of Edinburgh, 2005.

Phenolic Oxime Copper Complexes:
A Gas Phase Investigation

CHAPTER 5: Using Mass Spectrometry to Determine Relative Ligand Binding Strengths

A study using mass spectrometry to rank ligand binding strengths in solution.

Table of Contents

5.1. Introduction

5.1.1. Aims

This chapter investigates the use of electrospray ionisation mass spectrometry as a tool to probe the equilibria of copper(II) complex formation with phenolic oximes in solution. The initial aim was to determine whether or not mass spectrometry could be applied to determine the relative complexation strengths of a series of 3-X-substituted salicylaldoxime ligands[1] (and see Chapter 1 Section 1.5.3.) in a single phase, (Figure 5.1) and if a correlation can be made with ligand extraction strength in solvent extraction experiments.

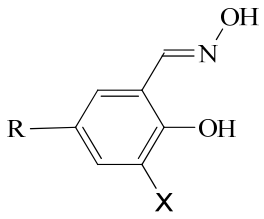

Figure 5.1: The basic salicylaldoxime ligand indicating the substituted 3-position. R = ^{t}Bu, ^{t}Oct , X = Br, Cl, H, ^{t}Bu.[1]

The developed methodology is also applied to more industrially applicable mixed ligand systems, blends of aldoximes (**L1H** and **L8H**) and the corresponding methyl-ketoximes (**L1bH** and **L8bH**). (Figure 5.2)

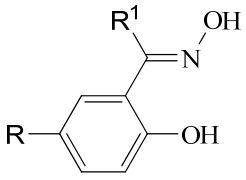

L1H, R=^{t}Bu R^1= H **L1bH**, R=^{t}Bu R^1= Me
L8H, R=^{t}Oct R^1= H **L8bH**, R=^{t}Oct R^1= Me

Figure 5.2: 5-*t*-Butyl-2-hydroxybenzaldehyde oxime (**L1H**) and 5-*t*-butyl-2-hyroxybutylacetophenone (**L1bH**)

The use of relative intensities of ions observed in the gas phase to predict the relative concentrations of the related complexes in solution requires an understanding of how ionisation efficiencies compare.

5.1.2. Using electrospray mass spectrometry for quantification

5.1.2.1. ESI-MS in solution equilibria studies

In an ideal system ESI-MS allows the acquisition of mass spectra directly from solution, analysis all of the equilibrium species in their starting environment with minimal ionisation influence and a direct correlation between solution phase concentrations and gas phase peak intensities. In a "real experiment", however, this is not the case as in most instances the ionisation process is not equally efficient for all analyte species.[2,3] In other cases the ions produced can undergo gas-phase reactions before reaching the analyser.[2,3]

The possible perturbations produced *via* the ionisation processes include changes in volume;[3,4] changes in species concentration as well as in temperature and pH.[3,5-7] As the mechanism for ion formation is still under debate[2,8] the reactions occurring are not fully understood, although it is widely accepted that reactions and rearrangements can occur both upon desolvation/ionisation and in the gas phase.[9,10]

Other problems reported involve the formation of solvent adducts which in can exist in solution but in certain cases can be attributed to ESI. The formation of metallated ions (e.g. with Na^+)[4,11] during ESI is very common but such occurrences almost never exist at equilibrium in solution.[4,11] ESI is also extremely sensitive to the instrumental parameters employed, such as spray voltage, tube lens voltage and offset, but in particular capillary temperature and cone voltage.[4,11-14] Possibly the most important variable when looking at solution equilibria with ESI-MS is that different chemical species have different response factors to ionisation,[2,5,6,11,15] due to

the different efficiencies of the processes which lead to the production of gas phase ions from species in solution.

5.1.2.2. Ionisation Efficiencies (IE's) of Analytes in Electrospray Ionisation

Despite the broad application of ESI and the numerous studies that have been undertaken, there is still insufficient knowledge to predict the IE of a particular compound at a known concentration.

As discussed in Chapter 1, two models, based on different assumptions, relating the MS signal intensity $I(A^+, ms)$ of an ion A^+ and its concentration in the electrosprayed solution $[A^+]$ have been proposed.

Based on the ion evaporation model of Iribarne and Thomson[16,17] and on the assumption that the rate of evaporation of an ion from a droplet is proportional to the concentration of the ion in the droplet, Tang and Kebarle,[2,15,18] derived the following relationship:

$$I(A^+, ms) = Pf \frac{k_A[A^+]}{k_A[A^+] + k_E[E^+]} I \qquad \textbf{5.1}$$

where E^+ refers to all the other electrolytes in the solution, k_A and k_E are rate constants for the transfer of the ions from the droplets to the gas phase, I is the electrospray current, f is the fraction of the droplets, charge that is converted into gas-phase ions, and P expresses the 'sampling efficiency' of the system (not all ions formed in the electrospray source are detected by the mass spectrometer due to losses during the transport of ions within the machine itself).

The parameters *k*, *f* and *P* are all dependent on the properties of the ions and on the solvent that is electrosprayed. Measurement of these parameters could give an almost complete quantitative picture of the ionization process. This, however, is a difficult task and in practice relative values that permit comparison are often sufficient.

Enke[19] also reached a similar conclusion, but with slightly different reasoning. He maintained that, according to the laws of electrostatics, the whole excess charge of a droplet should be located at its surface with the interior of the droplet remaining neutral. Based on this assumption he introduced a second model that leads to the Equation **5.2**:

$$R_A = Pf \frac{K_A C_A}{K_A C_A + K_E C_E}[Q] \qquad \textbf{5.2}$$

where *P* again denotes the efficiency of gas-phase ion transfer into the mass spectrometer and *f* is the fraction of an ions surface excess charge transferred into gas-phase ions. The selection of *P* and *f* for these constants follows the convention of Kebarle.

When this equation is compared with the Kebarle method it can be seen that they have the same form. In other words, the fraction of [*Q*] that is [A^+]s in **5.2** is the same as the fraction of *I* that is carried by A^+ in **5.1** except that, in **5.1**, the *k*'s are ion evaporation rate constants and, in **5.2**, the *K*'s are equilibrium constants for the phase distribution reaction.

Leito *et al.*[20] have proposed a method to quantify relative ESI ionisation efficiencies of a series of structurally similar analytes under predefined ionisation conditions. They detail the relative ionisation efficiencies of mono-protonated species at varying concentrations.

5.1.2.3. Matrix Effects and Ion Suppression

A second problem encountered when using any mass spectrometry technique as a quantitative analytical tool is matrix effects; the effects that contaminants and, in complex solutions, other analytes have on the observed mass spectrum of a desired analyte.

Ion suppression is one of the major matrix effects in mass spectrometry that spray-based ionisation methods suffer from, regardless of the sensitivity or selectivity of the mass analyzer used. It occurs in MS when a co-eluted material in the sample suppresses the ionisation of the analytes. In the case of direct injection techniques this co-elution is constant and unavoidable.

Ion suppression can ffect analysis in many ways, including influencing the detection capability, precision, and accuracy of the machine. The lack of insight into, and the knowledge of, the origin and mechanism of ion suppression makes it a difficult problem to solve. Protocols have, however, been developed over recent years not only to test for its presence but also to account for its effects and eliminate the risk of ion suppression altogether. These protocols are heavily orientated towards LC-MS methods but some of the information afforded can also be directly applied to direct-injection MS methods.

In the early 1990's many studies reported difficulties with reproducibility and accuracy when analyzing small quantities of analytes in complex mixture samples such as biological fluids.[2,21,22] Kebarle and Tang[2] originally described the phenomenon as the result of coeluted matrix components in LC-MS, affecting the detection capability, precision, or accuracy for the analytes of interest. Ion suppression was so termed due to these early indications of its existence showing a decrease in analyte signal. However, depending upon the type of sample, it also can be seen as an increase in the response of the analyte.[23] The term ion suppression was coined by Buhrman and coworkers[21] in their original work in 1996. The authors described it quantitatively as:

$$(100 - B)/(A \times 100) \quad \textbf{5.3}$$

where A and B are the unsuppressed and suppressed signals, respectively. Ion suppression occurs when a component in a sample influences the ionization of an analyte. Consequently it is important to realize that MS–MS methods are just as influenced by ion suppression effects as single MS techniques as the phenomena occurs before the initial MS stage and the advantages of MS–MS begin only after the ion formation.[24]

5.1.2.4. Mechanisms of Ion Suppression

Electrospray ionisation is usually a sensitive detection method for polar molecules. However, at high concentrations (>10^{-5} M), the approximate linearity of the ESI response often is lost.[25] This loss in response is thought to be due to a limited amount of charge available on ESI droplets upon formation.[25] It has also been suggested that a saturation of the ESI droplets at high analyte concentrations inhibits the ejection of ions trapped inside the droplets. In any case the mechanism is irrelevant as, in samples of high concentrations, competition for either space or charge most likely is occurring and suppression of signal is observed.

As mentioned above, both the characteristics and concentration of an analyte determine the efficiency of its ionization. The characteristics that decide whether a compound will out-compete others for the limited charge or space on the surface of the droplet include its surface activity and its basicity, as they directly influence the energy required for desolvation.[26]

In some of the studies presented in this chapter the presence of species other than the analyte is a major concern, as possible alteration of analyte signal intensities could occur. Fortunately there are several factors in the following studies that should significantly reduce ion suppression, these are:

- The basicity and size of the ligands used, which are not high compared with contaminants found in biological systems.
- It has been reported that, as fewer compounds give a response in negative mode, the analytes often are less subject to ion suppression.[27] This may be the case true for the complexes analysed in this study.
- In the cases where a Q-ToF system is used, the sample injection is automated with the amount of solution injected as low as 1-6uL. It was reported that low ESI flow rates lead to reduced signal suppression due to the generation of smaller, more highly charged droplets that are more tolerant to saturation.[28]

5.1.3. Using mass spectrometry to determine solution phase concentrations

For 3-X-substituted phenolic oxime extractants discussed in Chapters 1-4, strength as an extractant for copper(II) has been shown to be related to both the pK_a of the ligand[29] and the effects the 3-X-substituent has on the outer-coordination sphere of the resultant [Cu(**L**)$_2$] complex. This chapter considers whether mass spectrometry can be used to determine whether these influences on extraction strength can still determine the relative stabilities of complexes in a single phase solution.

If two different ligands, **LXH** and **LYH** are mixed with Cu^{2+}, three complexes can form; [Cu(**LX**)$_2$], [Cu(**LY**)$_2$] and [Cu(**LX**)(**LY**)], see Figure 5.3. If the species are prepared in a single phase, their relative concentrations can be represented by the equilibria shown in equation **5.4**.

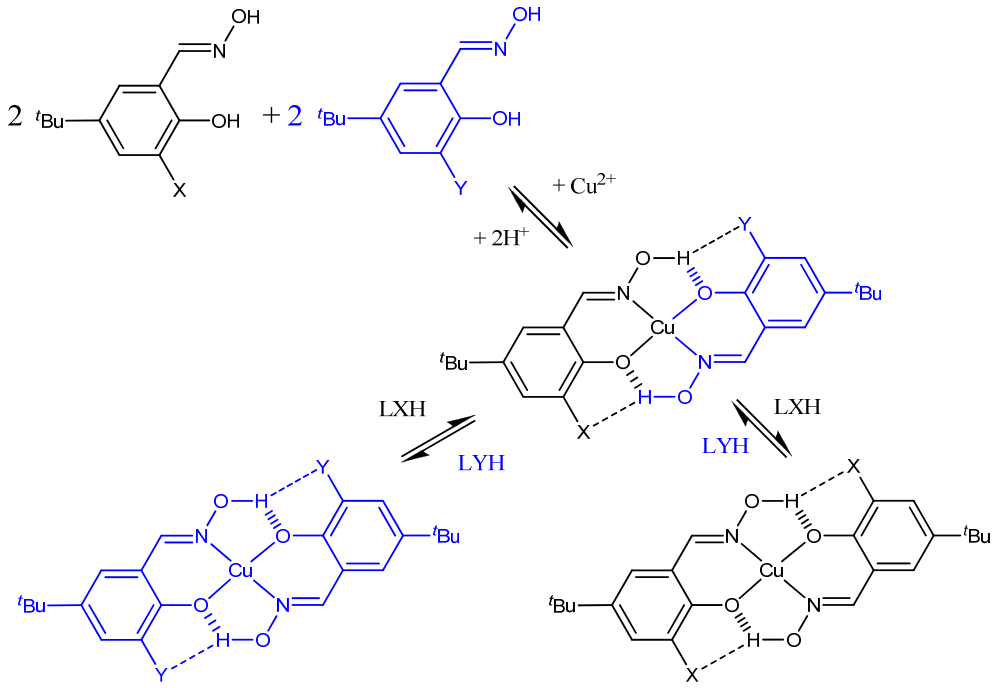

Figure 5.3: Solution equilibria when two different oxime ligands are present.

$$2\mathbf{LXH} + Cu^{2+} \overset{K_{[(\boldsymbol{LX})_2]}}{\rightleftharpoons} [Cu(\mathbf{LX})_2] + 2H^+$$

$$2\mathbf{LYH} + Cu^{2+} \overset{K_{[(\boldsymbol{LY})_2]}}{\rightleftharpoons} [Cu(\mathbf{LY})_2] + 2H^+ \qquad \mathbf{5.4}$$

$$\mathbf{LXH} + \mathbf{LYH} + Cu^{2+} \overset{K_{[(\boldsymbol{LX})(\boldsymbol{LY})]}}{\rightleftharpoons} [Cu\mathbf{LXLY}] + 2H^+$$

In a single phase, the relative concentrations of the $[Cu(\mathbf{L})_2]$ complexes are determined by the equilibrium constants, K in **5.4**. These in turn this will be related to the strengths of the ligands, **LH**, as *extractants* in a 2 phase system.

If the solvation energies and solubilities of ligands and complexes are not dependent on variations in ligand structure (see also Chapter 4 Section 4.2), $[Cu(\mathbf{L})_2]$ complexes with similar structures and solvation energies, should have similar ionisation efficiencies and the relative intensities of the $[Cu(\mathbf{L})(\mathbf{L}\text{-H})]^-$ ions (see Figure 5.4) resulting from the $[Cu(\mathbf{L})_2]$ complexes will be proportional to their concentrations in solution.

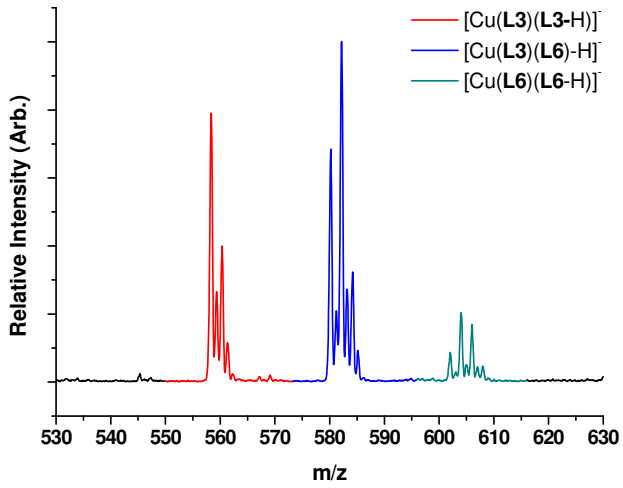

Figure 5.4: Mass spectrum obtained from a methanolic solution of equimolar amounts of **L3H** to **L6H** to Cu(II) , showing the relative intensities of the anions [Cu(**L3**)(**L3**-H)]$^-$, [Cu(**L3**)(**L6**)-H]$^-$, [Cu(**L6**)(**L6**-H)]$^-$.

The peak intensities of the [Cu(**L**)(**L**-H)]$^-$ species may not, however, be directly related back to the [Cu(**L**)$_2$] concentrations in solution as the ionisation efficiencies of the individual [Cu(**L**)(**L**-H)]$^-$ species may differ. It should be possible to detect changes in the position of solution equilibria caused by changing the stoichiometries of constituents, by monitoring changes in the relative peak intensities in the mass spectrum.

By measuring the relative [Cu(**L**)(**L**-H)]$^-$ peak intensities derived from a series of 2:1 **LH** to Cu^{2+} solutions with varying proportions of **LXH** and **LYH**, a relationship between the **LXH** to **LYH** ratio and the intensities of the [Cu(**L**)(**L**-H)]$^-$ species can be established. If the relative concentrations of complexes in solution can be effected by changing the **LH** to Cu^{2+} ratio, a shift in the peak intensities in the mass spectrum should also be observed. The change in *relative* peak intensities could then be used to infer changes in the relative concentrations of the [Cu(**L**)$_2$] complexes in solution. This should indicate the relative stability of the [Cu(**LX**)$_2$], [Cu(**LY**)$_2$] and [Cu(**LX**)(**LY**)] complexes and the relative complexing strengths of the two extractants, **LXH** and **LYH**. Figure 5.5 shows a graph of the theoretical relative intensities of [Cu(**LX**)(**LX**-H)]$^-$, [Cu(**LY**)(**LY**-H)]$^-$ and [Cu(**LX**)(**LY**)-H]$^-$ anions

with increasing stoichiometries of **LYH** in solution. The graph shows an ideal system where the **LXH** and **LYH** ligands have the same complexation strengths with copper and the resulting complexes have the same stability in solution and ionisation efficiencies. The relative intensities are, therefore, defined statistically.

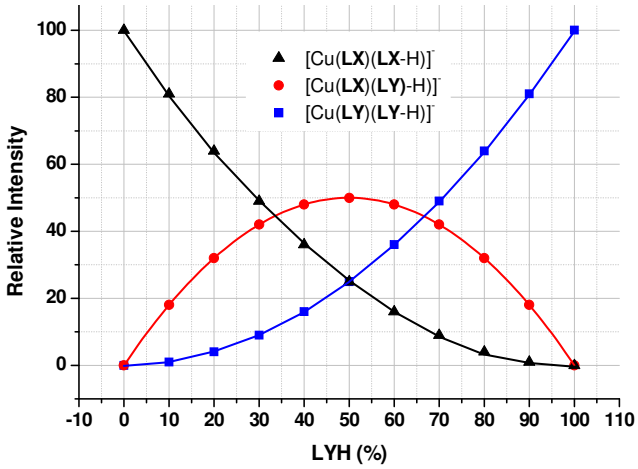

Figure 5.5: The theoretical relative intensities of [Cu(**LX**)(**LX**-H)]$^-$, [Cu(**LY**)(**LY**-H)]$^-$ and [Cu(**LX**)(**LY**)-H]$^-$ anions with increasing stoichiometries of **LYH** in solution.

The thesis is that, by applying a change to the system, *i.e* changing the speciation in solution, the relative intensities of the [Cu(**L**)(**L**-H)]$^-$ species can be altered and a change in the graph would be observed.

5.2. Results and Discussion

5.2.1. Solution concentrations of copper complexes of 3-X-substituted-5-*tert*-butyl-salicylaldoximes

The initial study was carried out using a Thermo-Fisher LCQ to define the effect of changing **LXH**:**LYH** ratios on the solution equilibria. Ligands **L1H**, **L3H** and **L6H** (X = H, ^{t}Bu and Br) were chosen for this study as they give the largest variation of extraction strength in solvent extraction experiments (see Chapter 1 Section 1.5.3.), with $pH_{0.5}$ values of 1.74, 2.64 and 0.42 respectively. The experiments were carried out as described in the experimental Section 5.4. Comparison between the relative intensities of [Cu(**LX**)(**LX**-H)]$^-$, [Cu(**LY**)(**LY**-H)]$^-$ and [Cu(**LX**)(**LY**)-H]$^-$ as the **LXH** to **LYH** ratios are varied when the total ligand to copper ratios are 2:1 and 4:1.

Three ligand competitions were studied; the first between **L1H** and **L6H**, (Figure 5.6 (a) and (b)) the second between **L1H** and **L3H** (Figure 5.6 (c) and (d)) and the third between **L3H** and **L6H**. (Figure 5.6 (e) and (f)). A convenient way to present the data from the [Cu(**LX**)(**LX**-H)]$^-$, [Cu(**LY**)(**LY**-H)]$^-$ and [Cu(**LX**)(**LY**)-H]$^-$ relative intensity plots in Figure 5.6 to establish whether a ligand, **LXH** (which is a known to be a stronger copper extractant in solvent extraction) competes with a weaker extractant, **LYH** in a single phase, is to define the % of **LXH** needed for the relative intensities of [Cu(**LX**)(**LX**-H)]$^-$ and [Cu(**LY**)(**LY**-H)]$^-$ to be equal. These data are presented in Table 5. 1.

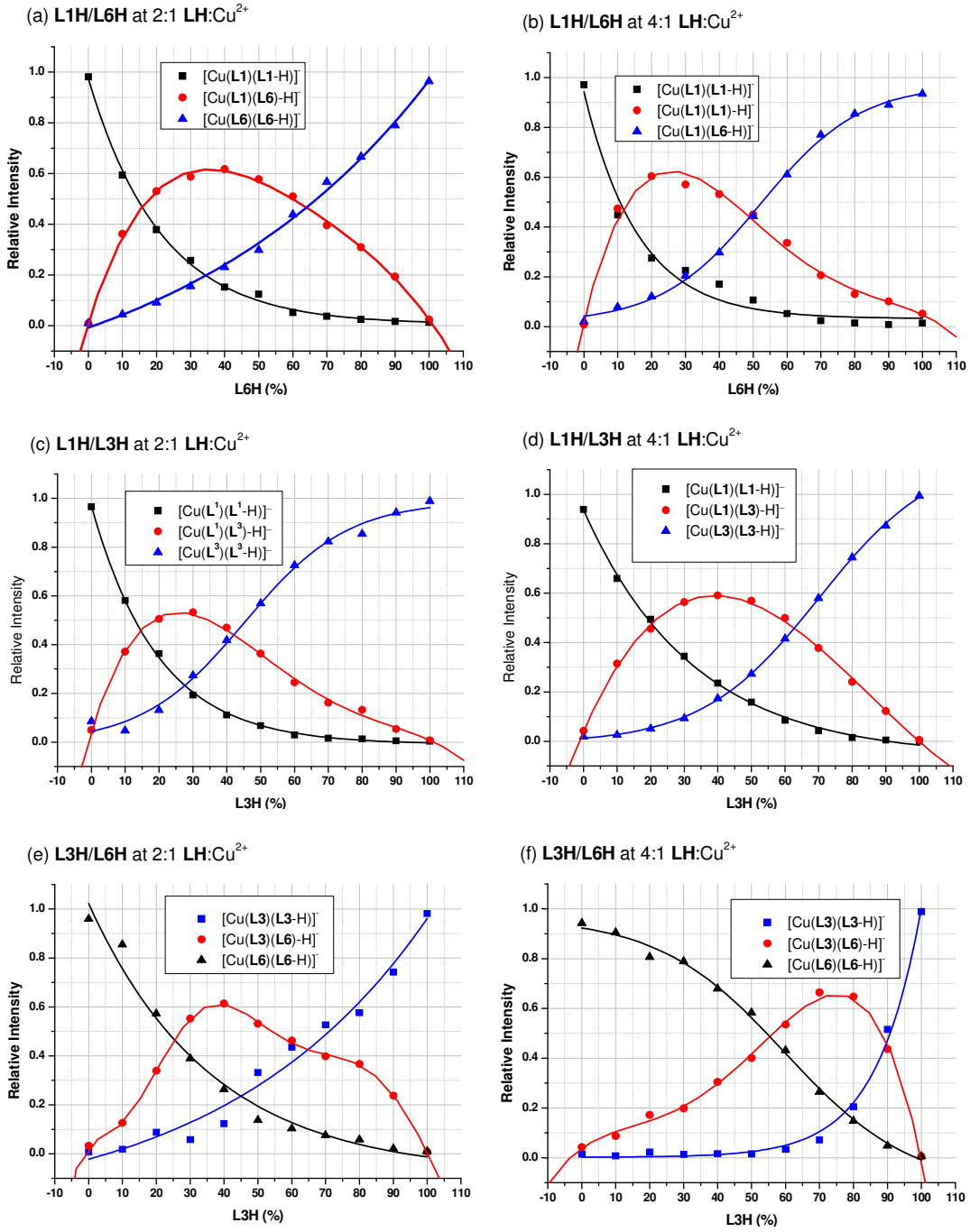

Figure 5.6: Plots of the relative intensities of [Cu(**LX**)(**LX**-H)]$^-$, [Cu(**LX**)(**LY**)-H]$^-$ and [Cu(**LY**)(**LY**-H)]$^-$ against the relative concentrations of **LXH** and **LYH** for (a) **L1H** and **L6H** at a 2:1 **LH**:Cu^{2+} ratio, (b) **L1H** and **L6H** at a 4:1 **LH**:Cu^{2+} ratio, (c) **L1H** and **L3H** at a 2:1 **LH**:Cu^{2+} ratio, (b) **L1H** and **L3H** at a 4:1 **LH**:Cu^{2+} ratio, (a) **L3H** and **L6H** at a 2:1 **LH**:Cu^{2+} ratio and (b) **L3H** and **L6H** at a 4:1 **LH**:Cu^{2+} ratio.

Table 5. 1: Showing the % of **LXH** needed to form equal relative intensities of [Cu(**LX**)(**LX**-H)]$^-$ and [Cu(**LY**)(**LY**-H)]$^-$ (the crossing point) in both the 2:1 and 4:1 **LH**:Cu^{2+}experiments, and the difference between the two, Δ_x.

LXH ($pH_{0.5}$)	**LYH** ($pH_{0.5}$)	[**LH**]:[Cu^{2+}] 2:1	[**LH**]:[Cu^{2+}] 4:1	Δ_x
L6H (0.41)	**L1H** (1.68)	34.5 %	29.1 %	-5.4 %
L1H (1.68)	**L3H** (2.64)	72.4 %	56.5 %	-15.9 %
L6H (0.41)	**L3H** (2.64)	55.0 %	22.5 %	-32.5 %

As expected, in each of the above experiments, when the LH to Cu^{2+} stoichiometry is increased from 2:1 to 4:1, the amount of the stronger extractant, **LXH**, required to observe equal amounts of [Cu(**LX**)(**LX**-H)]$^-$ and [Cu(**LY**)(**LY**-H)]$^-$ is reduced. When the **LH** to Cu^{2+} ratio of the solutions is 2:1 (Figure 5.6 (a), (c) and (e)) the graphs do, however, differ significantly from that of the "ideal" graph presented in Figure 5.5 This could be due to slight differences in the ionisation efficiencies of the [Cu(**LX**)$_2$], [Cu(**LY**)$_2$] and [Cu(**LX**)(**LY**)] complexes.

As changing the Cu^{2+} to **LH** concentration from 2:1 to 4:1 showed a significant change in the observed [Cu(**L**)(**L**-H)]$^-$ peak intensities, the next logical step was to vary the total **LH** to Cu^{2+} ratio further and keep the **LXH** to **LYH** ratio constant. This enabled more information to be obtained using fewer samples and simplified both sample analysis and data interpretation.

For this experiment **L1H** (X = H), **L5H** (X = Cl) and **L6H** (X = Br) were used. The **LXH** to **LYH** ratio was fixed at 1 : 1 and the total **LH** to Cu^{2+} ration was varied from 1 : 1 to 16 : 1, according to procedures outlined in Section 5.4.1.2., causing the copper to preferentially complex with one of the ligands. (Figure 5.7). For the competition between **L1H** and **L5H,** (a) in Figure 5.7, an exponential increase in the intensity of [Cu(**L5**)(**L5**-H)]$^-$ is observed and the intensities of the Cu(**L1**)(**L1**-H)]$^-$ and [Cu(**L1**)(**L5**)-H]$^-$ decrease accordingly as the supply of Cu^{2+} is fixed. This shift in intensities indicates that the copper preferentially binds with **L5H** over **L1H**, which is consistent with **L5H** being the stronger extractant in a two phase system.

The intensity of [Cu(**L1**)(**L1**)-H]$^-$, the less stable homoleptic complex, falls to almost zero when an excess of **L5H** in solution (relative to Cu^{2+}) but the intensity of the heteroleptic species [Cu(**L1**)(**L5**)-H]$^-$ does not fall below 20%.

A similar pattern is observed in the competition between the unsubstituted (**L1H**) and 3-bromo substituted (**L6H**) ligands (see Figure 5.7 (b)). The homoleptic [Cu(**L6**)(**L6**-H)]$^-$ species dominates and in this case the intensity of the heteroleptic [Cu(**L1**)(**L6**)-H]$^-$ species falls to *ca.* 5%, significantly lower than for the heteroleptic species, [Cu(**L1**)(**L5**)-H]$^-$ just described. This is consistent with the order of **LH** strength as extractants for copper, **L6H > L5H > L1H.**

The competition between the two relatively strong extractants the 3-chloro (**L5H**) and 3-bromo (**L6H**) substituted ligands is shown in Figure 5.7 (c). In this case the heteroleptic complex, [Cu(**L5**)(**L6**)-H]$^-$, dominates and its relative intensity/ concentration remains fairly constant as the **LH** to Cu^{2+}ratio is increased. The increase in the intensity of the [Cu(**L6**)(**L6**-H)]$^-$ species relative to the [Cu(**L5**)(**L5**-H)]$^-$ species is, again, consistent with **L6H** being the stronger ligand/extractant.

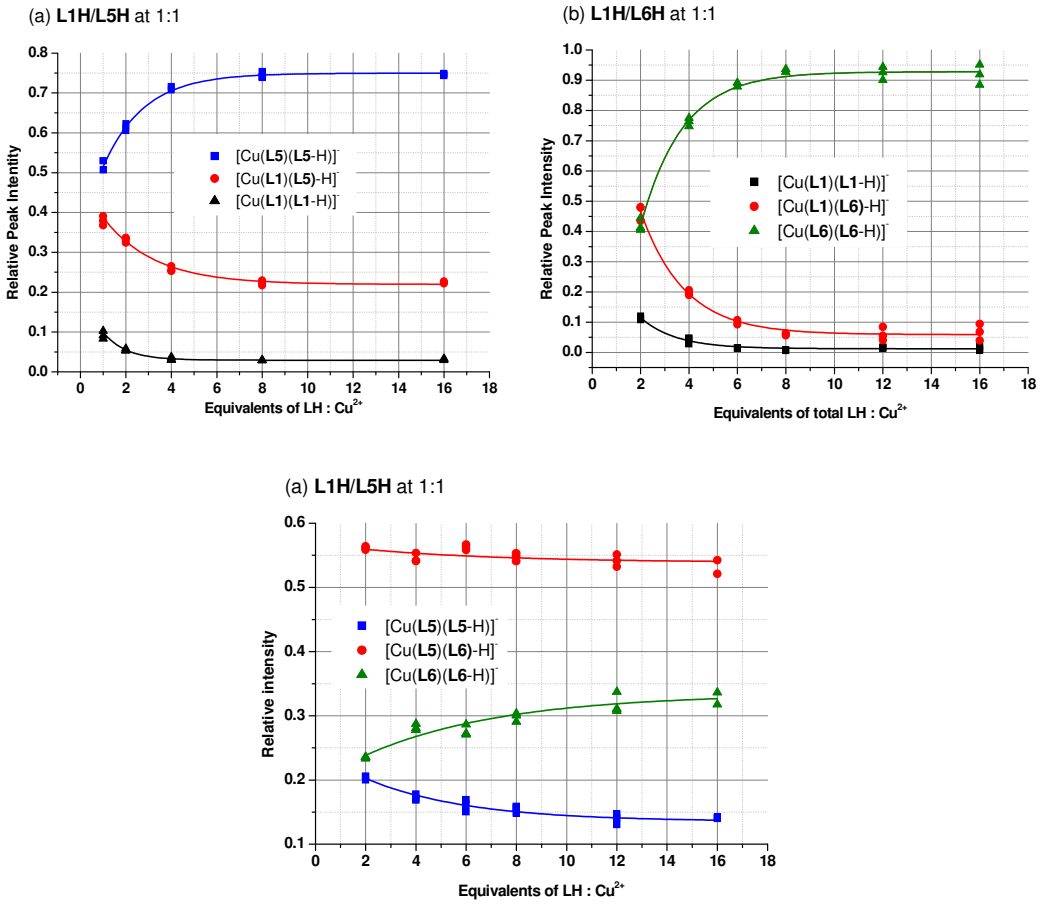

Figure 5.7: Plots of the relative intensities of [Cu(**LX**)(**LX**-H)]$^-$, [Cu(**LX**)(**LY**)-H]$^-$ and [Cu(**LY**)(**LY**-H)]$^-$ against increasing equivalents of **LH** to Cu^{2+} for (a) **L1H** and **L5H** at, (b) **L1H** and **L6H** and (c) **L5H** and **L6H.**

In each case a heteroleptic species, [Cu(**LX**)(**LY**)-H]$^-$ is observed but with varying relative intensities. When **LXH** and **LYH** have similar complexation strengths, as seen in the case for **L5H** and **L6H,** the formation of the heteroleptic species seems to be governed more by statistics, in that it is twice more likely to form than the two homoleptic analogues. As the difference in complexation strength between the ligands increases, the formation of the mixed species is governed more by the competition between the two ligands, and the heteroleptic complex forms to a lesser extent with increasing amounts of **LH**, as seen in the case for **L1H** and **L6H**.

The next section focuses on the application of the methods developed above to more industrially relevant ligands notably phenolic aldoximes and their corresponding methyl-ketoximes. (see also Figure 5.8)

5.2.2. Determining solution concentrations of copper complexes with phenolic aldoximes and ketoximes

Phenolic ketoximes are slightly weaker extractants for copper from sulphate leach solutions than aldoximes.[30] Structurally they differ from aldoximes by having an alkyl or aryl group in the R^1 position (see Figure 5.1). The presence of the R^1 group reduces the tendency of the oxime to hydrolyse under highly acidic stripping conditions. Introduced commercially in 1968, ketoximes in the formulations of 2-hydroxybenzophenone oxime were the first extractants used in the hydrometallurgical recovery of copper. These were followed by the introduction of other ketoxime based formulations or first generation extractants using 2-hydroxy-5-nonylacetophenone.[31]

5.2.2.1. Aldoxime/ketoxime extraction blends

In 1983, Henkel reported that mixtures of strong aldoxime extractants such as LIX 860 with moderately strong ketoxime extractants such as LIX 64N and LIX 84, are reagents with the fast kinetics and good copper extraction performance of the ketoximes without the detrimental properties of modifiers which used to be added to pure aldoxime extractants to enhance stripping.[32] Aldoxime/ketoxime mixtures today produce more copper than any single reagent system.[33] (Figure 5.8)

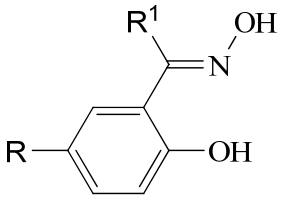

R	R^1	Commercial Name
C_9H_{19}	H	P50
C_9H_{19}	$C_6H_5CH_2$	P17
C_9H_{19}	CH_3	LIX84
$C_{12}H_{25}$	C_6H_5	LIX64
C_9H_{19}	C_6H_5	HS-LIX 65N
C_9H_{19}	C_6H_5	LIX70
$C_{12}H_{25}$	H	LIX860

Figure 5.8: Structures of some phenolic oximes used commercially

The modes by which ketoximes improve the efficiency of aldoximes in extractant blends is not fully understood.

5.2.2.1.1. Determining extraction strengths of L1bH and L1H/L1bH blend

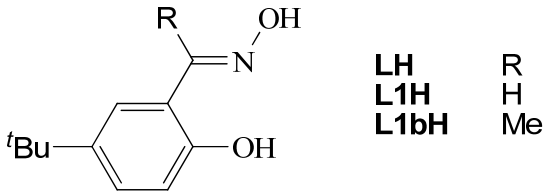

Figure 5.9: Structures of aldoxime **L1H** and ketoxime **L1bH**.

Experiments were carried out to assess the relative "strengths" as Cu^{2+} extractants of **L1H** and **L1bH** and a 1:1 mixture of **L1H** and **L1bH** (Figure 5.9). Stoichiometric quantities of the ligands in chloroform and copper sulphate in water at different pH values were mixed overnight, separated, the copper content of the organic phase determined by ICP-OES (see Section 5.4.3.) and the equilibrium pH of the aqueous phase recorded. (Figure 5.10) Figure 5.11 shows the deep green colour associated with uptake of copper(II) by a chloroform solution of **L1H** and **L1bH**.

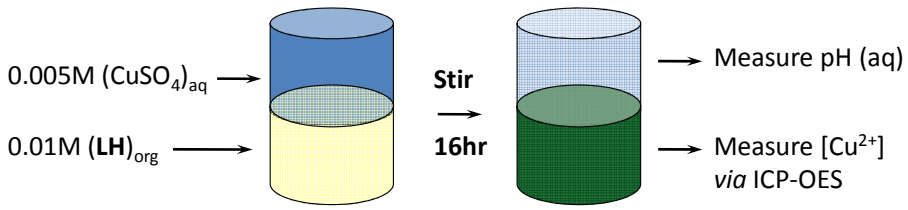

Figure 5.10: Solvent extraction protocol for the measurement of relative extractive efficacies of the extractant series. Equal volumes (5 ml) of the aqueous and chloroform solutions were used.

The percentage of theoretical loading of copper in the organic phase was plotted against equilibrium pH to give S-curves. (see also in Chapter 1)

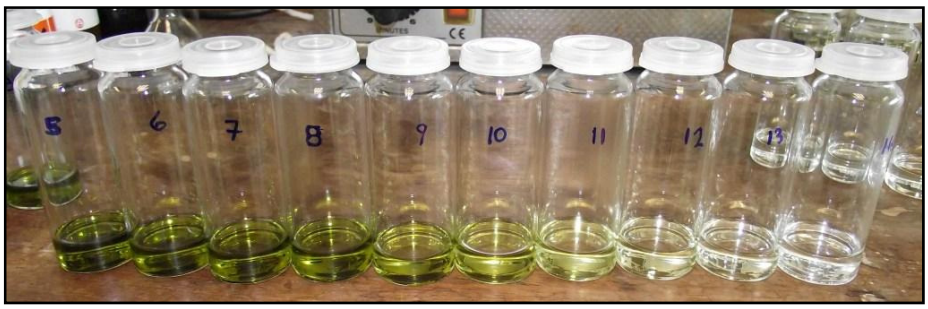

Figure 5.11: The organic phases after extraction of Cu^{2+} by an **L1H**:**L1bH** 1:1 solution in chloroform using the protocol defined in Figure 5.10.

It was not possible to obtain loading data for **L1bH** over the pH-range required to obtain a complete "S-curve" due to the limited solubility of its Cu^{2+} complex in n-butanol (the solvent used for ICP-OES). Extrapolation of the measurements made at low pH (Figure 5.12 (b)) enabled the $pH_{0.5}$ value to be estimated as 2.07.

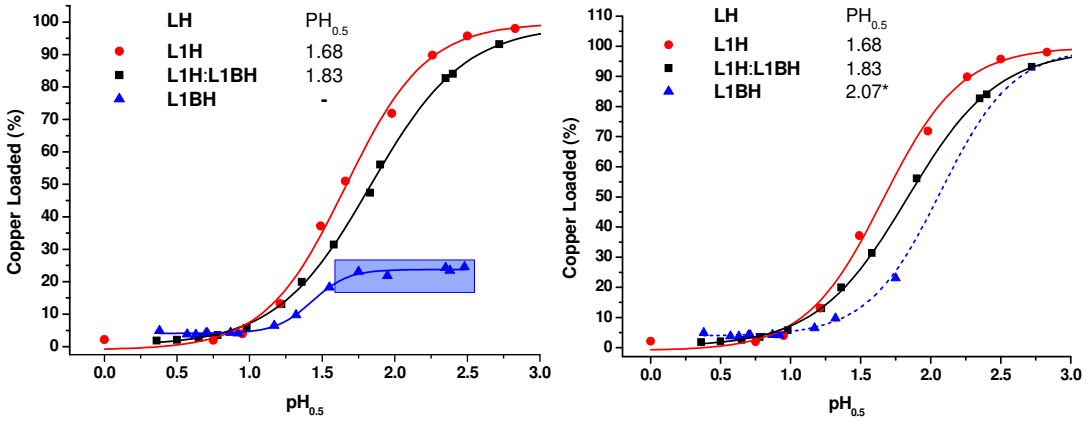

Figure 5.12: The extraction S-curves for **L1H** (red), **L1bH** (blue) and a 1:1 mix of **L1H** and **L1bH** (black) are shown on the left. The broken blue line in the plot on the right is a calculated full extraction S-curves for **L1bH,** extrapolated using the data obtained at low pH.

The measured extraction S-curve for **L1H** and that extrapolated for **L1bH** have similar slopes. The slope of the measured extraction S-curve for the mixed extractant experiment is distinctly different, with loading occurring over a larger pH range. The slope could potentially be tailored using different stoichiometries of each ligand or by increasing the stoichiometry of the extraction experiment so that **L1H** and **L1bH**

would be in competition to extract the Cu^{2+} ions in a similar way as shown in the experiments in the following section using mass spectrometry.

5.2.3. Competition between of 5-*tert*-butylsalicylaldoxime (L1H) and 2-hyroxy-5-*tert*-butylacetophenone (L1bH)

The competition between **L1H** and **L1bH** for copper in a single phase (acetonitrile solution) was carried out in a similar manner to the experiments in Section 5.2.1 following the solution composition using ESI-MS to determine the relative intensities gas phase anions of the type [Cu(**L**)(**L**-H)]$^-$. A comparison was made between the relative intensities of these anions with **LH** to Cu^{2+} ratios in solution of 2:1 and 4:1. (Figure 5.13 (a) and (b))

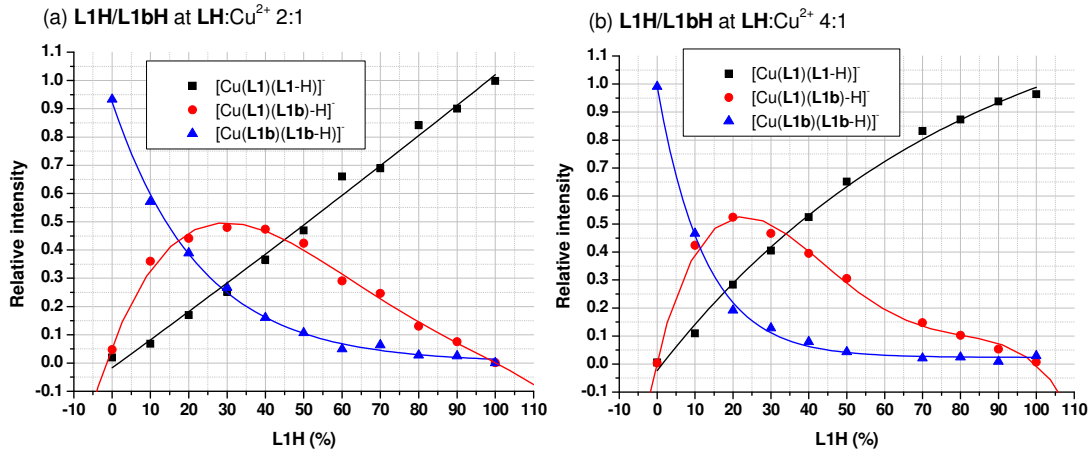

Figure 5.13: Plots of the relative intensities of [Cu(**L1**)(**L1**-H)]$^-$, [Cu(**L1**)(**L1b**)-H]$^-$ and [Cu(**L1b**)(**L1b**-H)]$^-$ against the relative concentrations of **L1H** and **L1bH** for at (a) a 2:1 **LH** to Cu^{2+} ratio and (b) a 4:1 **LH** to Cu^{2+} ratio.

When the ligand to Cu^{2+} ratio is increased from 2:1 to 4:1 the amount of the stronger extractant, **L1H,** required in solution for the intensities of [Cu(**L1**)(**L1**-H)]$^-$ and [Cu(**L1b**)(**L1b**-H)]$^-$ to be equal is reduced (from 28.4 % to 17.7 %). This confirms that **L1H** is the stronger complexant is a single phase solution when the Cu^{2+} concentration is limited.

When the **LH** to Cu^{2+} ratios in solution were varied whilst maintaining a fixed **L1H**:**L1bH** ratio of 1:1, The relative peak intensities of the anions Cu(**L1**)(**L1**-H)]$^-$, [Cu(**L1**)(**L1b**)-H]$^-$ and [Cu(**L1b**)(**L1b**-H)]$^-$ varied as shown in Figure 5.14 (a). A second experiment maintaining a fixed **L1H**:**L1bH** ratio of 3:7 was also carried out in order to confirm that similar trends can be observed when the weaker extractant, **L1bH**, is present in excess.

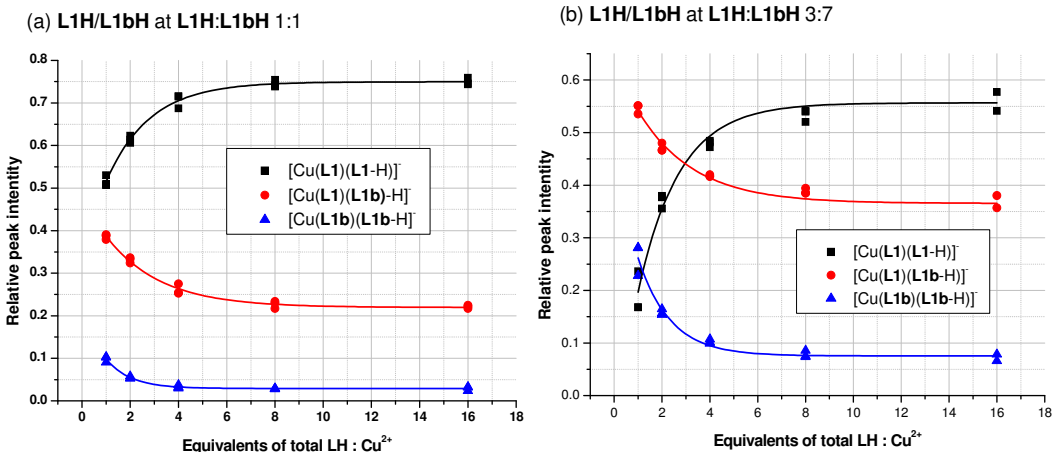

Figure 5.14: The relative intensities of [Cu(**L1**)(**L1**-H)]$^-$, [Cu(**L1**)(**L1b**)-H]$^-$ and [Cu(**L1b**)(**L1b**-H)]$^-$ with increasing **LH**:Cu^{2+}ratio at **L1H**:**L1bH** of (a) 1:1 and (b) 3:7.

Table 5.2: Showing the relative peak intensities of [Cu(**L1**)(**L1**-H)]$^-$, [Cu(**L1b**)(**L1b**-H)]$^-$ and [Cu(**L1**)(**Lb1**)-H)]$^-$ of **L1H** : **L1bH** ratios of 1 :1 (figure (a)) and 3 : 7 (figure (b)) at **LH** : Cu^{2+} ratios of 1:1 and 16:1 with the difference between the two difined as Δ_x.

	L1H : **L1bH** 1:1			**L1H** : **L1bH** 3:7		
LH:Cu^{2+}	1:1	16:1	Δ_x	1:1	16:1	Δ_x
[Cu(**L1**)(**L1**-H)]$^-$	0.525	0.75	**0.225**	0.2	0.55	**0.35**
[Cu(**L1**)(**L1b**)-H]$^-$	0.385	0.22	**-0.165**	0.54	0.36	**-0.16**
[Cu(**L1b**)(**L1b**-H)]$^-$	0.09	0.03	**-0.06**	0.26	0.07	**-0.19**

In both graphs in Figure 5.14 exponential growth in the relative intensity of [Cu(**L1**)(**L1**-H)]$^-$ is observed, indicating preferential complexation of **L1H** over **L1bH**. This increase plateaus at a **LH**:Cu^{2+} ratio of around 8:1.

In Figure 5.14 (a) The relative intensity of [Cu(**L1**)(**L1b**)-H]$^-$ decreases with an increasing **LH** to Cu^{2+} ratio, but again this decrease plateaus at a **LH** to Cu^{2+} ratio of 8:1 with a relative intensity of around 25%. This is surprising as the mixed species has a much higher intensity than [Cu(**L1b**)$_2$-H]$^-$, which has a relative intensity of 0.03% from a **LH** to Cu^{2+} ratio of 4:1 upwards, suggesting that the **L1bH** ligands in solution preferentially form the mixed [Cu(**L1**)(**L1b**)] complex over the [Cu(**L1b**)$_2$] complex.

In Figure 5.14 (b)) the relative intensity of the species [Cu(**L1**)(**L1b**)-H]$^-$ again decreases with an increasing **LH** to Cu^{2+}, but this decrease plateaus at a **LH** to Cu^{2+} ratio of 8:1 with a relative intensity this time of over 37.5%.. The [Cu(**L1b**)$_2$-H]$^-$ species shows a relative intensity of 7.5% from a **LH** to Cu^{2+} ratio of 8:1 upwards, indicating that the formation of [Cu(**L1**)(**L1b**)-H]$^-$ and [Cu(**L1b**)(**L1b**-H)]$^-$ is related to the concentration of **L1bH** relative to **L1H** in solution.

The comparison of the relative strengths of the aldoxime **L1H** and methyl-ketoxime, **L1bH**, as copper complexing agents as revealed by the relative intensities of the complex anions in the mass spectra is in accordance with the observed strengths as extractants, as defined by the solvent extraction experiments in Section 5.2.2.1. In order to make a similar comparison between ligands which more closely represent those used in commercial operations 5-*t*-octyl-2-hydroxyphenyl)ethanone oxime, **L8bH,** was synthesised to compare with the 5-*t*-octylsalicylaloxime, **L8H**. Plots of the relative peak intensities of the resultant anionic complexes with copper(II), [Cu(**L8**)(**L8**-H)]$^-$, [Cu(**L8**)(**L8b**)-H]$^-$ and [Cu(**L8b**)(**L8b**-H)]$^-$ against increasing equivalents of **LH** to Cu^{2+}(Figure 5.15) were recorded in a similar manner to those obtained for the competition between **L1H** and **L1bH**. The results are very similar and are again concordant with the aldoxime being the stronger complexing agent.

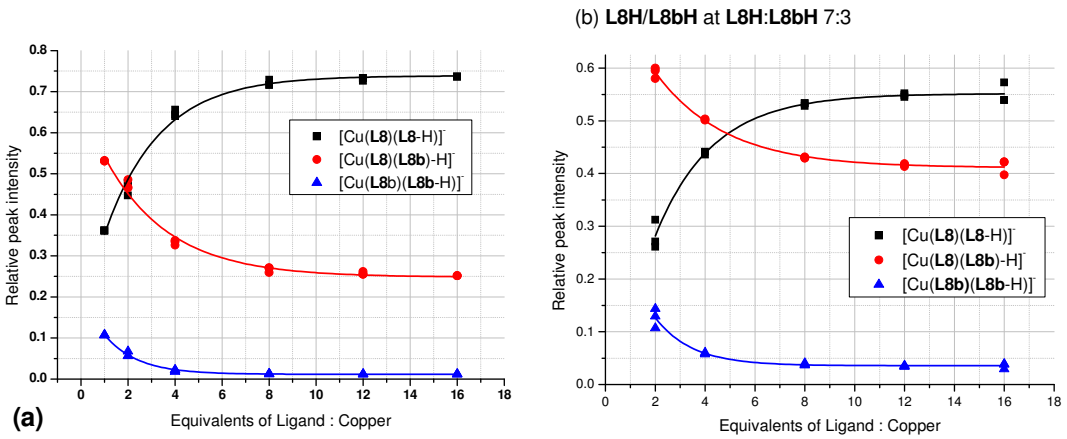

Figure 5.15: The relative intensities of [Cu(**L8**)(**L8**-H)]$^-$, [Cu(**L8**)(**L8b**)-H]$^-$ and [Cu(**L8b**)(**L8b**-H)]$^-$ with increasing **LH**:Cu^{2+}ratio at **L8H**:**L8bH** of (a) 1:1 and (b) 3:7

The availability of the two aldoximes **L1H** and **L8H**, which differ only in the nature of their 5-substituent (*t*-butyl vs. *t*-octyl) and show similar extraction strengths for copper ($pH_{0.5}$ 1.68 vs.1.73)[34], allows a comparison between two systems which can be assumed to have inner-coordination spheres of very similar stability but might show differences in gas phase analyses based on differing solvation energies. Whilst solvation energies of **L1H** and **L8H** and of [Cu(**L1**)$_2$] and [Cu(**L8**)$_2$] in acetonitrile might be expected to differ significantly on account sizes and shapes of the 5-*t*-butyl and 5-*t*-octyl groups, the *differences* between those of the free ligand and its complex less so. The free ligands are thought to preorganise, forming free ligand dimers which present a very similar size and shape to the surrounding solvent as the cooper complex. (Figure 5.16)

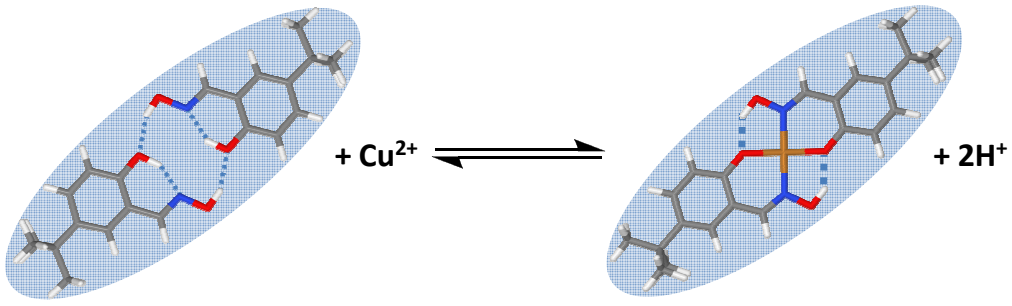

Figure 5.16: Relative sizes of the ligand dimer [(**L1**)$_2$] and the copper complex [Cu(**L1**)$_2$].

Plots of the relative peak intensities of the anionic complexes of **L1H** and **L8H** with copper(II), [Cu(**L1**)(**L1**-H)]$^-$, [Cu(**L1**)(**L8**)-H]$^-$ and [Cu(**L8**)(**L8**-H)]$^-$ against increasing equivalents of **LH** to Cu^{2+} (Figure 5.17) were recorded in a similar manner to those obtained for the competition studies described above. The relative intensities of the three anionic complexes show little change with increasing **LH** to Cu^{2+} ratio, indicating that no observable change is occurring in solution as seen when the aldoxime ligands (**L1H** and **L8H**) were subjected to competition with the corresponding ketoximes (**L1bH** and **L8bH**).

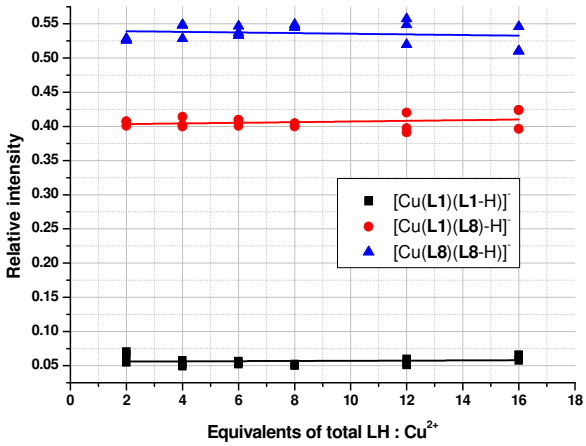

Figure 5.17: The relative intensities of [Cu(**L1**)(**L1**-H)]$^-$, [Cu(**L1**)(**L8**)-H]$^-$ and [Cu(**L8**)(**L8**-H)]$^-$ with increasing **LH**:Cu^{2+}ratio at **L8H:L8bH** of 1:1.

If the complexation strengths of the two ligands were similar in acetonitrile as in chloroform and the ionisation efficiencies of the copper complexes were the same then, statistically, the relative intensity of the heteroleptic anion, [Cu(**L1**)(**L8**)-H)]$^-$ should be twice that of [Cu(**L1**)(**L1**-H)]$^-$and [Cu(**L8**)(**L8**)-H]$^-$ as demonstrated in Figure 5.18.

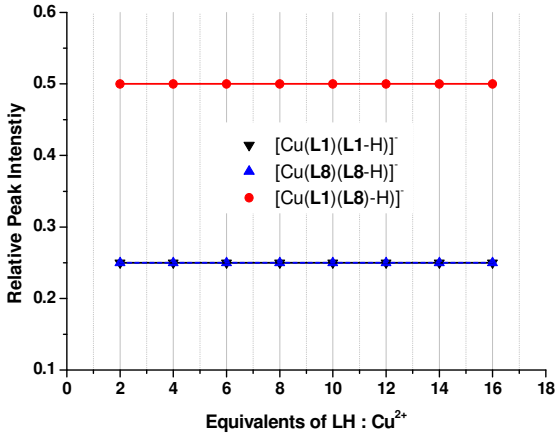

Figure 5.18 : Theoretical relative intensities of [Cu(**L1**)(**L1**-H)]$^-$, [Cu(**L1**)(**L8**)-H]$^-$ and [Cu(**L8**)(**L8**-H)]$^-$ with increasing **LH** to Cu^{2+}ratio at **L8H** to **L8bH** of 1:1 if the ionisation efficiencies of each species were equal.

In practise, however, although the relative intensities of [Cu(**L8**)(**L8**)-H)]$^-$, [Cu(**L1**)(**L1**-H)]$^-$ and [Cu(**L1**)(**L8**)-H)]$^-$ *don't* vary with increasing **LH** to Cu^{2+} stoichiometry, the relative intensity of the [Cu(**L8**)(**L8**)-H)]$^-$ is greater than that of the [Cu(**L1**)(**L1**-H)]$^-$ and [Cu(**L1**)(**L8**)-H)]$^-$ species. The difference between the theoretical and observed relative intensities for the [Cu(**L**)(**L**-H)]$^-$ species could be due to the rates/efficiencies of ionisation of each of the species. Solutions of a fixed **L1H** to **L8H** ratio of 1:1 and a **LH** to Cu^{2+} ratio of 16:1 were prepared with copper(II) concentrations of 5-80 μM. The relative intensities of the resultant [Cu(**L**)(**L**-H)]$^-$ species did not change with solution concentration, (see Figure 5.19) although the sum of the actual [Cu(**L**)(**L**-H)]$^-$ intensities increases. (Figure 5.19 (b))

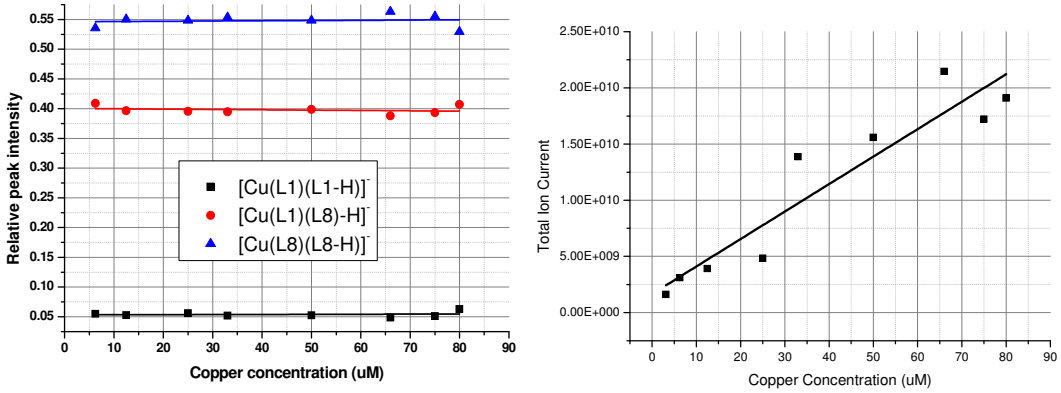

Figure 5.19: The relative intensities of [Cu(**L1**)(**L1**-H)]$^-$, [Cu(**L1**)(**L8**)-H]$^-$ and [Cu(**L8**)(**L8**-H)]$^-$ with fixed **LH** to Cu^{2+}ratio of 16:1 and **L8H** to **L8bH** of 1:1 with increasing copper concentration (a) and (b) the sum of actual intensities of the [Cu(**L**)(**L**-H)]$^-$ species with increasing copper concentration of the solution.

As the relative intensities of the anionic complexes do not vary with increasing ligand to Cu^{2+} stoichiometry *or* total solution concentration it is difficult to ascertain the origin of the relative intensities. One explanation could be that there is a linear relationship between ionisation efficiency and concentration which would account for little change in relative intensities with both increasing concentration and increasing **LH** to Cu^{2+} ratios. This does not, however explain the relative intensities of the [Cu(**L1**)(**L1**-H)]$^-$, [Cu(**L1**)(**L8**)-H]$^-$ and [Cu(**L8**)(**L8**-H)]$^-$ species and further studies are needed to explore the relationship between solvation energies and ionisation efficiencies.

5.2.4. Calculating formation constants for [Cu(L)$_2$] species using relative gas phase intensities

Theoretical plots for the data from Figure 5.15 (a) were calculated by Doug Harris at Cytec Ind., Stamford using the solver function of Excel to determine the relative formation constants of [Cu(**L8**)$_2$], [Cu(**L8**)(**L8b**)] and [Cu(**L8b**)$_2$]. The relative K values were determined by solving the simultaneous equations **5.5**.

$$K_{[Cu(L8)_2]} = \frac{[Cu(L8)_2]}{[L8H]^2[Cu^{2+}]} \quad K_{[Cu(L8)(L8b)]} = \frac{[Cu(L8)(L8b)]}{[L8H][L8bH][Cu^{2+}]} \quad K_{[Cu(L8b)_2]} = \frac{[Cu(L8b)_2]}{[L8bH]^2[Cu^{2+}]} \qquad \mathbf{5.5}$$

The relative concentrations of [Cu(**L8**)$_2$], [Cu(**L8**)(**L8b**)] and [Cu(**L8b**)$_2$] were taken from the observed data and the concentrations of **L8H**, **L8bH** and Cu^{2+} were varied to determine the values for $K_{[Cu(\mathbf{L8})2]}$, $K_{[Cu(\mathbf{L8b})2]}$ and $K_{[Cu(\mathbf{L8})(\mathbf{L8b})]}$. for this model the ionisation efficiencies were taken as being equal for [Cu(**L8**)$_2$], [Cu(**L8**)(**L8b**)] and [Cu(**L8b**)$_2$].

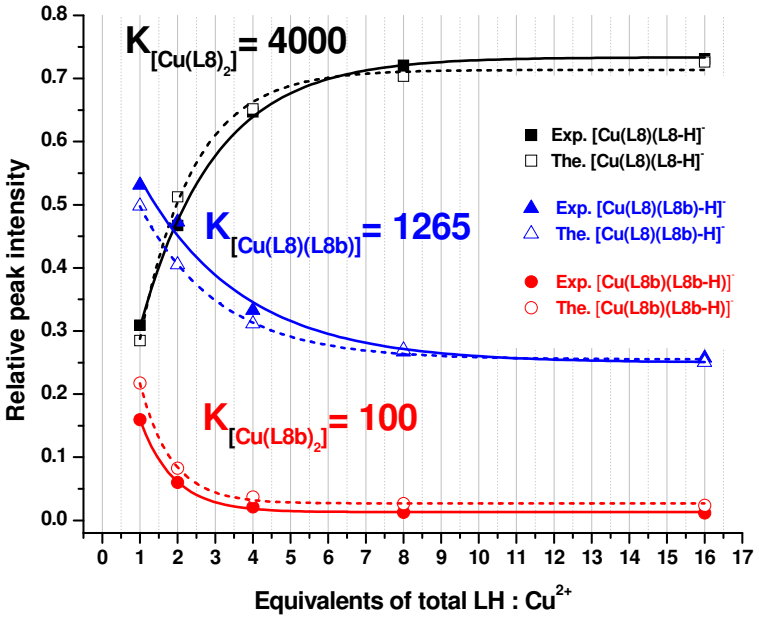

Figure 5.20: The relative intensities of [Cu(**L8**)(**L8**-H)]$^-$, [Cu(**L8**)(**L8b**)-H]$^-$ and [Cu(**L8b**)(**L8b**-H)]$^-$ with increasing **LH**:Cu^{2+}ratio at **L8H**:**L8bH** of 1:1 (solid lines), and the theoretical relative concentrations of [Cu(**L8**)$_2$], [Cu(**L8**)(**L8b**)] and [Cu(**L8b**)$_2$] used to calculate the relative formation constants, K.

As expected, the relative formation constant for [Cu(**L8**)$_2$] was the largest at 4000, that calculated for [Cu(**L8**)(**L8b**)] was 1265, and that for [Cu(**L8b**)$_2$] was 100, 40 times less than that for [Cu(**L8**)$_2$].

5.2.5. Relating actual peak intensities to solution concentration

In each of the experiments increasing the total **LH** to Cu^{2+} ratio (Figure 5.13 - Figure 5.15) the relative intensity of the anion derived from the complex of the stronger extractant was seen to increase and that of the anion derived from the complex of the

weaker extractant was seen to decrease. Interestingly, the stronger ligand didn't fully displace the weaker, even when present in sufficient quantities to completely complex all Cu^{2+} ions.

Further competition studies were carried out with **L8H** and **L8bH**. Here, instead of looking at the relative peak intensities the actual peak intensities with increasing **LH** to Cu^{2+} ratios, the actual intensities of the [Cu(**L8**)(**LX**-H)]$^-$, [Cu(**L8b**)(**L8b**-H)]$^-$ and [Cu(**L8**)(**L8b**)-H]$^-$ species were measured. Figure 5.21 shows the sum of the peak intensities for [Cu(**L8**)(**L8**-H)]$^-$, [Cu(**L8b**)(**L8b**-H)]$^-$ and [Cu(**L8**)(**L8b**)-H]$^-$ ratio showing an exponential increase.

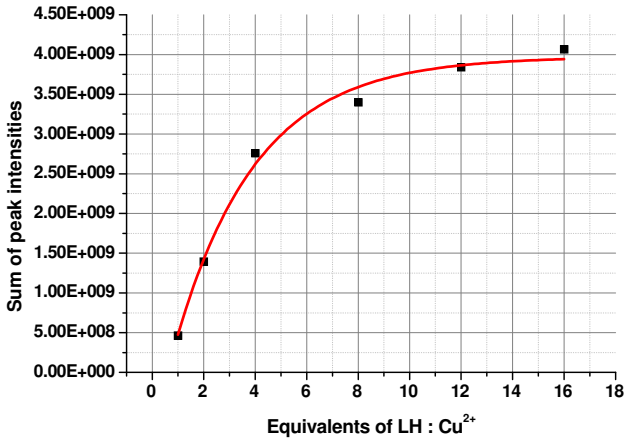

Figure 5.21: Sum of the peak intensities for [Cu(**L8**)(**L8**-H)]$^-$, [Cu(**L8**)(**L8b**)-H]$^-$ and [Cu(**L8b**)(**L8b**-H)]$^-$ with increasing **LH**:Cu^{2+} ratio.

What is unusual is that even at **LH** to Cu^{2+} ratio of 12:1 the exponential curve has not yet reached a plateau. In a two phase system at similar pH's the Cu^{2+} ions would be almost completely complexed with a **LH** to Cu^{2+} of 2:1[29,35] and so one would expect to see similar efficiencies in a single phase system.

The reason for this is that the equilibria for complexation must differ considerably in a single phase system as the anion of the copper salt is also present. This enables singly ligated complexes to form, the most currently observed in the gas phase being the zwitterionic [Cu^+(**L**-H)$^-$] species (highlighted red in equation **5.6**). (see also Chapter 6) What is apparent is that singly ligated species have a tendency to form at low **LH** to Cu^{2+} ratios.

$$LH + Cu(Oac)_2 \overset{K^1}{\rightleftharpoons} [(CuL)^+(Oac)^-] + HOac \overset{K^2}{\rightleftharpoons} [Cu(L)_2] + 2HOac$$

$$K^3 \updownarrow$$

$$[(Cu^+(L\text{-}H)^-] + 2HOac$$

5.6

This observation alters the way these experiments should be viewed, not as a competition between **LXH** and **LYH**, but as the propensity of each ligand to form the $[Cu(\mathbf{L})_2]$ species (defined by K^2 in equilibria). This does not detract from the validity of the study as the $[Cu(\mathbf{L})_2]$ species forms preferentially in the presence of sufficient amounts of **LH.**

The second issue that isn't taken into account in this study, and which will be discussed in Chapter 6, is the formation of metallated species such as $[Cu(\mathbf{L}\text{-}H)_2Na]^-$ and metallated aggregates such as $([Cu(\mathbf{L})_2\text{-}H]_2Na)^-$. Formation of such species will also influence from the total Cu^{2+} seen as $[Cu(\mathbf{L})_2\text{-}H]^-$ species in the mass spectra.

Figure 5.22, exploring these observations further, shows individual peak intensities for $[Cu(\mathbf{L8})(\mathbf{L8}\text{-}H)]^-$, $[Cu(\mathbf{L8b})(\mathbf{L8b}\text{-}H)]^-$ and $[Cu(\mathbf{L8})(\mathbf{L8b})\text{-}H]^-$ with increasing **LH** to Cu^{2+} ratio.

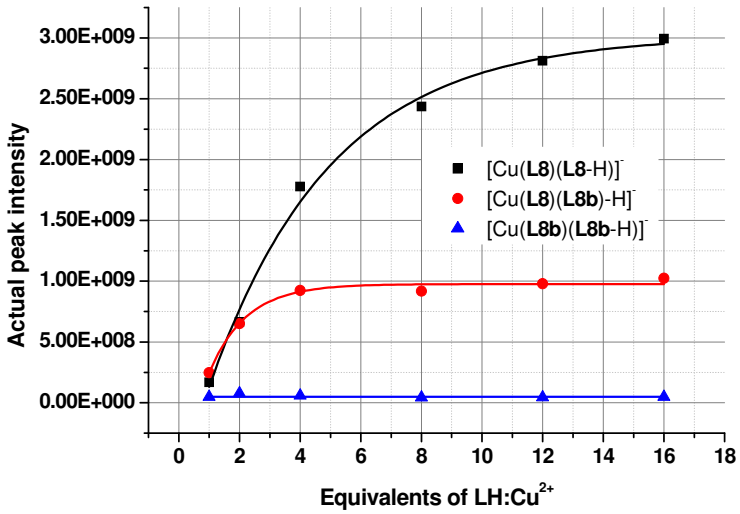

Figure 5.22: Peak intensities of $[Cu(\mathbf{L8})(\mathbf{L8}\text{-}H)]^-$, $[Cu(\mathbf{L8})(\mathbf{L8b})\text{-}H]^-$ and $[Cu(\mathbf{L8b})(\mathbf{L8b}\text{-}H)]^-$ with increasing **LH**:Cu^{2+} ratio.

An exponential increases in formation of [Cu(**L1**)(**L1**-H)]$^-$ is observed which, doesn't plateau even at a **LH** to Cu^{2+} ratio of 16:1. The curves for the [Cu(**L1**)(**L1b**)-H)]$^-$ and [Cu(**L1b**)(**L1b**-H)]$^-$ do, however, plateau at fairly low **LH** to Cu^{2+} ratios indicating that the formation of the mixed species is influenced heavily by the weaker extractant **L1bH**.

Although the LCQ has a fairly quick throughput, the direct injection source is not very suitable for quantitative analysis. A Waters Quadrupole-Time-of-Flight (Q-ToF) mass spectrometer was used in conjunction with an Aquity Sample Manager and Binary solvent Manager which enabled controlled autosampler injection.

The competition experiment was carried out as described in Section 5.4.1.2. using **L1H** and **L1bH**. This investigation was carried out in quadruplicate with the sum of the average [Cu(**L**)(**L**-H)]$^-$ peak intensities with increasing **LH** to Cu^{2+} ratio shown in Figure 5.23 (a) and the averaged intensities for the individual [Cu(**L1**)(**L1**-H)]$^-$, [Cu(**L1b**)(**L1b**-H)]$^-$ and [Cu(**L1**)(**Lb**)-H)]$^-$ species with increasing **LH** to Cu^{2+} ration shown in Figure 5.23 (b).

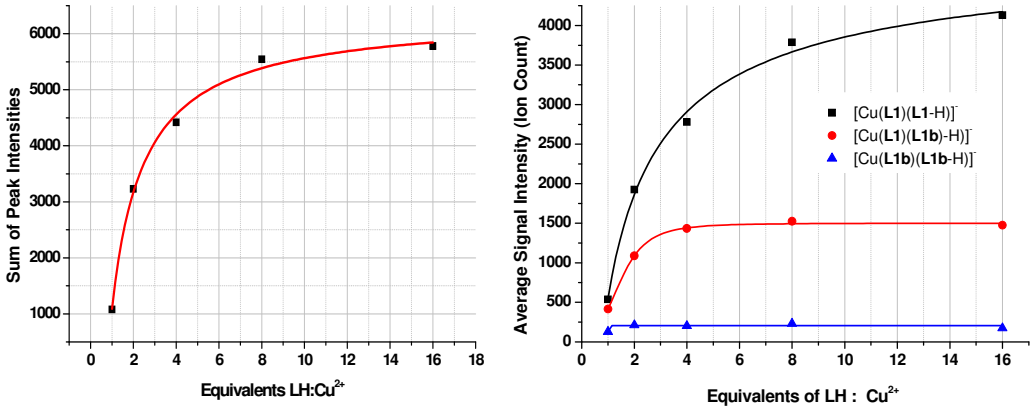

Figure 5.23: Sum of (a) and (b) average peak intensities for [Cu(**L1**)(**L1**-H)]$^-$, [Cu(**L1**)(**L1b**)-H]$^-$ and [Cu(**L1b**)(**L1b**-H)]$^-$ with increasing **LH**:Cu^{2+} ratio.

The Q-ToF data in Figure 5.23 confirmed the trends of the [Cu(**L**)(**L**-H)]$^-$ intensities observed using the LCQ in Figures 5.21 and 5.22.

Assuming that the [Cu(**L1**)(**L1**-H)]$^-$, [Cu(**L1**)(**L1b**)-H]$^-$ and [Cu(**L1b**)(**L1b**-H)]$^-$ have similar ionisation efficiencies, which, due to the small differences in size and hydrophobicity of the two ligands **L1H** and **L1bH** and the hydration energies of the resultant complexes, is possible, the data presented in Figures 5.22-5.23 corresponds well with the relative formation constants described in Figure 5.20.

The shapes of the curves for [Cu(**L1**)(**L1b**)-H]$^-$ and [Cu(**L1b**)(**L1b**-H)]$^-$ in Figures 5.21 and 5.23 are not fully understood and more work is needed to investigate both the formation and importance of the heteroleptic species and the influence **L1bH** has on its formation in a single phase system.

5.2.6. Importance of the heteroleptic [Cu(LX)(LY)] species

From the studies using relative peak intensities and the studies using actual peak intensities it was determined that the heteroleptic species observed could play an important role in the strength and efficacy of extractant blends. This was hypothesised as in the single phase experiments, even in cases where the strength of **LXH** was orders of magnitude greater than that of **LYH**, the [Cu(**LX**)(**LY**)-H]$^-$ species was always observed in significant quantities. In cases where the total **LH** to Cu^{2+} ratio was 16:1 and the **LXH** to **LYH** was 1:1 there was four times the amount of **LXH** required for complete complexation of the Cu^{2+} ions yet the [Cu(**LX**)(**LY**)-H]$^-$ species was always observed .

Figure 5.24 shows the relative peak intensities of [Cu(**L1**)(**L1**-H)]$^-$, [Cu(**L1**)(**L1b**)-H]$^-$ and [Cu(**L1b**)(**L1b**-H)]$^-$ derived from solutions of [$Cu(OAc)_2$] with **L1H** and **L1bH** with increasing mol% of **L1bH**, maintaining a **LH** to Cu^{2+} ratio of 16:1.

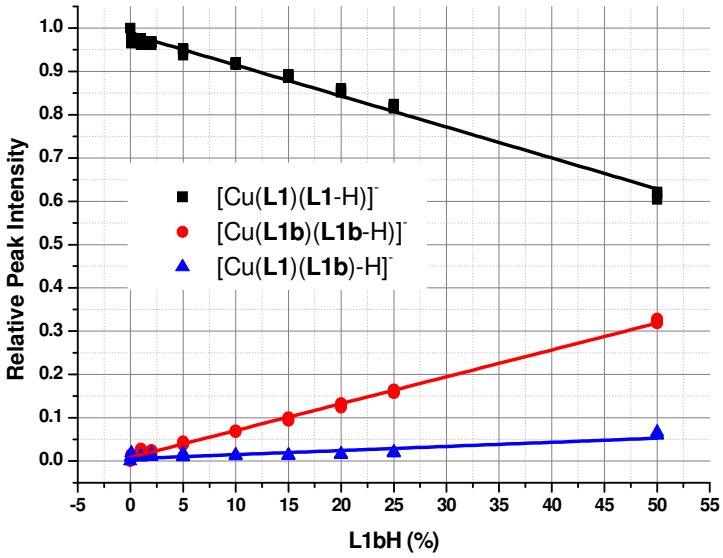

Figure 5.24: The relative peak intensities of [Cu(**L1**)(**L1**-H)]$^-$, [Cu(**L1**)(**L1b**)-H]$^-$ and [Cu(**L1b**)(**L1b**-H)]$^-$ derived from solutions of [Cu(Oac)$_2$] with **L1H** and **L1bH,** with increasing mol% of **L1bH**, maintaining a **LH** to Cu^{2+} ratio of 16:1.

Even at a **LH** to Cu^{2+} ratio of 16:1 the relative intensity of [Cu(**L1b**)(**L1b**-H)]$^-$ shows a linear increase with increasing mol% of **L1bH.** At 5mol% of **L1bH**, a **L1H** to **L1bH** of 19:1, the relative intensity of the [Cu(**L1**)(**L1b**)-H]$^-$ species is 5%. In this case the **L1H** to **L1bH** to Cu^{2+} is 76:4:1, so the [Cu(**L1**)(**L1**-H)]$^-$ species could potentially form 38 times over yet still we see 5% of the Cu^{2+} as [Cu(**L1**)(**L1b**)-H)]$^-$

The mixed extractant complex, [Cu(**L1**)(**L1b**)], seems to be an important species in solution, its formation being *significantly* more favourable than that of the bis-ketoxime complex, [Cu(**L1b**)$_2$]. These studies have demonstrated that the formation of the mixed, [Cu(**L1**)(**L1b**)], complex could have a significant influence on the mode and efficiency of extraction of Acorga® OPT modified extractant blends.[36]

5.3. Conclusions and Future Work

An investigation into the use of electrospray ionisation mass spectrometry to probe the solution equilibria revealed that, when two ligands **LXH** and **LYH** were mixed with copper(II) acetate three complexes form, [Cu(**LX**)$_2$], [Cu(**LY**)$_2$] and the mixed ligand complex, [Cu(**LX**)(**LY**)].

The formation of copper(II) complexes with 3-X-substituted phenolic oximes could be *monitored* but not quantified using the peak intensities of the deprotonated species, [Cu(**LX**)(**LX**-H)]$^-$, [Cu(**LY**)(**LY**)]$^-$ and [Cu(**LX**)(**LY**)-H]$^-$, *i.e.* changes in solution equilibria could be monitored using ESI-MS but the actual concentrations of the [Cu(**L**)$_2$] complexes in solution could not .

A Study to determine whether two ligands with different strengths could be ranked using mass spectrometry showed that the relative extraction strengths of both 3-X-substituted salicylaldoximes and phenolic aldoximes/ketoximes could be successfully defined using the relative intensities of the [Cu(**L**)(**L**-H)]$^-$ species.

The ionisation efficiencies of the [Cu(**L**)$_2$] complexes were also investigated. It was determined that the size, stability and solvation energy of each of the copper(II) complex would define the amount of corresponding anion, [Cu(**L**)(**L**-H)]$^-$ observed in the mass spectrum.

In each study the relative intensity of the mixed ligand complex, [Cu(**LX**)(**LY**)-H]$^-$, was important. It was shown that the intensity of the [Cu(**L1**)(**L1b**)-H]$^-$ species is linearly related to the concentration of the weaker extractant, **L1bH,** even in the presence of excess of the stronger extractant, **L1H.**

The stability of the mixed extractant complex, [Cu(**L1**)(**L1b**)], is surprising, its formation being *significantly* more favourable than that of the bis-ketoxime complex, [Cu(**L1b**)$_2$], and could have a significant influence on the mode and efficiency of extraction of Acorga® OPT modified extractant blends.[36]

5.4. Experimental

5.4.1. Sample preparation

All samples were prepared using LCMS analytical grade acetonitrile received from Aldrich. **LH** purity was verified prior to use (R.S. Forgan, B. D Roach). The Cu^{2+} source for each of the studies covered in this chapter was copper acetate monohydrate ($Cu(OAc)_2.6H_2O$, Aldrich). 3 types of sample preparation are described in this chapter varying the [**LH**] to [Cu^{2+}] ratio in the samples; varying **LXH** to **LYH** ratio in the samples; and varying the total Cu^{2+} concentration in the samples

Unless otherwise stated for the preparation of samples varying the [**LH**] to [Cu^{2+}] ratio or varying **LXH** to **LYH** ratio, the Cu^{2+} concentration was maintained at 50 μM and the experiments were performed in triplicate.

5.4.1.1. Studies varying the **LXH** to **LYH** ratio

Samples were prepared using stock solution of each of the ligands and diluting appropriately to give a range of **LXH** : **LYH** ratios (1:0, 9:1, 8:2, 7:3, 6:4, 1:1, 4:6, 3:7, 2:8, 1:9 and 0:1). For a total LH : Cu^{2+} ratio of 2:1 the **LH** concentration would be 100 μM and for a total **LH** : Cu^{2+} ratio of 4:1 it would be 200 μM.

5.4.1.2. Studies Varying **LH** to Cu^{2+}

Solutions of [Cu(**L**)$_2$] (50 μM) were prepared using fixed molar ratio of each ligand of 1:1 or 3:7, with varying L:Cu ratios, although the concentration of the ligands increased the concentration of the Cu^{2+} remained constant, ensuring that the resulting solutions had the same total [Cu(**L**)$_2$] concentration.

5.4.1.3. [Cu(**L8**)$_2$] Standards

Standards for appendix 8.5.4 were prepared from [Cu(**L8**)$_2$], prepared as described in Chapter 2. To ensure accurate sample concentrations, a 1 mmol stock solution of [Cu(**L8**)$_2$] in acetonitrile was prepared. A series of samples of concentrations varying from 2.5 - 100 μM were prepared *via* dilution with sample concentration confirmed via UV/Vis spectroscopy.

5.4.2. Sample Measurement

5.4.2.1. LCQ

A Thermo-Fisher LCQ mass spectrometer was used with a direct injection ESI source. All studies were carried out using the same experimental conditions:

Sample flow rate:	5μL/min
Sheath gas flow rate:	46 (Arb. Units)
Aux. gas flow rate:	0 (Arb. Units)
Capillary temperature	190°C
RF amplitude	560V
Spray Voltage	4.5kV
Capillary Voltage	-26.5V
Octapole 1 offset	6.8V
Lens Voltage	13V
Octapole 2 offset	10.5V
Tube lens offset	0V

Each sample was sprayed under the above conditions and 250 scans were taken in order to achieve accurately averaged spectra. The data was then extrapolated using Thermo-Fisher's Xcalibur Qualbrowser 2.0 software exported into Excel 2007. The intensities of the peaks were normalised other and graphs were plotted using Origin 8.0. The data manipulation procedures are detailed in appendix 8.2.3.

5.4.2.2. Q-ToF

A Waters Quadrupole-Time-of-Flight (Q-ToF) mass spectrometer was used in conjunction with an Aquity Sample Manager and Binary solvent Manager. All studies were carried out using the same experimental conditions:

Sample injection volume:	6µL
Desolvation gas flow rate:	800L/h
Aux. gas flow rate:	30L/h
Source temperature	90°C
Desolvation Temperature	350°C
Spray Voltage	2.2kV
Extraction Cone	4.0
Sampling Cone	80
Ion Guide	2.0

Each sample was sprayed under the same conditions using direct injection and 4 x 20 scans were taken in order to achieve accurately averaged spectra. The data was then extrapolated using Waters MassLynx software and the relative intensities of the peaks were normalised against each other and plotted into a graph. Data manipulation procedures can be found in pppendix 8.2.3.

5.4.3. pH Dependence of Copper(II) Loading from Sulphidic Media

Experiments were carried out by contacting chloroform solutions (5 ml) of the ligands at concentrations of 0.01 mol dm^{-3}, with aqueous solutions (5 ml) of $CuSO_4.H_2O$ at concentrations of 0.005 mol dm^{-3}. The aqueous solution was prepared from 4 ml of 0.0125 mol dm^{-3} $CuSO_4$ solution, to which was added 1 ml of 0.1 mol dm^{-3} sodium hydroxide/water or 1 ml of 2.5 mol dm^{-3} sulphuric acid/water solution to change pH. After vigorous stirring for 16 h at room temperature, the mixtures were

separated and 0.5 ml aliquots of the organic phase were taken, the solvent removed and diluted in butanol (10 ml) for copper analysis by ICP-OES. The calculated percentage Cu^{2+} uptake into the organic phase was plotted against the measured equilibrium pH of the aqueous phase to give s-curves. $pH_{0.5}$ values were calculated by plotting $\log([Cu]_{org}/[Cu]_{aq})$ vs pH for intermediate values of copper loading, with the $pH_{0.5}$ taken as the point where the linear fitted expression crossed the x axis. All solvent extraction data are located in appendix. 8.5.4.

5.5. References

(1) Forgan, R. S.; Wood, P. A.; Campbell, J.; Henderson, D. K.; McAllister, F. E.; Parsons, S.; Pidcock, E.; Swart, R. M.; Tasker, P. A. *Chem. Commun.* **2007**, 4940.

(2) Kebarle, P.; Tang, L. *Anal. Chem.* **1993**, *65*, A972.

(3) Wang, H. J.; Agnes, G. R. *Anal. Chem.* **1999**, *71*, 3785.

(4) Hao, C. Y.; March, R. E. *J. Mass Spectrom.* **2001**, *36*, 509.

(5) Gatlin, C. L.; Turecek, F. *J. Mass Spectrom.* **2000**, *35*, 172.

(6) Gatlin, C. L.; Turecek, F. *Electrospray Ion Mass Spectrom.* **1997**, 527.

(7) Vaisar, T.; Gatlin, C. L.; Rao, R. D.; Seymour, J. L.; Turecek, F. *J. Mass Spectrom.* **2001**, *36*, 306.

(8) Rohner, T. C.; Lion, N.; Girault, H. H. *Phys. Chem. Chem. Phys.* **2004**, *6*, 3056.

(9) Lavanant, H.; Hecquet, E.; Hoppilliard, Y. *Int. J. Mass Spectrom.* **1999**, *185*, 11.

(10) Matsumoto, A.; Fukumoto, T.; Adachi, H.; Watarai, H. *Anal. Chim. Acta.* **1999**, *390*, 193.

(11) Hao, C. Y.; March, R. E.; Croley, T. R.; Smith, J. C.; Rafferty, S. P. *J. Mass Spectrom.* **2001**, *36*, 79.

(12) Takats, Z.; Wiseman, J. M.; Gologan, B.; Cooks, R. G. *Anal. Chem.* **2004**, *76*, 4050.

(13) March, R. E. *Journal of Mass Spectrometry* **1997**, *32*, 351.

(14) Gaskell, S. J.; Bolgar, M. S.; Riba, I.; Summerfield, S. G. *Selected Topics in Mass Spectrometry in the Biomolecular Sciences* **1997**, *504*, 3.

(15) Tang, L.; Kebarle, P. *Analytical Chemistry* **1993**, *65*, 3654.

(16) Thomson, B. A.; Iribarne, J. V. *Journal of Chemical Physics* **1979**, *71*, 4451.

(17) Iribarne, J. V.; Thomson, B. A. *J. Chem. Phys.* **1976**, *64*, 2287.

(18) Tang, L.; Kebarle, P. *Anal. Chem.* **1991**, *63*, 2709.

(19) Enke, C. G. *Analytical Chemistry* **1997**, *69*, 4885.

(20) Leito, I.; Herodes, K.; Huopolainen, M.; Virro, K.; Kunnapas, A.; Kruve, A.; Tanner, R. *Rapid Commun.s Mass Spectrom.* **2008**, *22*, 379.

(21) Buhrman, D. L.; Price, P. I.; Rudewicz, P. J. *J. Am. Soc. mass Spectrom.* **1996**, *7*, 1099.

(22) Ikonomou, M. G.; Blades, A. T.; Kebarle, P. *Anal. Chem.* **1990**, *62*, 957.

(23) Matuszewski, B. K.; Constanzer, M. L.; Chavez-Eng, C. M. *Anal. Chem.* **2003**, *75*, 3019.

(24) Nelson, M. D.; Dolan, J. W. *LCGC Eur.* **2002**, *15*, 73.

(25) Bruins, C. H. P.; Jeronimus-Stratingh, C. M.; Ensing, K.; Dongen, W. D. v.; Jong, G. J. D. *J. Chromatogr., A* **1999**, *863*, 115.

(26) Annesley, T. M. *Clinical Chemistry* **2003**, *49*, 1041.

(27) Souverain, S.; Rudaz, S.; Veuthey, J.-L. *J. Chromatography* **2004**, *A*, 61.

(28) Gangl, E. T.; Annan, M.; Spooner, N.; Vouros, P. *Anal. Chem.* **2001**, 5635.

(29) Forgan, R. S.; Henderson, D. K.; McAllister, F. E.; Tasker, P. A.; White, F. J.; Campbell, J.; Swart, R. M. *Canadian Metallurgical Quarterly* **2008**, *47*, 293.

(30) Kordosky, G. A. *Int.l Solv. Ex. Conf., Cape Town, South Africa, Mar. 17-21* **2002**, 853.

(31) Avecia *Continued Evolution of Copper SX Reagents*, 2000.

(32) Kordosky, G. A.; MacKay, K. D.; Sudderth, R. B.; Sierakoski, J. M.; (Henkel Corp., USA). European Patent, 1983, p 62 pp.

(33) Jergensen, G. V. *Copper Leaching, Solvent Extraction, and Electrowinning Technology*; Society for Mining Metallurgy & Exploration, 1999.

(34) Forgan, R. S., PhD Thesis, University of Edinburgh, 2008.

(35) Gordon, R. J., PhD Thesis, University of Edinburgh, 2008.

(36) Tinkler, O.; Shiels, D.; Soderstrom, M. In *Hydrometallurgy Conference 2009* The Southern African Institute of Mining and Metallurgy, 2009.

CHAPTER 6: Aggregation of Phenolic Oxime Complexes in the Gas Phase; The Discovery of Novel Trinuclear Copper Complexes.

A gas phase investigation into the novel coordination chemistry of phenolic oximes with copper.

Table of Contents

6.1. Introduction

6.1.1. Aims

As discussed in Chapter 1 (Section 1.5.7), ESI has been applied to a wide range of inorganic systems both to monitor solution phase speciation and we have considered the relationship between species in solution and those observed in mass spectra for copper complexes of phenolic oximes in some detail in Chapter 5. The work described in this chapter initially considers the solution phase speciation of phenolic oximes with copper under conditions that are not commonly found in extraction processes, using ESI MS as an analytical tool. This analysis suggested that oligomeric complexes of doubly deprotonated ligands were present in solution. Work to isolate and characterize trinuclear-μ_3–oxocomplexes is described in the second half of the chapter.

At the outset we aimed to:

- study aggregation of phenolic oxime copper complexes,
- investigate the effects of proton concentration in a single solvent system on complex formation
- investigate the effects of variation of **LH** to Cu^{2+} ratios in a single solvent system with particular interest in the formation of phenolic oximes when Cu^{2+} is present in excess, and
- develop a novel "soft" ionisation source that could maintain non-covalent interactions upon ionisation to a greater extent.

The following section details the use of mass spectrometry to look at aggregation and speciation of phenolic oxime with Cu(II) systems in the gas phase. In order to maintain both weak covalent interactions and non-covalent interactions, ionisation sources other than ESI were also investigated, these include Sonic-spray ionisation (SSI) and Cold or Cryo-spray ionisation (CSI).

6.1.2. Sonic (SSI) and Cold-Sonic (CSI) Spray Ionisation

Other than electrospray several source designs have been explored, with the aim of transferring intact weak non-covalent associations in the gas phase. The detection of amino acid clusters using "sonic spray ionisation" (SSI) was reported by Takats *et al.* in 2003.[1] The sonic spray source pioneered by Hirabayashi, Sakairi, & Koizumi in 1994 applies no voltage between the capillary and the counter-electrode but, instead, employs extremely high nebulising gas flow rates.[2] The formation of charged droplets is attributed to statistical charge distribution during droplet formation.

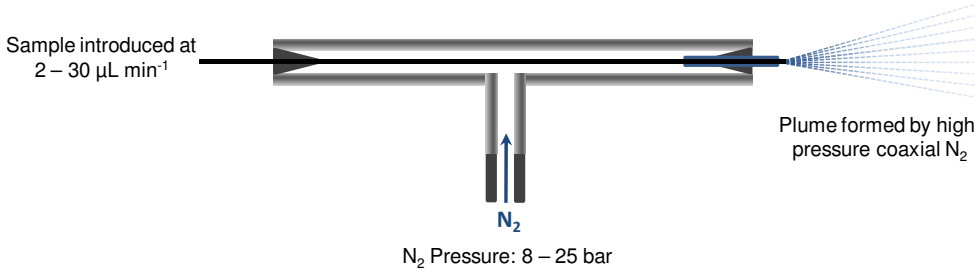

Figure 6.1: Sonic Spray Ionisation source.

Takats *et al.* compared the performance of a sonic spray source and an electrospray source, both coupled to a quadrupole ion trap mass spectrometer, using the same instrument settings.[1] The sonic spray source was found to be softer than the electrospray in terms of formation of intact clusters. The major difference between the two ionization methods is found in the charge density of the droplets. In electrospray, the concentration of excess charge[3] on a droplet is much higher than in sonic spray. Therefore, in sonic-spray ionisation, the Rayleigh limit is not likely to be reached, and shrinkage of the droplet until complete evaporation is supposed to occur.[1] This would result in a much "softer" desolvation process and could account for the increased observation of non-covalent interactions in the resultant mass spectrum.

Another source type that has been developed by Sakamoto *et al.* for the analysis of thermally labile assemblies is the "cold-spray" ionization (CSI) source.[4] In this case,

both the inlet capillary and the desolvation chamber can be cooled to -80°C. This source is especially useful for species which have low thermal stability in solution at room temperature, e.g. Grignard reagents.[5] The source can be operated in electrospray mode, with a high voltage on the capillary, and also in sonic spray mode[6] CSI has been applied to investigate the structures of many labile organic species, including unstable reagents,[6] reaction intermediates and asymmetric catalysts.[7] CSI can also generate multiply charged molecular ions with many solvent molecules attached.[7] and has been adopted for investigations of large hydrogen bonded systems[8] and more recently used for flexible self-assembling supramolecules.[9]

CSI exploits the increased polarizability of solvents and compounds at lower temperatures[7] due to an increased dielectric constant as the temperature of the nebulising and curtain gas is lowered. The increased dielectric constant increases the energy of non-covalent interactions.

6.2. Results and Discussion

6.2.1. Design of Cold-Sonic-Spray ionisation Source

In this thesis coupling the increased polarizability of polar solvents at lower temperatures and the "softness" of the sonic-spray ionisation technique has been used to develop a new "variable temperature" cold-sonic spray source.

In order to increase the sensitivity of the SSI technique to species held together by non-covalent interactions and to couple the ionisation source to a Thermo-Fischer LCQ mass analyser a simple "hybrid" ionisation source was designed using Autocad 2009[10] and built by Stuart Mains at the University of Edinburgh. (Figure 6.2).

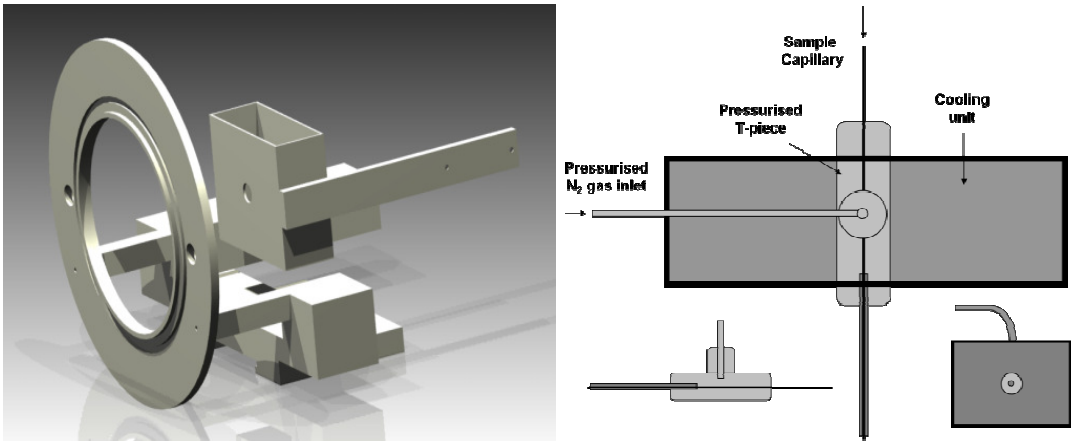

Figure 6.2: (left) Model of new cold-SSI source designed in Autocad 2009[10] and (right) graphical interpretation of cold-SSI head unit and operating mode.

The three main features of the source are:

- It can be securely coupled to the LCQ mass analyser. This maintains spray stability and maximises the throughput of ions to the mass analyser.
- The source has the potential for cooling of the "source head" unit with solid carbon dioxide mixed with a variety of solvents.
- The system can withstand high N_2 gas pressures.

6.2.1.1. Other potential uses for the cold-sonic spray source

The design of the source has enabled the incorporation of simple features that open it up to a wide range of techniques. As well as the variable temperature and nebulising gas flow rates, the head unit is electrically insulated and a charge can be applied to the source needle, giving the source ESI capabilities. A second electrically isolated junction is also present before the sample reaches the ionisation source and a charge could potentially be applied here giving the electro-sonic spray ionisation variation as described by Takats *et al.*[11] In ESSI the sample is "pre-charged" before entering the SSI source and it has been successfully applied to aqueous solutions of various proteins at neutral pH.[11] By use of a polythene "sheath" the high flow rates of the N_2

gas could provide an atmosphere with significantly reduced water and oxygen content and, together with the removed charge potential, could provide an ideal setting to investigate air-sensitive species. (Figure 6.3)

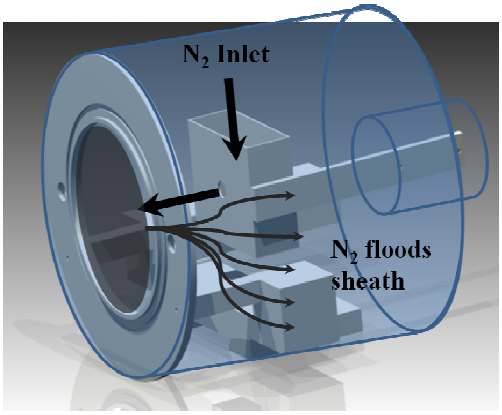

Figure 6.3: Possible polythene "sheath" for investigating air-sensitive species.

6.2.2. Effects of proton concentration on gas phase

The effects of pH and proton concentration on two phase extraction systems involving phenolic oxime extractants have been well documented[12] (see Chapter 1). It is known that the efficacies of the extractant systems are dependent on a series of complex equilibria.[13] The most important equilibria are dependent on the pH of the system, defining the extraction and stripping stages. (**6.1**)

$$Cu^{2+}_{(aq)} + 2\mathbf{LH}_{(org)} \rightleftharpoons [Cu(\mathbf{L})_2]_{(org)} + 2H^{+}_{(aq)} \qquad \mathbf{6.1}$$

However, in a single phase system, the equilibrium involved is different as the copper complexes $[Cu(\mathbf{L})_2]$ and free ligands **LH** are not separated from the protons and their conjugate base by a phase boundary. The copper is also not constrained to neutral complexes, as seen in two phase systems.

The effects of increasing mol% of formic acid on the speciation of 40μM solutions of $[Cu(\mathbf{L1})_2]$ in methanol were investigated using SSI. Figure 6.4 shows the mass spectrum derived from a 40μM solution of $[Cu(\mathbf{L1})_2]$ in methanol with no formic acid added, as can be seen there are already a large series of different species visible.

A series of clusters with the general formula $[X(Cu\mathbf{L}_2\text{-}H)(Cu\mathbf{L}\text{-}H)_nH]^+$ where X = H, Na or K.

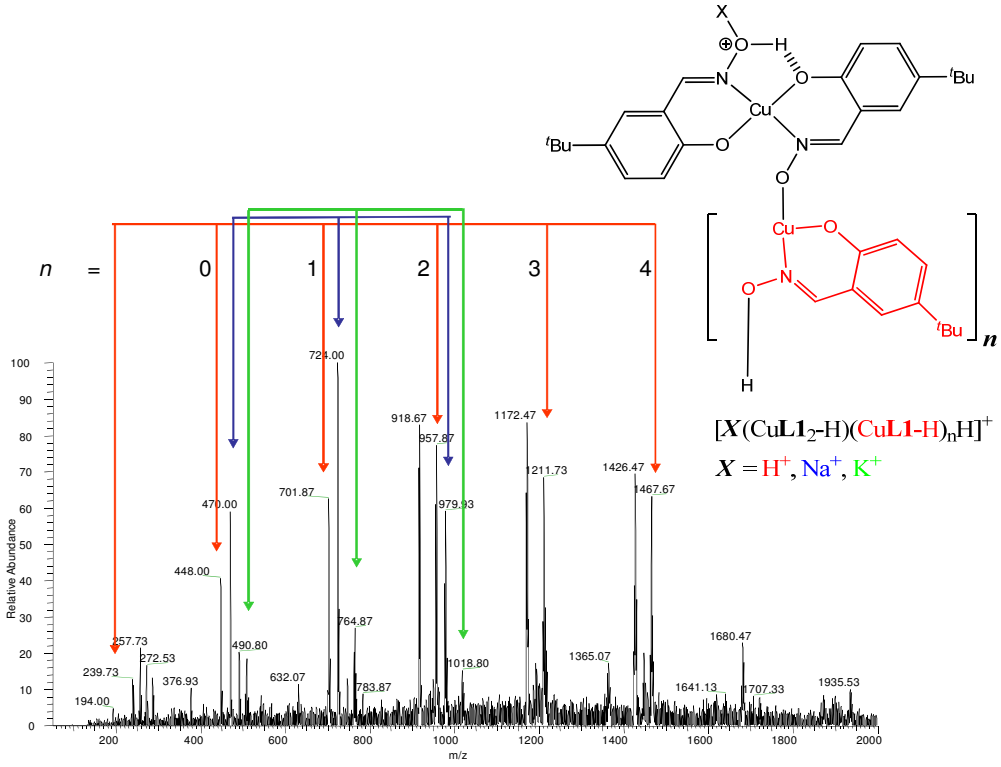

Figure 6.4: SSI mass spectrum of a 40μM solution of $[Cu(\mathbf{L1})_2]$ showing species of the general formula $[X(Cu\mathbf{L1}_2\text{-}H)(Cu\mathbf{L1}\text{-}H)_nH]^+$ where X = H^+, Na^+ and K^+. Inset: proposed "oligomeric" structural formulae for observed cationic species'

The intensities of the peaks for metallated clusters are greater than or equal to those of the protonated series, suggesting that metallated species are not very abundant in solution, as previously reported. The baseline of the mass spectrum is also very noisy and the signal-to-noise ratio is not very good. As increasing equivalents of formic acid are added to the $[Cu(\mathbf{L1})_2]$ solution the resultant mass spectra change considerably and the intensity of the peaks of metallated species are dramatically reduced probably due to the increased proton concentration (see equation **6.2**). The overall peak distribution is also changed slightly and intensities of the larger polynuclear species are reduced (Figure 6.5). As we increase the concentration of formic acid from 50 to 500 and 1000 mol % two differences can be observed; the overall peak intensities increase resulting in sharper mass spectra and the peak seen at m/z 194.1 increases in intensity with proton concentration.

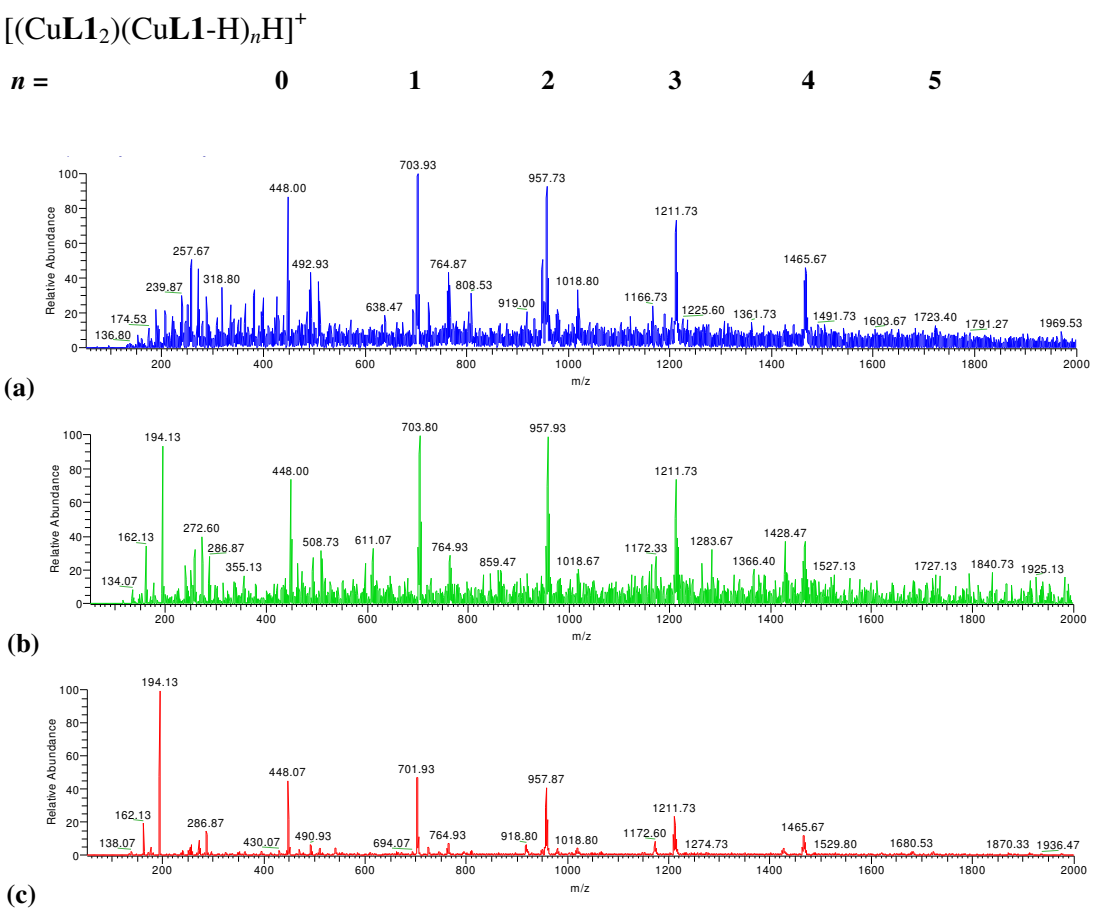

Figure 6.5 : SSI mass spectrum of a 40µM solution of [Cu(**L1**)$_2$] with (a) 50 mol % (b) 500 mol % and (c) 1000 mol % formic acid.

Both changes could be due to the cation exchange equilibria occurring according to equation **6.2.**

$$[Cu(\mathbf{L1})_2] + 2H^+ \rightleftharpoons [Cu(\mathbf{L1})]^+ + \mathbf{L1}H_2^+ \qquad \mathbf{6.2}$$

As the proton concentration is increased a cation exchange reaction could be occur similar to that observed in two phase systems. Free ligand **L1H** is liberated and a cationic complex, [Cu(**L1**)]$^+$ is formed. This unit could potentially form the monomeric unit that is the basis of the observed "polymeric" species. The liberated free ligand can then in turn be protonated causing the **L1H**$_2^+$ peak seen at m/z 194.1 increasing.

A study of the effects of increasing the Cu^{2+} concentration confirmed that species incorporating the [Cu(**L**-H)] unit, could also be observed in the negative ion spectrum.

L3H was used in a study of the effect of copper concentration on speciation in a $[Cu(\mathbf{L})_2]$ and species analogous to other 3-X-substituted ligands were observed. Figure 6.6 shows mass spectra derived from a 50 µM solution of $[Cu(\mathbf{L3})_2]$, (a), and the effect of adding stoichiometric equivalents of copper acetate, (b).

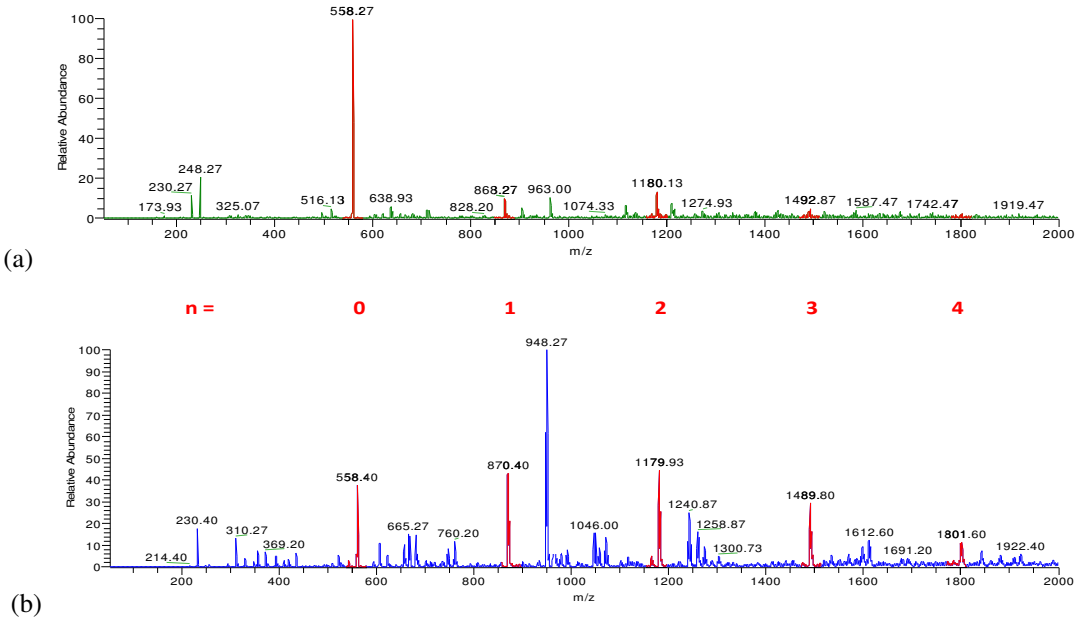

Figure 6.6 : ESI mass spectrum derived from a 50µM solution of (a) $[Cu(\mathbf{L3})_2]$ and (b) $[Cu(\mathbf{L3})_2]$ with 1 equivalent of $Cu(OAc)_2.H_2O$.

Three major differences were noted between the two spectra. The intensity of the peak at m/z 558 ($[Cu(\mathbf{L3})(\mathbf{L3}\text{-H})]^-$) is significantly reduced upon addition of one equivalent of Cu^{2+} indicating a shift in solution speciation. A series of peaks highlighted red in Figure 6.5 increases in intensity upon addition of Cu^{2+}. The enhanced peaks in this series are analogous to those observed in Figures 6.4 and 6.5.

The proposed anionic oligomeric structure is shown in Figure 6.7 together with the equilibria involved in the formation of the [Cu(**L3**-H)] species as described by equation **6.3.**

$$[Cu(\mathbf{L3})_2] + Cu(OAc)_2 \overset{K^1}{\rightleftharpoons} 2[(Cu\mathbf{L3})^+(OAc)^-] \overset{K^2}{\rightleftharpoons} 2[(Cu(\mathbf{L3}\text{-H})] + 2HOAc \qquad \textbf{6.3}$$

A shift in speciation in solution must be occurring as each of the [Cu(**L3**-H)] units has been released from a [Cu(**L3**)$_2$] complex.

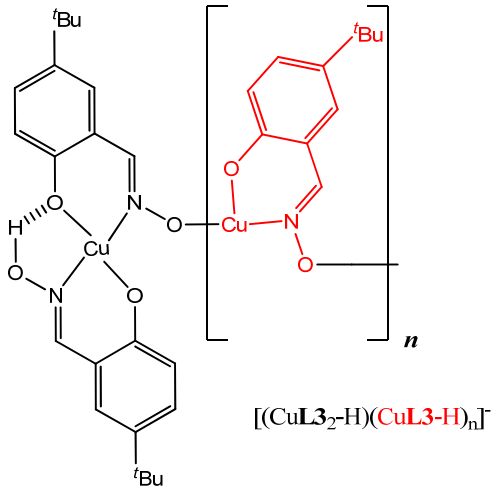

Figure 6.7: Proposed "polymeric" structural formulae for observed anionic species'.

Upon addition of an equivalent of Cu^{2+} the likely species formed in solution is that of a mono-ligated copper with an acetate counterion which could result in the formation of zwitterionic [Cu^+(**L3**-H)$^-$] units that form polymeric species upon release of HOAc. Similar "polymeric" species have previously been suggested with α-acyloin oximes in two-phase systems at "lower ligand concentrations".[14] Oligomeric complexes of 5,8diethyl-1-hydroxy-6-dodecanone oxime (industrial extractant LIX63) with Cu(II) and Ni(II) have previously been synthesised.[15-17] The systems are reported to be flat systems consisting of 5-membered chelate rings with association numbers in toluene for [Cu(**L**-H)]$_n$ of 7-10.[15-19]

The most interesting change in the spectra obtained from solutions of **L3H** containing high concentrations of Cu^{2+} is the appearance of the peak at m/z 948.27 which is highlighted in Figure 6.8.

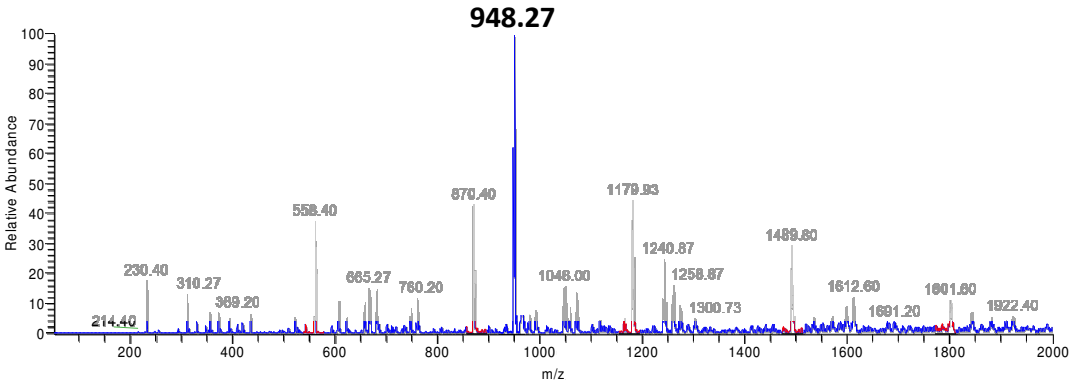

Figure 6.8 : ESI mass spectrum derived from a 50µM solution of $[Cu(\mathbf{L3})_2]$ with 1 equivalent of $Cu(OAc)_2.H_2O$ with highlighted peak at m/z 948.27.

The species does not appear to be aggregated, as seen for the species discussed above, and its m/z value and isotopic ratio infer that three [Cu(**L3**-H)] units form a single species around a central oxide ion in the structure proposed in Figure 6.9.

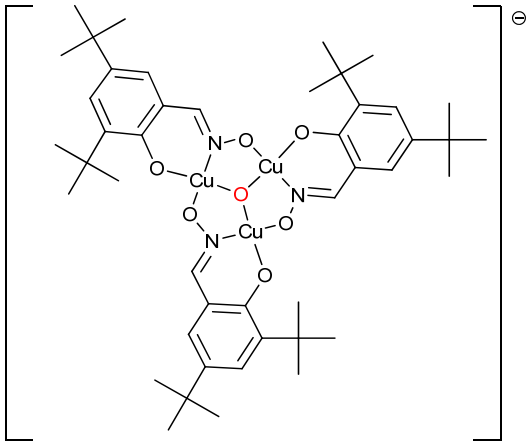

Figure 6.9 : Proposed structure of the monoanion observed at m/z 948.27 in Figure 6.8

Trinuclear-μ_3-oxocopper complexes, $[Cu_3\mathbf{L}_3O]^+$, have been observed previously, but with *monoanionic* bidentate ligands, **L**. A brief review of such complexes is presented in the following section.

6.2.3. Trinuclear copper(II) complexes

Triangular copper(II) complexes have been extensively studied, especially in trhe context of their magnetic, structural and redox properties. $[Cu_3\mathbf{L}_3OH]X_2$ salts (where **LH** = 2-pyridinaldoxime and X = ½ SO_4^{2-}, NO_3^-, ClO_4^- and OH^-, see Figure 6.9) were reported by Green *et al.*[20] as early as 1963. The first crystal structure[21] of a closely related 3-membered copper metallocycle was consistent with magnetic data that suggested a trinuclear copper core in which strong metal-metal interactions allowed the pairing of two of the three unpaired electrons (Figure 6.10).

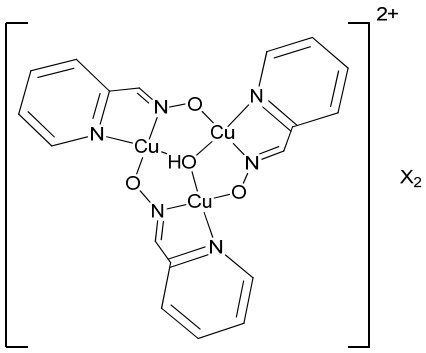

Figure 6.10: The trinuclear copper structure suggested by Green *et al.* [20], where X = ½ SO_4^{2-}, NO_3^-, ClO_4^- and OH^-.

The first trinuclear copper complex containing aliphatic monoanionic bidentate ligands, $[Cu_3(\mathbf{L}_3)OH_{1/2}](ClO_4)_{2/3}$ (where **LH** = 2-propylamino-methyl-3-butanone oxime) was described by Young *al.*[22] The magnetic properties indicated a similar to that of the pyridinealdoximato complex (above) and this was confirmed by X-ray structure determination.[23] The identity of the μ-bridging group (μ-O or μ-OH) was not confirmed. A 50:50 mixture was assigned to account for the charge balance in the structure.

In 1978 a one electron quasi-reversible redox reaction of a trinuclear copper system (Figure 6.11) was described by Chakravorty *et al.* who also reported that the system had a single unpaired electron (S = ½).[24]

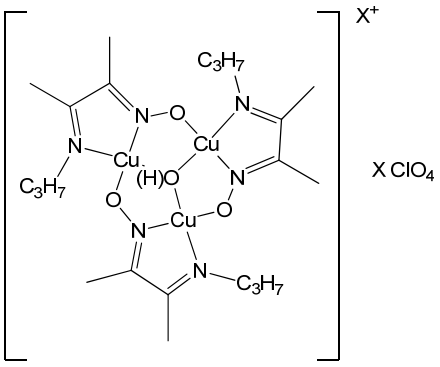

Figure 6.11: Trinuclear copper system as described by Chakravorty *et al.*[24]

Both μ-OH[20,21,23-29] and μ-O[23-25,27,28] central units have been reported in similar complexes, with the oxo oxygen atom lying closer (0.35 Å)[25] to the plane of the three copper atoms than oxygen atom in the hydroxyl derivatives (0.48-0.93 Å).[21,23,25,26,29] Compounds containing two Cu_3 units in a hexanuclear complex (see also the section below) usually have the Cu_3 units arranged parallel to each other,[30] although an orthogonal orientation has also been reported.[26,29]

Electrochemical studies have shown that monoelectronic transfers are possible and that the $[Cu_3(\mu\text{-}O)]$ unit can be reduced to generate $[Cu^{III}Cu^{II}_2(\mu\text{-}O)]$ complexes.[24,27,28] In the early 80's Chakravorty *et al.*[27,28,31] showed that the $[Cu_3(\mu\text{-}O)]$ core of a $[Cu_3(\mathbf{L}_3)O](ClO_4)_2$ complex where **L**H = Pyridine-2-carbaldoxime can be reduced to the related $[Cu_3(\mu\text{-}OH)]$ complex with NEt_3 and reoxidised with perchloric acid (Figure 6.12). They demonstrated that the system underwent a one electron oxidation or reduction depending on whether a proton was present or absent on the bridging oxygen atom.

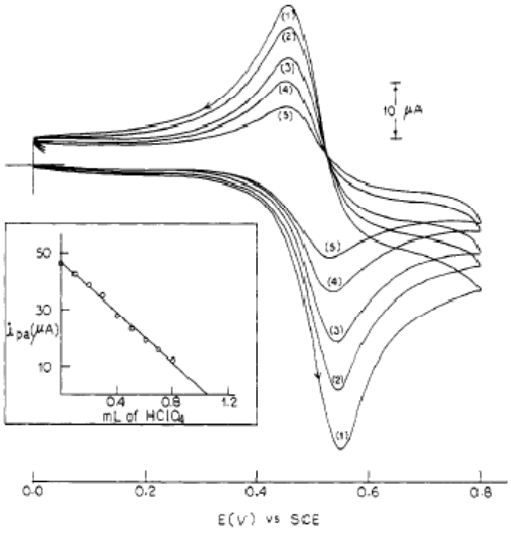

Figure 6.12: Effect of the addition of perchloric acid to a solution of $[Cu_3(\mathbf{L}_3)O](ClO_4)_2$ complex where **LH** = Pyridine-2-carbaldoxime in DMF. The inset shows anodic peak current as a function of the volume of perchloric acid added with least square fit.[27]

6.2.3.1. Recent studies on copper oxime trinuclear complexes

The use of $[Cu_3(\mu_3\text{-}OH)]^{2+}$ units as building blocks for polymers containing pyrazole ligands and acrylate anons as bridging units had been reported recently.[32] Stamatatos *et al.* formed $[Cu^{II}_3(\mu_3\text{-}OH)]^{5+}$ cores using di-2-pyridyl ketone oximes, which existed as centrosymmetric pairs with antiferromagnetic interactions similar to those shown previously.[33] A hexanuclear Cu^{II} complex with two $[Cu_3\mathbf{L}_3(\mu_3\text{-}O)]$ units (where L = pyrazole) linked with disubstituted pyrazole ligands as shown in Figure 6.12 has also been reported.[34] Cyclic voltammetry indicated two one-electron redox processes and that these processes are ligand dependent and can be tuned. An interesting point made is that the electronic communication between the $(Cu_3\mu_3\text{-}O)$ units might involve short Cu-Cu interactions instead of through ligand interaction.

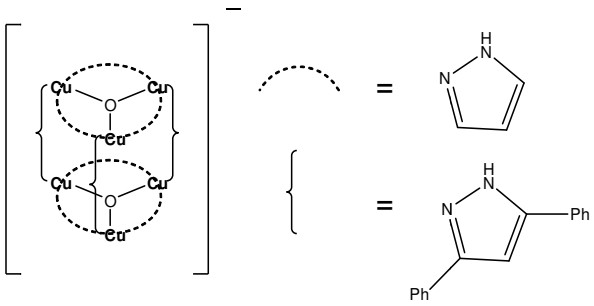

Figure 6. 13: Linked $[Cu_3\mathbf{L}_3(\mu_3\text{-}O)]$ units (where L = pyrazole) with disubstituted pyrazole staps.[34]

Curtis *et al.*[35] reported a hexanuclear complex, $[(Cu_3\mathbf{L}_3O)_2H][ClO_4]_3$, (where **L**H = 4-amino-4-methylpentan-2-one oxime) containing two Cu_3O units linked by a proton between the oxygen atoms. Although the proton could not be located in the X-ray structure determination, the short O···O contact distance (2.47 Å) and the charge balance infer the presence of a O-H···O bridge (Figure 6.13)

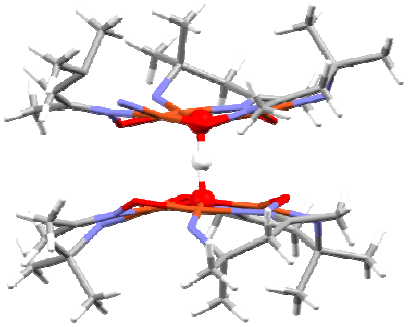

Figure 6. 14: The internally hydrogen bonded $[(Cu_3\mathbf{L}_3O)_2H][ClO_4]_3$ complex (where **L**H = 4-amino-4-methylpentan-2-one oxime) reported by Curtis *et al.*[35]

Di-2-pyridyl ketone oxime has been used with various counter ions (OH^-, alkanato, ClO_4^-) to yield trinuclear complexes which were characterized as inverse-9-metallacrown-3 compounds which accommodate guest ligands and showed large antiferromagnetic interactions between the Cu(II) ions.[36] Theoretical calculations based upon DFT, using crystal structures and model compounds comparing the doublet and quartet states of the system, showed that both e_g and t_{2g} orbitals contribute to the magnetic exchange coupling.[36]

The recent interest in the development of molecular magnets has led to an increase in the use of oximate ligands to prepare polynuclear metal complexes. Most of the work in this area has involved transition metals in +3 oxidation states (see below).

6.2.3.2. Polynuclear phenolic oxime complexes.

Singly deprotonated salicylaldoximes generally form bis-complexes with M^{2+} ions but once doubly deprotonated have the possibility to bind through the phenolate oxygen, the oxime nitrogen and the oximato oxygen (Figure 6.4), giving great potential for polynuclear complex formation and, as a consequence, a large number of complexes of metals such as Mn,[37-42] Co,[37,43,44] Ni,[37,43] and Fe[45-48] have been reported.

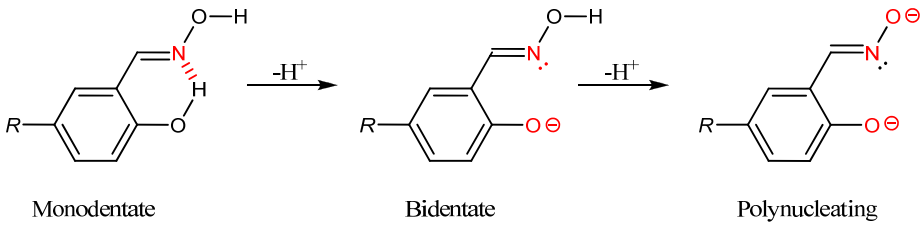

Figure 6.15: The various bonding modes of phenolic oximes

The coordination chemistry of Mn^{III} with such ligands has been extensively studied for its relevance to the field of single molecule magnetism, resulting in many structures with remarkable properties, including a single molecule magnet with the highest energy barrier to magnetisation reversal currently known.[42]

6.2.3.3. Polynuclear copper phenolic oximes complexes with [Cu_3-μ_3-O(H)] units

Of the many reported polynuclear complexes containing [$M_3\mu_3$-O(H)] units with bridging, doubly deprotonated, phenolic oxime ligands, only one has been reported which contains copper. A hexanuclear copper species containing two [Cu_3(salox)$_3$-μ_3-O] units linked together by three doubly protonated [-

$CH_2NH(CH_3)C_5H_{10}NH(CH_3)CH_2$-] straps (Figure 6.15) was developed in a collaborative project between various groups at the University of Edinburgh and the Plieger group at Massey University.[49]

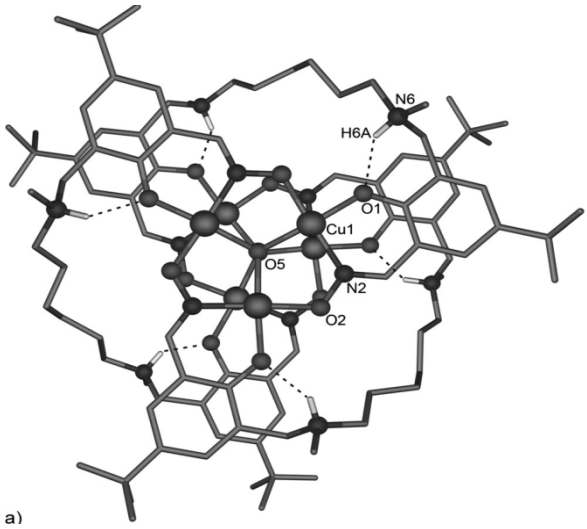

Figure 6.16: A hexanuclear copper species formed by two [Cu_3salicylaldoximato)-μ_3-O] units linked together by three doubly protonated [-$CH_2NH(CH_3)C_5H_{10}$ $NH(CH_3)CH_2$-] straps as reported by Plieger *et al.*[49]

Charge balance and geometry suggest that the two [Cu_3(**L**)$_3$-μ_3-O] units are also linked via a bridging proton (see Section 6.2.3). The incorporation of 3-aminomethyl groups within the salicylaldoxime framework facilitates the formation of the Cu^{II}_3-μ3-oxo(salicyladiminato^{2-})$_3$ framework more commonly formed by *trivalent* first transition series metals. It is also suggested that the protonation of the 3-aminomethyl group and the formation of hydrogen bonds to the phenolate oxygen atom reduces the charge density provided by the *di*anionic NO_2^{2-} donor set of the salicylaldoximate. This results in values more comparable with those provided by the *mono*anionic N_2O^- donor set in trinuclear complexes of β-iminoketonate and related ligands reported previously (see Section 6.2.3.2).

6.2.3.4. Importance of the [Cu_3-μ_3-O] framework

The [Cu_3-μ_3-O] unit present is in the active site of multicopper oxidases that facilitate the four electron reduction of dioxygen to water.[50] It has been shown that within

these enzymes two mononuclear and one binuclear copper containing sites are present.

Chan *et al.* confirmed the existence of a trinuclear copper cluster within particulate methane monooxygenase proteins and modelled the system to demonstrate the facile oxo-transfer activity, confirming the cluster as the site of the hydroxylation reactions performed by the protein. Their most recent study, employing a synthetic, catalytically active, Cu_3-model system has identified a triangular, formally [$Cu^{II}_2Cu^{I}$-μ_3-O] intermediate as the O-transfer species (Figure 6.16).[51]

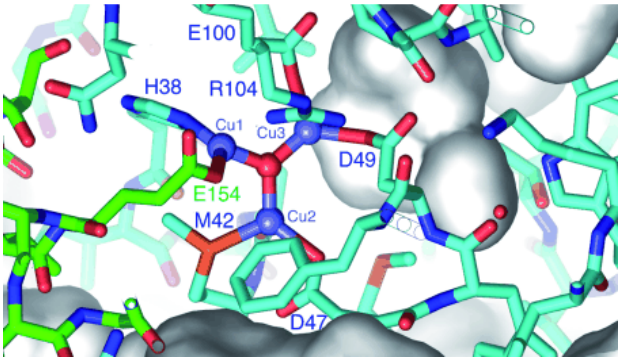

Figure 6.17: The modelled active site of a methane monooxygenase protein, a triangular, formally [$Cu^{I}_2Cu^{II}_1(\mu_3$-O)] intermediate.[51]

The formation of the [Cu-μ_3-O] unit and its involvement in the catalytic cycles shown by multicopper oxidases have been modelled.[50] Figure 6.17 shows the two types of copper-containing sites, mononuclear T2, and binuclear T3, being bridged by a μ_3-O atom as part of the unit responsible for catalytic reduction of O_2 to water.

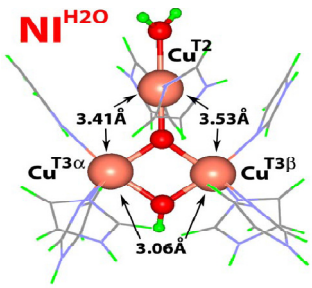

Figure 6. 18: The two types of copper sites, mononuclear T2, and binuclear T3, bridged by a μ_3-O atom in a multicopper oxidase as modelled by Yoon *et al.*[50]

6.2.3.5. Electrochemical properties of trinuclear copper complexes

Riverra-Carrillo *et. al* have described an extensive series of trinuclear Cu complexes (Figure 6.18) with the formula $[Cu^{II}_3\text{-}\mu_3\text{-E-}\mu\text{-4-R-pyrazole}_3X_3]^{\pm n}$ (where E = O or OH; R = H, Cl, Br, CH(O) or NO_2; X = Cl, NCS, CH_3COO or pyridine.[52] Using cyclic voltammetry and spectroelectrochemistry they investigated the influence of terminal ligands on the one electron redox process of $[Cu_3\text{-}\mu_3\text{-O}]^{4+/5+}$. X-ray structure determination was also used to define the influence of the terminal ligands on the nature of the bridging unit in the solid state and showed that electron withdrawing ligands (e.g. Cl, a in Figure 6.18) favour a $[Cu_3\text{-}\mu_3\text{-O}]$ unit, whereas electron donating ligands (e.g. pyridine, b in Figure 6.18) favour a $[Cu_3\text{-}\mu_3\text{-OH}]$ unit.[52]

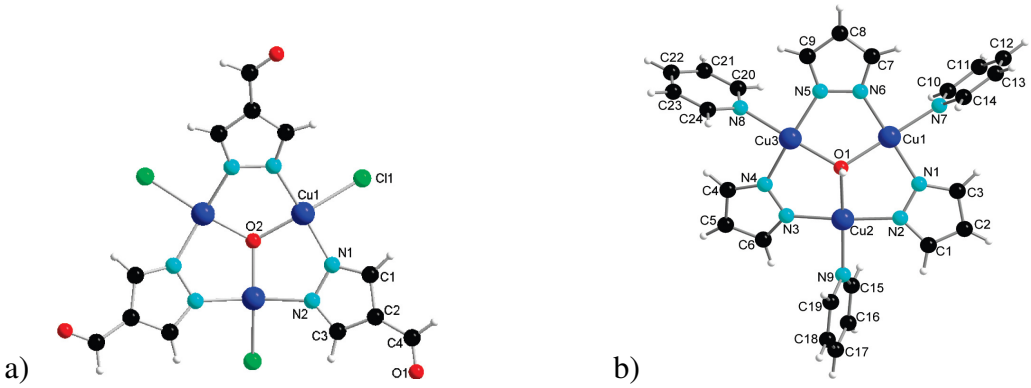

Figure 6. 19: Trinuclear Cu^{II} complexes of the formula $[Cu^{II}_3(\mu_3\text{-E})(\ \mu\text{-4-R-pz})_3X_3]^{\pm n}$ (where E = O and OH; R = H, Cl, Br, CH(O) and NO_2; X = (a) Cl and (b) pyridine as reported by Riverra-Carrillo *et al.*[52]

Mezei *et al.* carried out cyclic voltammetry on the series of hexanuclear pyrazoles complexes (see Figure 6.12) and showed that they underwent two one electron oxidation processes, leading to mixed-valent copper complexes.[34] The introduction of substituents and terminal ligands can dramatically shifted redox potentials.

6.2.4. Mass spectrometry of phenolic oximes complexes formed from copper acetate

In this chapter the systematic study of the aggregation and gas phase speciation of copper/phenolic oxime systems was extended to establish what effect a high ratio of copper to **LH** in solution had on the species detected in the ES MS. Figure 6.19 shows the mass spectra resulting from solutions of varied Cu^{2+} to **L8bH** Important peaks are highlighted and structures are suggested for the gas phase anions in Figure 6.20.At low Cu^{2+} to **LH** ratios when the ligand, **L8bH**, is in excess, *e.g.* when two ligand molecules are present for each copper ion in solution, the expected [Cu(**L8b**)(**L8b**-H)]$^-$ complex (highlighted in green in Figure 6.20 and Figure 6.21) is seen along with the sodiated dimer [(Cu(**L8b**)(**L8b**-H))$_2$Na]$^-$ (highlighted in purple). At Cu^{2+} to **L8bH** ratios where the copper is in excess a peak at m/z 990, analogous to that described in Section 6.2.2. was observed.

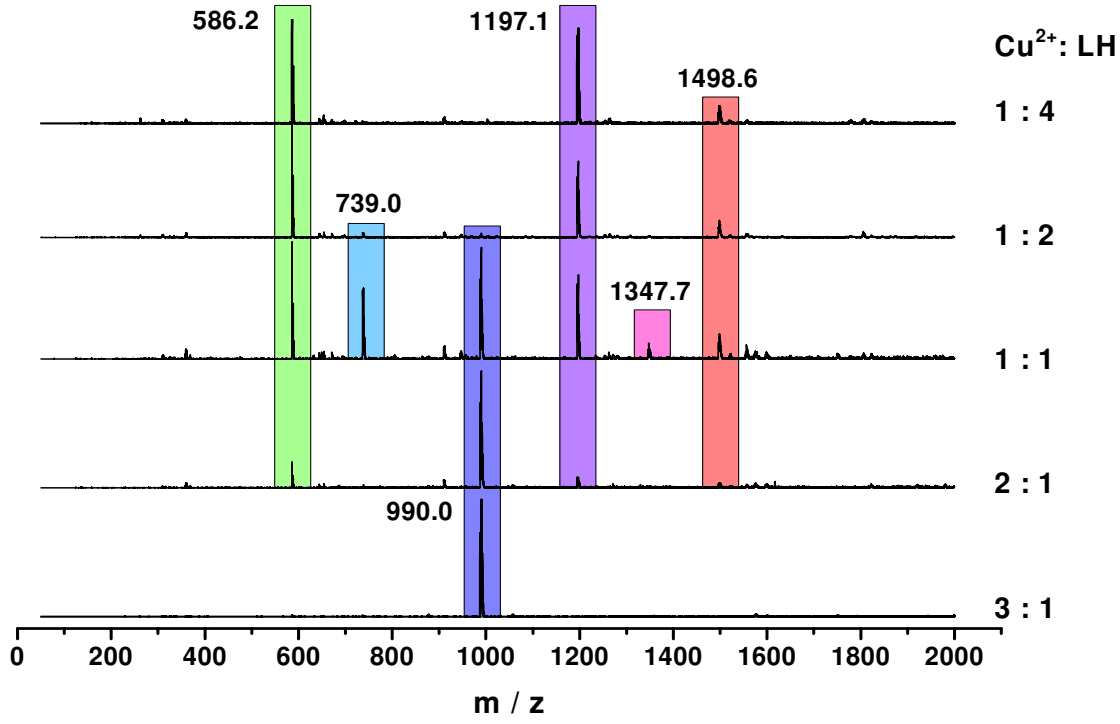

Figure 6.20: Mass spectra resulting from solutions having varied the Cu^{2+} to **L8bH** concentrations.

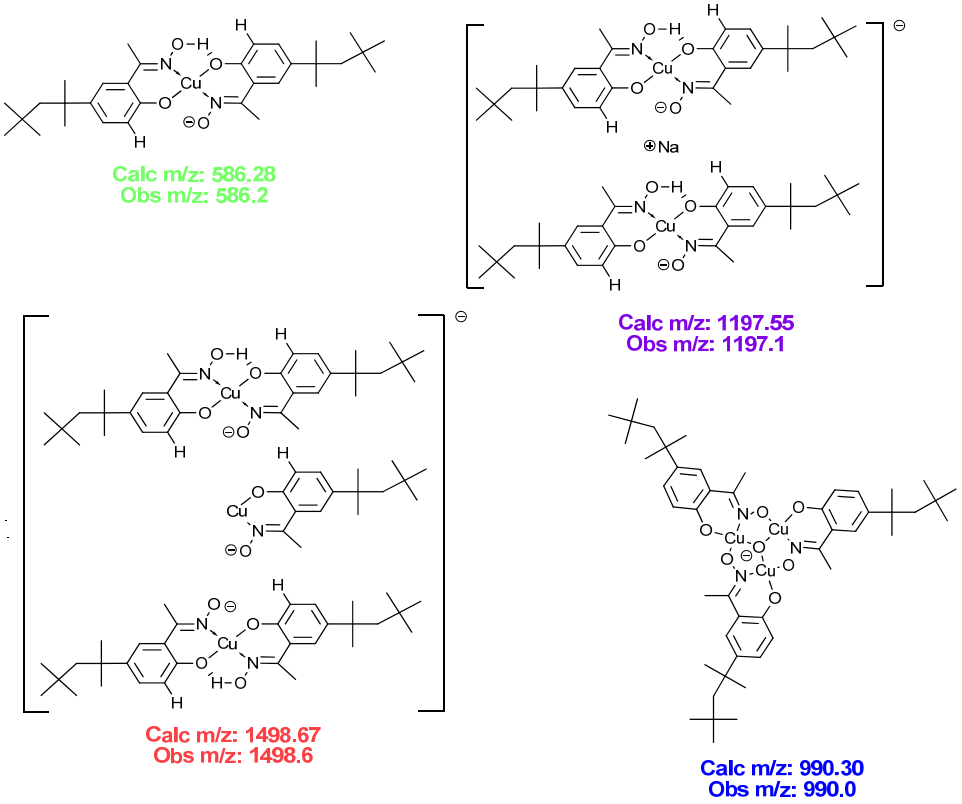

Figure 6.21: Suggested structures for some of the anionic species observed in the mass spectra in Figure 6.16, together with their observed and calculated monoisotopic masses.

At Cu^{2+} to **L8bH** ratios greater than 1:1 the $[Cu_3(\mathbf{L8b}\text{-}H)_3\text{-}\mu_3\text{-}O]^-$ species, observed at m/z 990.0, dominates and eventually becomes the sole peak observed in the mass spectrum when the ratio is increased to 3:1.

Assignment of conventional oxidation states to atoms in the inner coordination shell of the peak at 990.0 presents some difficulties. If the copper atoms are all assumed to be divalent the three [Cu(**L8b-**H)] units are charge neutral and when combined with the central [μ_3-O] dianion, the $[Cu_3(\mathbf{L8b})_3\text{-}\mu_3\text{-}O]$ complex will be a dianion. The observed species is a monoanion. This could arise because one of the component copper atoms is formally trivalent (in practice we might expect charge delocalization over the Cu_3-μ_3-O unit) or because the central unit is a hydroxyl anion, not an oxide dianion. Following the observation that the trinuclear complex unit dominates the ESMS of complexes of **L8b**H when high concentrations of copper are present experiments were carried out to:

- confirm that the central atom is a μ_3-oxide ion and not a hydroxyl group,

- define whether $[Cu_3(\mathbf{L})_3\text{-}\mu_3\text{-}O]^-$ species also dominate the ESMS of solutions of complexes formed by other phenolic oxime ligands, and define whether similar complexes are formed in condensed phases and whether solid state structures could be determined by single crystal X-ray structure determination.

6.2.5. Gas Phase Characterization

High resolution mass spectrometry and collision induced dissociation was used to characterise polynuclear complex speciation. Various 3-X-substituted and 5-R-substituted ligands were screened in order to determine whether the trinuclear complex can form with other phenolic oxime ligands. The observed and calculated monoisotopic m/z values for each ligand tested are given in Table 6.1 along with the **LH** to Cu^{2+} ratio used. The $[Cu_3(\mathbf{L}\text{-}H)_3\text{-}\mu_3\text{-}O]^-$ peak was the base peak in every case when the ratio of Cu^{2+} to **LH** exceeded 1:1. (see Table 6.1)

Table 6.1: The ligands tested for formation of $[Cu_3(\mathbf{L}\text{-}H)_3O]^-$ species, indicating **LH**:Cu^{2+} ratio used, the observed and calculated monoisotopic m/z and the relative signal intensity of the $[Cu_3(\mathbf{L}\text{-}H)_3O]^-$ peak.

LH	LH:Cu^{2+}	Monoisotopic m/z $[Cu_3(L\text{-}H)_3O]^-$	Calculated Monoisotopic m/z $[Cu_3(L\text{-}H)_3O]^-$	Intensity (%)
L1H	1:2	779.93	780.07	100
L1bH	1:2	822.02	822.11	100
L8H	1:2	948.49	948.25	100
L8bH	1:3	990.01	990.30	100
L3H	1:1	948.27	948.30	100
L5H	1:2	881.73	881.95	100
L6H	1:2	1015.47	1015.80	100

The observed and calculated m/z values are consistent with the oxo-containing anion, $[Cu_3(\mathbf{L}\text{-}H)_3\text{-}\mu_3\text{-}O]^-$ rather than the hydroxy-analogue, $[Cu_3(\mathbf{L}\text{-}H)_3\text{-}\mu_3\text{-}OH]^-$, and this was later confirmed by high resolution mass spectrometry.

6.2.5.1. CID of $[Cu_3(\mathbf{L8}\text{-}H)_3O]$-

Collision induced dissociation experiments were carried out on the trinuclear complex of **L8H**, $[Cu_3(\mathbf{L8}\text{-}H)_3\text{-}\mu_3\text{-}O]^-$. A 50 μM solution of stoichiometric amounts of **L8H** and copper acetate was injected into an LCQ double octapole ion trap mass spectrometer. The $[Cu_3(\mathbf{L8}\text{-}H)_3O]^-$ species was observed as the base peak at m/z 948.49 and subjected to CID. The resulting species with likely fragmentation pathways are indicated in Figure 6.22, with the observed and calculated monoisotopic m/z given for each.

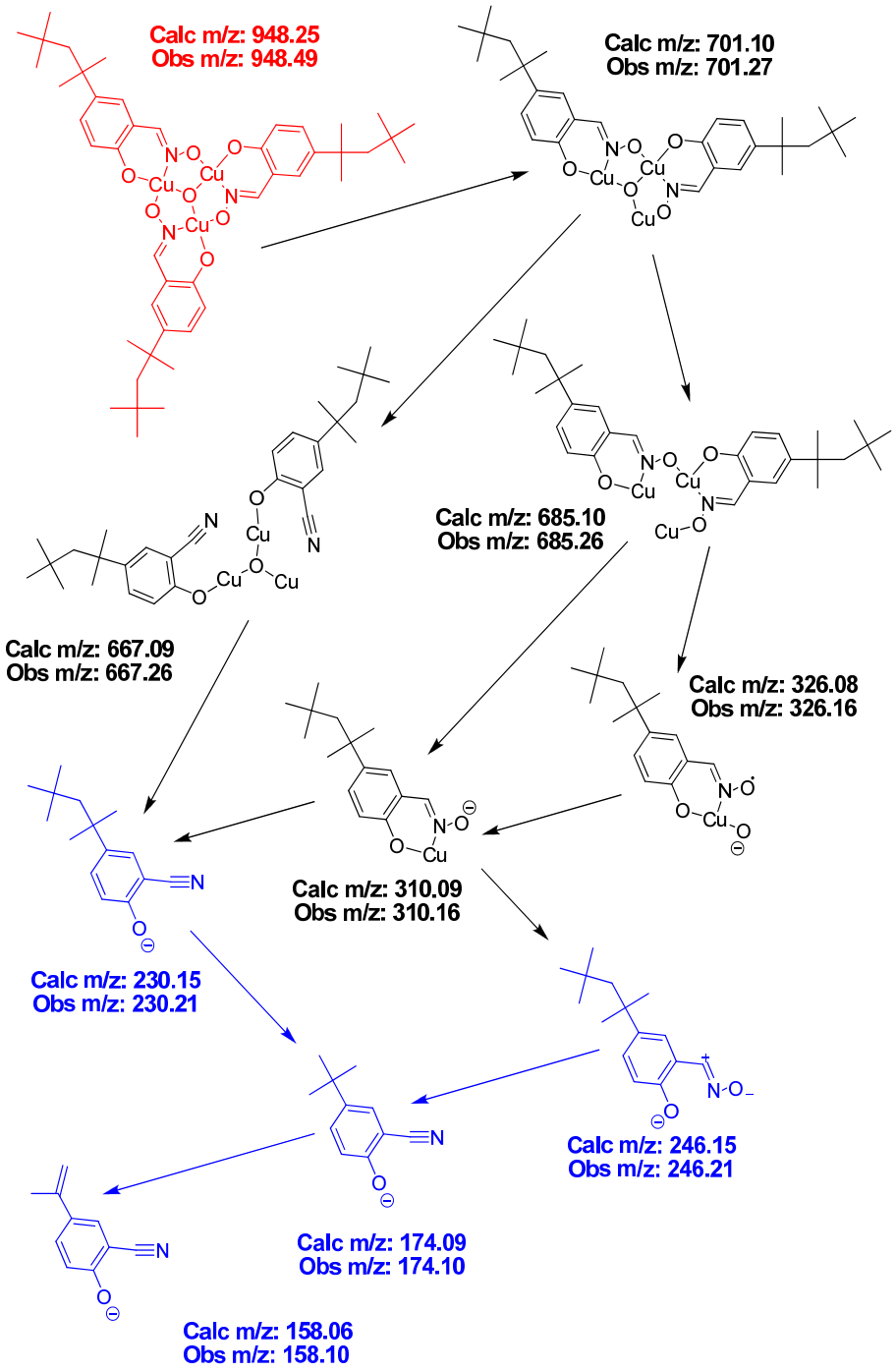

Figure 6.22: The CID fragment ions from $[Cu_3(\mathbf{L8}\text{-H})_3O]^-$ (highlighted red). The likely fragmentation pathways are indicated with the observed and calculated monoisotopic m/z given for each fragment. For clarity metallated fragments are shown in black and non-metallated fragment ions are shown in blue.

The initial fragmentation appears to be loss of an [**L8**-H] unit which requires higher collision energy indicating then that observed for the breakdown of $[Cu(\mathbf{L})(\mathbf{L}\text{-H})]^-$ species (see Chapters 2 and 3). The poly-metallated species undergo redox chemistry

upon dissociation, resulting in the formation of Cu(I)-containing fragments that rearrange readily to mono-metallated fragment ions. At higher collision energy the major species observed in the mass spectra are non-metallated ions (shown in blue in Figure 6.22) which show very similar rearrangements to those observed for the non-metallated species in the $[Cu(\mathbf{L})(\mathbf{L}\text{-H})]^-$ CID spectra (Chapters 2 and 3) forming unsaturated species due to neutral losses of H_2O and CH_4.

6.2.5.2. High Resolution mass spectrum of $[Cu_3(\mathbf{L8}\text{-H})_3O]^-$

Conformation that the base anions correspond to the oxo-containing anion, $[Cu_3(\mathbf{L}\text{-H})_3\text{-}\mu_3\text{-O}]^-$ rather than the hydroxy-analogue, $[Cu_3(\mathbf{L}\text{-H})_3\text{-}\mu_3\text{-OH}]^-$, was done by using a Waters Quadrupole-Time-of-Flight (Q-ToF) mass spectrometer in conjunction with an autosampler (Aquity Sample Manager and Binary solvent Manager) was used to obtain a high resolution mass spectrum. The experimental conditions are given in Section 6.4 and the resulting mass spectrum is shown in Figure 6.23 with the observed peak and the calculated peak for $[Cu_3(\mathbf{L8}\text{-H})_3O]^-$ inset.

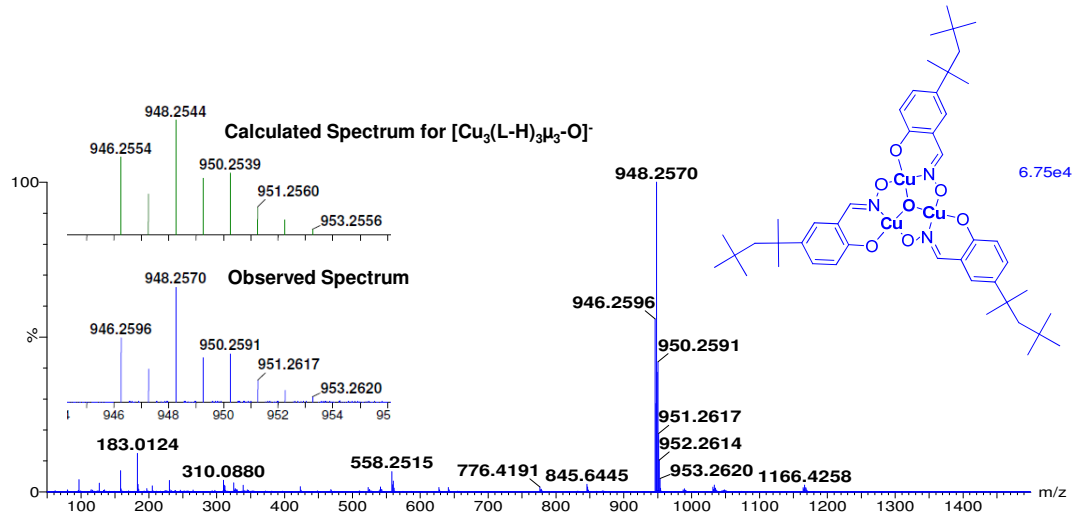

Figure 6.23: High resolution mass spectrum derived from a 50μM solution of L8H with copper acetate 1:1, with the observed base peak and the calculated peak for $[Cu_3(\mathbf{L8}\text{-H})_3O]^-$ shown inset.

The high resolution spectrum confirms to two decimal places that the observed singly charged peak is $[Cu_3(\mathbf{L8}\text{-H})_3O]^-$ and not $[Cu_3(\mathbf{L8}\text{-H})_3OH]^-$. The possible origin of this species is either the production of a formal Cu^{3+} which would have a d^8

configuration and would therefore have a stable square planar conformation. The Cu^{3+} could also form to accommodate the large negative charge of the ligand donor set (-8).

6.2.5.3. Mixed ligand $[Cu_3(\mathbf{L}\text{-}H)_3O]$- species

In Chapter 5, it was shown that when two ligands are mixed stoichiometrically with a Cu^{2+} salt, three mononuclear complexes are formed, $[Cu(\mathbf{LX})_2]$, $[Cu(\mathbf{LY})_2]$ and $[Cu(\mathbf{LX})(\mathbf{LY})]$. When excess of Cu^{2+} is present in solution, theoretically four trinuclear complexes could be observed: $[Cu_3(\mathbf{LX}\text{-}H)_3O]^-$, $[Cu_3(\mathbf{LX}\text{-}H)_2(\mathbf{LY}\text{-}H)O]^-$, $[Cu_3(\mathbf{LX}\text{-}H)\ (\mathbf{LY}\text{-}H)_2O]^-$ and $[Cu_3(\mathbf{LY}\text{-}H)_3O]^-$.

Figure 6.24 shows the mass spectrum resulting from a solution of copper(II) acetate (50 µM in Acetonitrile) with **L1H** and L6H. The Cu^{2+} to **L1H** to **L6H** ratio is 2:1:1.

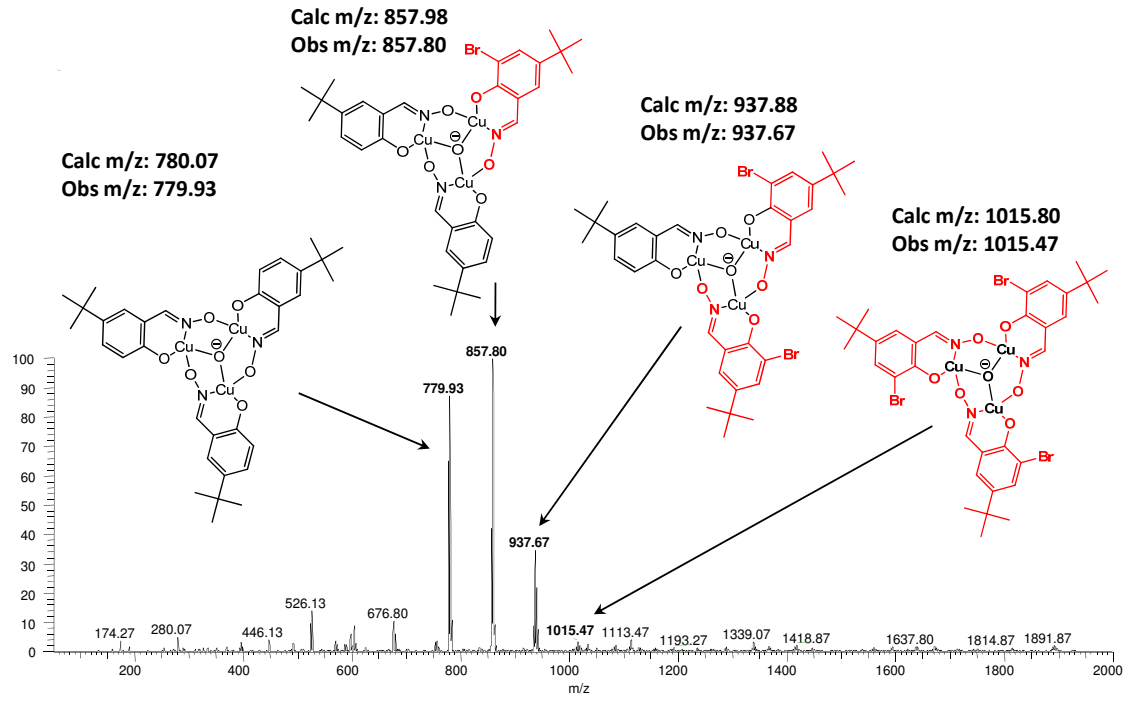

Figure 6.24: Mass spectrum derived from a solution of solution of copper acetate in acetonitrile (50 µM) with **L1H** and **L6H.** The Cu^{2+} to **L1H** to **L6H** ratio is 2:1:1. Proposed structures are given along with observed and calculated monoisotopic masses.

The observed ratio for the intensities of the $[Cu_3(\mathbf{L1}\text{-}H)_3O]^-$, $[Cu_3(\mathbf{L1}\text{-}H)_2(\mathbf{L6}\text{-}H)O]^-$, $[Cu_3(\mathbf{L1}\text{-}H)\ (\mathbf{L6}\text{-}H)_2O]^-$ and $[Cu_3(\mathbf{L6}\text{-}H)_3O]^-$ ions is 90 : 100 : 40 : 5. Statistically the $[Cu_3(\mathbf{L1}\text{-}H)_2(\mathbf{L6}\text{-}H)O]^-$, $[Cu_3(\mathbf{L1}\text{-}H)(\mathbf{L6}\text{-}H)_2O]^-$ species are three times as likely to form in solution than $[Cu_3(\mathbf{L1}\text{-}H)_3O]^-$ and $[Cu_3(\mathbf{L6}\text{-}H)_3O]^-$. The prevalence of the former suggests that either this is present in higher concentrations in solution or that its ease of ionisation is greater. As the ionisation process (as described in Chapters 1 and 5) is dependent on desolvation it is probable that the relative hydrophobicities of the complexes may influence the ionization efficiency. If the incorporation of more bromo-substituents into trinuclear complex increases the solvation energy in acetonitrile the relative ionisation efficiencies would be expected to follow the order: $Cu_3(\mathbf{L1}\text{-}H)_3O]^- > [Cu_3(\mathbf{L1}\text{-}H)_2(\mathbf{L6}\text{-}H)O]^- > [Cu_3(\mathbf{L1}\text{-}H)(\mathbf{L6}\text{-}H)_2O]^- > [Cu_3(\mathbf{L6}\text{-}H)_3O]^-$ and this, coupled with the statistical preference for $[Cu_3(\mathbf{L1}\text{-}H)_2(\mathbf{L6}\text{-}H)O]^-$ and $[Cu_3(\mathbf{L1}\text{-}H)(\mathbf{L6}\text{-}H)_2O]^-$ will account for the observed order of intensities

The results of the mass spectrometry studies described in this chapter have indicated that $[(Cu)_3(\mathbf{L})_3\text{-}\mu_3\text{-}O]^-$ containing complexes are the dominant species, formed by a range of phenolic oxime ligands in acetonitrile solutions containing an excess of copper(II) acetate.

As such trinuclear copper(II) complexes of phenolic oximes have not previously been isolated and characterised, attempts were made to study them in condensed phases (see below).

6.2.6. Solution phase characterization

6.2.6.1. UV/Vis studies

UV/Vis spectra were recorded of 80μM solutions of **L1bH** in MeCN mixed with varying concentrations of $Cu(OAc)_2.H_2O$**.** (Figure 6.25)

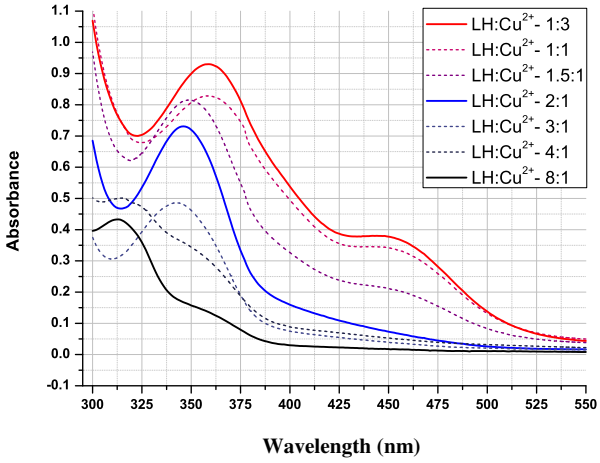

Figure 6.25: UV/Vis spectra of 80μM solutions of **L1BH** in MeCN containing varying concentrations of $Cu(OAc)_2.H_2O$**.** with the **L1BH** to Cu^{2+} ratio ranging from 1:3 to 8:1.

When the ligand is in large excess, the tail of the π-π* bands from the ligand in the UV region dominates the spectrum with an absorption maximum at 313 nm, but a shoulder band is also observed at around 360 nm. When the **LH** to Cu^{2+} is 2:1 a shift in the π-π* band from 313-346 nm is observed as the [Cu(**L1B**)$_2$] concentration increases. When the **LH** to Cu^{2+} is 1:1 a further shift is observed in the π-π* band to 359 nm which correlates with an increase in the delocalization of the π system. A second band with an absorption maximum at 446 nm is also observed. The two bands observed do not shift as the copper concentration is further increased which is consistent with the 1:1 stoichiometry in the trinuclear complex.

6.2.7. Solid state characterization

6.2.7.1. XRD crystallography

Attempts to isolate a solid sample containing the $[Cu_3(\mathbf{L8b}\text{-}H)_3O]^-$ from a reaction of equimolar quantities of **L8bH** and copper acetate species resulted in the formation of the conventional mononuclear complex [Cu(**L8b**)$_2$] with two ketoxime ligands. (Figure 6.26)

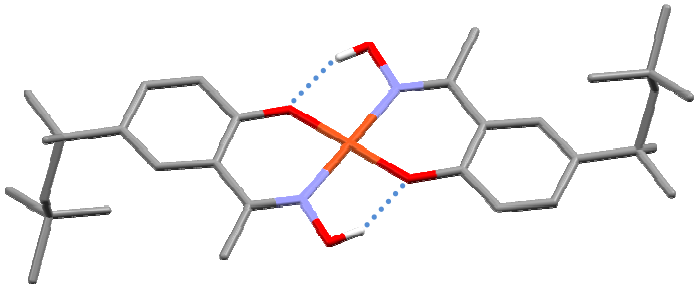

Figure 6.26: The solid state structure of [Cu(**L8b**)$_2$]. Hydrogen atoms not involved in H-bonding omitted for clarity. Space group: P 21/c, R Factor: 4.2%

Two polymorphs of [Cu(**L8b**)$_2$] were isolated under similar conditions, both having the space group P21/c. The first had unit cell dimensions of; a = 13.9072(4) Å, alpha = 90°, b = 7.0037(2) Å, beta = 100.478(2)°, c = 16.0899(4) Å, gamma = 90°. (Figure 6.27)

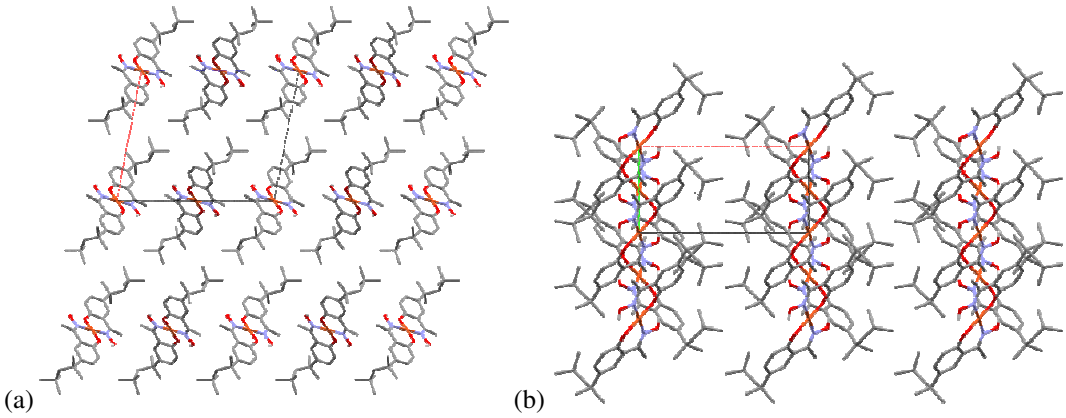

Figure 6.27: Solid state packing diagram polymorph 1 of [Cu(**L1B**)$_2$], looking down (a) the b-axis and (b) the c-axis. Hydrogen atoms omitted for clarity. Space group: P 21/c, R Factor : 4.25%

The second had unit cell dimensions of a = 6.1957(13) Å alpha = 90°, b = 13.211(3), Å beta = 99.295(3)°, c = 18.500(4) Å gamma = 90°. (Figure 6.28)

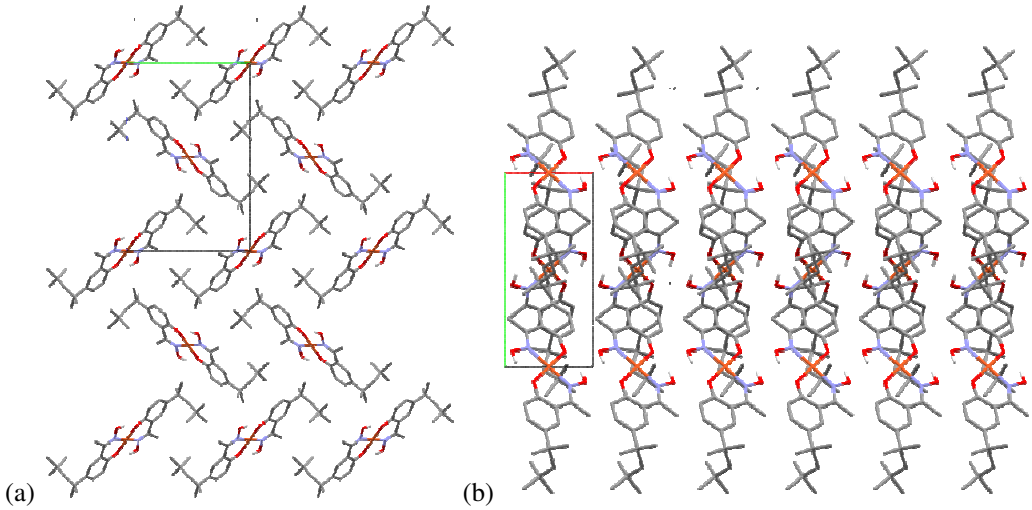

Figure 6.28: Solid state packing diagram of [Cu(**L8b**)$_2$] looking down (a) the a-axis and (b) the c-axis. Hydrogen atoms omitted for clarity. Space group: P 21/c, R Factor : 3.9%.

Attempts to isolate crystalline forms of the trinuclear complexes from solutions of the phenolic oximes **L1H**, **L3H**, **L1bH** and **L8bH** resulted in the mononuclear bisoximate complexes, [Cu(**L**)$_2$]. Introduction of a protonatable amine arm on the ligand provided greater success (Figure 6.29) (see below).

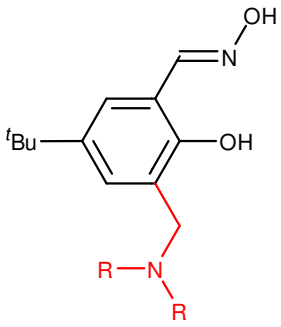

Figure 6.29: Phenolic oxime substituted in the 3-postition with a protonatable amine arm.

6.2.8. Introduction of protonatable arm

Protonatable amines have been looked at previously within the Tasker group in Edinburgh as a means of producing "*metal-salt*" extractants. This type of extractant

can load metal cations *via* cation exchange, as for the conventional reagents, and attendant anions by binding to the protonated arms. (see Figure 6.30)

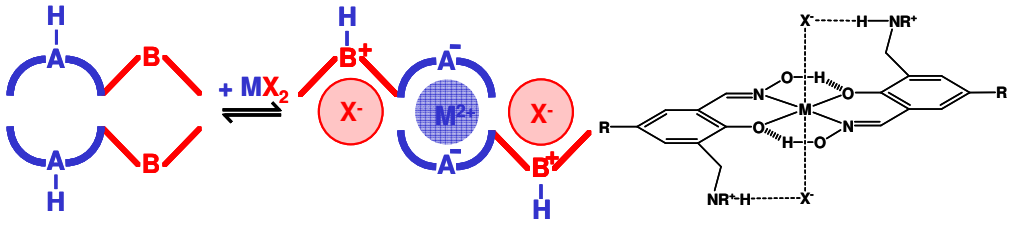

Figure 6.30: Representations (centre and right) of the *trans* coordinated complexes having tritopic assemblies, as formed by 5-*t*-butyl-3-piperidin-1-ylmethyl-salicylaldoxime (R = *t*-butyl; M = Cu; X = NO_3, BF_4 and CF_3CO_2 as described by R. S. Forgan.[53]

It was hoped that the amine arm of the simple salicylaldoximes of the type shown in Figure 6.29 would form trinuclear complexes of the type shown in Figure 6.31. Formation of hydrogen bonds from the protonated benzylammonium groups reduce the negative charge associated with the trinuclear inner-sphere complex and will generate a species with is a mono-cation.

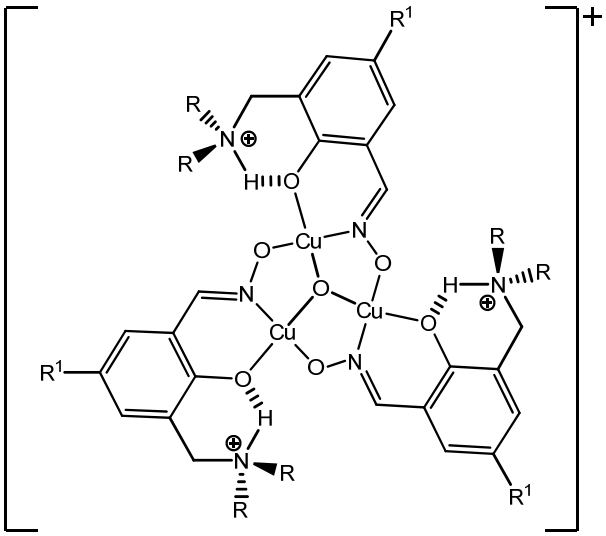

Figure 6.31: Possible structure for a trinuclear unit when protonatable amine arms are incorporated into the ligand design, and hydrogen bonded to the adjacent phenolate oxygen.

6.2.8.1. Ligand syntheses

The ligands **L16H**-**L18H** synthesised for this investigation are shown in Table 6.2 secondary amines were used to generate the benzylamine units as they are relatively rigid and have a higher propensity to form crystalline complexes.

Table 6.2: Structures for ligands **L16H**-**L18H.**

LH	R	$N(R^1)_2$
L16H	^{t}Bu	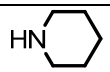
L17H	^{t}Bu	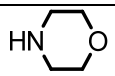
L18H	^{t}Bu	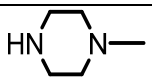

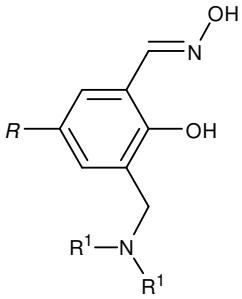

Ligand **L16H – L18H** were synthesised according to the scheme in Figure 6. 32 Incorporation of the pendant amine arm to the salicylaldehyde was achieved using two different approaches the first being a modified Mannich reaction,[53,54] and the second was a coupling reaction as described by Wang *et al.*[55]

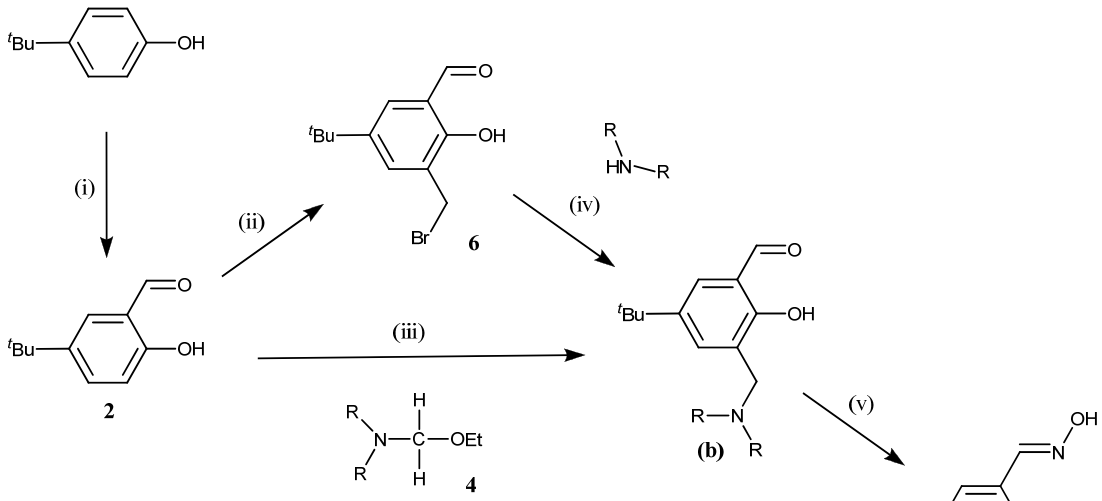

(i) - see Chapter 2

(ii) - **2** (1.0 eq.) in $HBr_{aq.}$(excess) with paraformaldehyde (2.0 eq.) and H_2SO_4 (cat.)/70 °C, 24 hours

(iii) - **2** (1.0 eq.) and **4** (1.1 eq.) in MeCN/ reflux 72 hours

(iv) - **4** (1.0 eq.) with Amine (1.1 eq.) and K_2Co_3 (1.5 eq.)/ reflux 6 hours

(v) - **(b)** (1.0 eq.) with $NH_3OH.HCl$ (1.2 eq) and KOH (1.2 eq.) in EtOH/ reflux 6 hours

Figure 6. 32: Synthesis routes to 3-amineomethyl-substituted salicylaldoximes **L16H**-**L18H**.

6.2.9. Copper complexes of L16H

L16H was reacted with copper(II) salts using various conditions in an attempt to isolate a trinuclear complex similar to those observed previously in the mass spectra and implied in solution by UV/Vis spectroscopy. The species first isolated by mixing stoichiometric amounts of **L16H** and copper acetate in methanol was the [Cu(**L16**)$_2$] complex (Figure 6.33 (a)). In the solid state this exists as a dimeric unit with the copper atoms showing a distorted square based pyramidal coordination making contact with phenolate oxygen atoms in adjacent units. (Figure 6.33 (b))

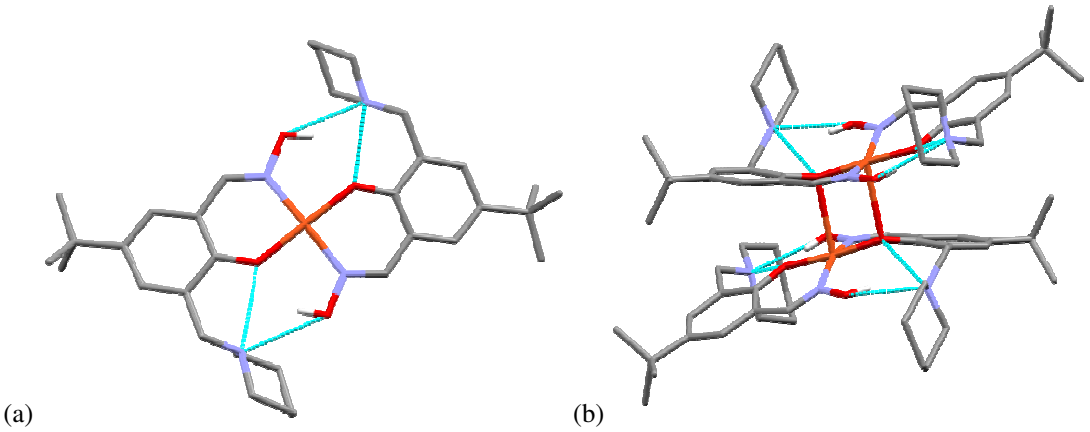

(a) (b)

Figure 6.33: The Solid state structure of $[Cu(\mathbf{L16})_2]_2.5(C_7H_8)$, showing (a) the $[Cu(\mathbf{L16})_2]$ unit and the dimer $[Cu(\mathbf{L16})_2]_2$ unit formed by association of the copper atoms with phenolate atoms in the adjacent complex. Hydrogen atoms not involved in H-bonding and the toluene solvent molecules are omitted for clarity. Crystal system; Triclinic, Space group; P -1, R factor: 4.74%

The crystal system was determined to be triclinic with a P-1 space group. Five toluene molecules cocrystallised with the $[Cu(\mathbf{L16})_2]_2$ dimers in each unit cell. (Figure 6.34)

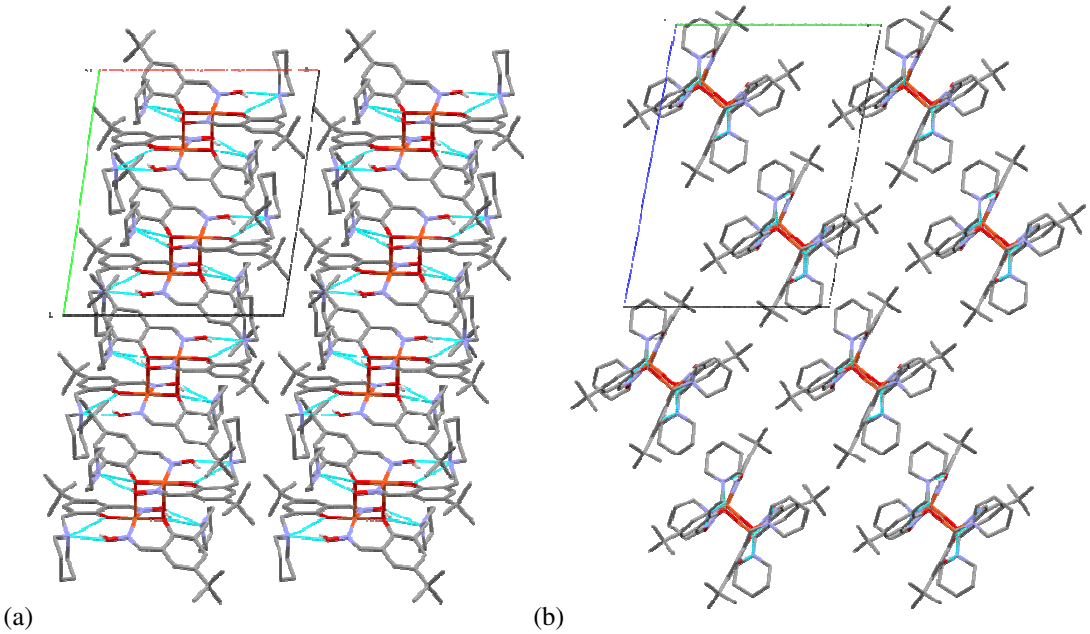

(a) (b)

Figure 6.34: Crystal packing diagrams of $[Cu(\mathbf{L16})_2]_2.5(C_7H_8)$, looking down (a) a-axis and (b) b-axis. Hydrogen atoms not involved in H-bonding and the toluene solvent molecules are omitted for clarity. Crystal system; Triclinic, Space group; P -1, R factor: 4.74%

L17H and **L18H** both yielded similar complexes under similar conditions. Their crystal structures ([Cu(**L17**)$_2$]$_2$ and [Cu(**L18**)$_2$].EtOH) and characterisation can be found in appendix 8.6.3.

Reacting stoichiometric amounts of **L16H** and copper chloride in MeCN yielded a mono ligated copper chloride complex, [Cu(**L16H**)Cl_2], previously observed by Forgan *et al.* The complex was isolated as a diethylether solvated dimer, [Cu(**L16H**)Cl_2]$_2$.Et_2O . (Figure 6.35).

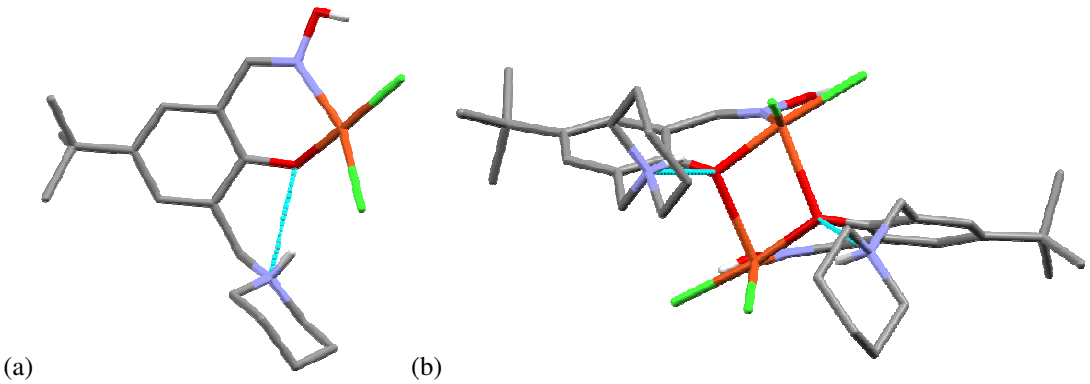

(a) (b)

Figure 6.35: Solid state structure of [Cu(**L16**H)]Cl_2]$_2$.Et_2O, showing (a) the monomeric [Cu(**L16**)Cl_2] unit and (b) the dimer [Cu(**L16**H)]Cl_2]$_2$ formed by association of the copper atoms with phenolate oxygen atoms in the adjacent complex. hydrogen atoms not involved in H-bonding and diethyl ether solvent molecules omitted for clarity. Crystal system; Monoclinic, Space group; P 21/c, R factor: 4.3%

As with the [Cu(**L16**)$_2$]$_2$ complex the copper atoms in the [Cu(**L16H**)Cl_2]$_2$ complex show distorted square based pyramidal coordination with elongated inter-unit axial Cu-phenolate oxygen bonds. (Figure 6.36)

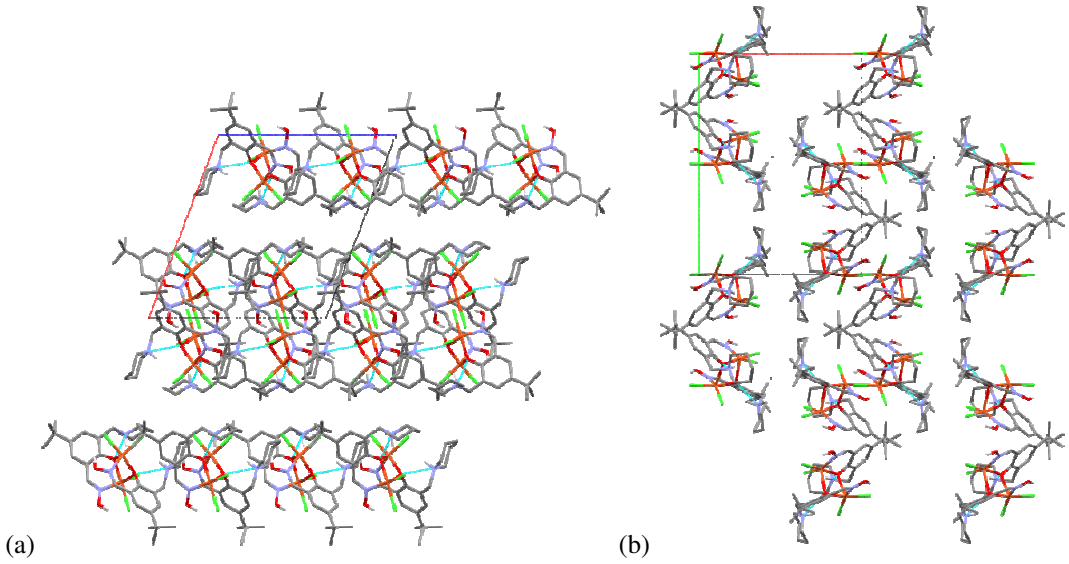

Figure 6.36: Crystal packing diagrams of [Cu(**L16**H)]$Cl_2]_2.Et_2O$ looking down (a) b-axis and (b) c-axis. Hydrogen atoms not involved in H-bonding and the diethyl ether solvent molecules are omitted for clarity. Crystal system; Monoclinic, Space group; P 21/c, R factor: 4.3%

When **L16H** was reacted with copper perchlorate in ethanol a dark green solution was formed. Upon addition of pyridine, in an attempt to ensure a doubly deprotonated **L16H**, a grey precipitate formed. The resultant species had little to no solubility in most solvents but from microanalysis a possible composition is [Cu(**L16H**)$(py)_2$][$ClO_4]_2$. This was soluble in nitriles yielding dark green/turquoise solutions. Diffusion of diethyl ether into a solution in MeCN, formed the species [Cu(**L16**-$C(CH_3)$NH)][py][$ClO_4]_2$ (Figure 6.37), which contains a tridentate ligand formed by addition of acetonitrile to the oxime group.

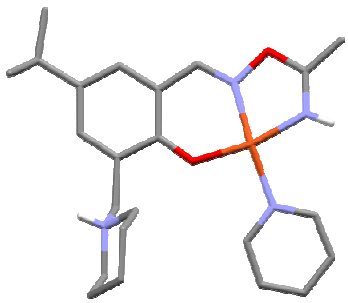

Figure 6.37: Solid state structure of [Cu(**L16**-$C(CH_3)$NH)(py)(ClO_4)][ClO_4], showing [Cu(**L16**-$C(CH_3)$NH)(py)] unit. Hydrogen atoms not involved in H-bonding are omitted for clarity. Crystal system; Triclinic, Space group; P -1, R factor: 3.55%

A possible reaction mechanism, detailed in Figure 6.38, involves deprotonation of the oxime by pyridine followed by nucleophillic attack on the carbon atom of a coordinated acetonitrile molecule.

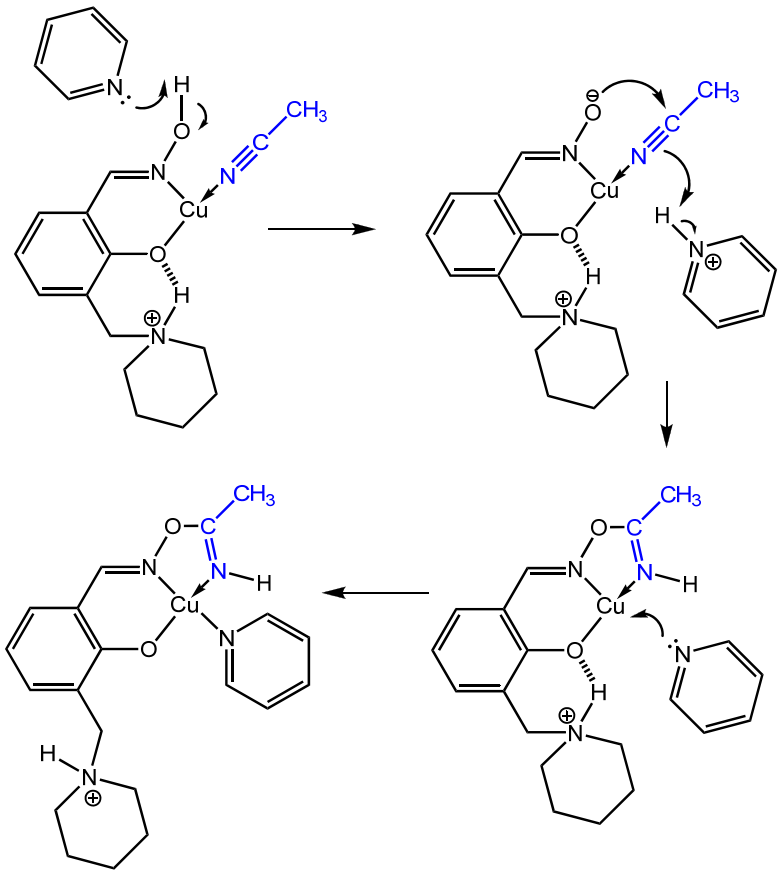

Figure 6.38: Possible reaction mechanism for the formation of the $[Cu(\mathbf{L}\text{-}C(CH_3)NH)py]^{2+}$ unit observed in the crystal structure of $[Cu(\mathbf{L16}\text{-}C(CH_3)NH)(Py)(ClO_4)][ClO_4]$.

The piperidyl arm is protonated but is not associated with the phenolate oxygen as observed for the $[Cu(\mathbf{L16H})Cl_2]_2$ complex. Instead a H-bond lattice is formed throughout the crystal between the piperidium nitrogen, the imine hydrogen and the two perchlorate counter ions. One of the perchlorate ions is weakly coordinated to the copper atoms

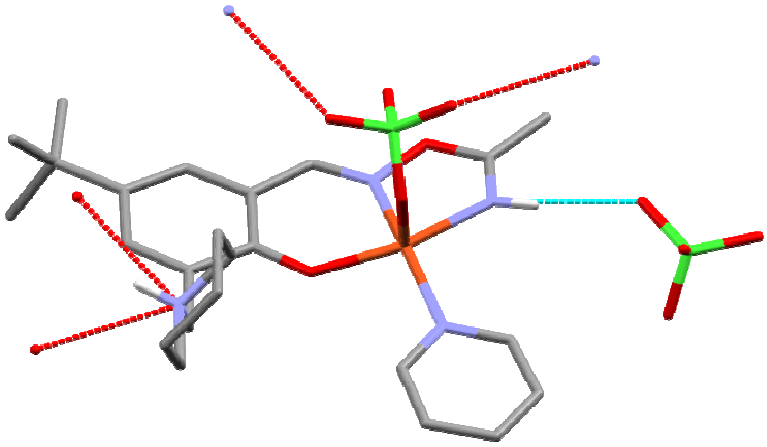

Figure 6.39: Solid state structure of [Cu(**L16**-C(CH_3)NH)(py)(ClO_4)][ClO_4] showing the H-bonding network. Hydrogen atoms not involved in H-bonding are omitted for clarity. Crystal system; Triclinic, Space group; P -1, R factor: 3.55%

A reaction of this type has been observed before for a simple phenolic oxime system by J. Grigg[56] with VO_2^{2+} as the metal source. The reaction of [Cu(**L16H**)$(Py)_2$][ClO_4]$_2$ was not limited to MeCN but occurred with other nitriles. Mass spectrometry data on the products formed with phenyl-, propyl- and butyro-nitrile can be found in Appendix 8.6.5.

6.2.10. Isolation of [Cu_3(L16)$_3$-μ_3-O/OH][ClO_4]$_2$

6.2.10.1. Gas phase and solution characterisation of [Cu_3(**L16**)$_3$-μ_3-O/OH][ClO4]$_2$ complex

Different solvents were investigated in order to determine To what extent the formation of the trinuclear unit was solvent dependent. Alcohols appeared to hinder the formation, as did all non-polar solvents, including chloroform and dichloromethane. Acetonitrile was the solvent that showed the most promise in the formation of the desired peak in the mass spectrum.

When stoichiometric amounts of **L16H** and copper acetate are mixed in acetonitrile, after removal of the solvent, the resulting dark green solid was soluble in water.

Upon addition of excess $KClO_4$ to this aqueous solution a dark green precipitate was formed with both low and high resolution mass spectrometry suggesting that the salt contained $[Cu_3(\mathbf{L16})_3O]^{2+}$ with presumably ClO_4^- counter ion. (Figure 6.40)

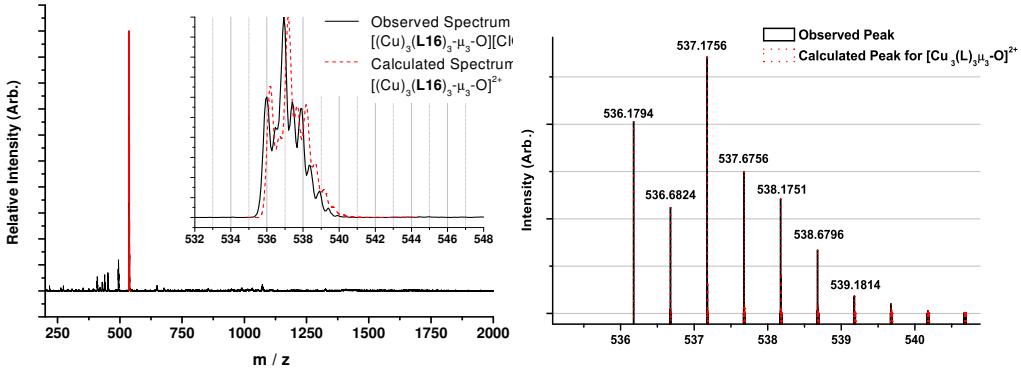

Figure 6.40: (left) The low resolution and (right) high resolution mass spectrum derived from 50μM solutions in acetonitrile of $[Cu_3(\mathbf{L16})_3$-μ_3-O/OH$][ClO_4]_2$ with the m/z for the $[(Cu)_3(\mathbf{L16})_3$-μ_3-O$]^{2+}$ species highlighted for each case.

The electronic spectra of solutions of $[Cu_3(\mathbf{L16})_3$-μ_3-O/OH$][ClO_4]_2$ in MeCN were obtained and compared with those for **L16H** and $[Cu(\mathbf{L16})_2]$ (Figure 6.41 (a)). The extinction coefficients for each of the 3 species were calculated and are shown in Figure 6.41 (b).

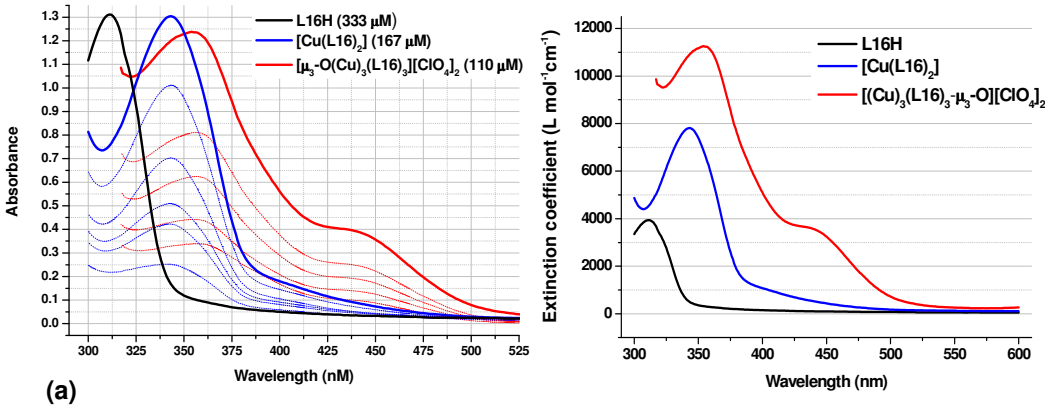

Figure 6.41: (a) The UV/Vis absorption spectra for varying concentrations of **L16H**, $[Cu(\mathbf{L16})_2]$ and $[Cu_3(\mathbf{L16})_3$-μ_3-O/OH$][ClO_4]_2$ and (b) their respective absorption coefficients.

The trends in the shifts of the absorption peaks are very similar to those observed for the **L1bH** system (see Section 6.2.6.1.) with a systematic red-shift of the π-π* band

with increasing conjugation of the π system and a second absorption observed for the $[(Cu)_3(\mathbf{L16})_3\text{-}\mu_3\text{-}O/OH][ClO_4]_2$ at 445 nm.

6.2.10.2. Solid state characterisation of $[(Cu)_3(\mathbf{L16})_3\text{-}\mu_3\text{-}OH(ClO_4)][ClO_4]$ complexes.

Reaction conditions were optimised to yield the of $[Cu_3(\mathbf{L16})_3\text{-}\mu_3\text{-}OH(ClO_4)][ClO_4]$ complex in 91% yield with microanalysis of the product found to be C, 47.1; H, 5.9; N, 6.4 with the calculated elemental analysis for $[Cu_3(\mathbf{L16})_3\text{-}\mu_3\text{-}OH(ClO_4)][ClO_4].1.5H_2O$ being C, 47.1; H, 6.1; N, 6.2. (full experimental given in Section 6.6). XRD quality crystals were obtained via slow cooling of a saturated solution of MeCN: H_2O: Ethyl acetate, 5:1:4. The obtained structure was a centrosymmetric dimer, $[Cu_3(\mathbf{L16})_3\text{-}\mu_3\text{-}OH(ClO_4)]_2[ClO_4]_2.2H_2O.2MeCN$ (Figures 6.42 and 6.43), in which the hydroxyl groups of the $Cu_3\text{-}\mu_3\text{-}OH$ units form hydrogen bonds to an oximic oxygen atom in a the neighbouring complex. Three of the oxygen atoms of one of the perchlorate ions lie over the axial sites of the copper atoms in the $Cu_3\text{-}\mu_3\text{-}OH$ unit, preserving a pseudo 3-fold symmetry (see Figure 6.42.).

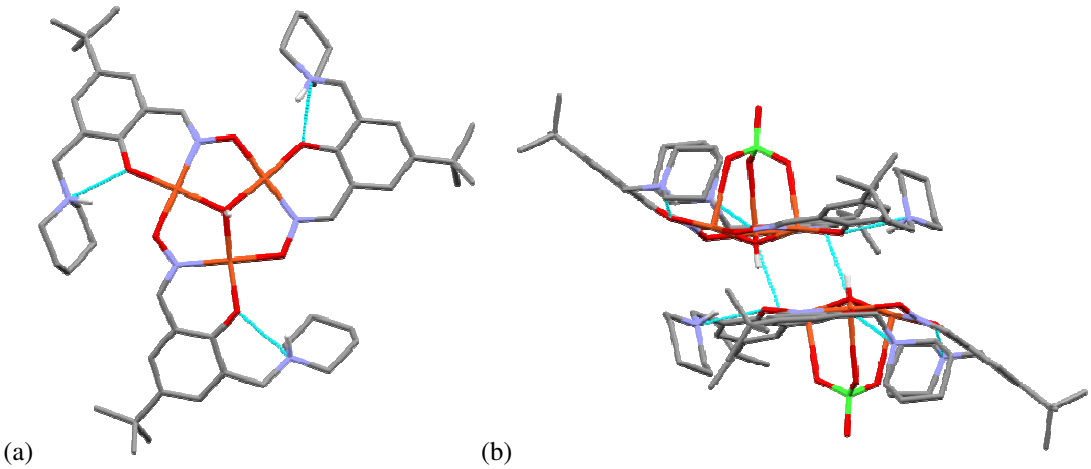

(a) (b)

Figure 6.42: Solid state structure of $[Cu_3(\mathbf{L16})_3\mu_3\text{-}OH(ClO_4)]_2[ClO_4]_2.2H_2O.2MeCN$ (structure **1**), showing (a) monomeric $[Cu_3(\mathbf{L16})_3\mu_3\text{-}OH][ClO_4]$ and (b) dimeric $[Cu_3(\mathbf{L16})_3\mu_3\text{-}OH]_2[ClO_4]_2$, hydrogen atoms not involved in H-bonding, solvent molecules and ClO_4^- counter ions omitted for clarity. Crystal system: Monoclinic, Space group: P -1, R factor: 5.68%.

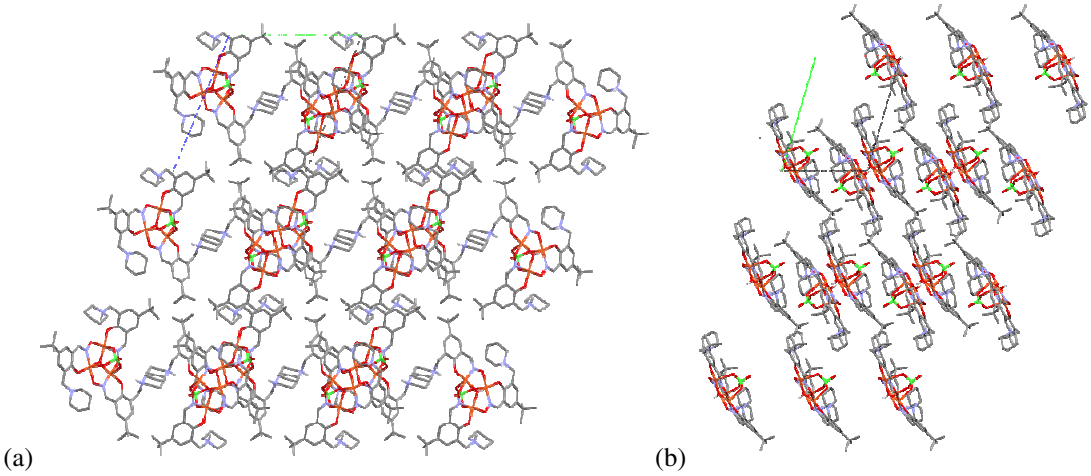

Figure 6.43: Solid state packing diagram of $[Cu_3(\mathbf{L16})_3\mu_3\text{-}OH(ClO_4)]_2[ClO_4]_2.2H_2O.2MeCN$ (structure **1**) looking down (a) a-axis and (b) b-axis, hydrogen atoms, solvent molecules and ClO_4^- counter ions omitted for clarity. Crystal system: Monoclinic, Space group: P -1, R factor: 5.68%.

The high solubility of the starting $[Cu_3(\mathbf{L16})_3\text{-}\mu_3\text{-}OH(ClO_4)]_2[ClO_4]_2$ salt in most polar solvents and the formation of the $[Cu(\mathbf{L16})_2]$ complex in non-polar solvents made repeated isolation of the $[Cu_3(\mathbf{L16})_3\text{-}\mu_3\text{-}OH(ClO_4)]_2[ClO_4]_2.2H_2O.2MeCN$ complex, using the above crystallisation method, difficult.

A second crystalline form was obtained by slow diffusion of a solution of $[Cu_3(\mathbf{L16})_3\text{-}\mu_3\text{-}OH(ClO_4)]_2[ClO_4]_2$ in a 1:1 mixture of MeCN and diethyl ether into H_2O (dist.). This (structure 2) has the composition $[Cu_3(\mathbf{L16})_3\text{-}\mu_3\text{-}OH(ClO_4)]_2[ClO_4]_2.11H_2O.2MeCN$ and also contains a centrosymmetric dimer, but with differences in contact distances between the two monomer units.

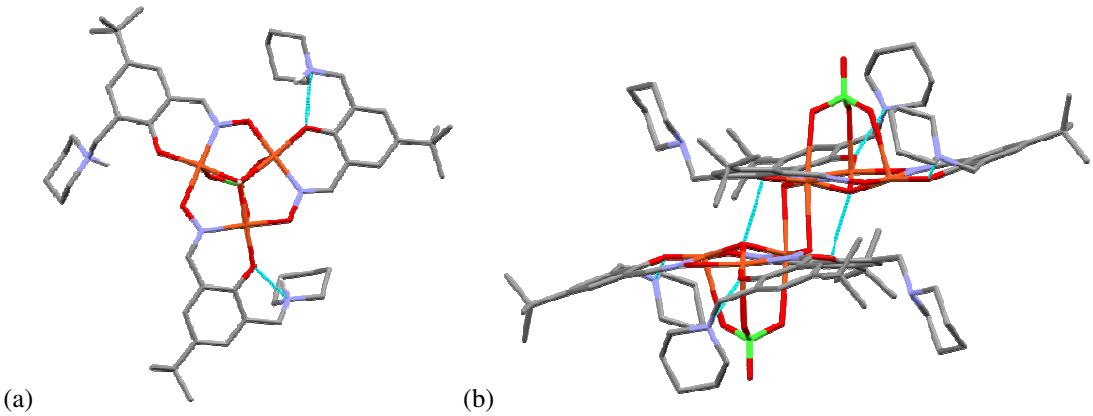

(a) (b)

Figure 6.44: Solid state structure of $[Cu_3(\mathbf{L16})_3\mu_3\text{-}OH(ClO_4)]_2[ClO_4]_2.11H_2O.MeCN$ (structure **2**), showing (a) monomeric $[Cu_3(\mathbf{L16})_3\mu_3\text{-}OH][ClO_4]$ and (b) dimeric $[Cu_3(\mathbf{L16})_3\mu_3\text{-}OH]_2[ClO_4]_2$, hydrogen atoms not involved in H-bonding, solvent molecules and ClO_4^- counter ions omitted for clarity. Crystal system: Triclinic, Space group: P -1, R factor: 4.72%.

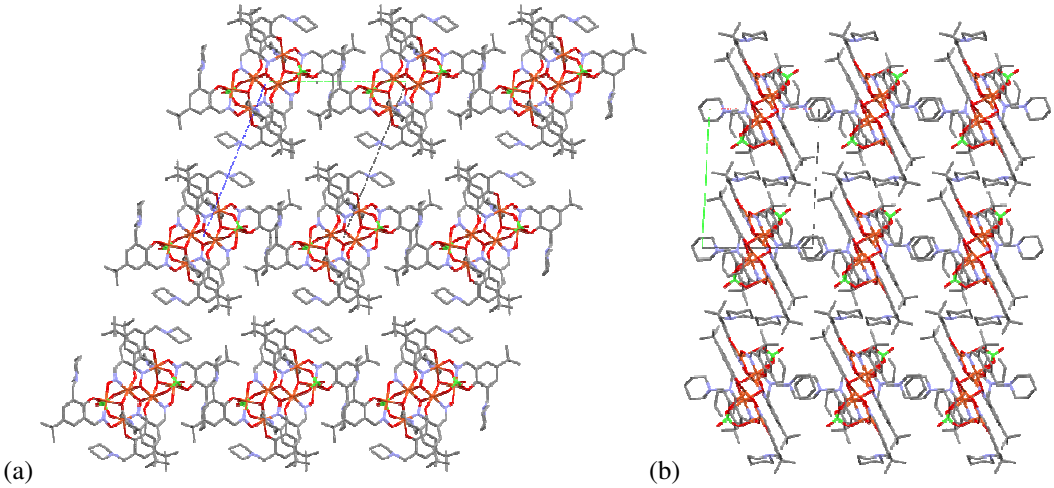

(a) (b)

Figure 6.45: Solid state packing diagram of $[Cu_3(\mathbf{L16})_3\mu_3\text{-}OH(ClO_4)]_2[ClO_4]_2.11H_2O.MeCN$ (structure **2**) looking down (a) a-axis and (b) b-axis, hydrogen atoms, solvent molecules and ClO_4^- counter ions omitted for clarity. Crystal system: Triclinic, Space group: P -1, R factor: 4.72%.

Structure **1** has a shorter μ_3-OH to oximic oxygen contact than that found in structure **2** (see Figure 6.46). In structure **1** the shortest contact distances in the dimer from the copper atoms are to phenolate oxygen atoms (2.871(3) Å) whereas in structure **2** they are to oximato oxygen atoms and are shorter (2.573(2) Å), falling in the range found[57] for Jahn-Teller distorted bonds for copper(II). Another difference between

the structures **1** and **2** is that in the latter one of the piperidinium nitrogen atoms is not hydrogen bonded to the adjacent phenolate oxygen atom, but approaches a water in the lattice (see below).

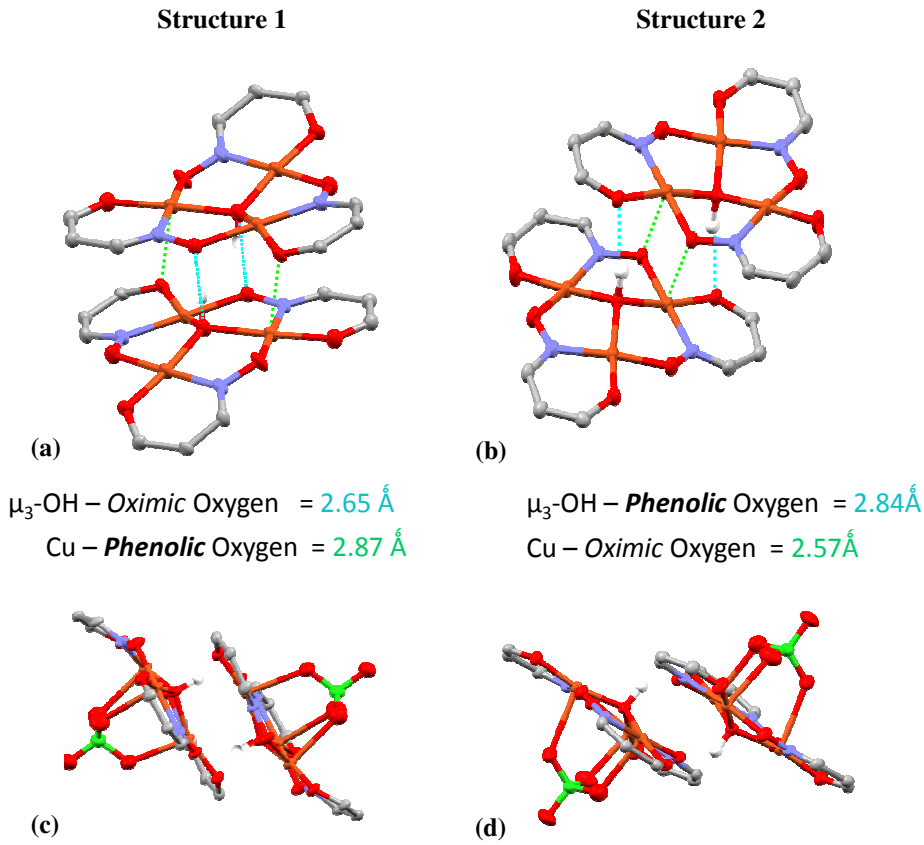

Figure 6.46: The core dimeric units of $[Cu_3(\mathbf{L16})_3\text{-}\mu_3\text{-}OH(ClO_4)]_2[ClO_4]_2.2H_2O.2MeCN$ (structure **1**) and $[Cu_3(\mathbf{L16})_3\mu_3\text{-}OH(ClO_4)]_2[ClO_4]_2.11H_2O.MeCN$ (structure 2) with the shortest Cu···O contact distances and the O···O distances associated with contacts made by μ_3-OH groups listed.

The differences between structures **1** and **2** extend beyond differences in the hydrogen bonding in the immediate outer coordination spheres of the complexes. The piperidinium NH···H_2O units in **2** are linked by two further lattice water molecules to form two straps between the two halves of the dimeric unit (Figure 6.47).

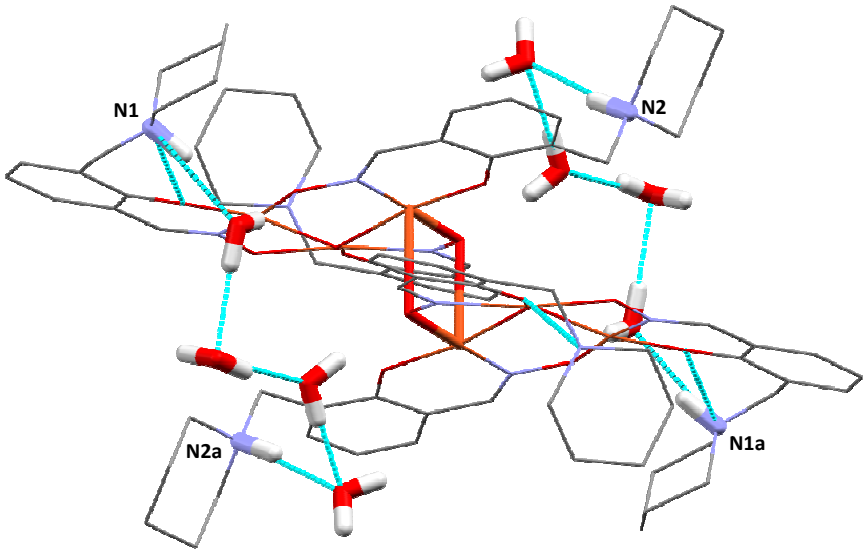

Figure 6.47: The dimeric unit $[Cu_3(\mathbf{L16})_3\text{-}\mu_3\text{-}OH_2]_2$ in structure **2** showing the four H-bonded water molecules which form straps between the monomer units. Hydrogen atoms and solvent molecules not involved in H-bonding network, *tert*-butyl substituents and ClO_4^- groups are omitted for clarity. Crystal system: Triclinic, Space group: P -1, R Factor : 4.72%.

A ring of six hydrogen bonded water molecules hydrogen bonded to piperidinium NH groups also forms a link *between* dimers (see Figure 6.48).

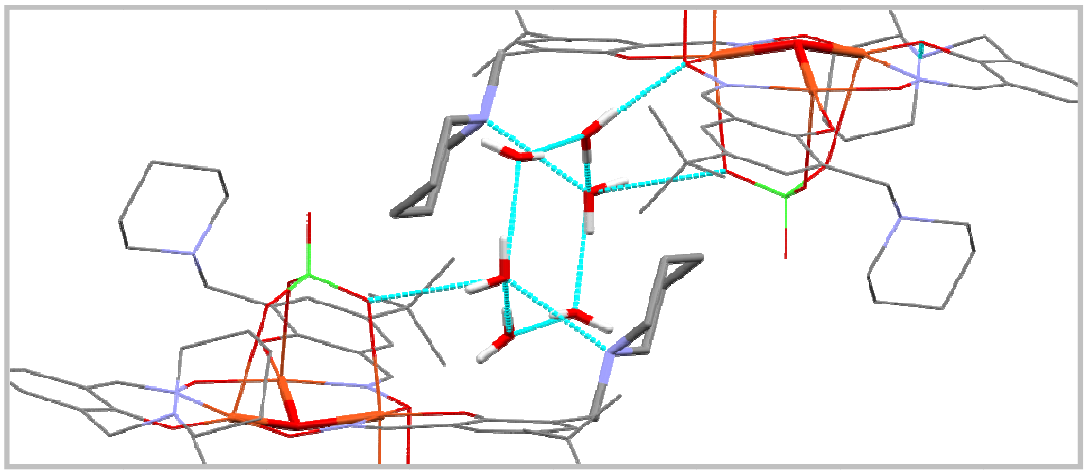

Figure 6.48: Part of the structure of $[Cu_3(\mathbf{L16})_3\mu_3\text{-}OH(ClO_4)]_2[ClO_4]_2.11H_2O.MeCN$ showing the ring of six hydrogen bonded water molecules which dimer units. Hydrogen atoms, solvent molecules not involved in the H-bonding network, *tert*-butyl substituents and the ClO_4^- ions not bound to copper are omitted for clarity.

6.2.11. Electronic structures and stabilities of μ_3-Y bridged trinuclear complexes

In the work reported above we have seen evidence for the formation of μ_3-oxo complexes (Y = O and X = 1 in the generic structure (a) in Figure 6.49) in the gas phase with a wide range of phenolic oxime ligands. These ionic complexes, $[Cu_3(\mathbf{L}\text{-}H_n)_3\text{-}\mu_3\text{-}O]^{(+2-n)}$, were obtained as the base peak in ESI-MS of solutions of all the phenolic oximes tested (see table in Figure 6.49)

It was only possible to isolate and characterized similar trinuclear complexes in the solid state with a μ_3-hydroxy group (Y = OH in the generic structure (a) in Figure 6.49) and with the ligands carrying 3-dialkylammoniummethyl substituents (X = R_2NHCH_2) which result in dicationc complexes $[Cu_3(L)_3\text{-}\mu_3\text{-}OH]^{2+}$.

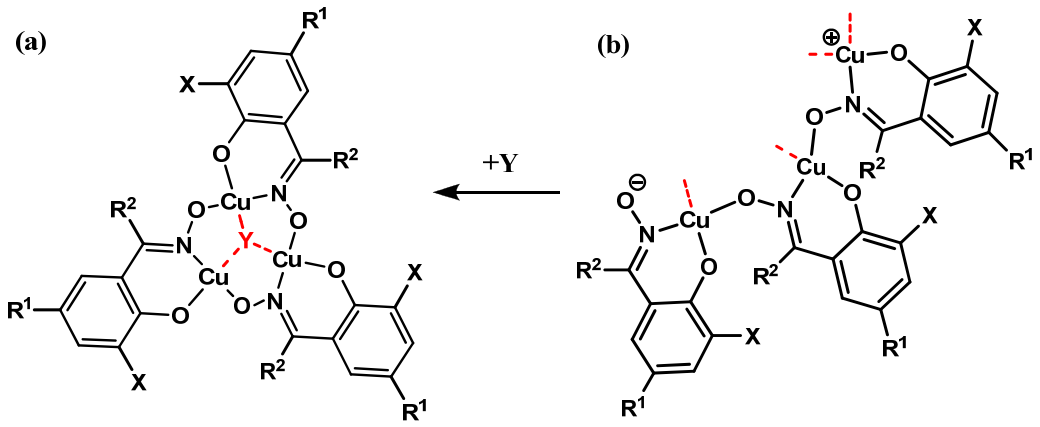

Ligand	R^1	R^2	X	Y	z	phase	reference
L1H	^{t}Bu	H	H	O^{2-}	-1	gas	6.2.2
L1bH	^{t}Bu	Me	H	O^{2-}	-1	gas	6.2.2
L8H	^{t}Oct	H	H	O^{2-}	-1	gas	6.2.2
L8bH	^{t}Oct	Me	H	O^{2-}	-1	gas	6.2.2
L3H	^{t}Bu	H	^{t}Bu	O^{2-}	-1	gas	6.2.2
L3H	^{t}Bu	H	^{t}Bu	OMe^-	-1	gas	6.2.11
L5H	^{t}Bu	H	Cl	O^{2-}	-1	gas	6.2.2
L6H	^{t}Bu	H	Br	O^{2-}	-1	gas	6.2.2
L16H	^{t}Bu	H	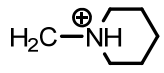	O^{2-}	+2	gas	6.2.10
L16H	^{t}Bu	H	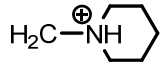	OH^-	+2	solid	6.2.10
*	^{t}Bu	H	$H_2C(NH_2^+)C_6H_{12}(NH_2^+)CH_2$	$O(H)^-$	+2	solid	Ref[49]
*	^{t}Bu	H	$H_2C(NH_2^+)C_6H_{12}(NH_2^+)CH_2$	OEt^-	+2	solid	Private commun.[58]

Figure 6.49: Trinuclear copper complexes of doubly deprotonated phenolic oxime ligands characterised in this thesis.*hexanuclear copper complexes of quadruply deprotonated ditopic phenolic oxime ligands as described by Plieger *et. al.*[49,58]

In principle these cyclic trinuclear complexes could be formed by combining the linear species ((b) in Figure 6.49), analogous to some of the aggregates reported

above with the appropriate μ_3 ligand Y. A μ_3-methoxy complex anion $[Cu_3(L)_3\text{-}\mu_3\text{-}OMe]^-$ can be detected in the mass spectrum derived from a 50μM solution of **L3H** with two equivalents of copper acetate in MeCN : MeOH 90:10.

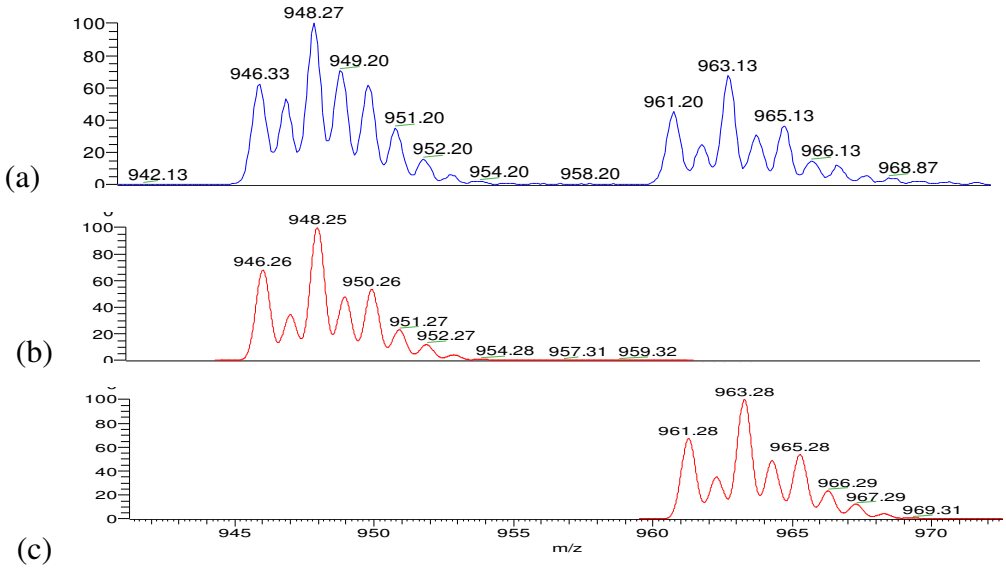

Figure 6.50: Mass spectrum (a) of a 40μM solution of **L3H** and $Cu(OAc)_2.H_2O$ (1:1) in MeCN/MeOH solution (1:1) and the simulated spectrum for $[Cu_3(\mathbf{L3}\text{-}H)_3\text{-}\mu_3\text{-}O]^-$ and $[Cu_3(\mathbf{L3}\text{-}H)_3\text{-}\mu_3\text{-}OMe]^-$ (b and c).

Some preliminary work is outlined in the following section which is aimed at understanding the electronic structures of complexes of the types shown in Figure 6.49 and how stability varies with protonation and oxidation levels, e.g. between the monoanions (a) and (b) in Figure 6.51, which formally differ only in the level of hydrogenation.

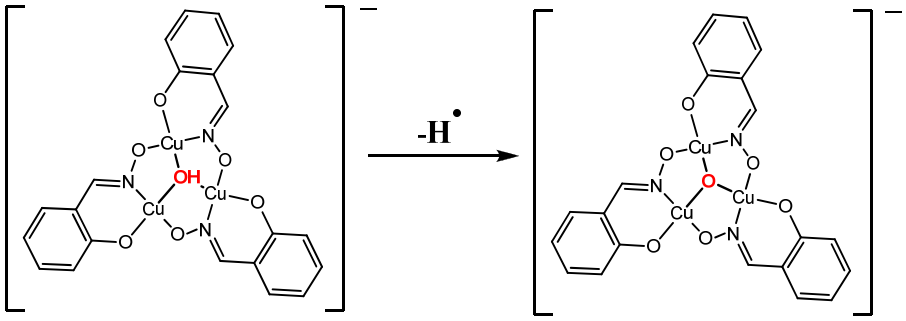

Figure 6.51: Structure of $[Cu_3(\mathbf{L}\text{-}H_n)_3\mu_3\text{-}OH]^{(+2-n)}$ and $[Cu_3(\mathbf{L}\text{-}H_n)_3\mu_3\text{-}O]^{(+2-n)}$ in the gas phase.

6.2.12. DFT investigation

Geometry optimisations were carried out on the four structures shown in figure 6.52, $[Cu_3(\mathbf{L0}\text{-}H)_3\text{-}OH]^-$, $[Cu_3(\mathbf{L0}\text{-}H)_3\text{-}OH]$, $[Cu_3(\mathbf{L0})_3\text{-}O]^{2-}$ and $[Cu_3(\mathbf{L0}\text{-}H)_3\text{-}O]^-$, using the Gaussian '03 program with the level of theory B3LYP[2-4]/6-31+G[5-14](d,p). The relative energies of each species are shown in Table 6.3 along with deprotonation enthalpies of $[Cu_3(\mathbf{L0}\text{-}H)_3\text{-}OH]^-$ and $[Cu_3(\mathbf{L0}\text{-}H)_3\text{-}OH]$ and ionisation enthalpies for $[Cu_3(\mathbf{L0}\text{-}H)_3\text{-}OH]^-$ and $[Cu_3(\mathbf{L0}\text{-}H)_3\text{-}O]^{2-}$.

Table 6.3: relative energies of $[Cu_3(\mathbf{L0}\text{-}H)_3\text{-}OH]^-$, $[Cu_3(\mathbf{L0}\text{-}H)_3\text{-}OH]$, $[Cu_3(\mathbf{L0})_3\text{-}O]^{2-}$ and $[Cu_3(\mathbf{L0}\text{-}H)_3\text{-}O]^-$, and the deprotonation enthalpies of $[Cu_3(\mathbf{L0}\text{-}H)_3\text{-}OH]^-$ and $[Cu_3(\mathbf{L0}\text{-}H)_3\text{-}OH]$ and ionisation enthalpies for $[Cu_3(\mathbf{L0}\text{-}H)_3\text{-}OH]^-$ and $[Cu_3(\mathbf{L0}\text{-}H)_3\text{-}O]^{2-}$.

Species	$[(Cu)_3(\mathbf{L0}\text{-}H)_3\text{-}OH]^-$	$[(Cu)_3(\mathbf{L0}\text{-}H)_3\text{-}OH]$	$[(Cu)_3(\mathbf{L0}\text{-}H)_3\text{-}O]^{2-}$	$[(Cu)_3(\mathbf{L0}\text{-}H)_3\text{-}O]^-$
Charge	-1	0	-2	-1
Multiplicity	4	3	4	3
E (au)	-6421.9645	-6421.8295	-6421.3514	-6421.3277
Energy (kJ mol^{-1})	-16860868	-16860513	-16859258	-16859196
E_{depro} $[(Cu)_3(\mathbf{L0}\text{-}H)_3\text{-}OH]^-$ (kJ mol^{-1})			**1609.7**	
E_{depro} $[(Cu)_3(\mathbf{L0}\text{-}H)_3\text{-}OH]$ (kJ mol^{-1})			**1317.4**	
$E_{ionisation}$ $[(Cu)_3(\mathbf{L0}\text{-}H)_3\text{-}OH]^-$ (kJ mol^{-1})			**354.5**	
$E_{ionisation}$ $[(Cu)_3(\mathbf{L0}\text{-}H)_3\text{-}O]^{2-}$ (kJ mol^{-1})			**62.2**	

The deprotonation energy for $[(Cu)_3(\mathbf{L0}\text{-}H)_3\text{-}OH]^-$ was larger than that calculated for $[(Cu)_3(\mathbf{L0}\text{-}H)_3\text{-}OH]$ (1671.9 and 1317.4 kJ mol^{-1} respectively). This is to be expected as it should be more difficult to increase the charge on the already negatively charged $[(Cu)_3(\mathbf{L0}\text{-}H)_3\text{-}OH]^-$ species. The relative energies of the above species and the relationship between them are illustrated in Figure 6.52.

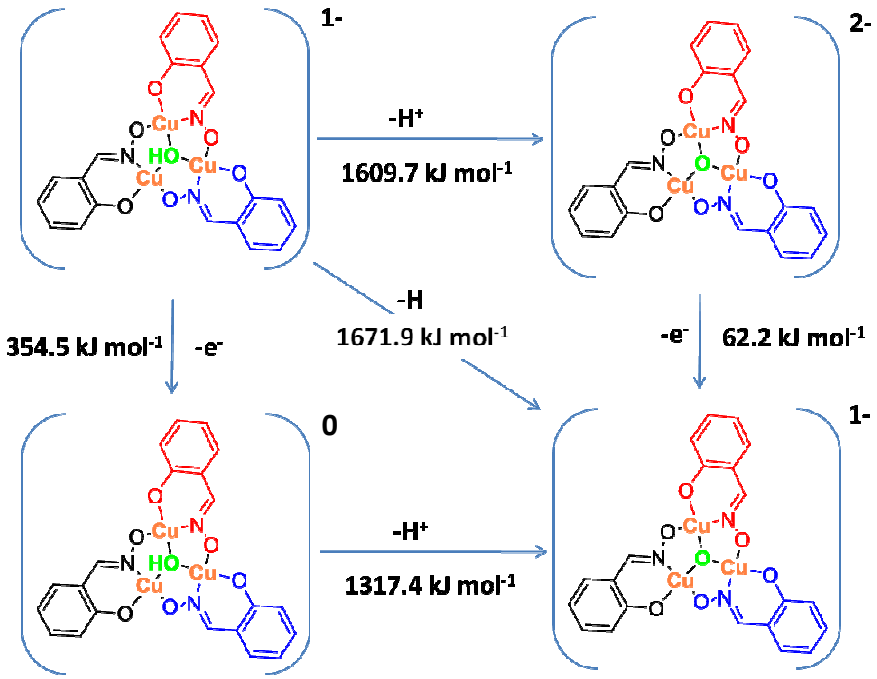

Figure 6.52: Energies of interconversion of the species shown in Table 6.3.

Figure 6.53 shows the geometry optimised structures for the four species described in Table 6.3 .

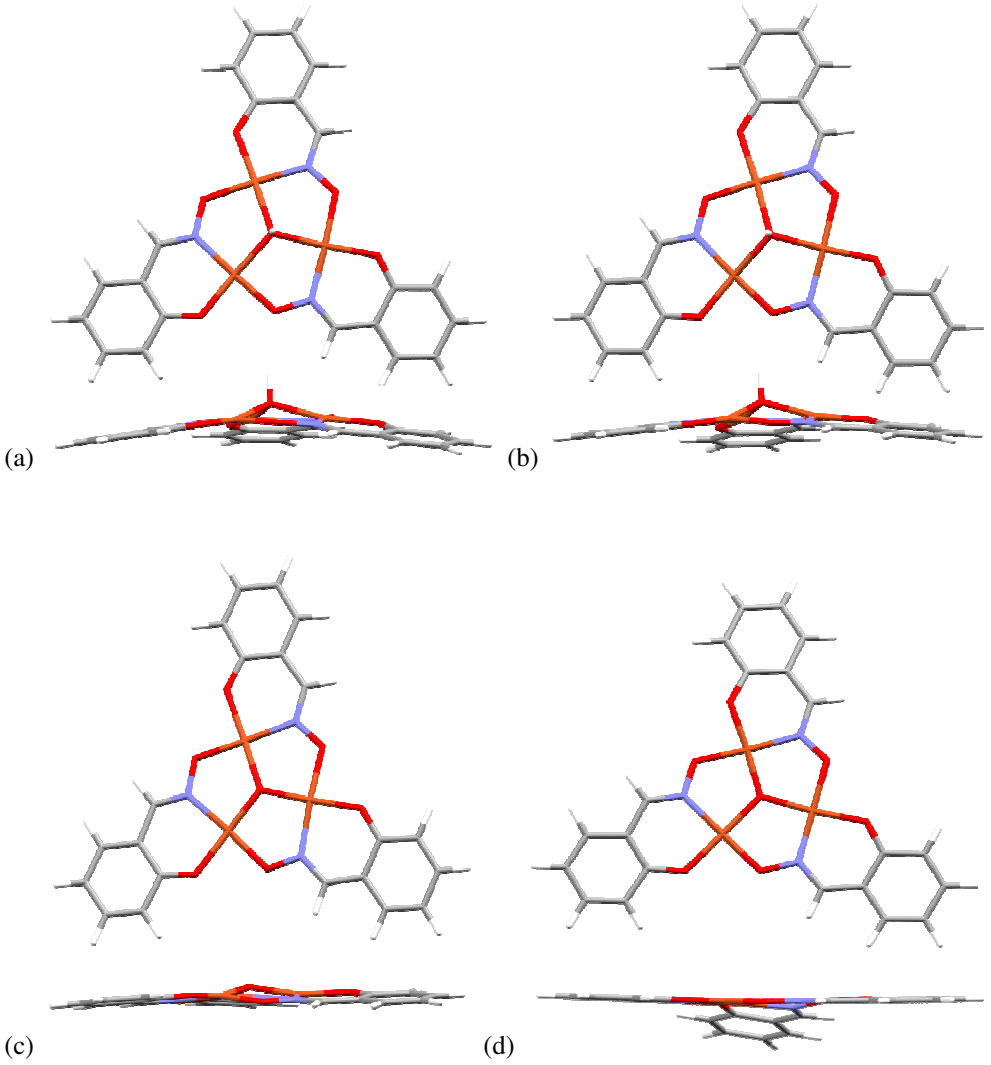

Figure 6.53: The energy minimised structures for (a) $[Cu_3(\mathbf{L0}\text{-}H)_3\text{-}OH]^-$ (b) $[Cu_3(\mathbf{L0}\text{-}H)_3\text{-}OH]$ (c) $[Cu_3(\mathbf{L0}\text{-}H)_3\text{-}O]^{2-}$ and (d) $[Cu_3(\mathbf{L0}\text{-}H)_3\text{-}O]^-$.

The planarity of the complex is dependent on the nature of the μ_3-Y unit. For $[Cu_3(\mathbf{L0}\text{-}H)_3\mu_3\text{-}Y]^n$ when the central Y = OH^-, (a) and (b) in Figure 6.53, the metallocycle unit is domed with the μ_3-OH oxygen atom lying 0.560 and 0.432 Å above the plane, displaced by the three copper atoms. When X = Y^{2-}, (c) and (d) in Figure 6.53, the central unit is much more planar with deviation of the μ_3-oxo atom of 0.052 and 0.002 Å above the Cu_3 plane as might be expected by the sp^2 hybridization of the former.

Table 6.4 shows how the NBO charges on the three chelate units of each of the calculated species, labelled red, black and blue as shown in Figure 6.54.

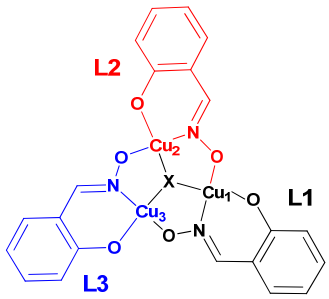

Figure 6.54: Labelling scheme for Table 6.4

Table 6.4: The NBO charges for each of the copper atoms and each of the chelates for the energy minimised structures of $[(Cu)_3(\mathbf{L0}\text{-}H)_3\text{-}OH]^-$, $[(Cu)_3(\mathbf{L0}\text{-}H)_3\text{-}OH]$, $[(Cu)_3(\mathbf{L0}\text{-}H)_3\text{-}O]^{2-}$ and $[(Cu)_3(\mathbf{L0}\text{-}H)_3\text{-}O]^-$.

$[(Cu)_3(\mathbf{L0}\text{-}H)_3\text{-}OH]^-$			$[(Cu)_3(\mathbf{L0}\text{-}H)_3\text{-}OH]$		
Unit	Identity	Charge	Unit	Identity	Charge
1	Cu1	0.22785	1	Cu1	**0.23308**
2	Cu2	0.22873	2	Cu2	**0.80776**
3	Cu3	0.22844	3	Cu3	**0.23545**
4	μ-***O***H	-0.63880	4	μ-***O***H	-0.57737
5	L1	-0.77005	5	L1	**-0.77666**
6	L2	-0.77087	6	L2	**-0.67940**
7	L3	-0.77002	7	L3	**-0.51057**
8	μ-O***H***	0.26472	8	μ-O***H***	0.26771

$[(Cu)_3(\mathbf{L0}\text{-}H)_3\text{-}O]^{2-}$			$[(Cu)_3(\mathbf{L0}\text{-}H)_3\text{-}O]^-$		
Unit	Identity	Charge	Unit	Identity	Charge
1	Cu1	0.23355	1	Cu1	**0.24965**
2	Cu2	0.23349	2	Cu2	**0.36902**
3	Cu3	0.23384	3	Cu3	**0.28992**
4	μ-O	-0.80307	4	μ-O	-0.61372
5	L1	-0.79937	5	L1	**-0.74905**
6	L2	-0.79934	6	L2	**-0.48025**
7	L3	-0.79910	7	L3	**-0.56557**

The removal of an electron from $[(Cu)_3(\mathbf{L0}\text{-}H)_3\text{-}OH]^-$ to give $[(Cu)_3(\mathbf{L0}\text{-}H)_3\text{-}OH]$ appears to arise principally from electron loss from just one of the copper atoms. This would be consistent with a description of the neutral complex as a mixed 2Cu(II)/Cu(III) compound with the monoanion being a 3Cu(II) complex. such assignments of formal charge are also consistent with the phenolic oxime ligands being dianionic and the μ_3-OH group being monoanionic.

Removal of an electron from $[(Cu)_3(\mathbf{L0}\text{-}H)_3\text{-}O]^{2-}$ to give $[(Cu)_3(\mathbf{L0}\text{-}H)_3\text{-}O]^-$ appears to arise through electron loss over the $[Cu_3\text{-}O]$ unit, as the charge changes for each of the copper atoms. This would be consistent with the μ_3-O being closer to the Cu_3 plane and greater charge delocalisation

From the DFT calculations it was determined that the most likely explanation for the presence of the $[Cu_3(\mathbf{L}\text{-}H_n)_3\mu_3\text{-}O]^{(+2-n)}$ species in the mass spectra is the electrospray process itself, but more work is required to relate the nature of the ions in the mass spectra with the DFT minimised energies.

6.2.1. A preliminary investigation of the electrochemical properties of the $[Cu_3(L16)_3\text{-}\mu_3\text{-}O/OH)]$ complexes.

The DFT calculations suggest that the trinuclear complexes described in this chapter should show facile redox reactions. Cyclic voltammogram of the $[Cu_3(\mathbf{L16})_3\text{-}\mu_3\text{-}O/OH]^{(+1/+2)}$ system using an Ag/AgCl reference electrode and varying the scan rates from 0.1 to 1.0 V/s are shown in Figures 6.55 A considerable number of processes are observed, for the most part *irreversible* one electron oxidations and reductions. The complexity of the system is enhanced by there being a possibility that different protonation levels are accessible for the cores of the clusters as seen in studies of other systems with $[Cu_3(\mathbf{L}_3)O]/ [Cu_3(\mathbf{L}_3)OH]$ cores.[27,28] It is also possible that oxidised forms will be extremely reactive, given their similar structures to the active sites of oxidases (see Section 6.2.3.4.) and that hydrogen abstraction from solvent

molecules could occur. It has been shown in model systems that the [Cu_3(μ-O)] core of a [Cu_3(**L**$_3$)O](ClO_4)$_2$ can be reduced to the [Cu_3(μ-OH)] with NEt_3 and re-oxidised to [Cu_3(μ-O)] with perchloric acid (see Section 6.2.3.).[27]

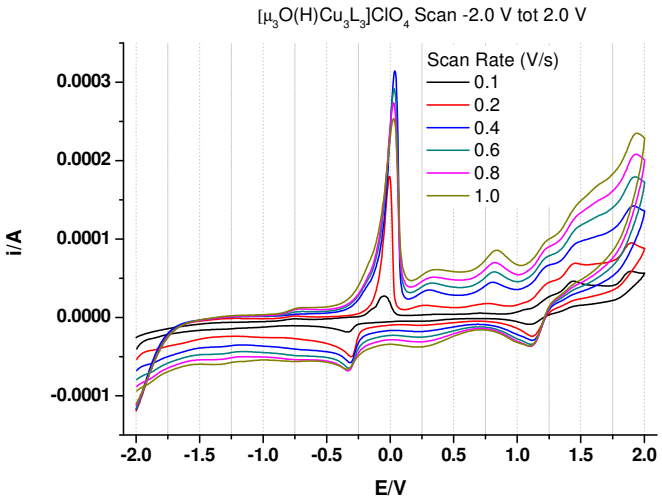

Figure 6.55: Cyclic voltammagram of a solution of [Cu_3(**L16**)$_3$-μ$_3$-O(H)(ClO_4)][ClO_4] in MeCN against an Ag/AgCl reference scanning from -2 to 2 volts at various rates.

Electronic spectra were recorded when [Cu_3(**L16**)$_3$-μ$_3$-O(H)(ClO_4)][ClO_4] or [Cu_3(**L17**)$_3$-μ$_3$-O(H)(ClO_4)][ClO_4] were treated with one molar equivalent of triethyl amine or one molar equivalent of perchloric acid (see Figure 6.56). The changes are striking and consistent.

When one equivalent of perchloric acid is added both complexes lose the bands in the near infrared and in the red regions of their spectra and the appearance of an absorption at around 380 nm indicates that the conventional bis-oxime complexes, [Cu(**L**)$_2$], are formed.

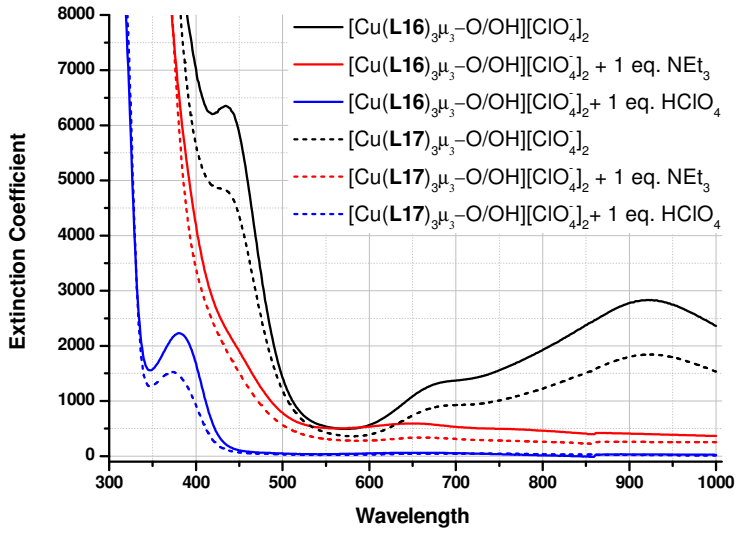

Figure 6.56: The UV/Vis spectra of solutions of $[Cu_3(\mathbf{L16})_3\text{-}\mu_3\text{-}O(H)(ClO_4)][ClO_4]$ or $[Cu_3(\mathbf{L17})_3\text{-}\mu_3\text{-}O(H)(ClO_4)][ClO_4]$ in MeCN (in black) and after treatment with one molar equivalent of triethylamine (in red) or one molar equivalent of perchloric acid (in blue).

Upon addition of one equivalent of triethylamine all features of the spectra in the visible and near infrared region are lost. Addition of base will promote the deprotonation of the tertiary amine nitrogen atoms in **L16** and **L17** and it is likely that this greatly destabilizes the trinuclear complexes, based on the evidence compiled in the work to prepare trinuclear copper(II) complexes, where it was shown that it was only possible to isolate such complexes when protonated pendant amine arms were present.

6.3. Conclusions and future work

Work in this chapter followed an unusual path in which the suggestion from mass spectrometric studies that trinuclear copper complexes of doubly deprotonated phenolic oxime ligands are present in solutions which contain a high Cu : ligand ratio at relatively high pH was followed by successful attempts to prepare, isolate and characterize such complexes in condensed phases.

The ESI-MS work has demonstrated that $[Cu^{(II)}(\mathbf{L}\text{-H})]$ units are effective building blocks for the formation of oligomeric complexes, indicating that polynuclear complexes of phenolic oxime ligands which have so far been observed largely only with trivalent transition metal ions can also be formed with copper(II). This work also suggested that in solutions of low pH and when the ligand : Cu ratio exceeds two then the well know mononuclear, $[Cu(\mathbf{L})_2]$ complexes are the predominant species. Complexes containing the $[Cu_3(\mathbf{L}\text{-H})_3\text{-O}]^-$ unit are favoured by a higher pH and by higher copper concentrations and can be formed by a wide range of phenolic oximes with a variety of 3-X- and 5-R-substituents and by both aldoximes and ketoximes. Heteroleptic, $[Cu_3(\mathbf{LX}\text{-H})_n(\mathbf{LY}\text{-H})_m\text{-O}]^-$ complexes, derived from solutions of two different ligands with copper acetate, were also observed.

The successful isolation of the trinuclear complexes was restricted to systems in which the ligand carries a dialkylaminomethyl substituent adjacent to the phenol which is protonated in the copper complexes and form intramolecular hydrogen bonds to the phenolate donor atoms. The electronic and magnetic properties of the new trinuclear complexes are of considerable interest and should be the subject of future research work.

6.4. Experimental

6.4.1. Ligand Synthesis

6.4.1.1. 1-Ethoxymethylpiperidine (4).

Piperidine (27.42 g, 320 mmol) was added to a suspension of potassium carbonate (59.51 g, 430 mmol) and paraformaldehyde (12.10 g, 400 mmol) in ethanol (1.5 l) dropwise over 30 minutes and the mixture left to stir for 72 h in an ice/water/NaCl bath. After filtration the solvent was removed *in vacuo* to give a colourless liquid, which was purified by vacuum distillation (19.8 g, 43%). ^{1}H NMR (250 MHz, $CDCl_3$): δ_H (ppm) 1.15 (t, 3H, C*H*$_3$), 1.31 (m, 2H, $NCH_2CH_2CH_2$), 1.50 (m, 4H, 2 x $NCH_2CH_2CH_2$), 2.50 (m, 4H, 2 x $NCH_2CH_2CH_2$), 3.72 (q, 2H, OCH_2CH_3), 4.00 (s, 2H, NCH_2O); ^{13}C NMR (63 MHz, $CDCl_3$): δ_C (ppm) 17.5 (1C, $OCH_2\mathbf{C}H_3$), 23.0 (1C, $NCH_2CH_2\mathbf{C}H_2$), 25.0 (2C, 2 x $NCH_2\mathbf{C}H_2CH_2$), 50.0 (2C, 2 x $N\mathbf{C}H_2CH_2CH_2$), 63.5 (1C, $O\mathbf{C}H_2CH_3$), 88.5 (1C, $N\mathbf{C}H_2O$)

6.4.1.2. 3-*tert*-Butyl-2-hydroxy-5-piperidin-1-ylmethylbenzaldehyde (**5**)

3-*tert*-Butyl-2-hydroxybenzaldehyde (3.31 g, 18.6 mmol) and **(4)** (2.93 g, 20.5 mmol) were refluxed in acetonitrile (25 ml) under nitrogen for 4 days. The solvent was removed *in vacuo* to yield an orange-brown oil which was used without further purification (4.96 g, 97%). (Anal. Calc. for $C_{17}H_{25}NO_2$: C, 74.1; H, 9.2; N, 5.1. Found: C, 70.1; H, 8.6; N, 4.1%); ^{1}H NMR ($CDCl_3$, 250 MHz): δ_H (ppm) 1.61 (9H, s, $C(CH_3)_3$), 1.57 (2H, d, $NCH_2CH_2CH_2$), 1.78 (4H, m, 2 x $NCH_2CH_2CH_2$), 2.57 (4H, m, 2 x $NCH_2CH_2CH_2$), 3.62 (2H, s, NCH_2Ar), 7.60 (2H, s, 2 x Ar*H*), 10.06 (1H, s, C*H*O), 11.89 (1H, s, O*H*); ^{13}C NMR ($CDCl_3$, 63 MHz): δ_C (ppm) 24.3 (1C, $NCH_2CH_2\mathbf{C}H_2$), 25.8 (2C, 2 x $NCH_2\mathbf{C}H_2CH_2$), 29.1 (3C, $C(\mathbf{C}H_3)_3$), 34.7 (1C, $\mathbf{C}(CH_3)_3$), 54.3 (2C, 2 x $N\mathbf{C}H_2CH_2CH_2$), 62.9 (1C, $N\mathbf{C}H_2Ar$), 120.2 (1C, aromatic **C**), 129.2 (1C, aromatic **C**), 131.9 (1C, aromatic **C**H), 135.2 (1C, aromatic **C**H),

137.7 (1C, aromatic **C**), 160.0 (1C, aromatic **C**), 197.1 (1C, **C**HO); FABMS *m/z* 84 (100 %), 276 $(MH)^+$ not observed.

6.4.1.3. 3-Bromomethyl-5-*tert*-butylsalicylaldehyde (**6**)

HBr 48% in water (16.87 g, 100.32 mmol) was added to a mixture of 5-*t*-butylsalicylaldehyde (3.00 g, 16.40 mmol) and paraformaldehyde (0.75 g, 26.4 mmol). A few drops (catalytic) of H_2SO_4 conc. were added. The resulting mixture was stirred and heated to 70°C for 20 hrs. This was then allowed to cool to room temperature before water (30 ml) was added and the product extracted into dichloromethane (30 ml). The organic phase was separated and dried over anhydrous Na_2SO_4, the solvent was removed *in vacuo* to yield a yellow oil (4.54 g, 97%). ^{1}H NMR (250 MHz, $CDCl_3$): δ_H (ppm) 11.31 (s, 1H, Ar-O*H*), 9.84 (s, 1H, C*H*O), 7.60 (d, 1H, Ar-*H*), 7.48 (d , 1H, Ar-*H*), 4.56 (s, 2H, CH_2), 1.31 (s, 9H, (CH_3)$_3$). ^{13}C NMR (63 MHz, $CDCl_3$): δ_C (ppm) 196.82 (1C, *C*HO), 157.60 (1C, Ar-*C*-OH), 143.10 (1C, Ar-*C*), 135.70 (1C, Ar-*C*H), 130.88 (1C, Ar-*C*H), 125.96 (1C, Ar-*C*), 120.44 (1C, Ar-*C*), 34.38 (1C, *C*(CH$_3$)$_3$), 31.44 (3C, C(*C*H$_3$)$_3$), 27.27 (1C, *C*H$_2$). ESI *m/z* 268 $(M)H^+$.

6.4.1.4. 5-*tert*-Butyl-3-(4-morpholinomethyl)salicylaldehyde (**7**)

Morpholine (0.87 g, 10 mmol) was dissolved in anhydrous acetonitrile (40 cm^3). To this 3-bromomethyl-5-*t*-butylsalicyladehyde (**6**) (2.74 g, 5 mmol) and K_2CO_3 (2.10g, 15. 0 mmol) were added. The mixture was stirred and heated to reflux under N_2 for 6 hrs. Thereafter the solution was allowed to cool to RT and filtered. The filtrate was evaporated by rotary evaporator to yield a yellow solid. This was redissolved in DCM, filtered and the filtrate taken to dryness to yield a yellow oil. This was purified by silica-60 wet flash column chromatography (3% MeOH in DCM eluent) to yield a pale yellow oil (2.63g, 90%). ^{1}H NMR (250 MHz, $CDCl_3$): δ_H (ppm) 10.30 (s, 1H, C*H*O), 7.60 (d, 1H, Ar-*H*), 7.27 (d, 1H, Ar-*H*), 3.70 (s, 2H, Ar-CH_2N), 2.58 (br, 8H, N(CH_2)$_2$(CH_2)$_2$N), 2.28 (s, 3H, NCH_3), 1.25 (s, 9H, (CH_3)$_3$). ^{13}C NMR (63 MHz, $CDCl_3$): δ_C (ppm) 191.93 (1C, *C*HO), 153.91 (1C, Ar-*C*-OH), 142.03 (1C, Ar-*C*),

133.04 (1C, Ar-*C*H), 124.91 (1C, Ar-*C*H), 122.96 (1C, Ar-*C*), 122.32 (1C, Ar-*C*), 66.65 (1C, *C*H_2), 58.99 (2C, CH_2N-(*C*H_2)$_2$), 52.46 (2C, CH_3N-(*C*H_2)$_2$), 34.04 (1C, *C*(CH_3)$_3$), 31.43 (3C, C(*C*H_3)$_3$).

6.4.1.5. 5-*t*ert-Butyl-3-(4-methylpiperazinomethyl)salicylaldehyde (**8**)

1-Methylpiperazine (1.0 g, 10 mmol) was dissolved in anhydrous acetonitrile (55 cm^3). To this 3-bromomethyl-5-*t*-butylsalicyladehyde (**6**) (2.73 g, 5 mmol) and K_2CO_3 (2.10g, 15. 0 mmol) were added. The mixture was stirred and heated to reflux under N_2 for 6 hrs. Thereafter the solution was allowed to cool to RT and filtered. The filtrate was evaporated by rotary evaporator to yield a yellow solid. This was redissolved in DCM, filtered and the filtrate taken to dryness to yield a yellow oil. This was purified by silica-60 wet flash column chromatography (5% MeOH in DCM eluent) to yield a pale yellow oil (2.60g, 95%). ^{1}H NMR (250 MHz, $CDCl_3$): δ_H (ppm) 10.30 (s, 1H, C*H*O), 7.60 (d, 1H, Ar-*H*), 7.27 (d, 1H, Ar-*H*), 3.70 (s, 2H, Ar-CH_2N), 2.58 (br, 8H, N(CH_2)$_2$(CH_2)$_2$N), 2.28 (s, 3H, NCH_3), 1.25 (s, 9H, (CH_3)$_3$). ^{13}C NMR (63 MHz, $CDCl_3$): δ_C (ppm) 191.93 (1C, *C*HO), 159.41 (1C, Ar-*C*-OH), 142.03 (1C, Ar-*C*), 133.04 (1C, Ar-*C*H), 124.91 (1C, Ar-*C*H), 122.96 (1C, Ar-*C*), 122.32 (1C, Ar-*C*), 60.12 (1C, *C*H_2), 55.02 (2C, CH_2N-(*C*H_2)$_2$), 52.75 (2C, CH_3N-(*C*H_2)$_2$), 46.06 (1C, *C*H_3), 34.27 (1C, *C*(CH_3)$_3$), 31.49 (3C, C(*C*H_3)$_3$).

6.4.2. Oximation

Oximation of **5**, **7** and **8** was carried out according to the gerneral oximation procedure described in Chapter 2 Section 2.4.2.4.

6.4.2.1. 5-*tert*-Butyl-2-hydroxy-3-(piperidin-1-ylmethyl)benzaldehyde oxime **(L16H)**

Hydroxylamine hydrochloride (1.10 g, 15.9 mmol) and potassium hydroxide (0.89 g, 15.9 mmol) were dissolved in ethanol (100 ml) and a white precipitate removed by filtration. The filtrate was added to **(16)** (4.37 g, 15.9 mmol) and heated under reflux for 2 hours to give an orange solution. The solvent was removed *in vacuo* to give a pale orange solid. Dichloromethane (3 x 30 ml) was added to the flask and the resulting orange suspension filtered. The solvent was removed from the filtrate *in vacuo* to yield a white solid (3.69 g, 80%). (Anal. Calc. for $C_{17}H_{26}N_2O_2$.EtOH; C, 67.82; H, 9.59; N, 8.33. Found: C, 67.6; H, 9.8; N, 8.3%); all other analysis was concordant with the literature reference.[51]

6.4.3. Complex Synthesis

6.4.3.1. [Cu(**L16**)$_2$]

A solution of **L16H** (0.292 g, 1.0 mmol) in MeOH (10 ml) was added to a solution of $Cu(OAc)_2.H_2O$ (0.100 g, 0.5 mmol) in MeOH (10ml) the resulting brown suspension was stirred for 20 minutes, filtered and dried under vacuum yielding a brown solid. (0.29 g, 91%). Crystals suitable for X-ray diffraction analysis were grown by slow evaporation of a hexane/DCM solution.

6.4.3.2. [Cu(**L16H**)Cl$_2$]

A solution of **L16H** (0.292 g, 1.0 mmol) in MeCN (10 ml) was added to a solution of $Cu(Cl)_2.4H_2O$ (0.205 g, 1.0 mmol) in MeCN (20ml) the resulting dark red solution was stirred for 30 minutes the solvent was removed by rotary evaporation and dried under vacuum yielding a dark red/purple solid. (0.392 g, 92%). Crystals suitable for X-ray diffraction analysis were grown by vapour diffusion of a diethyl ether into MeCN.

6.4.3.3. $[(Cu)_3(\mathbf{L16})_3\text{-}\mu_3\text{-}OH][ClO_4]_2$

A solution of $Cu(OAc)_2.H_2O$ (0.2 g, 1 mmol, 1.0 Eq.) in MeCN (20 mL) was added to the stirred solution of triethylamine (1.5 mL, 5 mmol, 5 Eq.) and **L16H** (0.290 g, 0.1 mmol) in MeCN (20 mL). The resulting dark green solution was stirred for 30 mins at room temperature and solvents were removed *in vacuo* yielding a dark green crystalline solid. The solid was redissolved in distilled water (20 mL) and to this a solution of lithium perchlorate (0.52 g, 5 mmol, 5 Eq.) in distilled water (10 mL) was added. The resulting dark green suspension was stirred for 30 mins and filtered yielding **2** as a dark green powder. (0.39 g, 91 %) Anal. Calc. for: $[(C_{51}H_{76}Cl_2Cu_3N_6O_{15})_2,3H_2O]$ Elemental Analysis: C, 47.1; H, 6.1; N, 6.2. Found: C, 47.1; H, 5.9; N, 6.4); ESIMS *m/z* 537.46 $[(Cu)_3(\mathbf{L16})_3\mu_3\text{-}O]^{2+}$

Crystals suitable for X-ray diffraction analysis were grown by slow diffusion of layered MeCN/diethyl ether into H_2O.

6.5. References

(1) Takats, Z.; Nanita, S. C.; Cooks, R. G.; Schlosser, G.; Vekey, K. *Anal. Chem.* **2003**, *75*, 1514.

(2) Hirabayashi, A.; Sakairi, M.; Koizumi, H. *Anal. Chem.* **1994**, *66*, 4557.

(3) Enke, C. G. *Anal. Chem.* **1997**, *69*, 4885.

(4) Sakamoto, S.; Fujita, M.; Kim, K.; Yamaguchi, K. *Tetrahedron* **2000**, *56*, 955.

(5) Sakamoto, S.; Imamoto, T.; Yamaguchi, K. *Org. Lett. 3* **2001** 1793.

(6) Sakamoto, S.; Nakatani, K.; Saito, I.; Yamaguchi, K. *Chem. commun.* **2003**, 788.

(7) Yamaguchi, K. *J. Mass Spectrom.* **2003**, *38*, 473.

(8) Therrien, B.; Vieille-Petit, L.; Suss-Fink, G.; Sei, Y.; Yamaguchi, K. *J.Organomet. Chem.* **2004**, *689*, 2820.

(9) Johnstone, K. D.; Yamaguchi, K.; Gunter, M. J. *Org. & Biomolecular Chem.* **2005**, *3*, 3008.

(10) Autodesk 2009.

(11) Takats, Z.; Wiseman, J. M.; Gologan, B.; Cooks, R. G. *Anal. Chem.* **2004**, *76*, 4050.

(12) Szymanowski, J. *Hydroxyoximes and Copper Hydrometallurgy*; CRC Press: Boca Raton, USA, 1993.

(13) Tasker, P. A.; Plieger, P. G.; West, L. C. *Comprehensive Coordination Chemistry II* **2004**, *9*, 759.

(14) Borowaik-Resterna, A.; Szymanowski, J. *J. Radioanalytical and Nuc. Chem.* **1991**, *150*, 435.

(15) Keeny, M. E.; Osseo-Asare, K. *Int. Solvent Extr. Conf.* **1983**, *7*, 345.

(16) Keeny, M. E.; Osseo-Asare, K. *Polyhedron* **1984**, *3*, 641.

(17) Rindorf, G. *Acta Chem. Scand.* **1971**, *25*, 774.

(18) O'Brian, P.; Thornbeck, J. R.; Szymanowski, J. *J. Coord. Chem.* **1983**, *13*, 11.

(19) Preston, J. S. *J. Inorg. Nucl. Chem.* **1975**, *37*, 1235.

(20) Green, R. W.; Svasti, M. C. K. *Aust. J. Chem.* **1963**, *16*, 356.

(21) Hoskins, B. F.; Beckett, R. *J. C. S. Dalton* **1972**, 291.

(22) Young, J.; Murmann, R. K. *J. Phys. Chem.* **1963**, *67*, 2647.

(23) Ross, P. F.; Murmann, R. K.; Schlemper, E. O. *Acta. Cryst.* **1974**, *B30*, 1120.

(24) Datta, D.; Maschrak, P. K.; Chakravorty, A. *Inorg. Chim. Acta* **1978**, *27*, L95.

(25) Butcher, R. J.; O'Connor, C. J.; Sinn, E. *Inorg. Chem.* **1981**, *20*, 537.

(26) Costes, J. P.; Dahan, F.; Laurent, J. P. *Inorg. Chem.* **1986**, *25*, 413.

(27) Datta, D.; Chakravorty, A. *Inorg. Chem.* **1982**, *21*, 363.

(28) Datta, D.; Chakravorty, A. *Inorg. Chem.* **1983**, *22*, 1611.

(29) Schmolander, K. *Acta. Chim. Scand.* **1983**, *A37*, 5.

(30) Agnus, Y.; Louis, R.; Metz, B.; Boudon, C.; Gisselbrecht, J. P.; Gross, M. *Inorg. Chem.* **1991**, *30*, 3155.

(31) Baral, S.; Chakravorty, A. *Inorg. Chim. Acta* **1980**, *39*, 1.

(32) Contaldi, S.; Di Nicola, C.; Garau, F.; Karabach, Y. Y.; Martins, L. M. D. R. S.; Monari, M.; Pandolfo, L.; Pettinari, C.; Pombeiro, A. J. L. *Dalton Trans.* **2009**, 4928.

(33) Stamatatos, T. C.; Vlahopoulou, J. C.; Sanakis, Y.; Raptopoulou, C. P.; Psycharis, V.; Boudalis, A. K.; Perlepes, S. P. *Inorg. Chem. Comm.* **2006**, *9*, 814.

(34) Mezei, G.; Rivera-Carillo, M.; Raptis, R. G. *Dalton Trans.* **2007**, 37.

(35) Curtis, N. F.; Gladkikh, O. P.; Heath, S. L.; Morgan, K. R. *Aust. J. Chem.* **2000**, *53*, 577.

(36) Afrati, T.; Zaleski, C. M.; Dendrinou-Samara, C.; Mezei, G.; Kampf, J. W.; Pecoraro, V. L.; Kessissoglou, D. P. *Dalton Trans.* **2007**, 2658.

(37) Smith, A.; Tasker, P. A.; White, D. J. *Coord. Chem. Rev.* **2003**, ***241***, 61.

(38) Inglis, R.; Jones, L. F.; Milios, C. J.; Datta, S.; Collins, A.; Parsons, S.; Wernsdorfer, W.; Hill, S.; Perlepes, S. P.; Piligkos, S.; Brechin, E. K. *Dalton Trans.* **2009**, 3403.

(39) Inglis, R.; Jones, L. F.; K.Mason; Collins, A.; Moggach, S. A.; Parsons, S.; Perlepes, S. P.; W.Wernsdorfer; Brechin, E. K. *Chem.-Eur. J* **2008**, *14*, 9117.

(40) Jones, L. F.; Inglis, R.; M.E.Cochrane; Mason, K.; Collins, A.; Parsons, S.; Perlepes, S. P.; Brechin, E. K. *Dalton Trans.* **2008**, 6205.

(41) Stoumpos, C. C.; Inglis, R.; Karotsis, G.; Jones, L. F.; Collins, A.; Parsons, S.; Milios, C. J.; Papaefstathiou, G. S.; Brechin, E. K. *Cryst. Growth Des.* **2009**, *9*, 24.

(42) Milios, C. J.; Inglis, R.; Vinslava, A.; Bagai, R.; Wernsdorfer, W.; Parsons, S.; Perlepes, S. P.; Christou, G.; Brechin, E. K. *J. Am. Chem. Soc.* **2007**, *129*, 12505.

(43) Dong, W.-K.; Duan, J.-G.; L.-Q.Chai; Liu, G.-L.; H.-L.Wu *J. Coord. Chem.* **2008**, *61*, 1306.

(44) Dong, W.-K.; Duan, J.-G.; Guan, Y.-H.; Shi, J.-Y.; Zhao, C.-Y. *Inorg. Chim. Acta* **2009**, *362*, 1129.

(45) Verani, C. N.; Bothe, E.; Burdinski, D.; Weyhermuller, T.; Florke, U.; Chaudhuri, P. *Eur. J. Inorg. Chem.* **2001**, 2161.

(46) Gass, I. A.; Milios, C. J.; Whittaker, A. G.; Fabiani, F. P. A.; Parsons, S.; Murrie, M.; Perlepes, S. P.; Brechin, E. K. *Inorg. Chem.* **2006**, *45*, 5281.

(47) Mason, K.; Gass, I. A.; Parsons, S.; Collins, A.; White, F. J.; Slawin, A. M. Z.; Brechin, E. K.; Tasker, P. A**.** *Dalton Trans.* **2010**, *39*, 2727.

(48) Thorpe, J. M.; Beddoes, R. L.; Collison, D.; Garner, C. D.; Helliwell, M.; Holmes, J. M.; Tasker, P. A. *Angew. Chem., Int. Ed.* **1999**, *38*, 1119.

(49) Wenzel, M.; Forgan, R. S.; Faure, A.; Mason, K.; Tasker, P. A.; Piligkos., S.; Brechin, E. K.; Plieger, P. G. *Eur. J. Inorg. Chem.* **2009**, *31*, 4613.

(50) Yoon, J.; Solomon, E. I. *Inorg. Chem.* **2005**, *44*, 8076.

(51) Chan, S. I.; Wang, V. C.-C.; Lai, J. C.-H.; Yu, S. S.-F.; Chen, P. P.-Y.; Chen, K. H.-C.; -L., C. C.; K., C. M. *Angew. Chem., Int. Ed.* **2007**, *46*, 1992.

(52) Rivera-Carillo, M.; Chakraborty, I.; Mezei, G.; Webster, R. D.; Raptis, R. G. *Inorg. Chem.* **2008**, *47*, 7644.

(53) Forgan, R. S. PhD Thesis, The University of Edinburgh, 2008.

(54) Henry, D. C. R. PhD Thesis, The University of Edinburgh, 2007.

(55) Wang, Q.; Wilson, C.; Blake, A. J.; Collinson, S. R.; Tasker, P. A.; Schroder, M. *Tetrahedron Lett.* **2006**, *47*, 8983.

(56) Grigg, J., PhD Thesis, University of Manchester, 1994.

(57) Forgan, R. S., PhD Thesis, University of Edinburgh, 2008.

(58) Plieger, P. G., Personal Communication to Roach, B. D., **2010.**

CHAPTER 7: Conclusions and Future Work

The Significance of the Work in this Thesis

7.1 Conclusions and Future Work

The aim of establishing to what extent mass spectrometry can be used to determine the relative stabilities of metal complexes of a coherent series of ligands and thus rank their strengths as metal extractants has been addressed successfully. One of the major issues which arises is that only charged species can be analysed in mass spectrometry and it is likely that their relative stabilities will not be the same as those of the parent neutral complexes which are formed in the non-polar liquids used in solvent extraction. Nevertheless, mass spectrometry proved to be a useful tool in understanding the effects of substituents on the inner- and outer-coordination spheres of phenolic oxime copper complexes of the type, [Cu(**L**)$_2$], shown in Figure 7.1.For a coherent series of complexes which undergo very similar fragmentation pathways in the mass spectrometer, collision induced dissociation provides the relative stabilities of the ionic species, [M(**L**)(**L**-H)]$^-$ and [M(**L**)(**L**+H)]$^+$ obtained by electrospraying solutions of the [M(**L**)$_2$] complexes, and it has been possible to interpret how these depend on the nature of the X, R and R^1 substituents (see Figure 7.1). The influence the substituents have on the stability of the inner and outer spheres of the complex ions is generally very similar to that of observed for the parent neutral complexes.

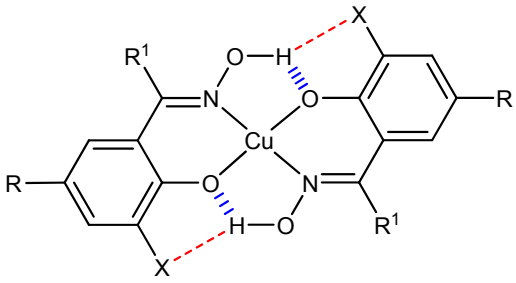

Figure 7.1: Structure of phenolic oxime based copper complexes of the type [Cu(**L**)$_2$].

In competition studies when two ligands of different extraction strengths are mixed with Cu(II) acetate the relative intensities of the ions of the homoleptic and heteroleptic complexes in electrospray mass spectra was consistent with the known relative strengths of the ligands as copper solvent extractants. This was true in every

case when just one of the X, R or R^1 substituents in Figure 7.1 were varied, suggesting that under these circumstances the ionization efficiencies of the complexes do not differ greatly and their peak intensities correspond to the concentration on the neutral complxes in solution. Further research into the use of mass spectrometry as a *quantitative* tool to determine actual complex concentrations in solution is needed.

The usefulness of ESI and SSI-MS techniques to probe solution speciation has been demonstrated by the work showed that trinuclear copper complexes of the type $[Cu_3(\mathbf{L}\text{-}H)_3\text{-}\mu_3O]^-$ can be formed Cu(II) is present in excess in solution. This has lead to subsequent characterisation in both solution and solid states of this novel coordination environment for phenolic oximes copper complxes. The electronic and magnetic properties of the new trinuclear complexes are of considerable interest and should be the subject of future work.

Density functional theory calculations which were initially undertaken to provide information on the bonding in the inner and outer-coordination spheres of the ions generated by electrospray techniques, have proved to be unexpectedly useful in guiding ligand design for extractants which form *neutral* $[M(\mathbf{L})_2]$ complexes. Energy minimisation of the gas phase structures of the ligands, **LH**, the ligand dimers, $[(\mathbf{LH})_2]$ and their $[M(\mathbf{L})_2]$ complexes has allowed enthalpies of formation of the $[M(\mathbf{L})_2]$ complexes to be determined. The calculated values for different ligands within a coherent series correlate remarkably well with their measured strengths as metal solvent extractants. DFT calculations offer the possibility of predicting substituent effects on the strength and selectivity of metal extractants when the variation of substituent does not result in major differences in the solvation energies of ligands and complexes, as is quite often the case when the water immiscible solvent has very low polarity. Other projects involving extractant development in the group at Edinburgh are now routinely using such calculations and these are proving to be particularly useful in the design of buttressing groups to enhance the strength of extractants. Several candidate extractants currently under development in the industrial sponsor's laboratory involve such groups.

Phenolic Oxime Copper Complexes:
A Gas Phase Investigation

CHAPTER 8:

Appendices

Electronic Supplementary Information for this Thesis

8.1. Appendices for Chapter 1

8.1.1. Diagrams and Figures

8.2. Appendices for Chapter 2

8.2.1. Diagrams and Figures
8.2.2. Origin Files
8.2.3. Data Manipulation
8.2.4. Calculation Data

8.3. Appendices for Chapter 3

8.3.1. Diagrams and Figures
8.3.2. Origin Files
8.3.3. Crystal Structures for **L1bH** and **L8bH**
8.3.4. Calculation Data

8.4. Appendices for Chapter 4

8.4.1. Diagrams and Figures
8.4.2. Origin Files
8.4.3. Calculation Data

8.5. Appendices for Chapter 5

8.5.1. Diagrams and Figures
8.5.2. Origin Files
8.5.3. Quantification Attempts
8.5.4. Extraction Data

8.6. Appendices for Chapter 6

8.6.1. Diagrams and Figures
8.6.2. Origin Files
8.6.3. Crystal Structure information
8.6.4. Calculation Data
8.6.5. Mass spectrometry data on nitriles

All appendices data to be found on attached disk along with an electronic copy of this thesis.